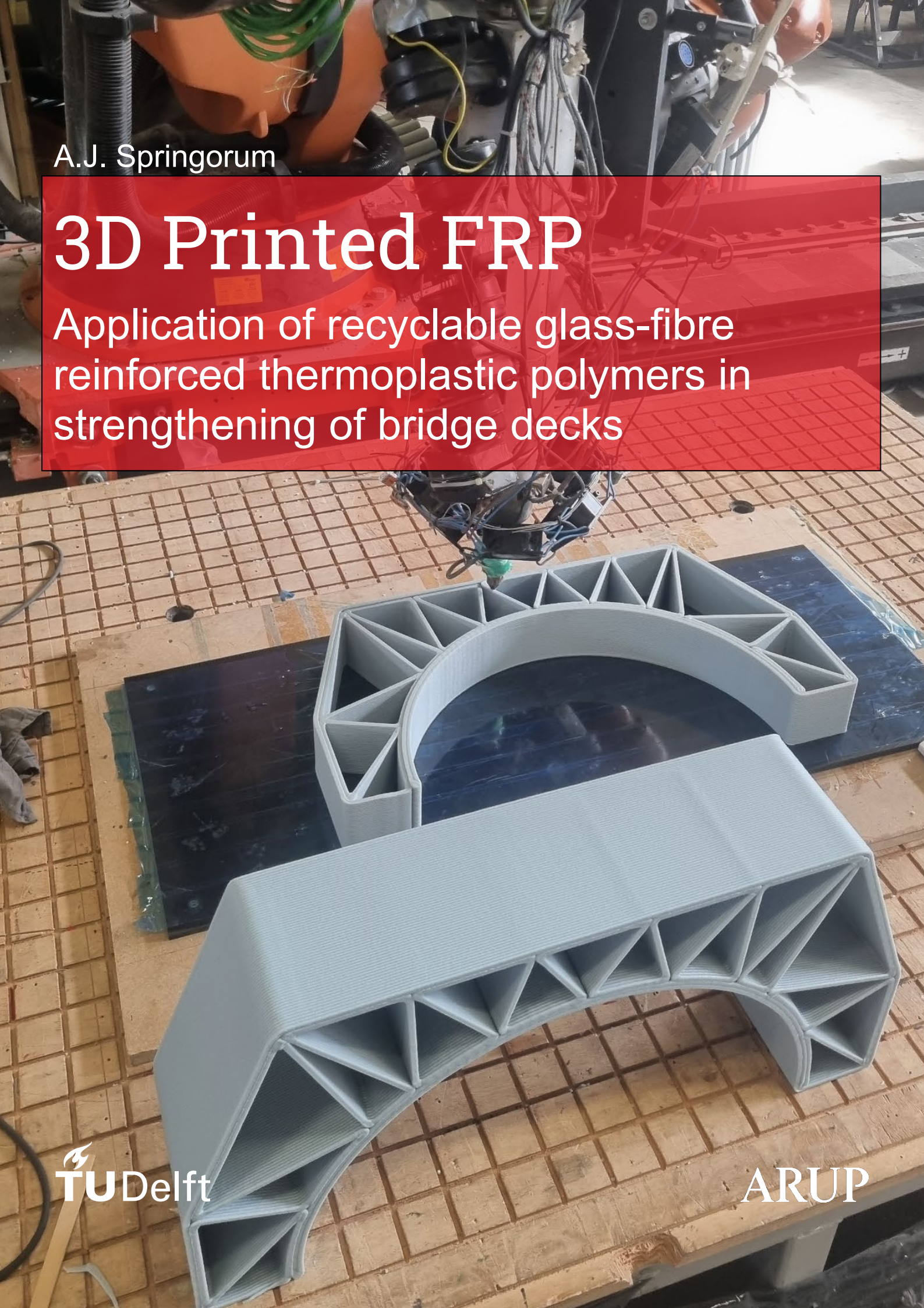

A.J. Springorum

3D Printed FRP

Application of recyclable glass-fibre reinforced thermoplastic polymers in strengthening of bridge decks

TU Delft

ARUP

3D Printed FRP

Application of recyclable glass-fibre reinforced thermoplastic polymers in strengthening of bridge decks

By

A.J. Springorum

in partial fulfilment of the requirements for the degree of

Master of Science
Structural Engineering | Steel, Timber, and Composite Structures

at the Delft University of Technology, Faculty of Civil Engineering and Geosciences
to be defended publicly on Monday, July 8th, 2024, at 01:30 PM.

Student number:	4888774	
Project duration:	September 2023 – July 2024	
Thesis committee:	Dr. M. Pavlovic	TU Delft
	Dr. O. Karpenko	TU Delft
	Dr. C. Ayas	TU Delft
	Ir. F. Csillag	Arup

TU Delft ARUP

Preface

This thesis marks the finalization of my Civil Engineering studies at the Delft University of Technology. After I finished my bachelor's degree at the Faculty Civil Engineering and Geosciences, I continued with the master track Structural Engineering with the specialization Steel, Timber, and Composite Structures. From the Fibre Reinforced Polymer Structures course, I got interested in composites and saw the potential it. With this research project, provided by a collaboration between Arup and TU Delft, I got the opportunity to combine the development of this relatively new construction material with 3D printing, a relatively new production technique. The combination of material research and design motivated me to incorporate manufacturing characteristics in the structural behaviour and analysis of the material.

This research project was a project within Arup at the behest of Rijkswaterstaat. During this project, several partners were involved. Mitsubishi Chemical Performance Polymers, department of the Mitsubishi Chemical Group, supplied the material investigated in this research. They produced the material and delivered it to HB3D. HB3D is the print partner in this project.

I would like to thank my thesis committee for their support and feedback during my thesis project. My daily supervisors Olena Karpenko from the TU Delft and Fruzsina Csillag from Arup guided and helped me with both the content of my thesis project as the practical parts of it. The chair of my committee, Marko Pavlovic, inspired me with some sharp analyses and critical questions. Regarding 3D printing, I learned a lot from the feedback of Can Ayas. Besides my thesis committee, I would like to express my gratitude to the technicians in the Stevinlaboratory of the Faculty Civil Engineering and Geosciences at the TU Delft, with Derek van Bochove in particular, who helped me a lot with preparing and executing the tests.

Arjen Springorum

Delft, July 2024

Summary

Since a lot of bridges in the Netherlands have degraded over time, they require strengthening or (partial) replacement [1]. Previously, the possibility to apply 3D printed fibre reinforced polymers (FRP) for strengthening of bridge decks was investigated by Arup. In this study was concluded that the field of movable bridges with timber decks has the highest potential. The timber deck, laid on steel stringers, should be replaced by an arch-shaped 3D printed FRP element, which will be placed in between the stringers [2]. The print/material partner from the previous study [1,2] retired and therefore, new research had to be done with material from another supplier, printed by another partner. This research focuses on the configuration and the properties of the new material, a recyclable thermoplastic glycol-modified polyethylene terephthalate (PETG) composite with glass fibres, and the optimization of the preliminary design.

The starting point of this research project was to investigate what the best material configuration was in terms of amount of fibres and way of printing. A fibre volume fraction (V_f) of 30% (GF30%) and 45% (GF45%) was considered. Is it possible to achieve more strength and stiffness by having a higher V_f without the material being too brittle or reducing the bond capacity of the layers? Since the fibres are orientated in the direction of printing, tensile tests in the principal direction will be performed to investigate the effect of the V_f.

With 3D printing, the element will be printed layer by layer. During the printing process, the material is melted, extruded, and cools down to harden. The longer it takes to print one layer, the more the material can cool down before the next layer is printed on top, the larger the temperature difference between the two layers will be. This difference in temperature determines the bond strength of the layers. Therefore, several layer times (80, 100, and 120 seconds) are considered to investigate what the maximum layer time should be before the bond strength decreases too much. This will be examined by tensile testing perpendicular to the print direction

The test results showed that the structural performance of the GF45% material has a better structural performance than GF30% without being more brittle or having a significant lower strength in transverse direction. The GF45% material had a strength of 102.1 MPa and a stiffness of 22,040 N/mm^2 in principal direction compared to 71.3 MPa and 13,920 N/mm^2 respectively for GF30%. The two materials, printed with 80 seconds layer time, had a comparable strength in transverse direction with 20.4 MPa (GF30%) and 19.7 MPa (GF45%). The increased layer time was tested with the GF30% material. When the layer time was increased to 100 and 120 seconds, the strength decreased: 8.7 MPa for 100s and 7.7 MPa for 120s. Thus, the optimal configuration for the material is a 45% V_f and a maximum layer time of 80 seconds.

Having the optimal configuration determined, the mechanical properties of this material configuration should be established to be able to make a model for the design of the bridge deck element. These properties will be used in the finite element analysis (FEA) of the final design. The mechanical properties of the material are derived from tensile tests in longitudinal and transverse direction, compression tests in both directions, and shear tests. The investigated shear strength is the shear strength between the print layers, called the interbead shear strength (IBSS). The values of the mechanical properties are given in Table 0-1.

Table 0-1 Mechanical properties of the V_f 45% material printed with a layer time of 80 seconds

Property	Characteristic strength value	Stiffness value
Tensile principal direction	$\sigma_{1,tk}$ = 93.8 MPa	$E_{1,t}$ = 21,430 N/mm^2
Tensile transverse direction	$\sigma_{2,tk}$ = 16.8 MPa	$E_{2,t}$ = 5,650 N/mm^2
Compression principal direction	$\sigma_{1,ck}$ = 93.5 MPa	$E_{1,c}$ = 8,010 N/mm^2
Compression transverse direction	$\sigma_{2,ck}$ = 29.8 MPa	$E_{2,c}$ = 2,380 N/mm^2
IBSS	$\tau_{21,k}$ = 11.6 MPa	G_{21} = 3,200 N/mm^2

With these mechanical properties known, the design of the bridge deck component was optimized. The arch shape of the preliminary design is kept. The infill, design of print path and thickness of the top plate, side plates and arch will be varied. In this way, three distinctive design variants were made. From the analysis, it was derived that: the print path should have the same start and end point to enable symmetric stacking of the layers; the most extensive infill of the three variants performs the best from a structural point of view; and the thicknesses of the top plate, the arch and the side plates should be 2t, 3t, and 1t – 2t respectively. The thickness t is the thickness of a print layer, which is the width of the bead (6.0 millimetres). Since local eccentricities, due to transition points from single to double or double to triple layers, introduces unfavourable bending and thus, an increase in local stresses, local eccentricities should be avoided in the design of the print path. Lastly, the shape of the arch was varied. The circular shaped arch is preferred over a parabolic shaped arch because of better printability, although the structural design checks were comparable. The final design of the strengthening bridge deck element is presented in Figure 0-1.

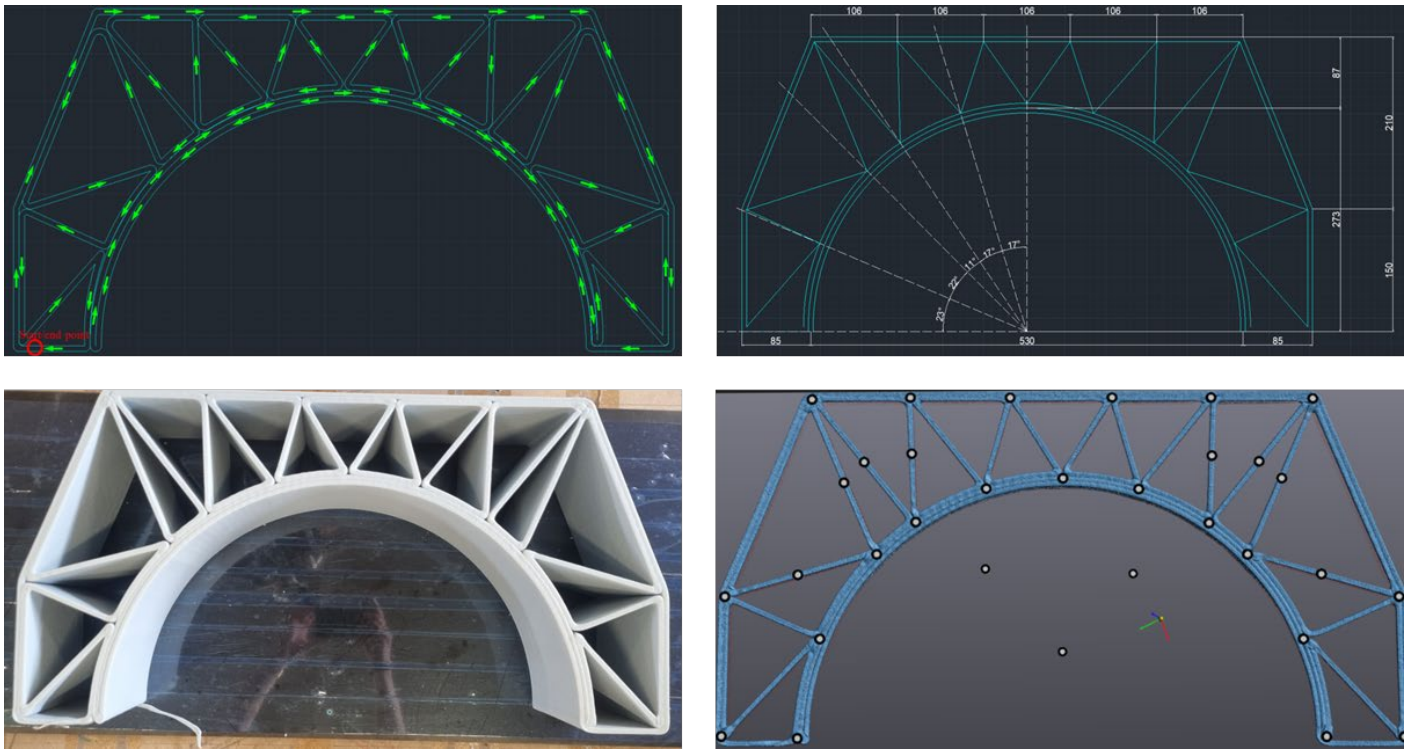

Figure 0-1 Final design of the bridge deck component

The results from the tests proved that a bridge deck element according to the final design is suitable for strengthening application. The two tested components showed consistent behaviour and were able to carry a wheel load. Moreover, a crack initiation and propagation failure mode occurred. This meant that the force remains at a certain load level above the required minimum equivalent wheel load without having collapsing failure. So, decks of movable bridges can be strengthened by the designed component with the 45% V_f and 80 s layer time configuration.

During the component tests, the failure mechanisms occurred was cracking at the intersection between the stiffeners and the arch. For follow-up, one could investigate a way to improve the connectivity between two stiffeners coming together at the arch, for example by increasing the overlap. Another issue for further research is the fatigue performance of the material and this component since this research is based on static analysis. Besides the properties and design aspect, assembly of the component should be investigated. Inverted T-girders with an additional plate on top could be an alternative to the I-girders as stringers, like in the preliminary design.

Contents

Nomenclature

List of abbreviations

3D	Three Dimensional
AFRF	Aramid (Kevlar) fibre-reinforced filaments
CF	Carbon fibres
CFAM	Continuous Fibre Additive Manufacturing
CFF	Continuous Filament Fabrication
CFRF	Carbon fibre-reinforced filaments
DIC	Digital Image Correlation
GF	Glass fibres
GF30%	FRP with 30% glass fibre volume fraction
GF45%	FRP with 45% glass fibre volume fraction
GF30_80s	Composite material with 30% glass fibres and printed with a layer time of 80 seconds
GF30_100s	Composite material with 30% glass fibres and printed with a layer time of 100 seconds
GF30_120s	Composite material with 30% glass fibres and printed with a layer time of 120 seconds
GF45_80s	Composite material with 45% glass fibres and printed with a layer time of 80 seconds
GFRF	Glass fibre-reinforced filaments
GFRF-HSHT	High-strength/high-temperature glass fibre-reinforced filaments
FDM	Fused Deposition Modelling
FEA	Finite Element Analysis
FEM	Finite Element Modelling
FFF	Fused Filament Fabrication
FRF	Fibre-reinforced filaments
FRP	Fibre Reinforced Polymer
IBSS	Interbead Shear Strength
ILSS	Interlaminar/Interlayer Shear Strength
LM1	Load Model 1 from NEN-EN 1991-2
LM2	Load Model 2 from NEN-EN 1991-2
long	longitudinal direction = the principal direction, in direction of printing
OSD	Orthotropic Steel Deck
PA6	Polyamide 6 (Nylon)
PET	Polyethylene Terephthalate
PETG	Polyethylene Terephthalate Glycol
PJM	Polyjet Modelling
rPET	Recycled Polyethylene Terephthalate

SLA	Stereolithography
SLS	Serviceability Limit State
SLS	Selective Laser Sintering
tran	transverse/transversal = perpendicular to the direction of printing
TS	Tandem system
UDL	Uniformly distributed load
ULS	Ultimate Limit State
V_f	Fibre volume fraction

List of symbols

Symbol	*Unit*	*Name*
A	mm^2	Area
α_{crit}	-	Load stability factor
γ	-	Shear strain
Δl	mm	Change in length
E_1	N/mm^2	Young's modulus in longitudinal direction (0°)
E_2	N/mm^2	Young's modulus in transverse direction (90°)
$\varepsilon_{1,c}$	-	Compressive strain in longitudinal direction (0°)
$\varepsilon_{1,t}$	-	Tensile strain in longitudinal direction (0°)
$\varepsilon_{2,c}$	-	Compressive strain in transverse direction (90°)
$\varepsilon_{2,t}$	-	Tensile strain in transverse direction (90°)
F	kN	Force
G_{12}	N/mm^2	In-plane shear modulus
G_{21}	N/mm^2	Interbead shear modulus
G_{23}	N/mm^2	Shear modulus out of plane
Λ	-	Stress ratio
L_{pp}	m	Print path length
l_0	mm	Original length
l_1	mm	Current length
v	-	Poisson's ratio
τ_{12}	MPa	In-plane shear strength
τ_{21}	MPa	Interbead shear strength
$\sigma_{1,c}$	MPa	Compressive stress in longitudinal direction (0°)
$\sigma_{1,t}$	MPa	Tensile stress in longitudinal direction (0°)
$\sigma_{2,c}$	MPa	Compressive stress in transverse direction (90°)
$\sigma_{2,t}$	MPa	Tensile stress in transverse direction (90°)
$\sigma_{xx,mid}$	MPa	Mid-plane stress in the principal print direction
$\sigma_{xx,top/bot}$	MPa	Top or bottom stress in the principal print direction
$\sigma_{yy,c,mid}$	MPa	Mid-plane compressive stress perpendicular to print direction
$\sigma_{yy,c,top/bot}$	MPa	Top or bottom compressive stress perpendicular to print direction
$\sigma_{yy,t,mid}$	MPa	Mid-plane tensile in the principal print direction

$\sigma_{yy,c,top/bot}$	MPa	Top or bottom tensile stress perpendicular to print direction
$\sigma_{xy,mid}$	MPa	In-plane shear stress at mid-plane
T_g	°C	Glass transition temperature
t	mm	Thickness (bead width)
V_f	%	Fibre volume fraction

List of Figures

List of Tables

1

Introduction

1.1 Problem context

In the Netherlands, a substantial portion of the infrastructure has been built over 50 years ago. Some structures are reaching the end of their lifetime or have degraded over time and require maintenance or repair. If this is not economically viable, structures will be renovated or replaced. To extend the lifespan, partial replacement and strengthening of a structure can be done [1]. Fiber Reinforced Polymer (FRP) can be an attractive option to apply for strengthening or replacement due to its high strength-to-weight ratio and its tailorability. The low self-weight of the material gives the possibility to strengthen the bridge without an enormous increase in permanent load. The purpose is to strengthen the bridge by applying 3D printed FRP elements in the deck of the superstructure. The application is an element which will be between the stringers and on top of the cross girders [2]. The deck will be finished with a FRP plate on top of those elements and the stringers. The main field of application will be in movable bridges to replace a timber deck. In those structures, a timber deck is laid on top of the stringers.

Regarding the production method of FRP, this research will focus on 3D printed FRP. 3D printing provides freedom of shape of the elements which will be applied. In combination with a recyclable thermoplastic polymer material, the innovative 3D printing technology represents a potential sustainable temporary solution.

Before this research, Arup studied the possibilities of applying 3D printed FRP for strengthening of bridge decks. This was done based on the Arnite material from Covestro. A preliminary design was made, based on mechanical properties provided by the material supplier. Some of these material properties were determined by testing and others were assumed. The design was made for the application to replace timber decks of movable bridge, which seemed to have the highest potential for this application. However, the partner retired from the project. This causes a drawback in the research development. With a new material supplier and 3D print partner, the research could continue by investigating the properties of the new, but still comparable, material and optimizing the preliminary design of the previous study for the application of strengthening of bridge decks.

1.2 Why this research?

This research project focuses on the evaluation and characterization of 3D printed FRP. The following material will be investigated and tested to apply it for strengthening bridge decks. But why is it relevant to apply FRP? And why should it be produced by 3D printing? This section will explain why 3D printed FRP an appropriate application is for strengthening bridge decks and the relevance of this this research.

1.2.1 Why 3D printing?

3D printing is a relatively new production method. It is not only applicable for small products, but nowadays 3D printing can also be used to produce structural elements. 3D printing has some significant benefits, which make it an interesting option to use. The main benefits of 3D printing are [3]:

- Fast production/assembly: Additive manufacturing is an automated process which can run continuously. Human labour can be saved because of the automated printing process. When the printing process is completed, the whole product is finished or several parts of the construction are manufactured, which only must be assembled. So, the modular components could be installed relatively quickly. This reduces the production time significantly. Moreover, with certain software, the element or product can directly be printed from the software in which it is designed.
- Efficient use of materials: Since the printer only uses the amount of material, which is needed, the waste of material is limited. The product can be built up layer by layer. Also, the use of recycled materials is possible, in favour of sustainability.
- Free formability: Additive manufacturing can make elements in different forms and shapes which suit the solution or application. The machine follows the print path and manufactures the product. No moulding, welding, bolting, etc is required.
- Reducing costs: Although the production method itself is not a cheap option, it saves some money on other aspects of a project. Due to the fast production and easy assembly, time and labour are saved. So, fewer man-hours are required. Moreover, due to the efficient use of materials, the costs for the (raw) materials can be minimized. Since recycled materials can also be used for additive manufacturing, the shadow costs of production can also be reduced, regarding sustainability.

1.2.2 Why 3D Printed FRP?

FRP has a lot of potential in bridge structure applications. The main benefits of an FRP composite are [4]:

- It is a lightweight material with good mechanical properties. FRP has a high strength/stiffness-density ratio. This is beneficial for the application to strengthen bridge decks. Because the material is lightweight, the permanent load from self-weight does not increase so much relatively. And because it still has a good mechanical performance, the bridge deck can be strengthened significantly.
- FRP is durable, due to its corrosion resistance and fatigue resistance. A good durability performance is desirable because of the number of bridges that must be renovated or replaced. When the durability is high, there is no need for maintenance or replacement for quite a while. This is a large benefit regarding the current problem of the state of the bridges nowadays.
- The material has free formability and is therefore a tailorable material. This is especially useful for the application of bridge strengthening. Strengthening elements should be applied to different (types of) bridges. The structures and/or dimensions of different bridges will vary. Therefore, it is desirable that the design of the strengthening element can be adjusted to the specific bridge it should fit.

The free formability of FRP forms the link with the production method of interest in this project, 3D printing. By 3D printing, shapes can be produced which are not possible to produce by pultrusion or injection moulding for example. The material is heated, melted, extruded, and cools down during production by 3D printing. This is only possible with a thermoplastic resin because thermoset polymers are not re-meltable. Since a thermoplastic polymer is re-meltable, it is better recyclable than thermoset material, which is beneficial in terms of sustainability. The material for the resin of the composite in this research project will be a recyclable thermoplastic polymer. On the other hand, the challenge with a thermoplastic is that the melting temperature and the glass transition temperature T_g are lower compared to thermosets. So, the service temperatures at which the material will be used, cannot be as high as for an application with a thermoset.

Since a lot of bridges must be renovated nowadays, it will be helpful if bridges that are already renovated or renewed, do not require a lot of maintenance. The benefit of strengthening with FRP elements is that those parts do not require a lot of maintenance, due to the fatigue strength and corrosion resistance of the material. Moreover, the life cycle costs are not that high because of the low maintenance it requires and the relatively fast production and easy assembly. In addition to this, FRP elements can be made modular. Elements can be quickly installed in a structure and these elements can be produced directly in the desired shape by 3D printing, due to its free formability.

1.2.3 What is the need for this research?

Bridges have degraded over time. Therefore, they should be renovated or replaced appropriately. Strengthening of bridges is a method that increases the performance of a bridge structure and does not require a complete replacement of a bridge. The strengthening method should increase the structural performance of the bridge without increasing the permanent load due to self-weight massively. From this perspective, FRP is a very potential material option for structural elements to strengthen a bridge, due to its positive strength/stiffness-density ratio.

However, FRP is a relatively new material. So, there is a lack of knowledge about the material behaviour and performance and a lack of design codes and standards. The ones that are available are mainly related to thermoset composites because thermosets are commonly used for structural application. However, with 3D printing, thermoplastics are used to which limited design codes/standard relate. The fact that the material is tailorable, does increase the variety of types of FRP materials. The type of matrix and fibres can be varied, the fibre length and orientation, the fibre volume fraction, etc. Especially the type of composite on which this research will focus is not often or commonly applied yet. Besides the material being relatively new, the production method is quite new, namely 3D printing. Because the composite material will be 3D printed, a thermoplastic matrix will be used. Most of the FRP structural elements in civil works are made with a thermoset matrix. So, the use of a thermoplastic polymer leads also to a solution which is not often applied yet.

So, it can be said that the knowledge about thermoplastic 3D printed FRP is limited. With this project, which includes testing and numerical modelling of the material, more data about the mechanical performance of the composite material will be gathered. Besides this, it will be useful to have the knowledge about the structural behaviour of this material to know if and how it can be applied to strengthen bridge decks. The application of 3D printed FRP will strengthen the bridge deck to extend the life span of the bridge. Thus, it will not serve the full life span of a bridge. Therefore, it is beneficial that the material is recyclable. Then, the structural element to implement in the bridge deck will be made from recycled material and may be recycled again when it reaches the end of use state.

1.3 Research objectives

Considering the context of this project, some goals can be set on how to contribute to a solution to the current problem. The general problem is that a lot of bridges in the Netherlands do not suffice nowadays. Therefore, those bridges should be renovated or renewed. This thesis focuses on the renovation of bridges, especially by strengthening bridge decks by 3D printed FRP elements. Since the knowledge about FRP, especially 3D printed, is not very extensive yet, this research project can have a useful contribution to the development of 3D printed FRP in structural engineering. To make it a useful contribution, this research has the following objectives:

- Acquire more knowledge and information about the mechanical properties of 3D printed FRP by performing tests on different scales. By testing different variants on basic mechanical properties, the optimal material, considering the recyclable polymers available, can be obtained.
- When the material is optimized, based on the tested basic mechanical properties, all the relevant mechanical properties should be established by testing.
- A Finite Element Analysis (FEA), based on the properties established by testing, should be performed to model the material. With this modelling, a proper design of the structural element can be made. The preliminary design can be optimized.
- By performing component tests, the load resistance and failure mechanisms of the material can be determined.

1.4 Research questions

From the research objectives, the research (sub-)questions can be derived. The main research question is:

How can decks of movable bridges be built/strengthened with 3D printed fibre-reinforced composite material with the recyclable thermoplastic polymer PETG?

This general research question can be split in several sub-questions. The research questions should be related to what is desired to be concluded and recommended. The questions which will be answered by the conclusions and recommendations are the sub-questions. The sub-questions together will contribute to the main research question of this project. The main research question and the research objectives contain different aspects. Those aspects are about the material composition, mechanical properties of the material, and design of an element in the superstructure of a bridge deck. Each of these aspects are related to a sub-research question. The sub-questions are as follows:

- Which combination of material compositions and print parameters leads to the best desired mechanical performance, or comes as closest to the desired properties? The material with different compositions, in terms of amount of fibres, is delivered to the printing company. The printing company produces in a way that gives the best possible performance of the material. The different layer times of the printing process is chosen in coordination with the printing company. The following parameters will be considered:
    - Fibre volume fraction V_f (30% or 45%).
    - Layer time (80, 100, or 120 seconds)
- What are the mechanical properties of the material with the configuration derived from the first sub research question?
    - Tensile strength and stiffness in longitudinal and transverse direction ($\sigma_{1,t}$, E_1, $\sigma_{2,t}$, E_2).
    - Compression strength in longitudinal and transverse direction ($\sigma_{1,c}$, $\sigma_{2,c}$).
    - Shear strength and stiffness between the print layers *(τ_{21}, G_{21})*, named the interbead shear strength (IBSS) in this report.
- What is the optimal form/design of a structural element in a bridge deck for movable bridges regarding the 3D printed composite polymer material?

1.5 Structure

The structure of this report is schematically elaborated in Figure 1-1. The appendices can be found in Part V, containing the collection of data from literature, nesting drawings for coupon cutting, the individual test results, and the finite element modelling and analysis.

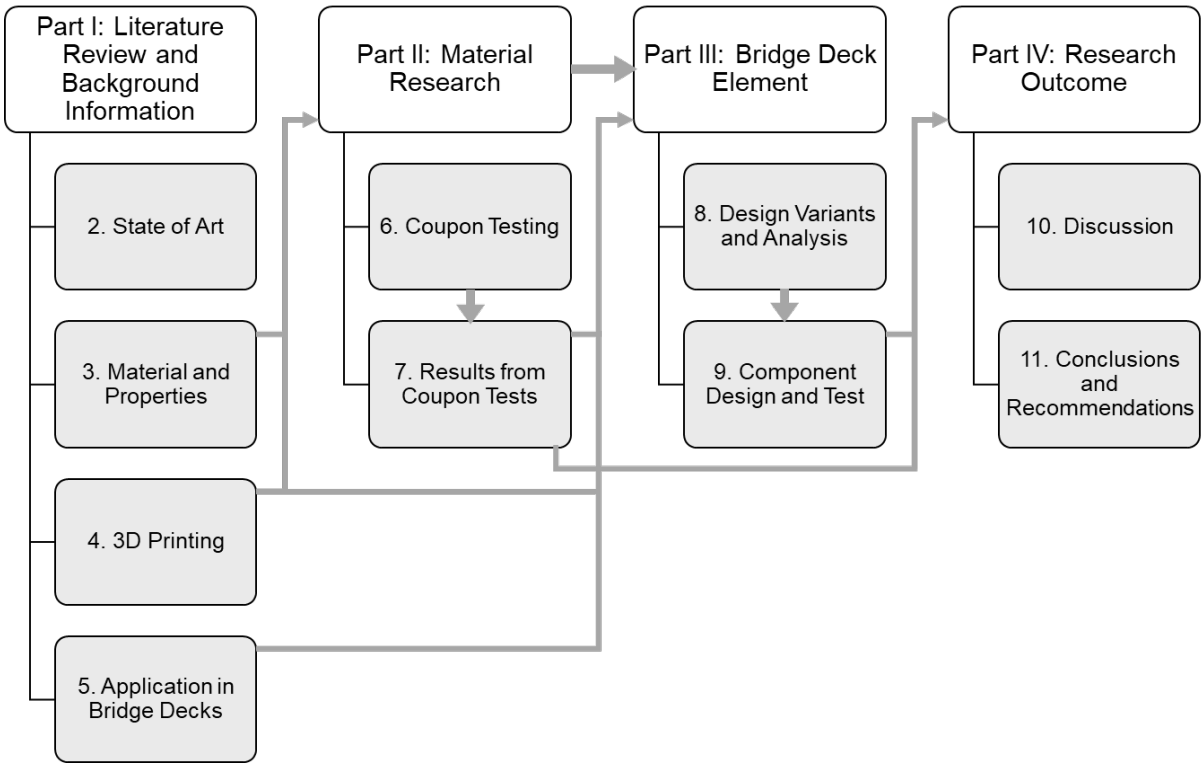

Figure 1-1 Structure of report

Part I:
Literature Review and Background Information

2

State of Art

2.1 Introduction

Is 3D printed FRP already applied in structures of bridges? And if that is the case, how is it done? The state of art of structural elements of bridges or bridge decks, which are made of 3D printed FRP, is elaborated in this Chapter. The starting point is the pre-study related to the Covestro print material regarding the mechanical properties and the preliminary design. Subsequently, several reference projects will be described. From these reference projects, some characteristics of that specific project will be highlighted. At those reference projects, what is the type and size of fibres and the type of resin of the applied composite? Which printing method and technique are used? What is the form and design of the element?

2.2 Previous study regarding 3D printed FRP with print partner Covestro

Previous to this research project, a study related to this topic was already performed by Arup. Different partners were involved compared to this research project. And so, a different printable composite material was considered. The material used in this study was Arnite AM8527G, which is a glass fibre (V_f = 36%) reinforced Polyethylene Terephthalate (PET) composite. The fibres are non-continuous and short in length. The type of resin, PET, is a thermoplastic polymer which is recyclable. The study covered some mechanical properties of the material and a possible field of application for strengthening of bridge decks with this material.

2.2.1 Mechanical properties

The material partner, Covestro, provided for this study some information about the properties of the material. Some material properties are derived from tests and other ones are assumed based on the results of those tests. The mechanical properties of this Arnite material relevant for the current research are given in Table 2-1. The other (thermal) properties can be found in Appendix A.

Table 2-1 Relevant properties of the Covestro material related to this research [1,2]

Property	Symbol	Value	Test method	Statistical data	Comment
Tensile strength ∥	$\sigma_{1,t}$	197 MPa	ISO 527-1/-2	5 specimens	Based on nominal, average wall thickness; characteristic value
Tensile strength ⊥	$\sigma_{2,t}$	16.4 MPa	ISO 527-1/-2	5 specimens	Based on nominal, average wall thickness; characteristic value

Property	Symbol	Value	Test method	Statistical data	Comment
Tensile strain ∥	$\varepsilon_{1,t}$	1.23%	ISO 527-1/-2	5 specimens	Characteristic value
Tensile strain ⊥	$\varepsilon_{2,t}$	0.23%	ISO 527-1/-2	5 specimens	Characteristic value
Compressive strength ∥	$\sigma_{1,c}$	206 MPa	EN ISO 14126		Assumed similar to tensile testing. Initial assumption based on moulded samples.
Compressive strength ⊥	$\sigma_{2,c}$	22 MPa	EN ISO 14126		Assumed similar to tensile testing. Initial assumption based on moulded samples.
Strain limit in compression ∥	$\varepsilon_{1,c}$	1.23%	EN ISO 14126		Assumed similar to tensile testing. To be verified with future testing.
Strain limit in compression ⊥	$\varepsilon_{2,c}$	0.23%	EN ISO 14126		Assumed similar to tensile testing. To be verified with future testing.
In-plane shear strength	τ_{12}	38.0 MPa	ISO 527-1/-2? EN ISO 14129		Characteristic value
Interlayer shear strength	ILSS	5.65 MPa	Comparable to ASTM D4255		Realistic values are not yet available. Values are estimated from single lap shear test.
Shear strain limit in-plane	γ_{12}	0.61%	ISO 527-1/-2? EN ISO 14129		Characteristic value
Tensile modulus ∥	$E_{1,t}$	20,000 MPa (±350 MPa)	ISO 527-1/-2	5 specimens, mean value	Based on nominal, average wall thickness, mean value is used.
Tensile modulus ⊥	$E_{2,t}$	7,100 MPa (± 92 MPa)	ISO 527-1/-2	5 specimens, mean value	Based on nominal, average wall thickness, mean value is used.
Compressive modulus ∥	$E_{1,c}$	20,000 MPa	EN ISO 14126		Assumed similar to tensile testing. Initial assumption based on moulded samples
Compressive modulus ⊥	$E_{2,c}$	7,100 MPa	EN ISO 14126		Assumed similar to tensile testing. Initial assumption based on moulded samples

Property	Symbol	Value	Test method	Statistical data	Comment
In-plane shear modulus	G_{12}	7004 MPa (± 199 MPa)	ISO 527-1/-2? EN ISO 14129		Mean value is used
Shear modulus ⊥	G_{23}	2540 MPa	-		-
Poisson's ratio ∥	v_{12}	0.38	ISO 527-4		-
Poisson's ratio ⊥	v_{23}	0.135	ISO 527-4		-

2.2.2 Preliminary design bridge deck component

Several options were explored for which types of bridge decks could be strengthened with 3D printed FRP and how could this be done. The application areas of three types of bridges were observed: steel bridges with an orthotropic steel deck (OSD); steel bridges with a concrete deck; and movable bridges with a timber deck. Due to the high need for renovation and the large amount in the bridge stock of Rijkswaterstaat, the focus was on the steel bridge with an OSD and the movable bridge with a timber deck. For the movable bridges with timber decks, design variants on top or in between the stringers and on top or in between the cross girders were made. For the steel bridges with OSD, stiffening elements supporting the troughs and a load distributor to trough legs were the design variants. It turned out that the application in steel bridges with an OSD was not very efficient. The added value of the FRP elements was limited. Movable bridges with a timber deck had more potential for the 3D printed FRP strengthening application [2]. Therefore, the application area will be movable bridges with a timber deck. An overview of these design decisions in the pre-study is given in Figure 2-1.

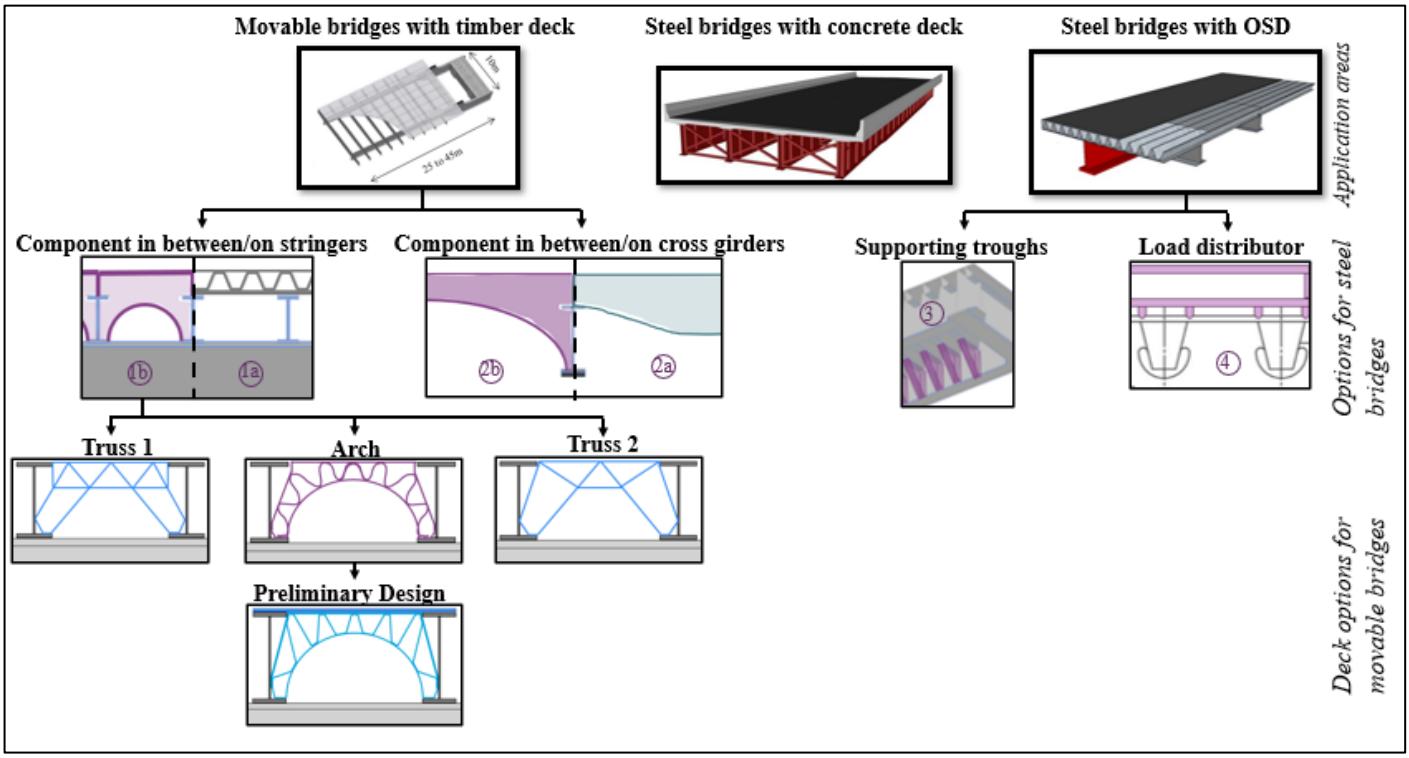

Figure 2-1 Overview of design decision in the pre-study for the preliminary design [2]

The variant, which was worked out further, was the variant with the element on top of the cross girders in between the stringers of movable bridges with timber deck. The idea was to make an arch-type or a truss-type of FRP component. After an FEA, the arch-type component seemed to be better. The preliminary design concept of the application of the 3D printed FRP is shown in Figure 2-2. The 3D printed FRP components will replace the old timber deck, which is laid on top of the stringers.

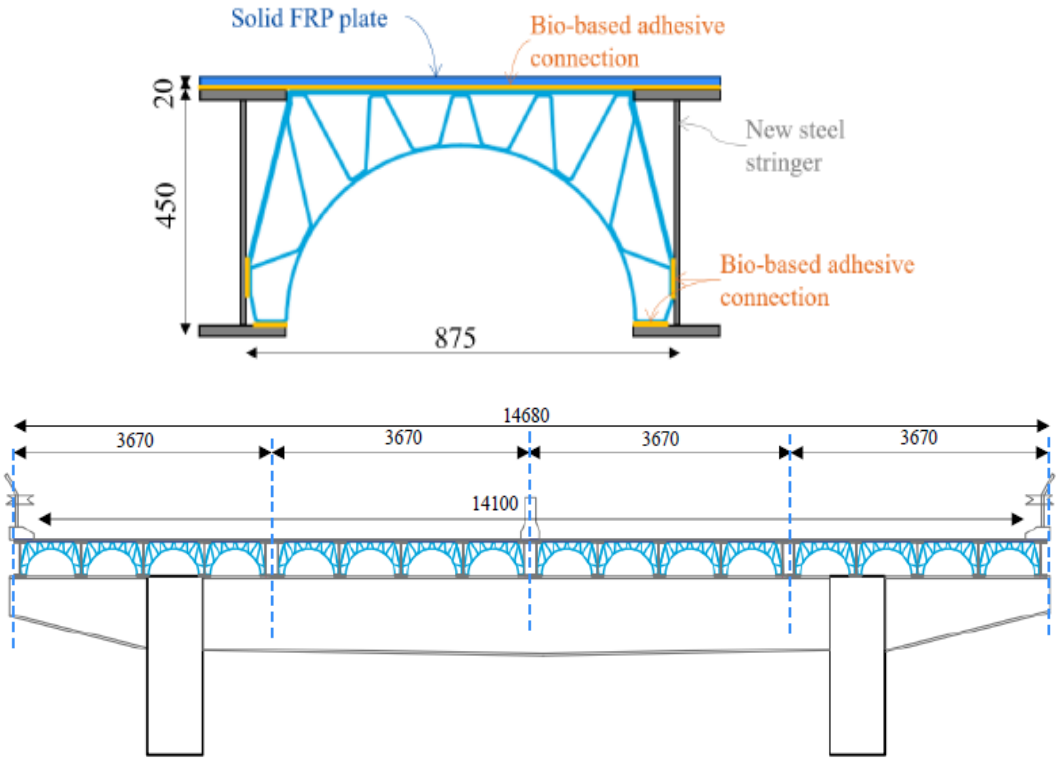

Figure 2-2 Concept design of the strengthened bridge deck with the 3D printed FRP components in between the steel stringers [2]

Although the preliminary design sufficed most of the design checks, there were two checks that did not suffice. The stress in the top plate (not the solid FRP plate but the upper part of the printed arch in Figure 2-2) perpendicular to the print direction in the outer fibre ($\sigma_{yy,top/bot}$) exceeded the design limit value. The structural performance perpendicular to the direction of printing is a critical factor because of the orthotropic behaviour of the 3D printed composite material. This was also the case for the alternative designs (truss-like shapes), which did have more checks that did not suffice on the strength in transverse direction. Besides the insufficient resistance in transverse direction in the top part of the arch, the print path was too long. Moreover, due to the design of the print path, the design will contain local eccentricities due to transitions from single/double to double/triple layered parts. These transitions can introduce a significant increase in local stresses due to local bending. These critical points from the preliminary design should form the starting point for the final design of the bridge deck component.

2.3 Reference projects

To investigate the possibilities of 3D printed FRP elements for strengthening bridges, projects in which 3D printed FRP is applied in bridges, will be observed. Some examples of reference projects are elaborated in the following.

2.3.1 (Prototype) 3D printed footbridge by Royal HaskoningDHV, CEAD and DSM

Royal HaskoningDHV, CEAD, and DSM have developed a 1.5-metre-long prototype bridge made of composite material and produced by 3D printing [5,6]. The prototype bridge is shown in Figure 2-3.The design of the cross section is a straight ribbed structure. The print path follows the upper part, the lower part, and the infill of the ribs is printed in one go attaching the upper and the lower layer. The material used is Arnite, a composite of a thermoplastic polymer PET and glass fibres. PET is a recyclable polymer, which is beneficial from a sustainability point of view. Fabrication-wise, 3D printing delivers the element immediately ready for

assembly, which saves some extra production steps. The technology which is used for printing is Continuous Fibre Additive Manufacturing (CFAM), executed by CEAD. CFAM is a print method of plastics that already contain fibres. The printer can combine the printable polymer with continuous fibres (glass or carbon fibres, for example). These fibres are carried by a filament to the extruder. This print head applies the fibres together with the melted print plastic at the same time [7]. With this technology, larger-scale continuous fibre-reinforced thermoplastic parts can be printed. The next step is to print a 4-metre-long element. Ultimately, the goal is to make a pedestrian bridge of 16 metres long. Another benefit of this production technique is the possibility of implementing sensors in the material. In this way, the structural element can be monitored continuously to predict and optimise maintenance and observe the condition in terms of structural behaviour and environmental aspects.

Figure 2-3 The 1.5-metre-long prototype bridge of Royal HaskoningDHV, CEAD, and DSM [5]

2.3.2 First 3D printed circular polymer composite bridge Alphen aan de Rijn

Though the bridge produced by Royal HaskoningDHV, CEAD, and DSM was just a prototype, a real 3D printed bridge has been realised in Alphen aan de Rijn. Composite Structures and the printing company 10XL developed a 3D printable thermoplastic composite reinforced with a synthetic polymer and short glass fibres [8,9]. The specific type of polymer is not specified in the articles. However, it is mentioned that the composite is made of recycled plastics and that the polymer has a glass transition temperature T_g of 140°C. Regarding this, it could be a similar material as developed by Royal HaskoningDHV, CEAD, and DSM, who used recycled PET for their 3D printed composite. Besides the use of recycled material, the bridge itself is also recyclable as thermoplastic composite is used. The material is delivered as granulate, which is heated to be printed. When the granulate is melted and mixed with the fibres, it can be printed by the extruder. In terms of sustainability, the material use of the bridge has a positive contribution. In addition, because of 3D printing and easy assembly, construction time and work are limited. The whole 7-metre span bridge is printed in a continuous process that took 90 hours to print. A picture of the assembly of the bridge can be seen in Figure 2-4. Moreover, the durability is also one of the benefits of this application.

However, the print process did not go as smoothly as planned. When the printer had printed about 2 metres of the bridge, cracks appeared over the whole cross section of the bridge. These cracks occurred due to thermal stresses, caused by the difference in temperature of the print layers [10]. The material is printed at a temperature of 220°C and when the new layer is printed on the previous layer, the previous layer has already cooled a bit, which results in a temperature difference and so, thermal stresses. The print path was adjusted to prevent this problem. Dilatations were incorporated in the print design, so there is some room to shrink and swell for the material. This is a proper example of the challenge of print path and layer time, which can be critical for the feasibility of the printed element.

Figure 2-4 3D printed bridge by 10XL in the factory [10]

2.3.3 3D printed bridges in China

Not only in the Netherlands but also in China, there is some development regarding 3D printed bridges. The School of Architecture and Urban Planning at Tongji University in Shanghai has created two 3D printed pedestrian bridges with a span of 11 and 4 metres respectively [11], see Figure 2-5. The bridges were created with the purpose of revolutionizing architecture and construction with innovative technologies. The printing process was done with a Kuka robotic arm and a custom 3D printing module and took 360 hours to complete. From the side can be seen that the structure has a truss-like shape with crosses between the top and the bottom part of the bridge.

Figure 2-5 The two 3D printed pedestrian bridges in Shanghai [11]

2.3.4 3D printed cycle bridge with recycled train wagons and wind turbine blades

In terms of recyclability, the 3D printed cycling bridge in Lansingerland is a proper example of recycling waste plastic in the construction of a bridge [12]. Parts of old train wagons, wind turbine blades, and pipelines are used for the structural elements of this bridge. The plastics were granulated and heated before printing. In addition to the recycled plastics, glass fibres are incorporated into the bridge elements. These also function as sensors, which can measure temperatures and strains in the structure. The use of these materials means that the bridge will be recyclable again when the bridge reaches its end of life.

The whole bridge is not printed in one go but consists of several printed parts. These parts are connected by bolted joints. The dimensions of the bridge were too large to make printing of the whole bridge in one go possible. The span of the bridge is 13 metres, and the width is 6 metres. The dimensions of the main girders are 500 mm high and 250 mm wide, and the edge girders are 400 mm high and 250 mm wide. The bridge is shown in Figure 2-6. The plastics are heated until 250°C before printing. When printed, the material cools again. This leads to shrinkage, which results in internal stresses and deformations. Therefore, in the design of the bridge, the shape of the element, the print path, the layer thickness, and the layer time should be carefully chosen.

Figure 2-6 3D printed bridge with recycled plastics in Lansingerland [12]

2.3.5 3D printed composite pedestrian bridge made of PETG and glass fibres

One of the most recent applications of 3D printed FRP in bridges is a pedestrian bridge in Putten, see Figure 2-7. The deck of the bridge was designed by Royal HaskoningDHV and Atelier Dutch and printed by Nedcam. The composite material applied consists of PETG from industrial waste reinforced with 30% V_f glass fibres [13]. Besides using industrial waste for the printed material, the bridge can be recycled or reused when it reaches its end of life. The bridge can be placed somewhere else, or the material of the bridge can be shredded and printed again.

Figure 2-7 3D printed pedestrian bridge in Putten from Royal HaskoningDHV, Atelier Dutch, and Nedcam [14]

2.4 Conclusion

Looking at the reference projects, it can be noticed that the FRP structural bridge elements have a truss-like shape or a web/rib-structured shape. This can also be seen on the SPARC Bridge website [15], a company that designs and creates 3D printed composite bridges. So, it can be said that also for the application in this research, structural elements with a truss-like/web-structured shape or a multi-web structure can have a high potential for the design. This type of design is also in line with the earlier designed element from the Covestro 3D printed FRP bridge strengthening element.

The reference projects of 3D printed FRP bridges, presented in this Chapter, are foot and/or cycle bridges. It can be said that 3D printed FRP is mainly used for light traffic bridges nowadays and that the application in heavy traffic bridges is not very common yet. This offers the opportunity and the potential to investigate the resistance of a 3D printed FRP bridge deck element under heavy traffic loading.

Moreover, printing a bridge (deck) is quite a challenge due to the differences in temperature between the material extruded by the print head and the layer on which the material will be printed. Especially the projects in Alphen aan de Rijn and Lansingerland showed that too large temperature differences can cause problems. That is why the print path and layer time should be adjusted and properly chosen for the design, or that it is even not possible to print a whole bridge in one go when the dimensions are too big.

3

Material and Properties

3.1 Introduction

FRP composite is a material that consists of a base material and a filler material. The base material is a polymer resin, and the filler material is the fibres. Different types of resin, also called matrix, and different types of fibres can be applied. Different configurations for the FRP composite lead to different mechanical and material properties. These properties can be determined by testing. This Chapter focuses on the possible type of resins and fibres, the relevant properties, how can be tested, and the possible failure modes are.

3.2 Materials used before

Several types of FRP composites have been tested already: different types of fibres, different implementations of the fibres in the composites, different types of resins, and different compositions. The designed composite can be quite varied. Therefore, the different kinds of composites produced by 3D printing which are tested in literature, will be listed below. The next step is to select the most suitable options for the materials in a composite applicable for strengthening bridge decks.

- Four types of continuous fibre-reinforced filaments (FRF): carbon fibres (CFRF), standard glass fibres (GFRF), high-strength/high-temperature glass fibres (GFRF-HSHT), and aramid (Kevlar) fibres (AFRF); short carbon fibre-reinforced filament branded Onyx (Nylon thermoplastic resin), and matrix-only filament Nylon [16].
- Fibre-Nylon composite: carbon fibres (uniaxial), glass fibres (biaxial), and Kevlar fibres (biaxial) [17].
- Polyamide 6 (PA6) reinforced with continuous carbon fibre [18]. Different configurations with isotropic or concentric reinforcement at the borders, borders and centre, or equidistant for compressive testing. For flexural testing, the reinforcement is isotropic or concentric, perpendicular, or parallel to the test force direction.
- Nylon White (engineering-grade nylon) and Onyx (nylon reinforced with 14 wt% short carbon fibres) [19]. Three print direction variations: Default flat (±45°); Parallel flat (0°); and On-edge print direction parallel to the loading direction (0°). Compression specimens in two orientations: Upright (print layer perpendicular to loading direction); and Flat (print layer parallel to loading direction).
- PET-based FRP composites. PET-polymers can be recycled (rPET) and can be used in combination with additives like glycol-modified PET (PETG). Composite with a PET resin can be reinforced by either glass fibres [20-22], carbon fibres [23], or natural fibres [24].

The resin of FRP composite materials in general can be a thermoset or a thermoplastic polymer. The main difference is that the long chain-like molecules of thermosets contain crosslinks, while the molecules of thermoplastics do not [25]. This means that thermoplastics are more prone to creep and have a lower glass

transition temperature (T_g) compared to thermosets. However, thermoplastics are re-meltable, and hence, recyclable. Therefore, thermoplastics are used in 3D printing of FRP.

Considering the different composite material configurations listed above, there are several options for the type of fibre to apply. However, the glass fibres are the most applied in civil engineering, due to its strong structural performance and relatively low price [25]. Except carbon fibres, glass fibres provide the highest strength and stiffness, but carbon fibres are expensive.

The properties of the composite material in terms of strength and stiffness are mainly dominated by the fibres. The type of fibre, the orientation of the fibres, and the V_f. Fibres are applied unidirectional, in both longitudinal and transverse direction, and under ±45° in general. The configuration determines the orthotropic behaviour of the material. However, when focussing on FRP produced by additive manufacturing, the possibilities of fibres orientations are limited.

3.3 Relevant properties

In literature, the tests that are carried out the most are tensile tests. To compare materials or different variations, basic tests are performed. Tensile tests are the most common to apply, obtaining the tensile strength and stiffness. An overview of the values of the mechanical properties of various types of 3D printed FRP composites and composites with (r)PET(G) is provided in Appendix A. This overview is summarized in Table 3-1. In this overview, there is quite a variety of types and configurations of FRP composites. Properties of 3D printed FRP composites in general and properties of composites consisting of PET as matrix and in most of the cases glass fibres, not necessarily 3D printed, are collected the most. The investigated and measured tensile strengths and stiffnesses are mainly in the principal direction of the composite material.

Table 3-1 Summary of tensile mechanical properties from literature [1,16,17,19-24,26-30]

Matrix	**Fibres**	**V_f [%]**	**$\sigma_{1,t}$ [MPa]**	**$\sigma_{2,t}$ [MPa]**	**E_1 [MPa]**	**E_2 [MPa]**
Nylon/PA6	Unreinforced	0	19 – 51		530 – 2,010	
	Glass	30 - 40	82 – 160		2,700 – 16,000	
	Carbon	21 - 69	228 – 692		10,110 – 52,000	
	Other	~40	70 – 140		1,400 – 8,700	
(r)PET(G)	Unreinforced	0	28 – 52	20 – 23	~2,000	1,630 – 1,870
	Glass	15	~100		~4000	
		30	~120		~8000	
		45	110 - 130		10,000 - 12,000	
		60	120 - 140		~16,000	
	Carbon	25wt%	605 – 697		34,200 – 39,700	
	Flax/hemp/wool	20	111 – 231		15,300 – 20,300	

Overall, the principal tensile strength $\sigma_{1,t}$ of 3D printed FRP composites with glass fibres, lies between 80 and 160 MPa, and the principal stiffness E_1 varies from 2,700 to 16,500 MPa. The type of matrix is in these cases mainly Nylon or PA6, which is often used for 3D printed composites. When looking at composites consisting of PET and glass fibres, there is a range of 30 – 200 MPa for the principal tensile strength $\sigma_{1,t}$ and 4,000 – 16,000 MPa for the principal stiffness E_1. So, there is quite a big scatter in data. It can be used to set some values which are desired to reach for the mechanical properties. However, this will also be dependent on the material which can be delivered by the material supplier.

The values and properties discussed before regard the mechanical performance in the principal direction, which is in the direction of printing. However, because of the orthotropic behaviour of the printed material, the mechanical performance in the transverse direction will be lower and can therefore be critical, as was the case for the preliminary design (Section 2.2). Additionally, the other variants (truss-like shapes) for the design of the component did not suffice the stress resistance perpendicular to the principal direction. So, the strength perpendicular to the print direction is one of the critical parameters of 3D printed composites.

Strength perpendicular to the print direction is determined by the bond strength between the print layers. This can be examined by the tensile strength in transverse direction ($\sigma_{2,t}$) and the shear strength between the layers. The shear strength between the print layers can be described as the interlayer shear strength, which would have the abbreviation ILSS. This can be confusing with the interlaminar shear strength, a mechanical property of laminated fibre reinforced polymers. Since an extruded layer is called a bead, the term ‘bead’ could be used instead of ‘layer’. Therefore, the shear strength between the print layers will be named the interbead shear strength (IBSS) in this report.

3.4 Testing

The strength and stiffness values of the mechanical properties of different (3D printed) FRP from the previous study and the references are either determined by testing or estimated based on results from those tests. In a similar way, the properties of the material (configurations) observed in this research should be established.

3.4.1 Test methods

In the references from which the values in the previous section are obtained, two types of standards are applied for testing. Mainly the ISO standard and the ASTM standard are relevant for testing. The following specific methods are used for different types of tests:

- For tensile tests, ISO 527 [31,32] is a commonly used method from the Eurocode. This method was also used for the testing of the specimens from Covestro [1]. Another option is the method guided by ASTM D638 [19,26,27] or ASTM D3039 [17,26,28,29].
- For compression tests, EN ISO 14126 was used for the testing of the specimens from Covestro [1]. ASTM D695 [18,19,27] can also be an option.
- For IBSS tests, one can think of ASTM D4255 [1]. However, this is not common to use, and it has some disadvantages, like the long overlap and eccentric loading. ASTM B831 [33] could be a suitable alternative, as it could be useful to have the same principal as a single-lap shear tests [34], despite this standard is regarding steel.
- For flexural tests, ASTM D790 is applied in other studies [18,28,29]. This method is comparable to the three-point bending test from ISO 178. This specific three-point bending test-type will not be applied. However, the designed component can be subjected to a three-point bending-like test.

3.4.2 Measuring techniques

When executing the tests, data must be measured to be able to determine the values of the mechanical properties of the material. During the test, the force in the specimen is measured by the test machine. The tests will be displacement driven and, by generating a displacement to the specimen, the specimen is loaded by a force, which is transferred to the clamps of the machine. So, from the test machine, the force in the specimen and the displacement of the jack can be obtained to construct a force-displacement diagram.

The force measured by the machine can be converted to a stress by dividing the force by the area (Equation (3-1)). Before the tests are executed, the dimensions of all specimens are measured. Afterwards, the area of

the failed surface is measured. This area is used to calculate the ultimate strength in terms of stress from the load at failure. The value of this area is compared with the area calculated from the dimensions before the tests, to check the effect of necking. As this material is stiff, this effect will be very minor.

$$\sigma = \frac{F}{A} \tag{3-1}$$

In case of a homogeneous specimen in length direction, the strain in the specimen can be calculated by dividing the measured displacement by the length of the specimen in direction of loading. However, this will not lead to a perfectly accurate strain estimation. To have a more accurate value of the strain, an extensometer can be used. This device determines the strain over the gauge length of a specimen. The gauge length of the extensometer used is 50 millimetres. Over this gauge length, the deformation is measured by the extensometer and converted to the strain according to Equation (3-2). To have a valuable test result, failure must occur within the gauge length of the extensometer. For coupon testing, it is likely that failure occurs in the middle of the specimen, due to the shape of the specimen. Therefore, the use of an extensometer is suitable for coupon testing.

$$\epsilon = \frac{\Delta l}{l_0} \tag{3-2}$$

When it is unknown where failure occurs or it is desired to observe deformations in multiple directions, digital image correlation (DIC) is a suitable measuring technique. DIC can derive the displacement, and so the strains, from recognition of image areas. At each timestep, a picture is taken of the observed surface or area of the specimen. The specimen is painted with a black-and-white pattern. This stochastic pattern results a certain grey value for each pixel of the image. Since individual pixels cannot be used for a precise homologous position recognition of 2D image coordinate, image areas, also called facets, are used to compute positions that can be clearly assigned. The similarity of these facets at different scanned locations and the difference between the original state and the deformed state determine the displacements of the pixels in the scanned positions (see Figure 3-1). The form, the sum of its coordinates, of a facet or solid changes in space over time. With the change of its form, stretch ratios Λ can be calculated (Equation (3-3)). With the stretch ratios in the different directions, the stretch tensor **U** is constructed (Equation (3-4)). The technical strains, as Equation (3-2) , can be derived directly from the stretch tensor. The stretch tensor contributes to the deformation gradient **F**, which also contains a rotational part **R** (Equation (3-5)). [35]

$$\Lambda = \frac{l_1}{l_0} = \frac{l_0 + \Delta l}{l_0} = 1 + \epsilon \tag{3-3}$$

$$\mathbf{U} = \begin{pmatrix} \Lambda_x & \Lambda_{xy} \\ \Lambda_{yx} & \Lambda_y \end{pmatrix} = \begin{pmatrix} \epsilon_x + 1 & \epsilon_{xy} \\ \epsilon_{yx} & \epsilon_y + 1 \end{pmatrix} \tag{3-4}$$

$$\mathbf{F} = \mathbf{R} \cdot \mathbf{U} \tag{3-5}$$

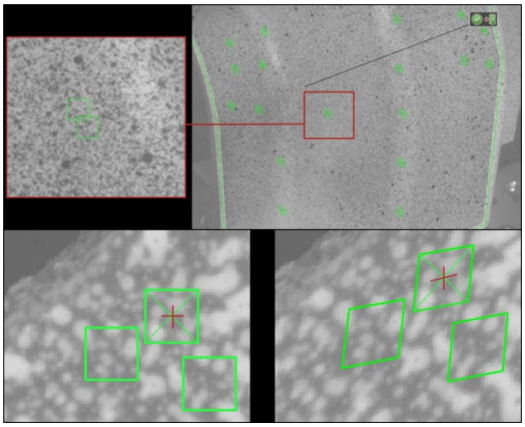

Figure 3-1 Facets on a stochastic pattern in their original and deformed state [35]

3.5 Failure mechanisms

FRP produced in another type of manufacturing than 3D printing, is mainly laminated composite. For laminated FRP, the failure mechanism can consist of multiple processes. These are matrix cracking, delamination, and fibre failure [36]. Since with 3D printing the material is layered instead of laminated, delayering is more suitable as failure pattern. From these failure processes, the failures that are likely to occur for the 3D printed material can be predicted.

With matrix cracking, cracks occur between the fibres. So, the fibres do not break. A difference of this failure mode between laminated and layered material is that the 3D printed material does not contain fibre laminated and the fibres are already chopped and mixed with the polymer. With laminated material, matrix cracking can initiate delamination. Although this is not the same failure pattern as for layered material, delayering can be initiated by (micro) cracks in the polymer. For the 3D printed material, these cracks will develop in between the beads. The bonding strength between the layers is governing for this failure mode.

Since 3D printed composite is an orthotropic material with its main strength in the direction of printing, fibre failure is likely to occur in longitudinal direction, which is the stronger orientation of the material. When the fibres are in tension, pull out of the fibres or fracture of the fibre is likely to happen. In compression, the fibres can kink. Since the fibres are governing for the resistance of the composite material, unstable failure will occur when the fibres fail.

In addition to the failure modes described before, propagation of cracks in materials can be analysed with fracture mechanics. After (micro)cracks are initiated, they will grow. Fracture mechanics focuses on this crack growth period. It can be used to determine the residual strength, the maximum tolerable crack size, and crack propagation speed. The theory of fracture mechanics describes three crack modes (see Figure 3-2): [37]

- **Mode I**: Crack opening mode in which cracks tend to grow on the plane of maximum tensile stress.
- **Mode II**: In-plane shearing or sliding mode.
- **Mode III**: Tearing or anti-plane shear mode.

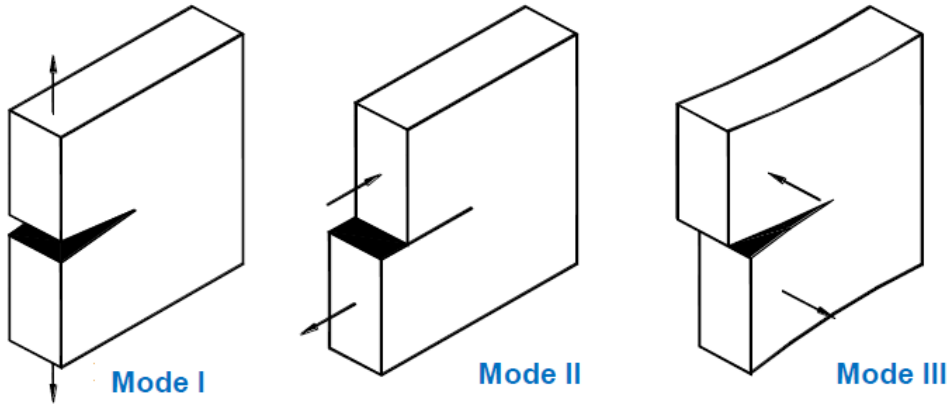

Figure 3-2 Three crack modes from fracture mechanics [37]

Lastly, what should be noticed is that due to the layered methodology of how 3D printed FRP is produced, there is a risk of fatigue crack initiation between the beads. Because of the layered build up, the cross section is not constant in transversely to the print direction. Hence, local stress concentration can occur when loaded in that direction. Although fatigue analysis is not part of the scope of this research, the effect of the ribbed surface of the material in relation to local stress is relevant to consider. Moreover, due to cooling after fabrication, shrinkage of 3D printed parts can result in locked-in stresses in the material.

3.6 Conclusion

From the collected data from literature, it became clear that there is quite a variety of mechanical properties of different configurations of FRP compositions. Therefore, it is necessary to establish the mechanical properties of the material used in this research project. As this research is a follow-up of the previous study that regards Arnite, it is very that this research will also consider a 3D printable composite containing (r)PET(G).

With several coupon tests, for the mechanical properties of the material can be obtained. In this way, the structural performance of the material will be expressed in numbers, which makes it possible to design a structural component of this material, based on this data. Since the strength perpendicular to the print direction, so the bond strength between the print layers, is a critical parameter, it can be useful to investigate some factors that influence that bond strength. In general, the fibre volume fraction has a large effect on the strength and stiffness of the material. Although the effect is mainly in the direction of fibres, so the direction of printing, the fibre volume fraction is still a very important parameter in the material composition regarding the mechanical properties. The factor that impacts the bond strength between the print layers is the difference in temperature between the previously printed material and the material that is printed on top of that previous layer. The temperature difference is due to the heating of the material to be printed and the printed material that is cooled. To minimize this difference, and thus achieve a better bond strength, the layer time should be as short as possible. Therefore, material variations should be tested to investigate what the maximum layer time can be while still the desired bond strength is achieved. Tensile tests in both longitudinal and transverse direction will be suitable to check the influence of the V_f and the layer time. For the characterization of the optimal material, compression and shear tests should also be performed.

For these tests, several codes prescribe how the design the set-up and how to execute the test. Both the ASTM standards and the ISO standards are used as design guides for testing. Since this project is performed in the Netherlands, the Eurocode design guide is valid. Therefore, the ISO standards should be applied for testing. ASTM standards or other sources can be used as a reference when the ISO standards do not provide enough information for the tests or in case adjustments to a test design have to be done After performing the tests, the data can be processed as described before and the failure mechanisms will be observed and compared the possible failure modes.

4

3D Printing

4.1 Introduction

3D printing is a production method which constructs an element or product layer by layer. 3D printing is also called additive manufacturing. The material will be heated and melted to be extruded by a print head. The material can be delivered in filaments or granulate (pellets), for example. Some important parameters regarding the print process will be described in this Chapter. The different techniques available for 3D printing will be listed. It will be elaborated how the material is produced and printed for this specific research. It should be known what the effects of which print parameters are and under which conditions the FRP composite material is printed, considered in this research project.

4.2 Relevant print parameters

The influence of the temperature of the surface on which the material is printed and the print speed was investigated previously [24]. By tensile testing, the strength and stiffness of the coupons are obtained for three different platform temperatures and two different print speeds. The platform temperature is the temperature of the surface on which the material is printed, so the temperature of the previously printed layer. The temperature itself is maybe not that important, but it is mainly about the difference in temperature between the extruded material and the surface (the previous layer) on which the material is printed.

The material that was used for this investigation was Onyx. An FRP composite with a Nylon matrix and short carbon fibres. Although this research focuses on a different type of matrix and fibres, the influence of temperature and print speed will be comparable. Both are FRP composites, which will be sensitive to a change in these conditions. Only the specific numbers of temperature, print speed, and mechanical properties will not be the same. The effects of different temperatures and print speeds will be relevant for the material used in this project in a relative way. The results show that a higher platform temperature and a higher print speed lead to a better structural performance, in terms of tensile behaviour. The Young's modulus and tensile strength increase by 10 % and 11 % by an increased platform temperature from 70°C to 110°C and the tensile strength increases by 14 % by increasing the print speed from 40 mm/s to 60 mm/s [24].

It can be said that it is beneficial for the structural performance of the material to have the time between printing layers as short as possible. Both an increased platform temperature and an increased print speed improve the mechanical properties. A higher platform temperature means in other words that the previous layer is not cooled too much before the new layer is printed. So, the difference in temperature between the previous layer and the printed layer on top of the previous layer is important for the (tensile) strength of the material. Of course, when the print speed is higher, the previous layer has less time to cool before the new layer will be printed. Therefore, the layer time between the print layers should not too long to obtain the best mechanical properties of the printed material. On the other hand, when the layer time is too short, the desired bond strength will not be obtained because the previous layer is not hardened sufficiently to be able to support

the next layer on top. Moreover, the slower the robot can print, the more accurate the material can be extruded according to the print path, so the better the quality of one layer will be.

4.3 Printing techniques

When applying additive manufacturing, one can considered different technologies. Below, several 3D printing techniques are listed and described:

- **Robotic arm extrusion** (Figure 4-1): This is the most commonly applied technology for printing of relatively larger structures. The robotic arm can move freely and prints layer by layer by extruding material from the nozzle. Extrusion is a continuous process, which follow a certain path for each layer. This path can be repeated or slightly modified layer by layer to build the structure. This automated construction process is also called contour crafting. The material to be printed enters the 3D printing machine as granulate in which the fibres and polymer are already mixed. [3,38]

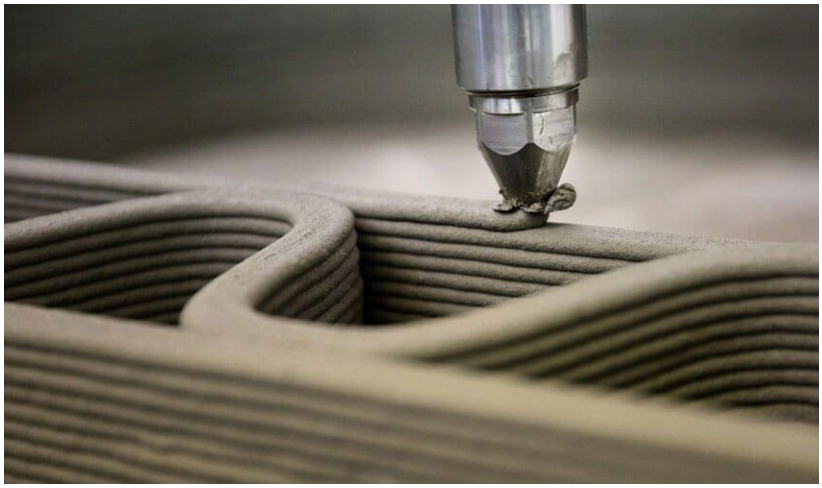

Figure 4-1 Robotic arm extrusion [3]

- **Fused Filament Fabrication (FFF)** (Figure 4-2): With FFF, the thermoplastic resin and the fibres enter the extruder separately from their spools. They are combined in a common printing head. In the extruder, the material is heated, which make the thermoplastic polymer melt. In the melting chamber in the machine, the resin comes together with the fibre filament prior to printing in the nozzle. The viscous reinforced thermoplastic polymer is then deposit on the a (pre-heated) bed or on top of previously printed layers. Before the fibre filament enters the melted thermoplastic filament, the fibres can be cut. If this the fibre filament is not cut, it is called continuous filament fabrication (CFF).[16,23,24]

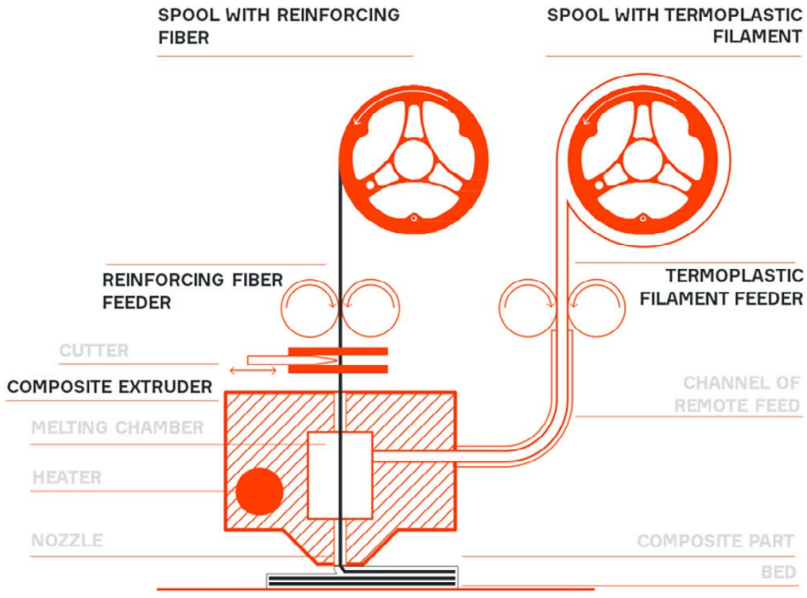

Figure 4-2 (Continuous) fused filament fabrication [23]

- **Fused Deposition Modelling (FDM)** (Figure 4-3): This printing technology is comparable to FFF. A thermoplastic material, which can be entered either as filament or as pellets, is melted and extruded. Fibres, continuous or non-continuous, can be extruded simultaneously via the nozzle. However, the orientation of each lamina or layer can be varied, as the thermoplastic polymer can be extruded and have concentric rings of fibres or fibres isotopically embedded in the printed material. [17,39]

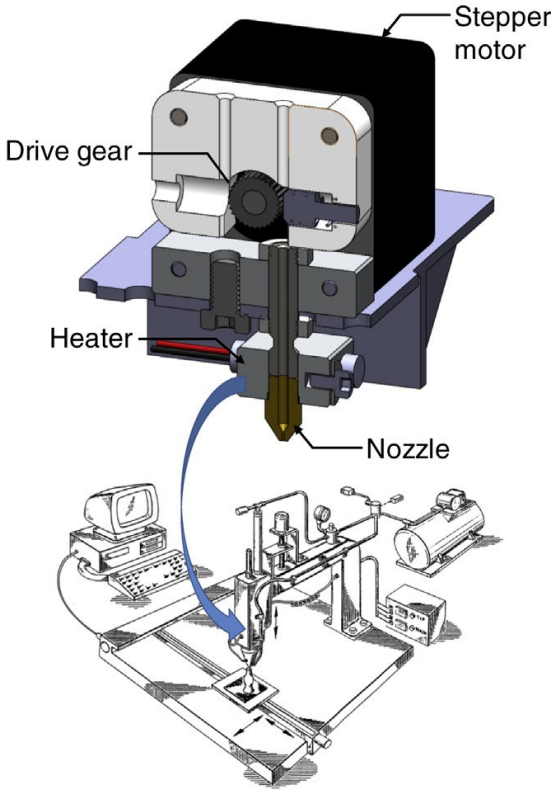

Figure 4-3 Fused deposition modelling [39]

- **Selective Laser Sintering (SLS)**: Sand 3D printing is another name for this technology, which also makes use of layer-by-layer printing. The layers are not extruded but spread as sand powder by the machine to harden in the structure's shape with a binder. The material is compacted and formed by pressure and/or heat without melting to the point of liquefaction. This process is called sintering. Small particles are fused by as scanning laser to build up parts layer by layer. After a layer is sintered, new powder is added and uniformly spread with a roller across the target surface for sintering of the next layer. [3,39]

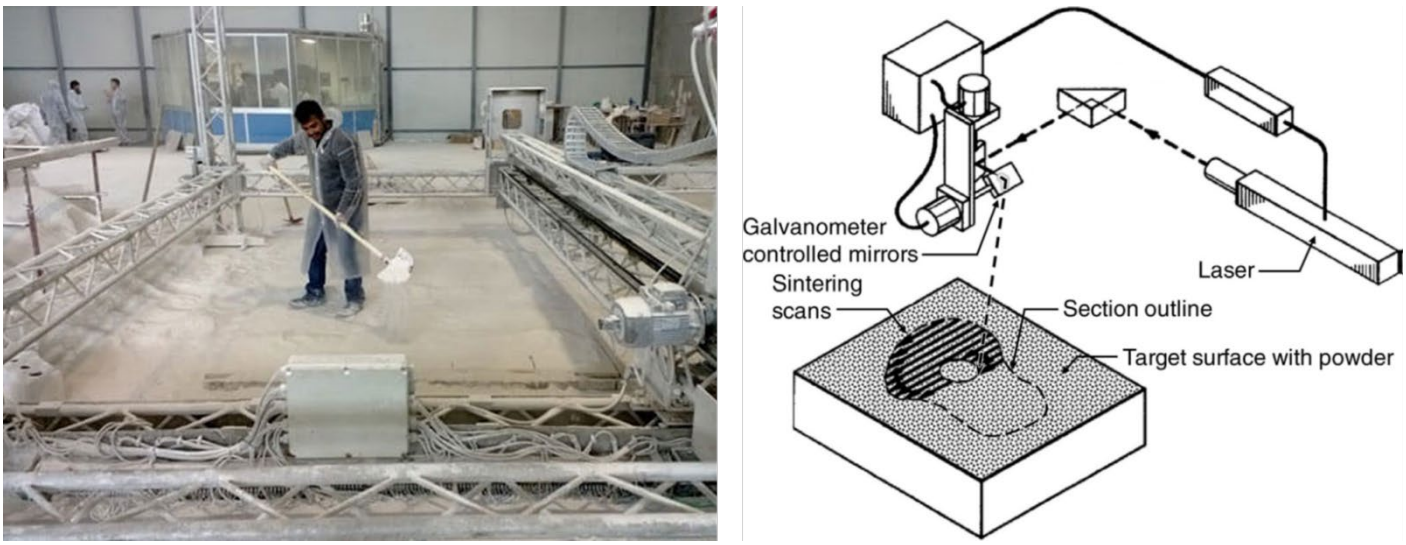

Figure 4-4 Selective laser sintering [3,39]

- **Stereolithography (SLA)**: With SLA, a cross-section of a designed part is selectively drawn by a pattern of light, laser, or radiation. The light is optically transmitted on the surface of a curable liquid (resin) in a vat. Due to the exposure to the light, the drawn cross section solidifies. After the cross section is cured, it lowers below the surface level of the liquid, allowing backfill of the liquid for curing and bonding of the subsequent cross sections. [39]

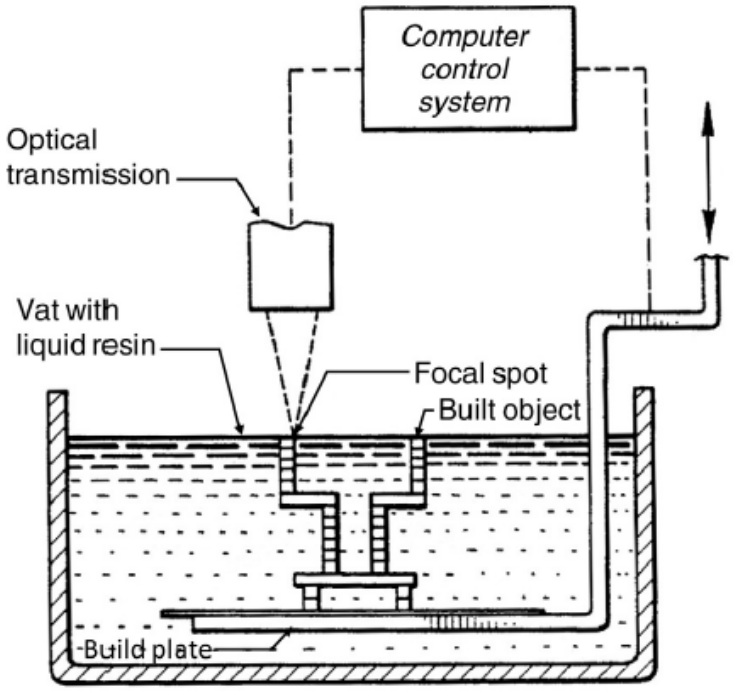

Figure 4-5 Stereolithography [39]

- **Polyjet Modelling (PJM)** (Figure 4-6): A print carriage with multiple print head, curing units, and other subsystems deposits small volumes (voxels) of curable liquid photopolymer onto a build tray. Each voxel of the primary build material is individually deposited through a print head to form a portion of the object's cross section. A uniform fill is ensured with removal of excess print material by a levelling system. Prior to adjusting the height of the build plate for deposition of the next layer, the printed material is immediately cured. [39]

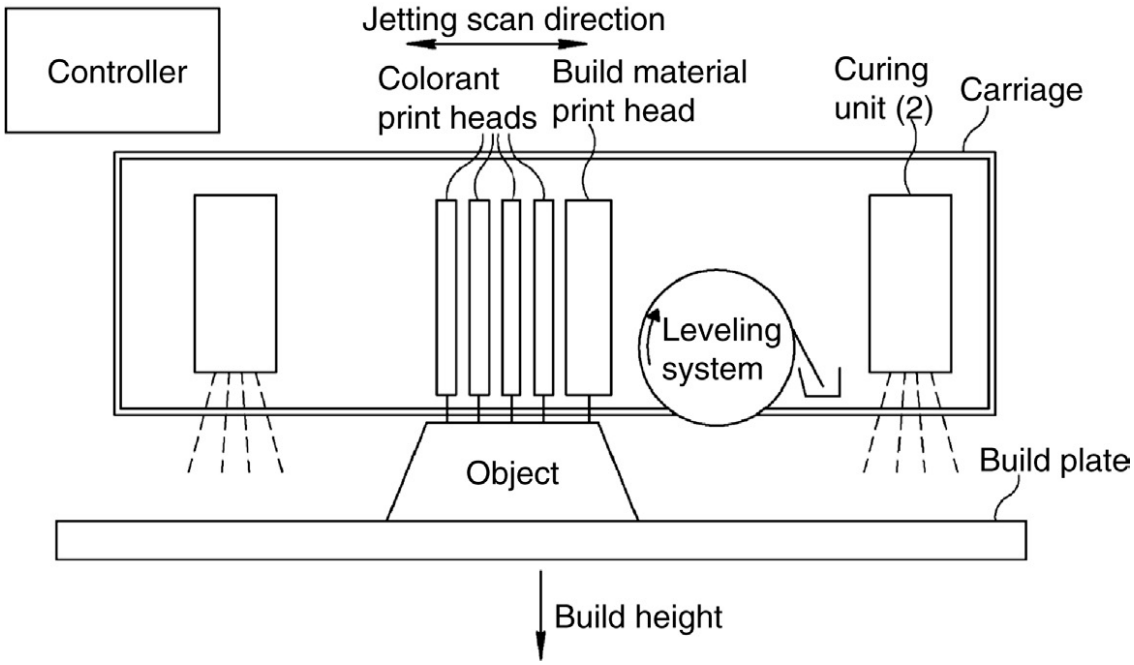

Figure 4-6 Polyjet modelling [39]

4.4 Additive manufacturing by HB3D

The producer of the material for this project is the additive manufacturing company HB3D. From the list of different printing techniques in Section 4.3, the robotic arm extrusion is the print method used by HB3D. In this section, the production process of the 3D printed composite material will be explained.

The material to be printed is delivered by the Performance Polymers department of the Mitsubishi Chemical Group (MCPP). The composite polymer material is delivered as granulate. The type of polymer is rPETG. The granulated rPETG already contains the short glass fibres. The length of these glass fibres is about 1.5 to 3 mm. Before the printing process can start, the granulated material must be pre-treated. The material is being dried for at least 4 hours under 65°C (in the green reservoir in Figure 4-7). This is done to prevent a too high moisture content in the material and to prevent the presence of too much air in the printed material.

When the granulate material is ready to be printed, the printing process can start. From the big reservoir where all the to-be-printed material is stored after drying (the black one in Figure 4-7), the granulate is led to a small reservoir (see the right picture in Figure 4-7). From the small reservoir, the granulate is directly transferred into the extrusion arm. In the extrusion arm, the pellets are heated and melted.

Figure 4-7 Reservoirs in which the granulated material is dried (green) and stored (black) before it goes to the small reservoir (pointed with the red arrow)

In the extrusion arm, the granulate is heated and melted. By a kind of screw, the melted material is pressed through the extrusion arm. The extrusion arm consists of several parts, but the screw goes through all the parts. At every part, the temperature is measured. See Figure 4-8 for the extrusion arm and the measured temperatures. However, this is not done directly in the material, but indirectly at the side of the metal part of the extrusion arm. Only in the last part before the nozzle, the temperature of the material itself is measured. This is done by a pen which sticks through and measures in the middle of the melted material in the extrusion arm. This temperature is 237°C. So, it can be stated that the material is heated and extruded at a temperature of 237°C. During printing of the boxes for the first stage of coupon testing, the ambient temperature during printing was 15.5°C.

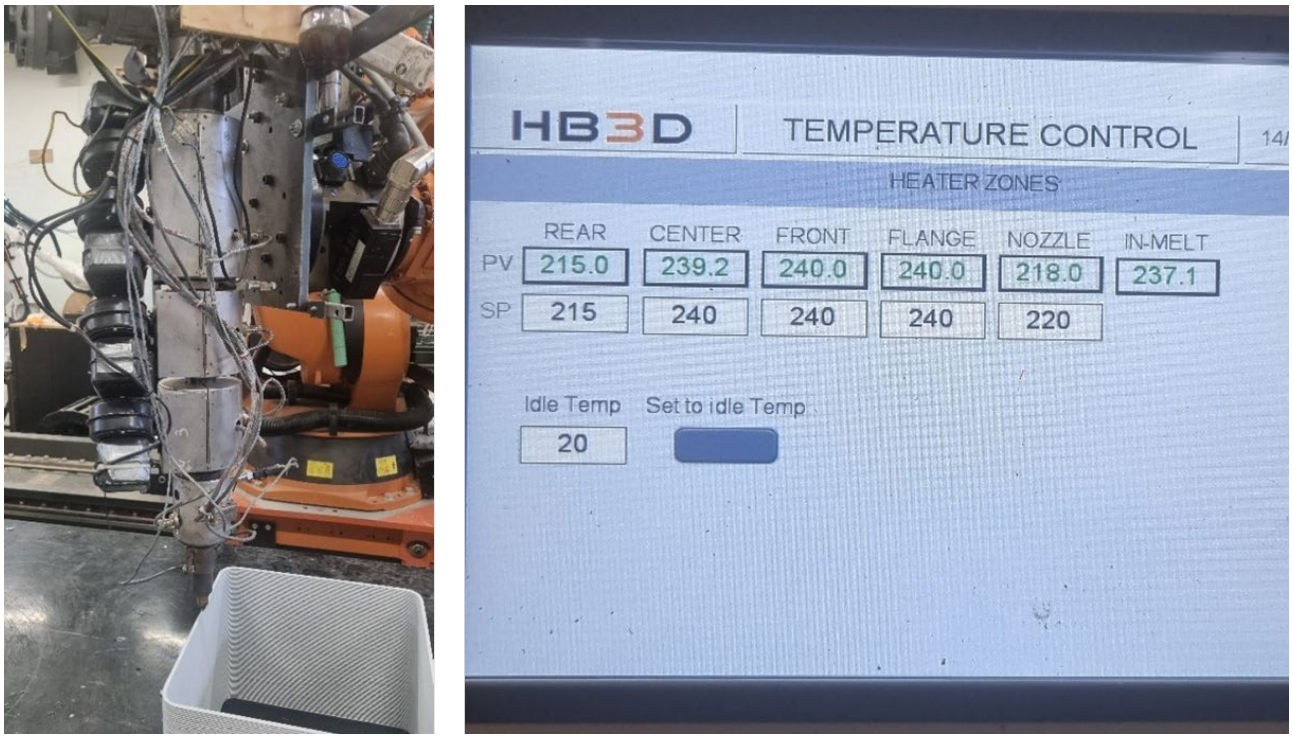

Figure 4-8 Extrusion arm and the measured temperatures at different points at the side of the extrusion arm (indirect measurement of temperature of melted material), only the last one ("IN-MELT") gives the temperature measured directly from the melted material

The melted material is extruded via the nozzle. A nozzle diameter of 5 mm is used for printing of the boxes. With this nozzle, a bead width of 6.0 mm was printed. This means that the thickness of the walls of the boxes, so the thickness of the test specimens, is 6 mm. The bead thickness, which is the thickness of one print layer, is 2.5 mm. This means that the number of layers for the boxes will be 320 mm / 2.5 mm = 128 layers. How the bead parameters, the dimensions of the cross section of one print layer, are set for the printer, can be seen in Figure 4-9. With layers times of 80 s, 100 s, and 120 s, the duration of printing of the boxes is 2.84 h (2 hours and 51 minutes), 3.56 h (3 hours and 33 minutes), and 4.27 h (4 hours and 16 minutes).

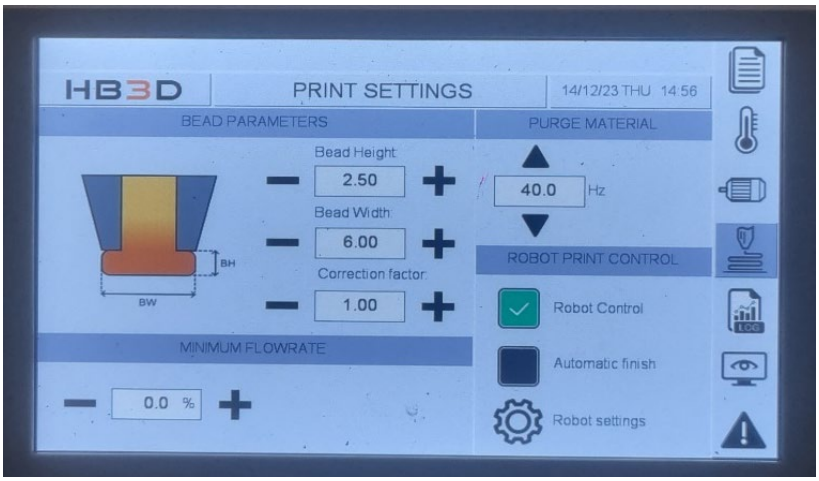

Figure 4-9 The bead parameters of the extruded material. These are the dimensions of the cross section of one printed layer

Besides the layer times, the maximum print speed should also be considered. The combination of the maximum layer time and the maximum print speed determine the maximum length of the print path. For the boxes, this maximum print path length will not be an issue. But for the design of the bridge deck element, it could be a limiting factor. Therefore, the maximum print path length corresponding to a certain layer time should be known. The print company HB3D holds as a rule of thumb for their printers a maximum print speed of 10 kg/h. With the three layers layer times considered in this research (80 s, 100 s, and 120 s), the bead dimensions from Figure 4-9, and the given density of $1.61*10^{-6}$ kg/mm^3 from the material supplier, the maximum print path lengths (L_{pp}) will be as follows (Equations (4-1) – (4-3)):

$$L_{pp} = 80s * \frac{10\,kg/h \Big/ 3600\,s/h}{1.61 * 10^{-6}\,kg/mm^3 * 6\,mm * 2.5\,mm} * 10^{-3} = 9.2\,m \quad (4\text{-}1)$$

$$L_{pp} = 100s * \frac{10\,kg/h \Big/ 3600\,s/h}{1.61 * 10^{-6}\,kg/mm^3 * 6\,mm * 2.5\,mm} * 10^{-3} = 11.5\,m \quad (4\text{-}2)$$

$$L_{pp} = 120s * \frac{10\,kg/h \Big/ 3600\,s/h}{1.61 * 10^{-6}\,kg/mm^3 * 6\,mm * 2.5\,mm} * 10^{-3} = 13.8\,m \quad (4\text{-}3)$$

With extrusion, the box is printed layer by layer. To have a neater extrusion, and thus a better print quality, the corners of box are rounded, since sharp corners can lead to heat accumulation and imperfections. The radius of the corner depends on the size of the printed object. There are two sizes for the boxes of the first stage of testing, namely 370 × 370 × 320 mm and 270 × 270 × 320 mm (L×b×h). The 370 × 370 × 320 mm box dimensions are also valid for the second stage of coupon testing. For the bigger box, the radius of the corner is 25 mm and for the smaller box 18.4 mm. Since the test specimens should be flat coupons, the corners cannot be used for the material to be tested. This means that the useful material of the sides of the boxes is the width of the sides minus the radius of the corners on both edges.

As mentioned before, the box is printed layer by layer, see Figure 4-10. There is somewhere a starting point of the print path. This starting point is also the ‘stacking point since each new print layer starts here. This stacking point results in a discontinuity. In general, it is desirable to have this discontinuity at a location which is least critical or least useful. Because the corners are rounded, they are not useful for the test coupons. So, the corners of the box will not be used. Therefore, the starting point of each layer should be in the corner to avoid discontinuity in one of the sides of the box. Since the coupons are cut from the sides of the box, this is useful material which should have as little imperfections as possible.

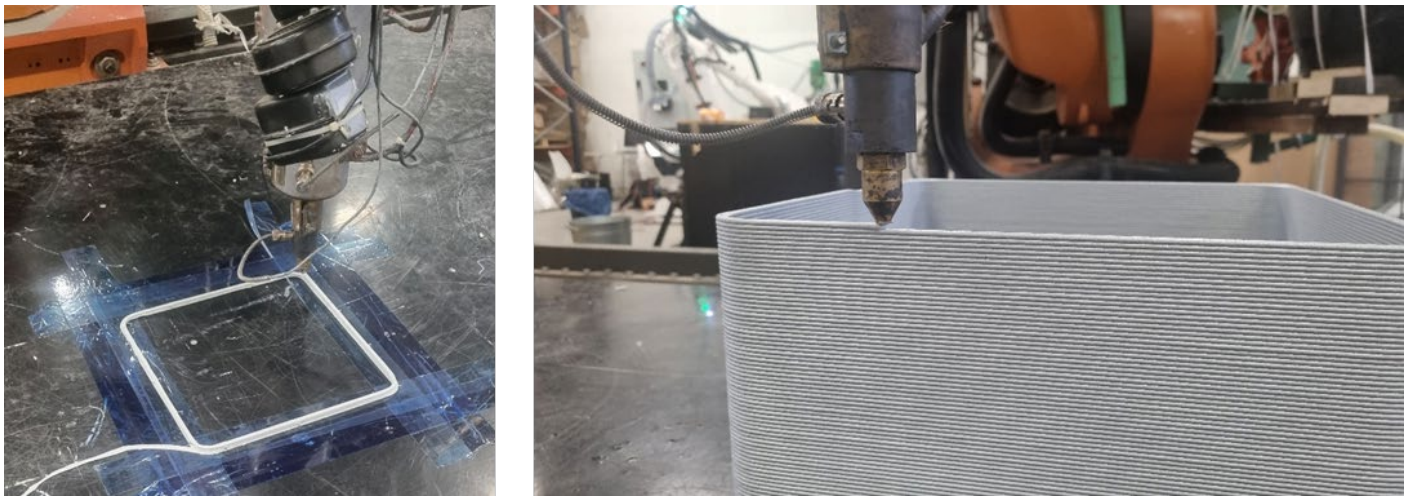

Figure 4-10 The printed box is built up layer by layer. In the left picture, the first layers are extruded. In the right picture can be seen how the next layer is printed on top of the previous layer

Because the 3D printed elements are layered products, some layers are extruded at first. The first layer is fixed to the surface on which is printed. To keep the material in its fixed position, some extra operations are done. The first layer is fixed by special tape and additionally by staples, if needed, to have a solid base for the rest of the printed material. Because the effect of cooling and shrinkage, and the fixation on the surface of those first layers is relatively large, some extra internal stresses will occur. Therefore, the first printed layers are not very representative. Moreover, the first printed layers cool quicker than layers printed later, since they are extruded on the table, which is colder than a previous printed layer. So, the optimal performance of the material will not be obtained by the firstly printed layers. Therefore, it should be avoided that the test coupon will be cut from a part of one of the first print layers.

4.5 Conclusion

A shorter layer time will be beneficial for the structural performance of the material. However, when designing and producing bridge elements, the layer time will increase because the structural elements are bigger. On the other hand, one should the apply a low print speed to obtain the most accurate extrusion. This will give the highest quality of the print layer, if the maximum layer time is not exceeded. So, it is important to know what the influence of the layer time is on the material tested in this research. What can be the layer time to still obtain the desired mechanical properties? This should be investigated and considered when the structural bridge element will be designed. The design of a possible print path will influence the layer time.

5

Application in Bridge Decks

5.1 Introduction

The main benefit of the application of FRP in bridges is the strong mechanical performance in relation to its low weight. How this can be applied in bridge deck will be discussed in this Chapter. There are some typical designs for the structure of a bridge deck. Although pedestrian bridges are the field of application of FRP bridge deck in most of the cases, the structural principles can still yield for road bridges. There is just a higher load to take into account from heavy traffic. The starting point of the design of the bridge deck element will be the preliminary design from the previous study.

5.2 Shapes and profiles

What are common designs for FRP elements used in bridge decks? There are several production methods for FRP elements. Of course, 3D printing is the production method which this research regards. Some examples of 3D printed bridge (deck) structures were already presented in Section 2.3. However, it is still useful to have a look at the shape and design of the FRP bridge deck elements made by other production methods. Some standard bridge deck panels are shown in Figure 5-1. The outer parts of FRP bridge deck structures are mainly the same. The infill parts or the cores vary the most. For the design, there is more freedom for the different shapes of this part of a bridge deck element.

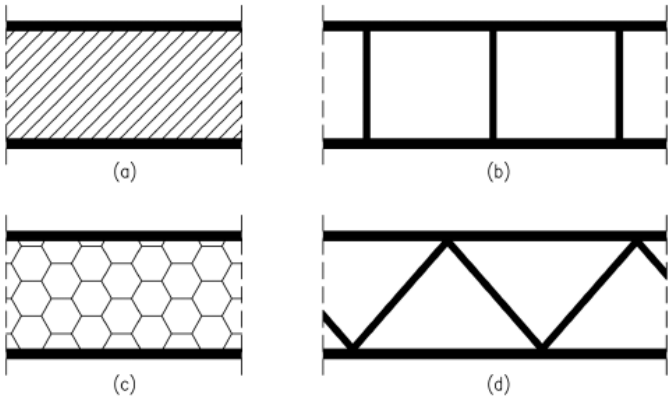

Figure 5-1 Basic types of cores in sandwich panels: (as) foam filling, (b) vertical webs, (c) honeycomb structure, (d) truss core [4]

There are some standard designs for pultruded profile decks. Examples are EZ-span decks, SuperDeck systems, DuraSpan systems, and Strongwell FRP deck systems [4]. These examples of bridge deck systems are shown in Figure 5-2. The design of pultruded profiles could be used as an inspiration for 3D printed elements. For both pultrusion and 3D printing, the FRP element produced will mainly have a unidirectional fibre orientation. However, the final design should not be too much like a pultruded profile. Otherwise, 3D printing will not be the beneficial manufacturing method, as it can also be pultruded. Another option is the

ASSET FRP deck system (Figure 5-3), which is one of the first and most popular FRP deck systems in Europe. The double triangular profiles are bonded and connected to each other. In these examples, the main variation is in the shape of the stiffeners in the infill part.

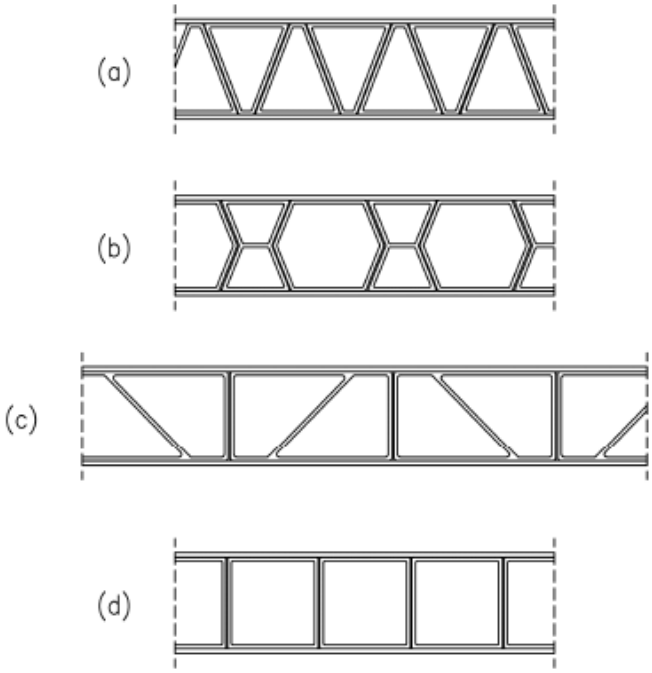

Figure 5-2 Examples of bridge decks made of adhesively bonded pultruded profiles: (a) EZ-Span, (b) Superdeck, (c) DuraSpan, (d) Strongwell FRP Deck System [4]

Figure 5-3 ASSET FRP deck profiles [4]

The print partner from the previous study provided some designs for a bridge deck. These are shown in Figure 5-4. The principle of this design is to print an outer plate, then the infill part with the stiffeners/ribs, the other outer plate, and a path back along one of the outer parts or via the infill in the “honeycomb” variant. With design B “inclined ribs”, a truss-like shape can be printed.

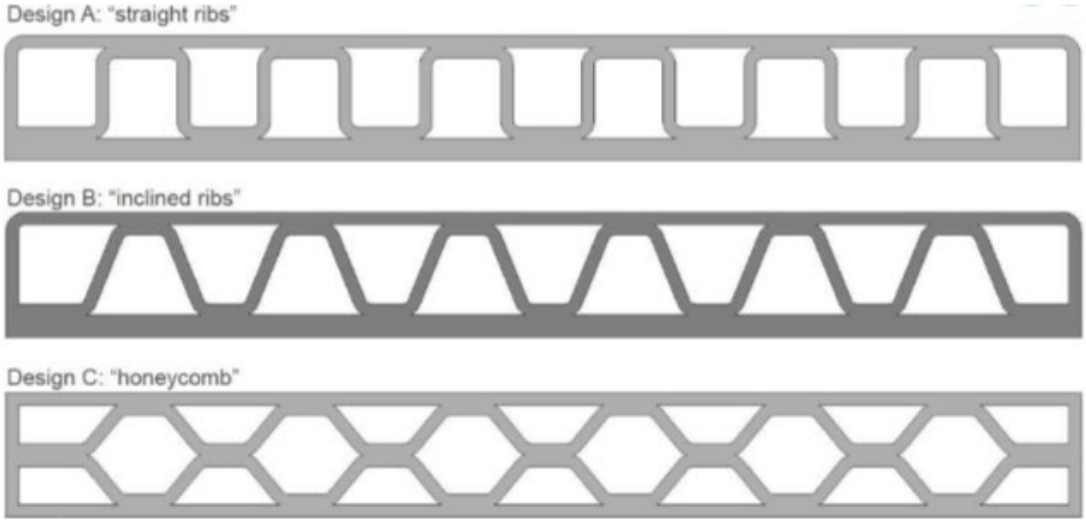

Figure 5-4 Initial deck designs of Covestro to test elements on component level [40]

A specific example of GFRP decks in road bridge is shown in Figure 5-5. In this design, the principle from the ASSET FRP deck profile is applied. Although this is not 3D printed, it is a road bridge application which could be combined with the preliminary design of the previous study.

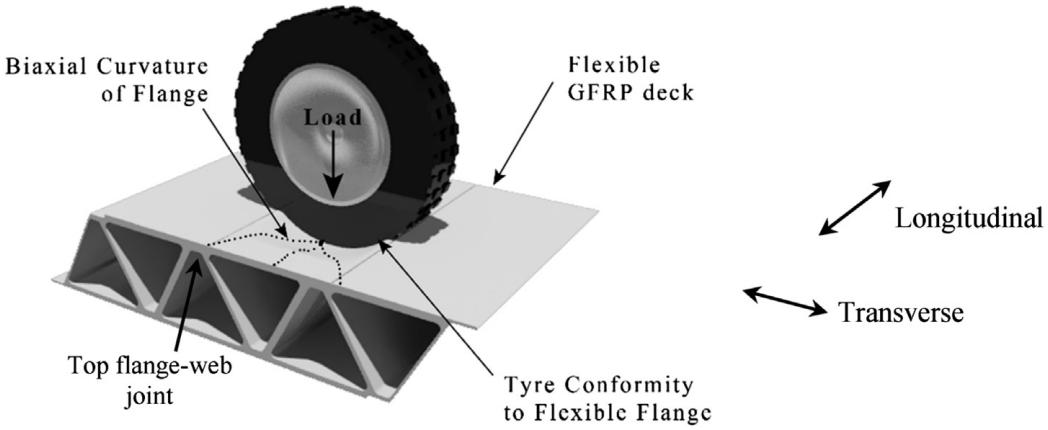

Figure 5-5 Near-field biaxial curvature in FRP deck's top flange due to tyre load [41]

5.3 Load distribution

For the loads on a bridge, NEN-EN 1991-2 can be applied. In this Eurocode, different load models for traffic loads on bridges are elaborated. The bridge deck component that will be designed in this research should be able to withstand the wheel load from one of those load models. Load model 1 (LM1) and load model 2 (LM2) are the most applied load models and these load models will be considered. Since the bridge deck element is a local component of the bridge, it is more relevant to observe the impact from the concentrated load. As the width of component is in the same order of magnitude as the width of the wheel load, the wheel loads from LM1 and LM2 will be focused on.

An overview of the characteristic load values and the application of LM1 is given in Table 5-1 and Figure 5-6. For each traffic lane, the load is specified. This load consists of a tandem system (TS) and a uniformly distributed load (UDL). For local checks, a TS should be unfavourably applied [42]. This TS consist of two axles and one axle consist of two wheels. The load area of one wheel load 400 × 400 mm. For the local check, the maximum characteristic load value should be applied. This is the lane 1 axle load, which has a value of 300 kN. Since the wheel load is half of the axle load, the governing characteristic value of the wheel load is 150 kN.

Table 5-1 Characteristic load values of LM1 [42]

Positie	**Tandemstelsel *TS***	**Gelijkmatig verdeelde belasting (GVB)**
	Aslast Q_{ik} (kN)	q_{ik} **(of** q_{rk}**)** (kN/m^2)
Rijstrook nummer 1	300	9
Rijstrook nummer 2	200	2,5
Rijstrook nummer 3	100	2,5
Overige rijstroken	0	2,5
Resterende oppervlakte (q_{rk})	0	2,5

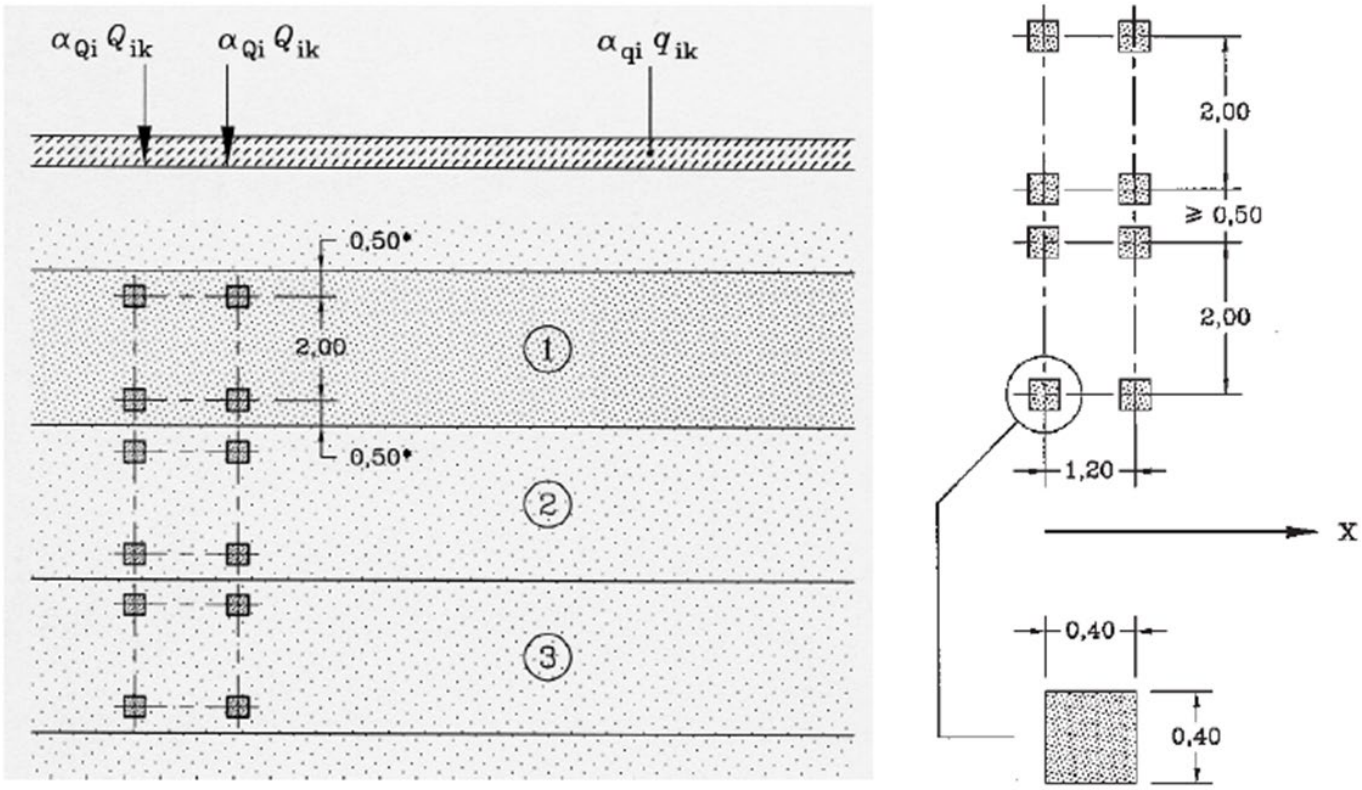

Figure 5-6 Application (of TS for local checks) of LM1 [42]

LM2 consists of a single axle load that can be applied on each (unfavourable) position on one of the traffic lanes. The characteristic value of this axle load is 400 kN. When relevant, a single wheel load of 200 kN can be considered. This is the case for the design of the bridge deck components in this research. The area of the wheel load of LM2 is 350 × 600 mm, see Figure 5-7.[42]

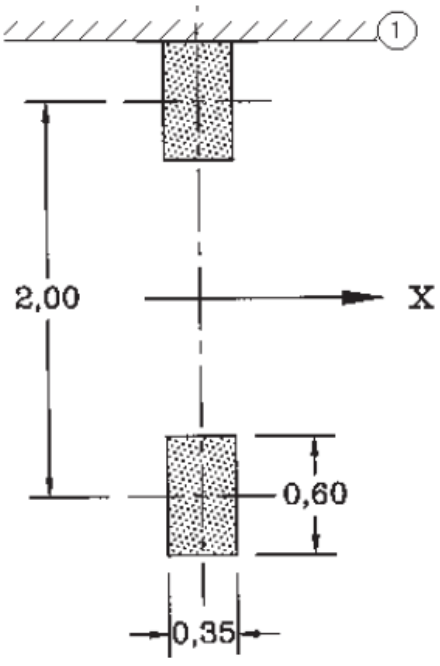

Verklaring

X Lengterichting van de brug
1 Stootrand

Figure 5-7 Application of LM2 [42]

5.4 Preliminary design

From the pre-study of this research project, a preliminary design was made as described in Section 2.2. This preliminary design was an arch-shaped component in between the stringers of the bridge deck. This component should replace the timber deck of a movable bridge. In Figure 5-8 is elaborated how the preliminary design can be printed; what the dimensions are and what the structural scheme is of the FE model with the boundary conditions. For the print path there were two options: one with an additional layer along the top part (upper left in Figure 5-8) and the other one with an additional layer along the bottom arch (lower left in Figure 5-8), both containing a sharp 180° turn. It turned out that the way back along the arch was more suitable and the positions of the stiffeners were better located. Therefore, the print path with the way back along the arch was modelled. The print path makes that the thickness of the different sections of the element vary in thickness. The element consists mostly of single and double layered sections, and a few parts are triple layered.

In the FEA, a wheel load from LM1 was applied in the middle of the top plate of the component. Since the component will be placed in between the stringers, the element is supported vertically at the bottom and horizontally at the sides. The infill part of the component can be described as a triangular pattern, which makes it a truss-like structural behaviour. However, due to the overlap of the print layers, those are not perfect triangles. So, there are some eccentricities in the connections. From the FEA turned out that the stress in the top plate of the element did exceed the limit. This was the only structural design check that did not suffice.

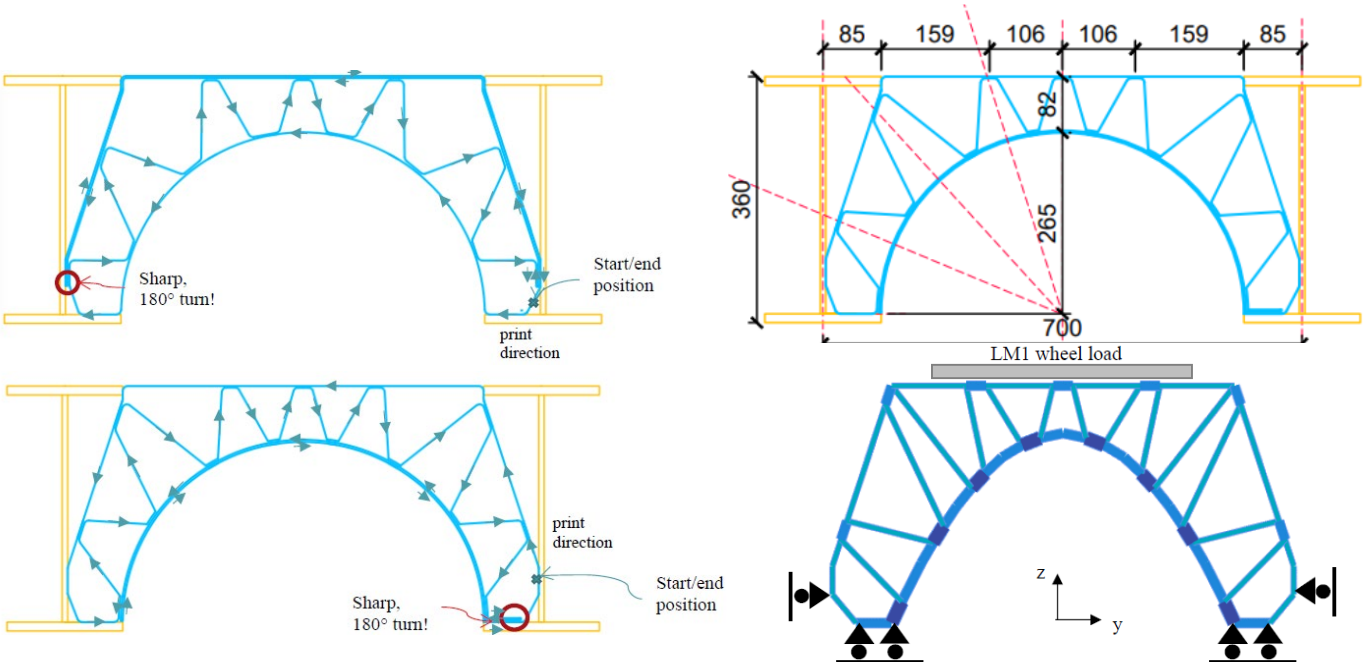

Figure 5-8 Print path (upper and lower left), dimensions (upper right), and the structural scheme of the FE model of the preliminary design

5.5 Conclusion

From the preliminary design of the previous study can be derived that the arch-shaped component is the most suitable option for the bridge deck element. From the shapes and profiles elaborated in Section 5.2, can be concluded that with inclined ribs for the infill of the element a truss-like shape can be made. The inclined ribs from the 3D print path from Covestro are not perfectly triangular. In the reference projects from Chapter 2 this principle was also applied. However, also in these cases, there was not a perfect truss-like shape. As the truss-shaped decks seems to have the potential for flat bridge decks, this principle could be combined with the preliminary arch design. By optimizing this preliminary design, one of the crucial aspects is to improve the top plate part, as this was not sufficient. The aim is to improve the infill part of the component while ensuring that the arch part, the top plate, and the sides still suffice. For the design of the component in this research, similar dimensions can be assumed as in the pre-study. By performing FEA and tests on a printed component could be checked whether the optimized design will suffice.

Part II:
Material Research

6

Coupon Testing

Coupon testing will be executed in two stages. The first stage is to investigate some different material configurations. One variation that will be tested is a difference in fibre volume fraction (V_f). The other parameter of interest is the influence of the layer time of printing. After the investigation of the influence of those two parameters, the optimal composition of the material will be chosen based on the variations tested before. The influence of the ribbed surface will also be investigated in the first stage of coupon testing. The optimized material will be tested in the second stage of coupon testing. In this test stage, the mechanical properties of the material will be characterized.

6.1 Preparing coupons

Before the coupon tests can be executed, there are some preparations steps needed to be done. To go from a printed box to a coupon, the coupons will be cut from the sides of the boxes by water jetting. For the tests for the influence of the ribbed surface, some coupons must be polished to compare the original coupons with coupon having a flat surface. Some coupons need some additional treatment like gluing aluminium tabs on it to be able to perform the test properly.

6.1.1 Coupon cutting

As described in Section 4.4, the material to be tested is printed in boxes. The printed boxes of the first stage of coupon testing can be seen in Figure 6-1. From these boxes, the coupons are cut. Cutting of the coupons is done by water jetting. Water jetting is a method of cutting in which the material is cut by a water jet. This is a very thin jet. The water is jetted by an extremely high pressure, around 4000 bar. Because the water jet is very thin and under high pressure, a fine cut can be made in the material. A picture of the machine cutting a coupon from one of the sides of a box is shown in Figure 6-2.

Figure 6-1 The four 3D printed boxes for the first stage of coupon testing ready to cut the specimens from

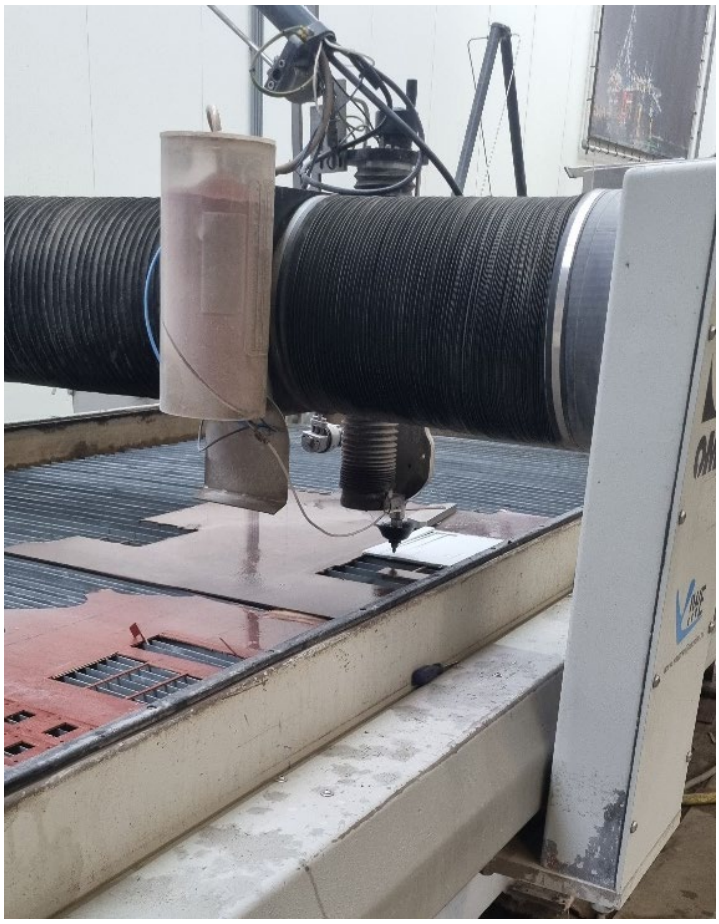

Figure 6-2 Water jetting machine cutting coupons from one of the sides of a box

Firstly, the four sides of the box are cut into four individual plates. A whole box is too high to fit in the machine, and when the coupons are cut from a plate, the quality of the cut will be better. The box can be cut at the edges because the edges will not be used since the edges are rounded and thus not suitable for testing. The coupons to be tested are namely straight specimens. It is just the surface of the coupons that is not flat. The surface is ribbed due to the way of production, namely 3D printing.

By cutting the coupons in different orientations, coupons with fibres in longitudinal and in transverse direction are obtained. These two different orientations are needed to be able to test in principal direction of fibres, so parallel to the direction of printing, and in the transverse direction of the fibres, so perpendicular to the direction of printing. The obtained coupons from cutting for the tensile tests of the first stage of testing are shown in Figure 6-3. The nesting drawing of the sides of the boxes can be found in Appendix B. These drawings show how and in which layout all the coupons of this project are cut from the different boxes.

Figure 6-3 Obtained tensile test coupons by water jetting. The upper one is the coupon for the longitudinal tensile test and the lower one for the transverse tensile test

6.1.2 Polishing coupons

As can be seen in Figure 6-3, the coupons have a ribbed surface. This ribbed surface is due to the 3D printing production method. Regarding the tensile tests, it could be the case that the ribbed surface of a coupon affects the stress distribution over the length of the coupon. Due to the ribs, local stress concentrations may occur. This phenomenon is less likely to happen for the coupons in longitudinal direction because the cross section of the coupon is not changing over the length of the coupon. For the coupons in transverse directions, it is more likely that local stress concentrations can occur. The printed layers make that the thickness of the coupon is not uniform over the length of the coupon. Between the beads, the coupons are a bit less thick than at the middle of the bead. So, the cross section of the transverse tensile test coupon is changing of the length of the coupon. To check if this has a significant effect, several coupons of some test series are polished. Three coupons of each of the following material specification of the test series were polished:

- GF30_80s longitudinal
- GF30_80s transversal
- GF45_80s transversal

The polished GF45_80s transversal coupons are shown in Figure 6-4. The surface of the coupons is flatter than before, but it is not perfectly flat. This is because the coupons are polished by hand and a relatively rough grinder is used to polish the ribbed surface. However, the variations in cross sectional area over the length of the coupon are less than it was the case with the original transverse coupons and the coupon do not have a ribbed surface anymore.

Figure 6-4 Polished coupons of the GF45_80s test series specification

6.1.3 Gluing aluminium tabs

For the tensile test in longitudinal direction, an issue with the clamps occurred. During a trial test, it turned out that the coupon slipped out of the clamp. This leads to incorrect measurements. Due to the slip, the force decreases. So, the measured force becomes much lower and will not be transferred anymore from the jack of the machine to the specimen. This means that the specimen will not reach failure.

The slip can be caused by the ribbed surface. Due to the ribs, the contact area between the clamp and the coupon is smaller. And the clamping force cannot be increased to its maximum, because of the compression resistance of the material. If the clamping force is too big, compressive stresses will occur that exceed the compressive strength of the material in transversal direction, which will break the coupon. To solve the issue, aluminium tabs are glued on the coupon. The aluminium tab has a smooth surface, so the contact area between the clamp and the specimen becomes sufficient. The glue in between the coupon and the aluminium tab is strong enough to transfer the forces from the clamping to the coupon. In Figure 6-5, the coupons of test series 1 (GF30% and layer time 80s) with the aluminium tabs glued on the clamping surface are shown. In this way the tensile test in longitudinal direction could be run successfully to obtain valid test results. The transversal tensile test did not have the clamping issue, so no gluing was necessary for those coupons.

Figure 6-5 Longitudinal tensile coupons GF30_80s with aluminium tabs glued on the clamping surface

6.2 First stage of coupon testing

6.2.1 Scope

An overview of the series of testing in the first stage is presented in Table 6-1. Three series of coupon tests are elaborated in this Table. In the first series, the base material will be tested. The base material is a standard material that the material supplier has regularly in stock. The base material has a standard V_f and a standard layer time. The standard V_f is 30%. So, the volume of the composite consists for 30% of glass fibres (GF). The standard layer time is set on 80 seconds. This is one of the common layer times used by the print partner.

In the second test series, an increased V_f is tested, and produced with the same standard layer time (80 s). The V_f is increased to 45%. This variation is related to the material composition in terms of the amount of fibres. A higher V_f should lead to better structural performance in terms of strength and stiffness. However, it is expected that the material could be more brittle when the V_f is higher. Therefore, the goal of the test is to investigate if a higher V_f is possible, without having more brittle failure of the material. A higher strength and stiffness are desired because this will increase the capacity of the element. On the other hand, it is desirable that the material still has some plastic behaviour, due to the 'warning-effect' of a structural element. When too brittle failure occurs, the element fails quite suddenly without 'warning' by deforming or cracking.

The layer time of the material with the standard V_f (GF30%) is varied in the third test series. Since two different layer times, compared to the standard layer time, are tested, test series 3 consists of two subseries, namely test series 3.1 and 3.2. The influence of the layer time is not related to the material composition but to the printing process (production). The longer the layer time, the weaker the bonding between different print layers, due to a larger difference in temperature between the extruded material and the previous printed layer. The layer time is affected by the print speeds and the length of the print path. The goal is to have the longest layer time possible while the bond strength, so tensile strength perpendicular and shear strength between the print layers, is still sufficient. The longer the layer time can be, the more freedom there is for the design of the element because the print path could be longer and/or the slower the robot can print to have a neater extrusion. The maximum layer time that the print partner advised was 120s. Therefore, this layer time is chosen as the ultimate layer time. The increased layer time is set at 100s. This is in the middle between the standard layer time and the maximum layer time.

It is assumed that the influence of a higher V_f will also be valid for the other layer times. The other way around, the same is valid. The influence of the other layer times will also be valid for the other V_f. That is why the increased V_f is not tested in combination with the increased and the maximum layer times and why the increased and maximum layer times are not tested in combination with the increased V_f. The goal of this first stage of coupon testing is to compare the different configurations (V_f and layer times). Therefore, it is not necessary to perform a lot of different types of tests. Only tensile tests will provide enough information to draw a conclusion for these comparisons.

Since the fibres are mainly orientated in the direction of printing, which is the principal direction, tensile tests in longitudinal direction will make clear what the influence is of the V_f on the tensile strength and stiffness of the material. Tensile tests in transverse direction will be performed to check if there is a difference and to be able to compare with the tests of the coupons with the longer layer times. Because the fibres are mainly oriented in longitudinal direction, it is expected that the tensile strength in transverse direction will not differ too much. The tensile strength in transverse direction is the parameter to obtain for the material with the longer layer times. These coupons are only tested in transverse direction since the strength of the bonding between the print layers is the point of interest. Moreover, when testing in longitudinal direction, the bond strength between the print layers is not tested. Therefore, the tensile test in longitudinal direction is not relevant for the test series with the longer layer times.

Table 6-1 Scope of the first stage (coupon test series 1, 2, 3.1, 3.2) of coupon testing

Test series	Purpose	Type of test	Number of coupons	Parameter to measure
1 Base material Layer time = 80s V_f = 30%	Standard material as a reference for comparison with the increase V_f and variations in layer time.	Tensile // (long.)	3	$\sigma_{1,t}$; E_1; $\varepsilon_{1,t}$
		Tensile ⊥ (tran.)	3	$\sigma_{2,t}$
2 Increased V_f Layer time = 80s V_f = 45%	Increased V_f to obtain higher strength and stiffness (in principal direction)	Tensile // (long.)	3	$\sigma_{1,t}$; E_1; $\varepsilon_{1,t}$
		Tensile ⊥ (tran.)	3	$\sigma_{2,t}$
3.1 Increased layer time Layer time = 100s V_f = 30%	Investigate the effect of layer time on the bond strength. What is the maximum layer time without a significant loss of performance? Relevant for the design of the component considering the print path.	Tensile ⊥ (long.)	3	$\sigma_{2,t}$
3.2 Maximum layer Layer time = 120s V_f = 30%		Tensile ⊥ (tran.)	3	$\sigma_{2,t}$

6.2.2 Tensile test coupon

The specimen for the tensile test is designed according to the Eurocode standard for tensile tests. The NEN-EN-ISO 527 standard is about the determination of tensile properties of plastics. In part 4 of this standard (NEN-EN-ISO 527-4 [43]), four different types of specimens are specified. Due to common way of performing tensile tests at the Stevinlab II at the TU Delft, the type 4 specimen from the standard will be used for the tests. The dimensions and the shape of this coupon are sketched in Figure 6-6. The coupon is narrowed in the middle. This causes a higher stress, due to the smaller cross sectional area, in the middle of the coupon than at the ends, where the coupon will be clamped. This tapering is applied so it is more likely that failure of the coupon will occur in the middle, which is desired to have valuable test results. At both ends, the coupon will be clamped. One of the ends will be displaced. This will cause tensile stresses and strains through the coupon. The ends of the coupon will be clamped over a length of about 50 to 55 mm.

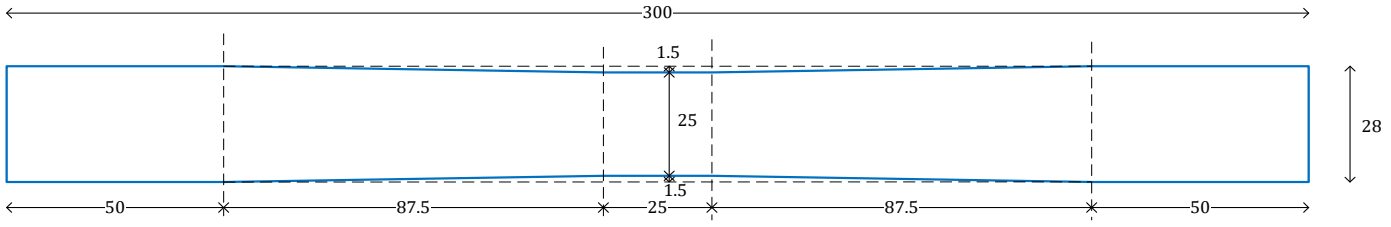

Figure 6-6 Type 4 tensile test coupon according to NEN-EN-ISO 527-4

6.2.3 Machines

For the tensile test, two different test machines are used. For one machine it was possible to use an extensometer for the strain measurement. This was for the machine on which the tensile coupon test in longitudinal direction were executed. These two machines are (see also Figure 6-7):

- Dowtey-Rotel for longitudinal tests with extensometer
- Instron 1122 for transverse tests without extensometer

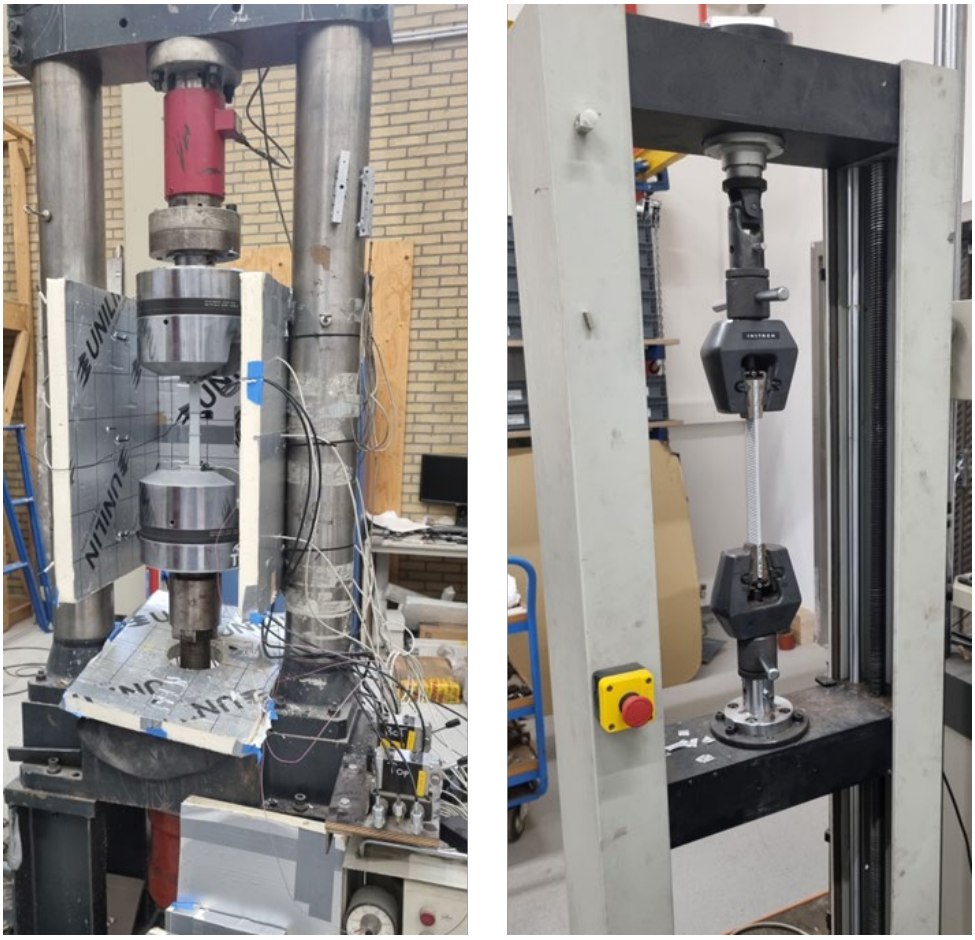

Figure 6-7 Machines used for the first stage of coupon testing. The Dowtey-Rotel machine (left) for the longitudinal tensile tests and the Instron1122 machine (right) for the transverse tensile test

6.3 Second stage of coupon testing

6.3.1 Scope

In the second stage of coupon testing, tests were performed to establish the mechanical properties of the material. An overview of the types of tests is provided in Table 6-2. Tensile, compression, and shear tests were done to determine strength and stiffness values of the material. The obtained strength and stiffness properties are needed for the design of the bridge deck element. These values will be used as the entries in the model for the structural analysis of the bridge deck element. For alle the types of tests yields that there should be at least five individual successful tests. To be able to determine a mechanical property of a material, valid results from at least five specimens are required, according to the standards.

Tensile tests in both longitudinal and transverse directions are performed to establish the tensile strength and stiffness in both directions. This will be done according to the NEN-EN ISO 527 standard. The strain could be observed quite accurately since measurements were done by an extensometer. The force at failure can be obtained from the measurements of the machine. This will be converted to the stress by dividing the force by the measured area of the failure surface. Because of the ribbed pattern of the specimens, an average surface will be considered for the stiffness in longitudinal directions. For the coupons in transverse direction, the area in between the ribs, so the thinner part of the coupon, was considered.

The compression tests in longitudinal and transverse direction are performed to determine the compression strength in both directions of the material. Because the distance between the clamps was too short to apply an extensometer for these tests, the strain will be estimated from the displacement of the jack and the distance between the end tabs of the coupon. The force measured by the machine is converted to stress in the same way as is done for the tensile tests. The design of the coupon, the test set-up and processing of the results is done based on the NEN-EN ISO 14126 standard. Only the length between the end grips is a bit longer than prescribed because the shortest possible distance of the machine was a bit longer.

The goal of the IBSS tests was to determine the shear strength of the bonding between the print layers. In this way, the shear strength on the weakest plane, and thus the minimum shear strength, of the material could be established. To be able to estimate the shear stiffness in this direction, an extensometer measured the strain. Because these strain measurements are done over a part of the specimens loaded in longitudinal tensile stress and over a part loaded in shear, they will not be perfectly accurate. But they will give a useful indication.

The IBSS test is not directly based on a specific code or standard. It was not possible to have a double layered specimen since the box was printed with a single layer thickness and all the coupons had to be obtained from the boxes. Because of this, the method from the ASTM-D4255 [44] could be an option. However, this test set-up was not feasible with the available test equipment. To have a similar principle of testing, the method from ASTM-B831 [33] will be applied. Although this standard is regarding steel specimens, the idea with precuts is also applicable for the material and the coupons in this research. In several references [45-51], the principle of a specimen with precuts was also applied, mainly for steel or aluminium specimens. In the previous study from Covestro [34], the principle of lap-shear testing was translated to a printable test coupon which can be cut from the box including the precuts, see Figure 6-8.

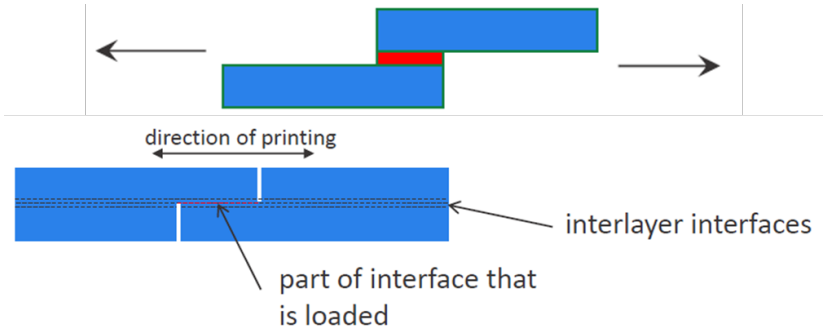

Figure 6-8 Principal of lap-shear testing translated into a printable coupon in which precuts are made [34]

For all the tests, the measurements were done in one direction. Therefore, the Poisson's ratio cannot be exactly determined. Also, the in-plane shear strength and stiffness properties cannot be derived directly from these tests. Only the shear properties in the weaker directions are obtained with the IBSS tests. However, based on the tests results from test series 4 and the properties of the previously studied Arnite material, a rough estimation could be done for these mechanical properties.

Table 6-2 Scope of the second stage (coupon series 4) of coupon testing

Test series	Purpose	Type of test	Number of coupons	Parameter to measure
4 Optimal material from test series 1, 2, 3.1 and 3.2	Characterization of the material that performed the best in the first stage of coupon testing. Besides the tensile strength in longitudinal and transverse direction, also the compression strength in both direction and the shear strength between the print layers will be obtained.	Tensile // (long.)	5	$\sigma_{1,t}$; $E_{1,t}$; $\varepsilon_{1,t}$
		Tensile ⊥ (tran.)	5	$\sigma_{2,t}$; $E_{2,t}$; $\varepsilon_{2,t}$
		Compression // (long.)	5	$\sigma_{1,c}$; $E_{1,c}$; $\varepsilon_{1,c}$
		Compression ⊥ (tran.)	5	$\sigma_{2,c}$; $E_{2,c}$; $\varepsilon_{2,c}$
		IBSS	5	τ_{21}, G_{21}

6.3.2 Tensile test coupon

As tensile tests were also performed in the first stage of coupon testing, the same type of coupon will be used in the second stage of coupon testing. The description of this type of coupon can be found in Section 6.2.2.

6.3.3 Compression test coupon

The design of the coupon for the compression tests is based on the NEN-EN ISO 14126 standard. The standard prescribes three types of specimens. The compression coupon used in this project is the most in line with the Type B2 specimen [52]. Since the clamps of the machines used for the compression tests, could not come to close to each other, the distance between the grips had to be a bit longer. Therefore, the distance between the end tabs was increased to 50 millimetres, resulting in a total length of 150 millimetres, see Figure 6-9.

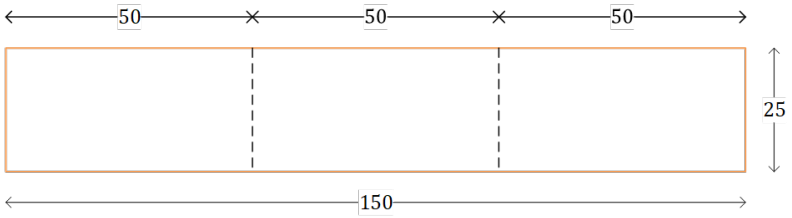

Figure 6-9 Compression test coupon, elongated version of the Type B2 specimen from NEN-EN-ISO 14126

6.3.4 IBSS test coupon

The coupon for the IBSS test is not directly obtained from a standard. Since all the coupons are cut from boxes with a single layer thickness, it is not possible to obtain a double layered coupon for example. A double layered coupon is often used for shear tests. An alternative for this is to make pre-cuts in the coupon with the single layer thickness. From the previous study and information provided to Arup, a shear test with straight pre-cuts was already performed but not all of them went successfully [34]. The ASTM D4255 standard was the reference for the principle of these tests. However, that standard prescribes eccentric load application and the failure area in shear is large [44]. The eccentric load application is not suitable for the available test machines in the lab and a large failure area is not desirable to local stress concentrations.

Therefore, alternative options of shear tests of single lapped/layered specimens with pre-cuts were observed. There are examples of steel or aluminium specimens with pre-cuts. Most of these examples are specimens with inclined pre-cuts. The pre-cuts in the specimens of these examples were mainly inclined cuts [45-49,51], although there were some with straight cuts [49,50]. Besides the variations in straight or inclined cuts, the overlap length is relative short. This overlap length is suitable for steel or aluminium, but the expectation is that the load at failure will be too low with such a short overlap length, based on the shear strength from the previous study. The failure load should be above a certain minimum. Otherwise, the specimens will fail too quickly which will lead to insufficient (amount of) data.

With the information and examples of the reference tests, some trial tests were performed on the different specimens. Two coupons with straight cuts and two different overlap lengths, and one with inclined cuts were tried. For the coupon with inclined cuts, it looked like local concentrations could occur, which seems to be less an issue with the straight cuts. To reach a failure load high enough to obtain reliable and valuable test results, the overlap length should be at least 15 mm. Based on the references and the trials, the IBSS test coupon was designed as shown in Figure 6-10.

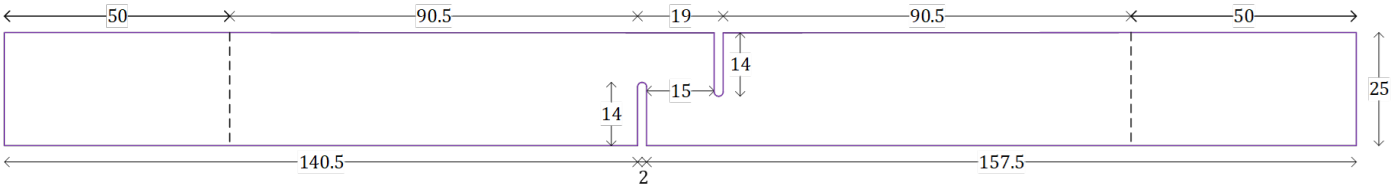

Figure 6-10 IBSS test coupon used in the second stage of coupon testing

6.3.5 Machines

The machines from Section 6.2.3 were also used during the second stage of coupon testing. As in the first stage of coupon testing, the longitudinal tensile tests were performed with the Dowtey-Rotel machine with the use of an extensometer for the strain measurements. Different to the first stage, the Instron 1122 machine was used including extensometer measuring. The tensile tests in transverse direction and the IBSS tests were run on this machine.

For the compression tests, another machine was used: the Schenk_S_600kN (see Figure 6-11). Because of the short distance between the clamps, it was not possible to use an extensometer for the compression tests. Therefore, the strain was estimated by dividing the measured displacements from the jack by the distance between the end tabs where the specimens were clamped.

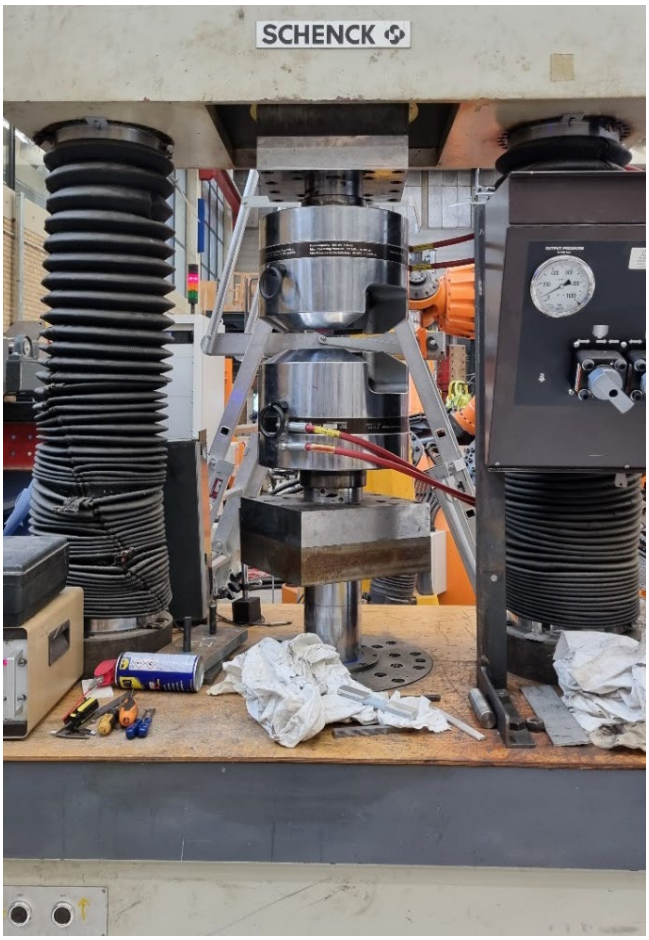

Figure 6-11 Schenk_S_600kn machine used for the compression tests

7

Results from Coupon Tests

The tests on coupon level are divided into two stages. In the first stage, the influence of the fibre volume fraction (V_f) and the layer time of printing was investigated. The material with the optimal V_f and layer time, based on the first stage of coupon testing, is characterized in terms of mechanical properties by more distinct types of tests in the second stage of coupon testing. The overview of what is tested with which type of test in which coupon test series is presented in Sections 6.2 and 6.3. This Chapter will describe the results from these series of coupon testing.

7.1 First stage of coupon testing

The first stage of coupon testing covered test series 1, 2, 3.1, and 3.2 (Table 6-1). Test series 1 and 2 are relevant to investigate the influence of the V_f. Test series 3 focuses on the impact of the layer time and can be compared with both test series 1 and test series 2. For test series 1, the material with 30% V_f and a layer time of 80 seconds (GF30_80s) was used. The material of test series 2 had a V_f of 45% and a layer time of 80 seconds (GF45_80s). The V_f of both test series 3.1 and 3.2 is 30% with a layer time of 100 seconds (GF30_100s) and 120 seconds (GF30_120s) respectively. Additionally, the influence of the ribbed surface was investigated if the ribbed surface did not cause (too much) local stresses which may lead to early failure. These different comparisons will be elaborated one by one. An overview of the results of the first stage of coupon testing is provided in Section 7.1.4. All the results of each individual test can be found in Appendix C.

7.1.1 Comparison different fibre volume fractions

Tensile test in longitudinal and transverse direction were performed on the coupons for the comparison for the different V_f's. The influence of the V_f will be mainly in the longitudinal direction, since the fibres are mainly orientated in the principal direction, which is the direction of printing. However, it is still needed to perform the test in transverse direction, both to check what the influence is of the V_f and to compare with the transverse strength of the material that is printed with the longer layer times (test series 3).

The average longitudinal tensile tests results are presented in a stress-strain diagram in Figure 7-1. During the longitudinal tensile tests, strain measurements were done with an extensometer. Therefore, the results can be analysed in terms of strain quite accurately. The results give information about the strength, stiffness, and elastic/plastic behaviour. As expected, the strength and stiffness of the 45% V_f material is higher than the strength and stiffness of the 30% V_f material. The strength of the 45% V_f material is 102.1 ± 0.8 MPa and the 30% V_f material has a strength of 71.3 ± 1.4 MPa. The stiffnesses of both materials is 22,040 ± 360 N/mm^2 and 13,920 ± 210 N/mm^2 respectively. These differences in strength and stiffness can clearly be seen in the stress-strain diagram. The graph of GF45_80s reaches a higher stress level than GF30_80s and it is also steeper. Surprisingly the GF45_80s graph showed more plastic behaviour of the material. It was expected that a higher amount of fibres would make the material even more brittle, so less plasticity, but that is not the case. Although, the material is still quite brittle, given a strain at failure between 1.1% and 1.2%.

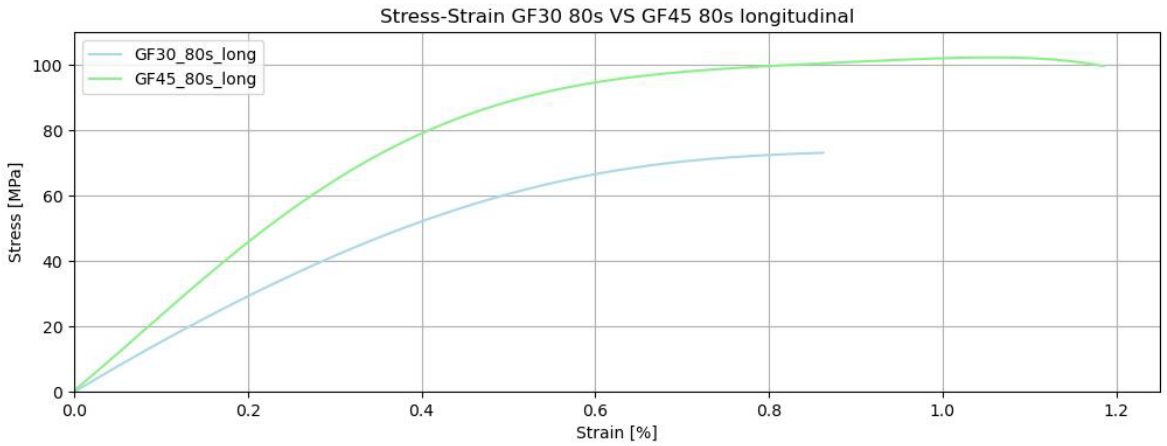

Figure 7-1 Stress-strain diagram of the tensile test results of GF30_80s and GF45_80s in longitudinal direction

The brittleness of the material was shown by the failure mechanism. In the stress-strain diagram in Figure 7-1 can be seen that the strain at failure is not very high, but also the way of how the coupons failed was a clear indication of the brittleness of the material (see Figure 7-2). The coupon failed quite suddenly during the tests and from a few coupons even a complete part broke out of the coupon (upper right picture in Figure 7-2). The only sign before failure was that the material coloured a bit white before failure. Also, the cross sectional area of the surface at the point of failure is similar as the dimensions measured before the tests were executed. So, there is no, or a limited, effect of necking, which implies that the material has a brittle failure mode.

Figure 7-2 Failure mechanisms of coupons tested in tension in longitudinal direction. The two pictures on top are two GF30_80s coupons and the lower the picture are a GF45_80s coupon

Besides the tests in longitudinal direction, the GF30_80s and GF45_80s coupon were tested in tension in transverse direction. Because these tests were executed by using another machine than the tensile tests in longitudinal direction, it was not able to use an extensometer for strain measurements. Therefore, the results are presented in a stress-displacement diagram in Figure 7-3. The curves are the averages of the test results. The main difference between the behaviour of GF30_80s and GF45_80s in transverse behaviour is the stiffness. The graph of the behaviour of GF45_80s is a bit steeper than the graph of GF30_80s.

An indication of the values of the stiffness can be made based on a rough estimation. Considering the displacement of the jack and the length of the coupon, strain over the whole coupon can be determined. This strain estimation is just a rough indication to compare the two configurations because the strain is not constant over the length of the coupon, as the cross section area is not constant. From this strain and the calculated stress, the tensile Young's modulus in transverse direction can be estimated. The estimated stiffnesses in transverse direction are approximately 3,150 N/mm^2 and 2,290 N/mm^2 for GF45_80s and GF30_80s respectively. These approximated values of the transverse tensile Young's modulus may be a bit lower than

the actual stiffness in transverse direction, but it still gives an indication of what the transverse stiffness (at least) will be.

It can be said that the approximate value is a bit lower than the actual stiffness based on the results of the tests in longitudinal direction. For these tests, both the displacement of the jack and the strain, quite accurately by extensometer, were measured. So, a comparison could be made between the strain data from the extensometer and the strain data calculated from the measurement of the displacement of the jack. The estimated strain is a bit higher than the strain measured by the extensometer, meaning that the slope of the stress-strain graph is a bit lower. So, the calculated estimation of the stiffness is slightly lower than the actual stiffness.

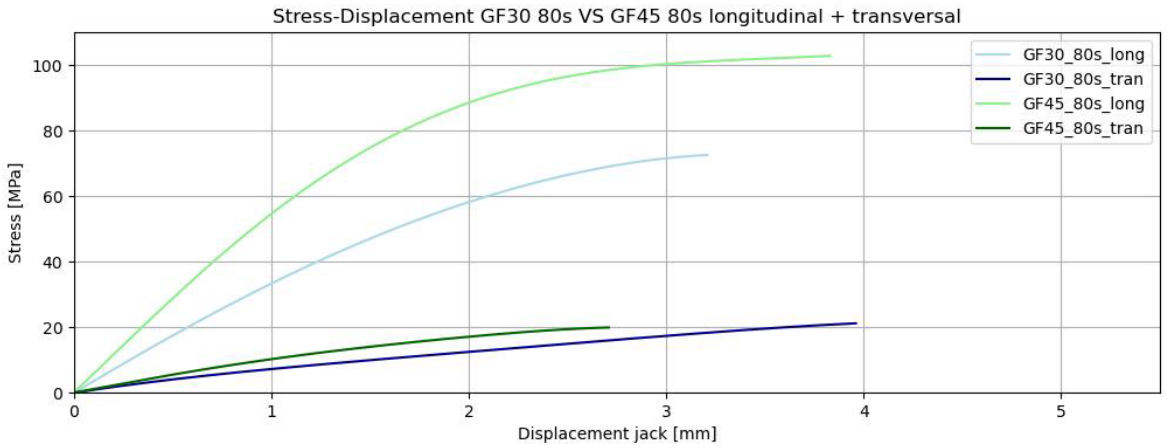

Figure 7-3 Stress-displacement diagram of the tensile test results of GF30_80s and GF45_80s in longitudinal and transverse direction

The specimens did fail as expected. For all the coupons tested, failure occurred between the print layers. This means that the bond strength of the beads is lower than the transverse tensile strength of the material itself. Thus, the bond strength of the print layers is the critical factor. Which is logical, because the bond strength of the bead is dependent on the initial transverse strength and the heating and cooling effect of the material. Due to the extrusion of the bead on the previous printed bead, there is a difference in temperature of the layers, which makes that the bonding of the two layers will not be as strong as the initial transverse strength. Therefore, the failure modes occur in between the bead, as can be seen in Figure 7-4.

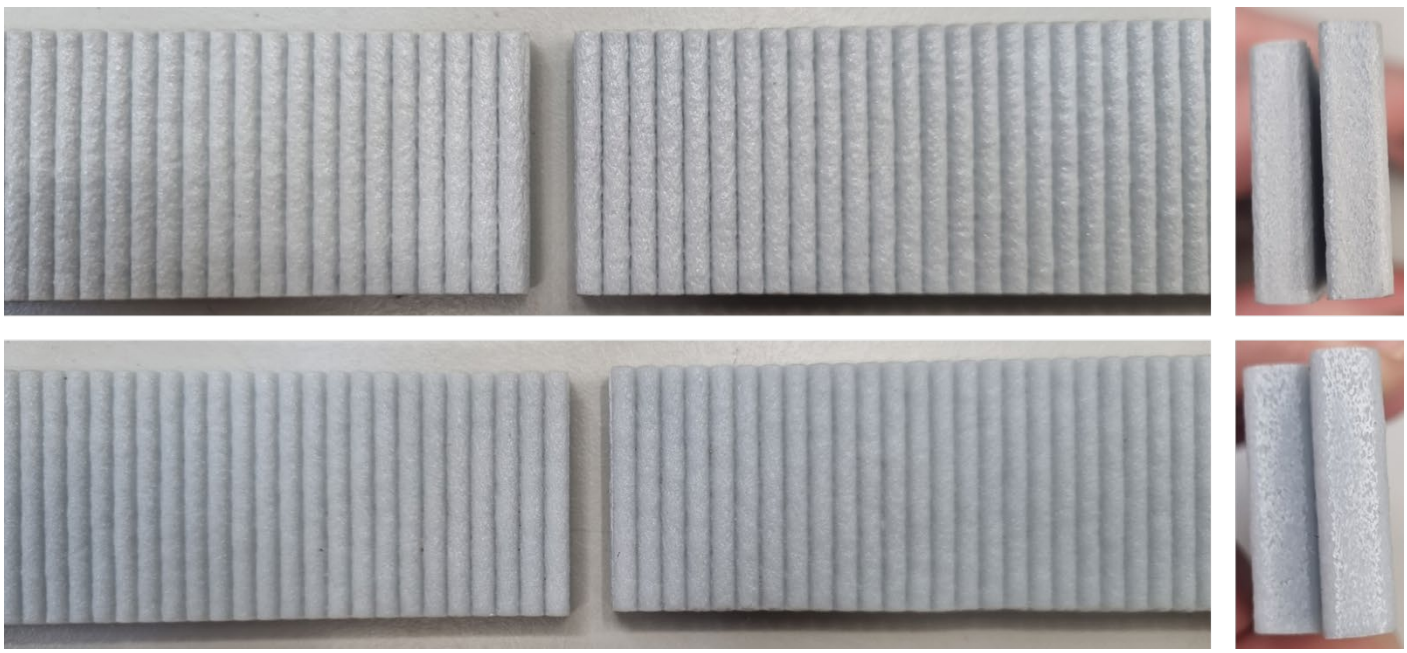

Figure 7-4 Failure mechanisms of coupons tested in tension in transverse direction. Both GF30_80s (above) and GF45_80s (below) failed in between the print layers

7.1.2 Comparison different layer times

The results of the tensile tests in transverse direction from test series 1 and 2, will be compared with the results of test series 3. This test series is split into 3.1 and 3.2, corresponding with the 30% V_f material printed with 100 seconds (GF30_100s) and 120 seconds (GF30_120s) layer time respectively. The stress-displacement diagram of the average results of transverse tensile tests of these series is presented in Figure 7-5. As can be seen, the graph of GF30_100s is not as smooth as the other graphs. This is due to a certain scatter in the test results of test series 3.1 (see Appendix Section C.1.3).

Despite a slightly varying behaviour of the GF30_100s material, the test results are still valuable enough to draw a conclusion from these results. From the graphs, it is clear that the transverse tensile strength of the material with the shortest layer time (GF30_80s and GF45_80s) is much higher than the transverse tensile strength of the material with the longer layer times (GF30_100s and GF30_120s). The values of the transverse tensile strength are 20.4 ± 0.7 MPa (GF30_80s) and 19.7 ± 0.3 MPa (GF45_80s) for the shortest layer time. The longer layer times lead to a transverse tensile strength of 8.7 ± 1.8 MPa (GF30_100s) and 7.7 ± 0.7 MPa (GF30_120s). This shows that a longer layer time than 80 seconds lead to a significant decrease in strength in transverse direction.

Although a layer time of 80 seconds lead to a much better bond strength of the beads than a layer of 100 or 120 seconds, the difference in transverse tensile strength between GF30_100s and GF30_120s is not big. Especially when the difference between 100 s and 120 s is compared with the difference between 80 s and 100 s, the effect of 20 seconds more layer time than 100 s is limited. This can be explained by the time it takes for the material to cool down to the temperature of the environment in which the material is printed. It could be that after 100 s, the extruded material already approaches the ambient temperature. So, when the time between extrusion of the layer is longer than this increased layer time, the material will not cool down a lot further, which makes that the difference in temperature between the previous printed layer and the extruded material will not really increase anymore. This means that the bond strength, and thus the tensile strength in transverse direction, will be comparable. The higher the difference in temperature of the previous printed layer and the extruded material, the worse the bonding between the beads will be, and so the transverse tensile strength.

Figure 7-5 Stress-displacement diagram of the tensile test results of GF30_80s, GF45_80s, GF30_100s, and GF30_120s in transverse direction

The GF30_100s and GF30_120s coupons failed in the same way as the GF30_80s and GF45_80s coupons subjected to the tensile test in transverse direction, see Figure 7-6. Failure of the coupon occurred in between the beads. Meaning that the bond strength between the beads is governing. Which is even more likely for material with the longer layer times because a longer layer time leads to a weaker bonding. Even an imperfection in the bead (picture at the right in Figure 7-6) was not critical. Failure of this coupon also occurred in between the layers. Even though this is a GF30_120s coupon.

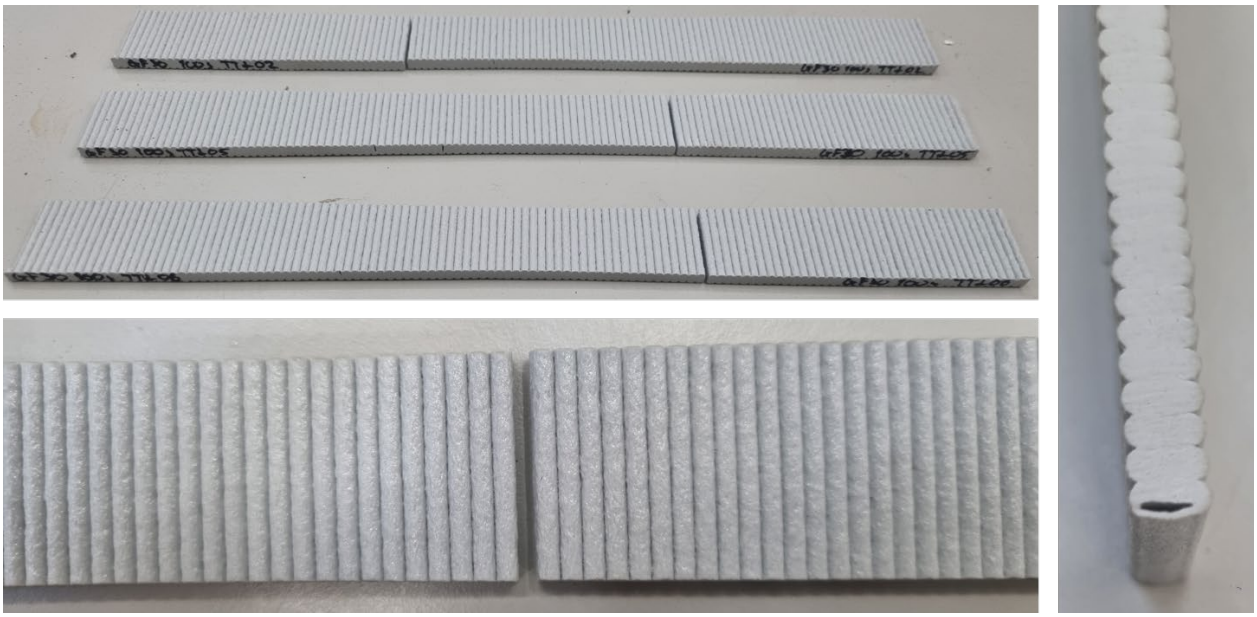

Figure 7-6 Failure mechanisms of GF30_100s (above) and GF30_120s (below) coupons tested in tension in transverse direction. At the right, a GF30_120s coupon that also failed in between the layers and not at the imperfection (air bubble) in the bead

7.1.3 Influence of ribbed surface

As described in Section 6.1.2, the effect of the ribbed surface was investigated additionally. Both the longitudinal and transverse coupons of the GF30_80s material were observed. From the GF45_80s, the coupons in transverse direction were considered.

Just like the other performed tensile tests in longitudinal direction, these tensile tests could be measured with an extensometer. This was not possible for the tensile test results in transverse direction. So, the comparison of the polished and unpolished coupons in longitudinal direction is given in a stress-strain relation in Figure 7-7, and the comparison in transverse direction in a stress-displacement of the jack relation in Figure 7-8. In these Figures, also the average curves of the test results are presented.

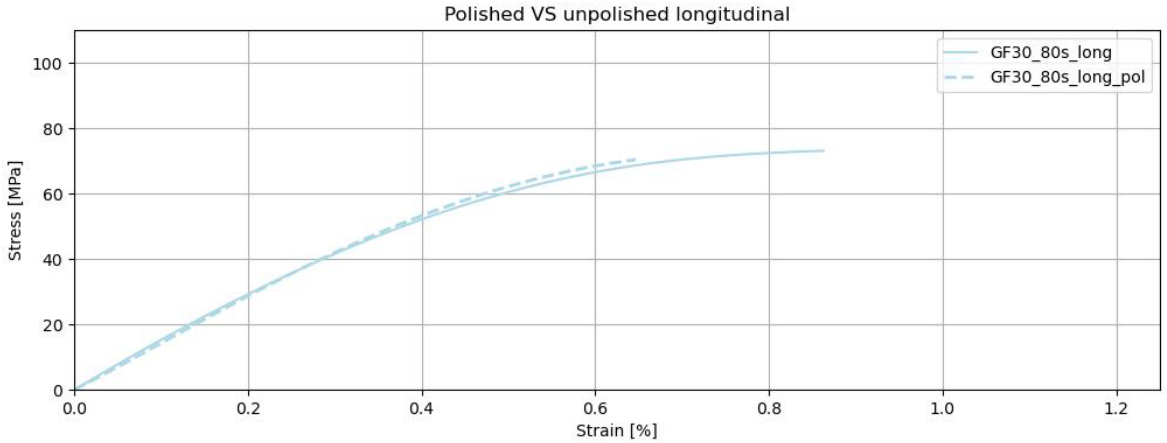

Figure 7-7 Stress-strain diagram of the tensile test results of the original and the polished GF30_80s coupons in longitudinal direction

As expected, the difference in behaviour in longitudinal is minor. The dotted graph (polished) coincides with the solid graph (unpolished) in Figure 7-7 until failure. The polished coupons failed a bit earlier than the unpolished. Based on this point of failure and the similar behaviour, it can be said that the ribbed surface does not affect the stress distribution in longitudinal direction. This was also not the expectation since the cross section of the coupon does not change over the length of the coupon. The slightly earlier failure does not have a relation with the ribbed surface because if that was the case, the failure should have occurred later and not earlier. This difference in point of failure could be due to imperfections of polishing. The coupons were polished by hand, so they were not perfectly flat and straight.

The transverse tests of the GF30_80s had just one valuable result. This test result of a polished coupon did not show significantly different behaviour than the unpolished coupons, given that the GF30_80s graphs of unpolished (blue, solid) and polished (blue, dotted) are similar in Figure 7-8. The GF45_80s transversely tested coupons contained three valuable test results. For these coupons also, the behaviour between unpolished (green, solid) and polished (green, dotted) is comparable. Though, the polished coupons last a bit longer than the original coupons. So, the varying cross section over the length of the coupon, due to the ribs, may cause local stress concentrations, which lead to earlier failure. However, it is not very feasible to polish a whole structural element, or multiple ones, when printed.

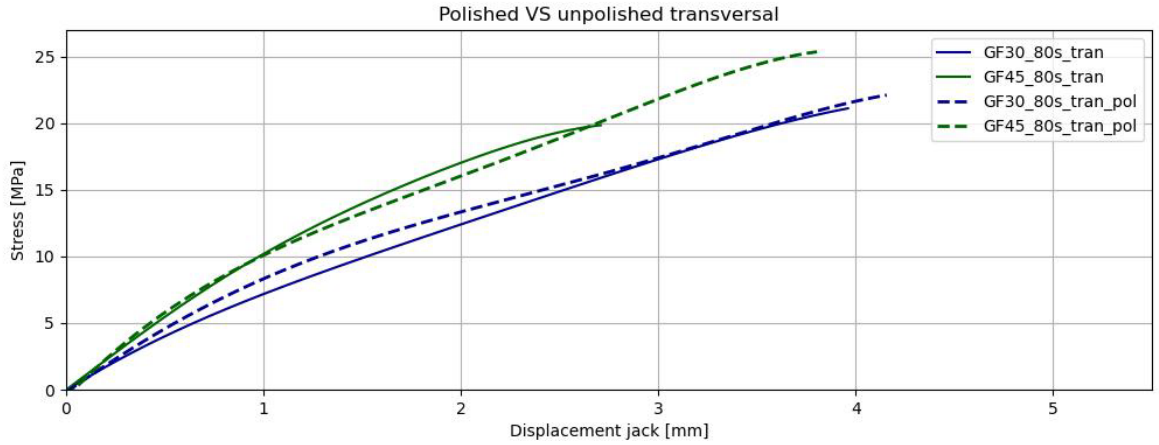

Figure 7-8 Stress-displacement diagram of the tensile test results of the original (solid) and polished (dotted) GF30_80s and GF45_80s coupons in transverse direction

Regarding the failure mechanisms, no difference was observed between the original coupons and the polished ones. The crack and the crack with a broken-off piece of the polished coupon in Figure 7-9, is a similar failure mode as the original coupons showed (Figure 7-2). In transverse direction, all the original coupons failed in between the beads. This failure mode was also the case for the polished coupons, see Figure 7-10. Although the coupons were polished, it is still noticeable where the print layers are. The coupons split in between the print layers.

Figure 7-9 Failure mechanisms of two GF30_80s coupons tested in longitudinal tension after polishing

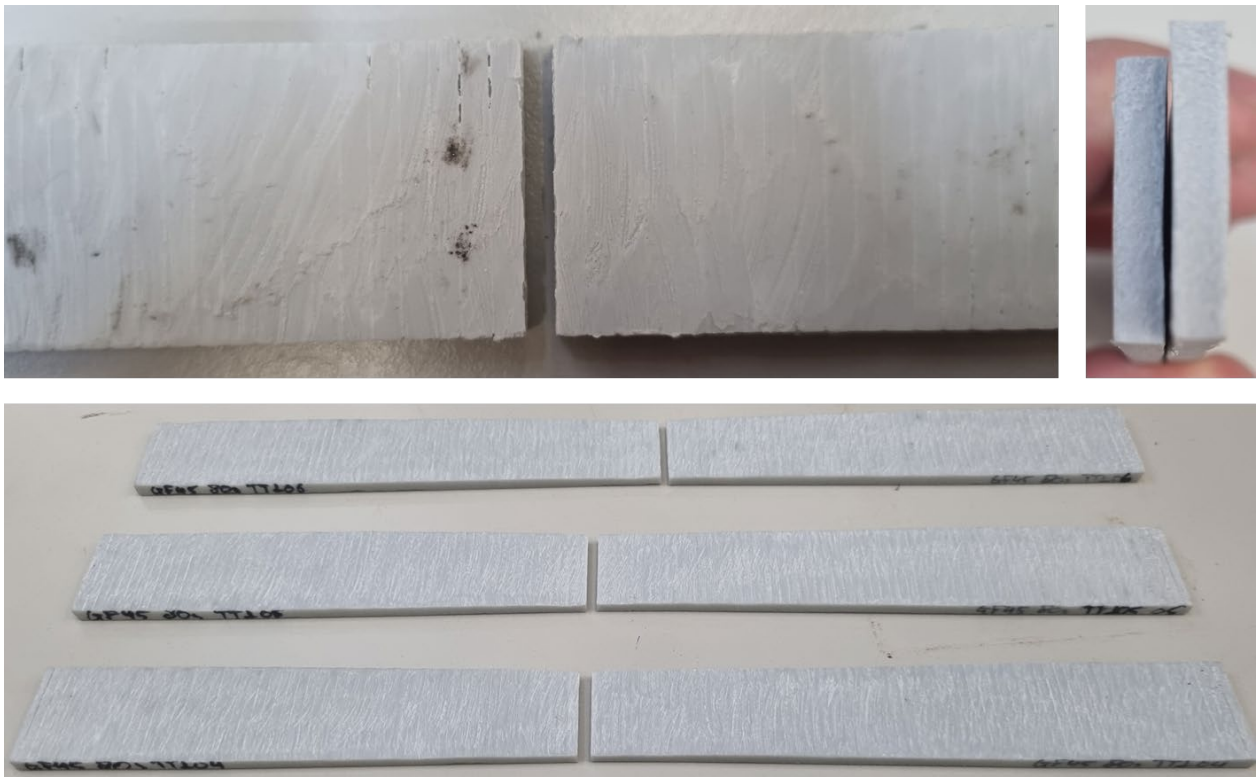

Figure 7-10 Failure mechanisms of a GF30_80s coupon (above) and the GF45_80s coupons tested in transverse tension after polishing

7.1.4 Summary

An overview of the results of the first stage of coupon testing is presented in Table 7-1. The tensile strength in longitudinal and transverse direction of the different material configurations and the tensile modulus in longitudinal direction are given. As the results showed, V_f of 45% with a layer time of 80 s leads to the best material configuration.

Table 7-1 Summary of the results of the first stage of coupon testing: the tensile strength and modulus in longitudinal direction of test series 1 and 2 and the transverse tensile strength of test series 1, 2, 3.1 and 3.2

Test series	Coupon	$\sigma_{1,t}$ [MPa]	$E_{1,t}$ [N/mm^2]	$\sigma_{2,t}$ [MPa]
GF30_80s	Unpolished only	71.25 ± 1.43	13,922 ± 209	20.42 ± 0.73
	Polished only	70.02 ± 2.53	14,287 ± 92	22.24
	Both combined	70.64 ± 1.96	14,068 ± 252	20.88 ± 1.08
GF45_80s	Unpolished only	102.07 ± 0.76	22,041 ± 357	19.65 ± 0.27
	Polished only	-	-	24.05 ± 1.55
	Both combined	-	-	21.85 ± 2.61
GF30_100s	Unpolished	-	-	8.72 ±1.77
GF30_120s	Unpolished	-	-	7.68 ± 0.73

7.2 Second stage of coupon testing

Test series 4, the material characterization, was executed in the second stage of coupon testing. The second stage of coupon testing covers the characterization of the mechanical properties of the material with the configuration derived from the first stage of coupon testing. As explained in Section 6.3, certain types of tests were performed to determine strength and stiffness properties of the material: tensile tests in longitudinal and transverse direction, compression tests in longitudinal and transverse direction, and interbead shear tests. The obtained data is evaluated according to the standard corresponding to the type of test. The characteristic values are determined according to Annex D of EN 1990. The results from the different types of tests will be presented in Sections 7.2.1 - 7.2.5. An overview of the mechanical properties obtained from the test results is provided in Section 7.2.6. The results of the individual test can be found in Appendix C.

7.2.1 Tensile longitudinal

Besides the characterization of the tensile mechanical properties in longitudinal direction, the results of the tests are also compared with the results from the tensile test in longitudinal direction of the GF45_80s material of the first stage of coupon testing.

7.2.1.1 Results

The stress-strain curves of the tested coupons are shown in Figure 7-11. The stresses are obtained by the dividing the force, measured by the machine, by the failure surface area of the specimens. An extensometer measured the strains over the part of the coupon where failure occurred. Coupon number 1 is not included due to failure at the clamp, so this was not a valid test run. Two extra coupons were tested because there was a bit scatter in the strain at failure. In the end, the behaviour of all the specimens is quite similar, as can be seen in the graph.

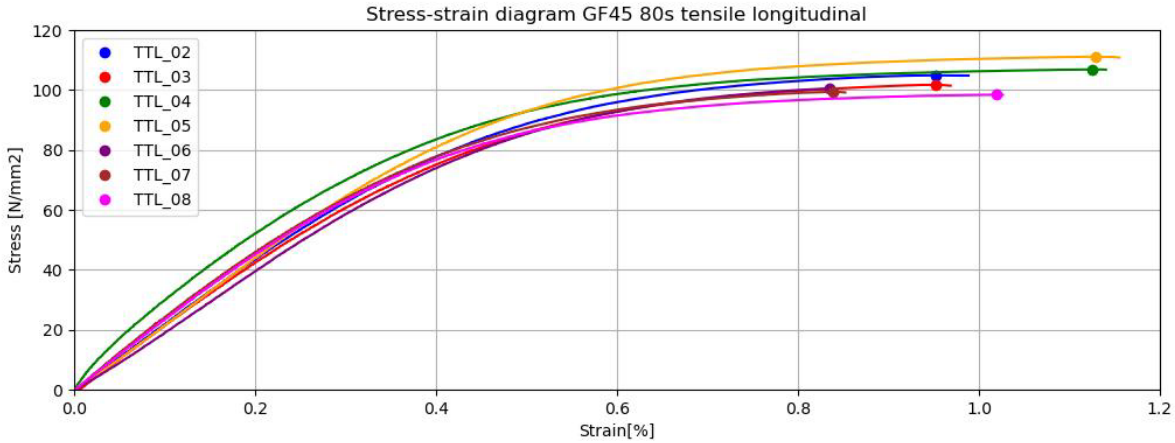

Figure 7-11 Stress-strain diagram of the results obtained from the tensile tests in longitudinal direction

From the test results, the following values for the tensile mechanical properties in longitudinal direction were derived:

- $\sigma_{1,tm}$ = 103.3 ± 4.6 MPa
- $\varepsilon_{1,t}$ = 0.98 ± 0.12 %
- $E_{1,t}$ = 21,430 ± 690 N/mm^2
- $\sigma_{1,tk}$ = 93.8 MPa

The stiffness is obtained from the stress-strain curves following the method from NEN-EN ISO 527-1. The chord slope of the stress-strain curve in the interval between 0.05% and 0.25% strain is the tensile modulus. Following the calculations from Annex D of NEN-EN 1990, the characteristic principal tensile strength is determined.

The failure mechanism is similar as in the first stage of coupon testing. The coupon fails quite suddenly. At the moment of failure, the microcracks develop into a larger crack through the whole specimen, which could

be either straight or inclined, see Figure 7-12. The white bits are the microcracks. In some cases, the cracks develop in multiple directions. Due to this behaviour, a part of the coupon broke completely out of the specimens for some coupons.

Figure 7-12 Failure mechanism of some of the longitudinal tensile test coupons in the second stage of coupon testing

7.2.1.2 Comparison with first stage of coupon testing

To have an extra check on the validity of the results from test series 4, regarding the tensile tests, the results from the second stage of coupon testing where compared with the results of the GF45_80s material from the first stage of coupon testing (test series 2). The comparison based on the longitudinal tensile tests, is presented in Figure 7-13. The graphs presenting the average test results from the first and second stage of coupon testing are almost identical. Only when at the higher strains, the curves go a bit apart from each other. This could be caused by the fact that some coupons failed already before they reached this strain, so the curve gets less averaged. Based on this consistency, the results from the longitudinal tensile tests are really accurate and the mechanical properties derived from these test results will be representative.

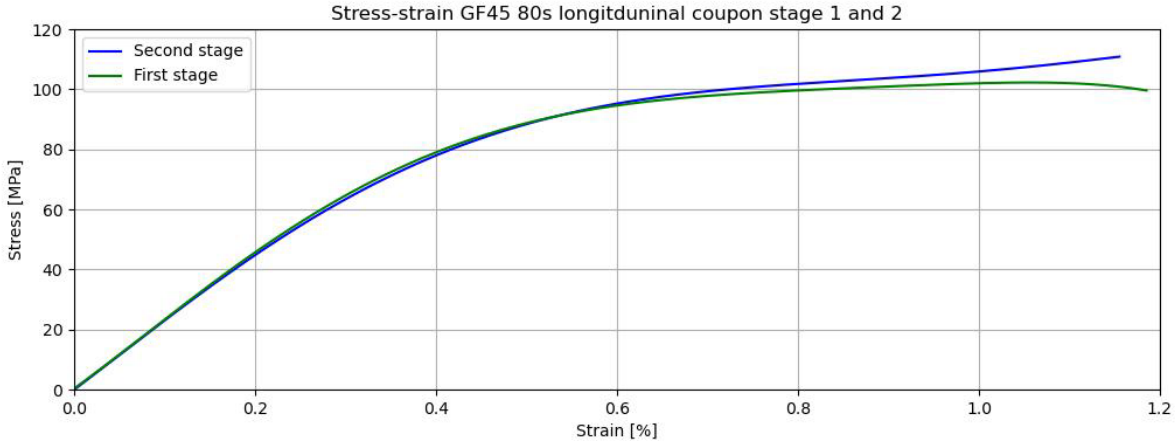

Figure 7-13 Averaged stress-strain diagram of the tensile behaviour in longitudinal direction from the first and second stage of coupon testing

7.2.2 Tensile transverse

Besides the characterization of the tensile mechanical properties in transverse direction, the results of the tests are compared with the results from the tensile test in transverse direction of the GF45_80s material of the first stage of coupon testing.

7.2.2.1 Results

In Figure 7-14, the stress-strain curves of the tested coupons are presented. These stress-strain curves represent the tensile behaviour in transverse direction. The stresses are obtained by the dividing the force measured by the machine by the area of the failure surface of the specimens. An extensometer measured the strains over the part of the coupon where failure occurred. The five specimens show similar stress-strain behaviour until failure, which means that the results obtained from the tests are accurate and the material behaves consistent.

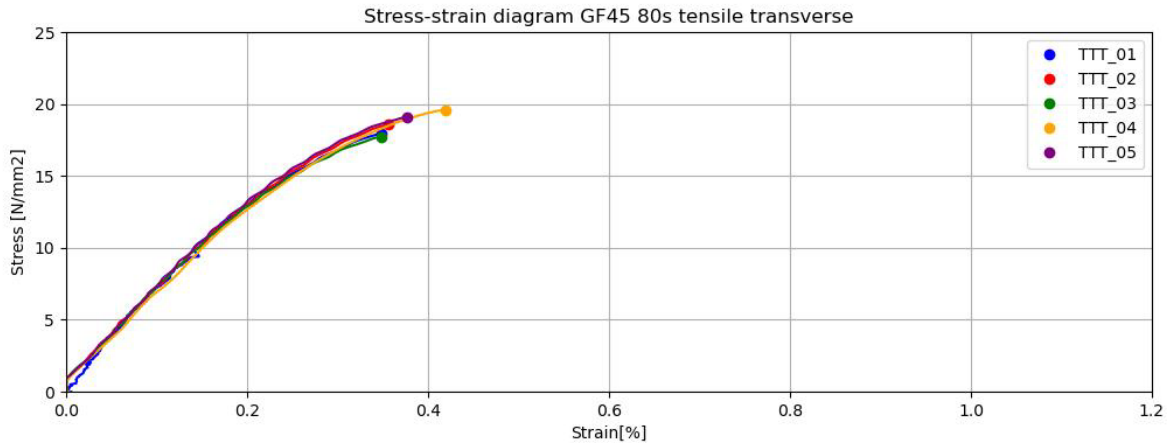

Figure 7-14 Stress-strain diagram of the results obtained from the tensile tests in transverse direction

From the test results, the following values for the tensile mechanical properties in longitudinal direction were derived:

- $\sigma_{2,tm}$ = 18.6 ± 0.8 MPa
- $\varepsilon_{2,t}$ = 0.37 ± 0.03 %
- $E_{2,t}$ = 5,650 ± 77 N/mm^2
- $\sigma_{2,tk}$ = 93.8 MPa

The stiffness is obtained from the stress-strain curves following the method from NEN-EN ISO 527-1. The chord slope of the stress-strain curve in the interval between 0.05% and 0.25% strain is the tensile modulus. Following the calculations from Annex D of NEN-EN 1990, the characteristic transverse tensile strength is determined.

The failure mechanism is the same as in the first stage of coupon testing. All the specimens failed between the print layers. As can be seen in Figure 7-15, failure occurred between the beads, caused by delayering. So, the bond strength between the beads is governing for the tensile strength in transverse direction.

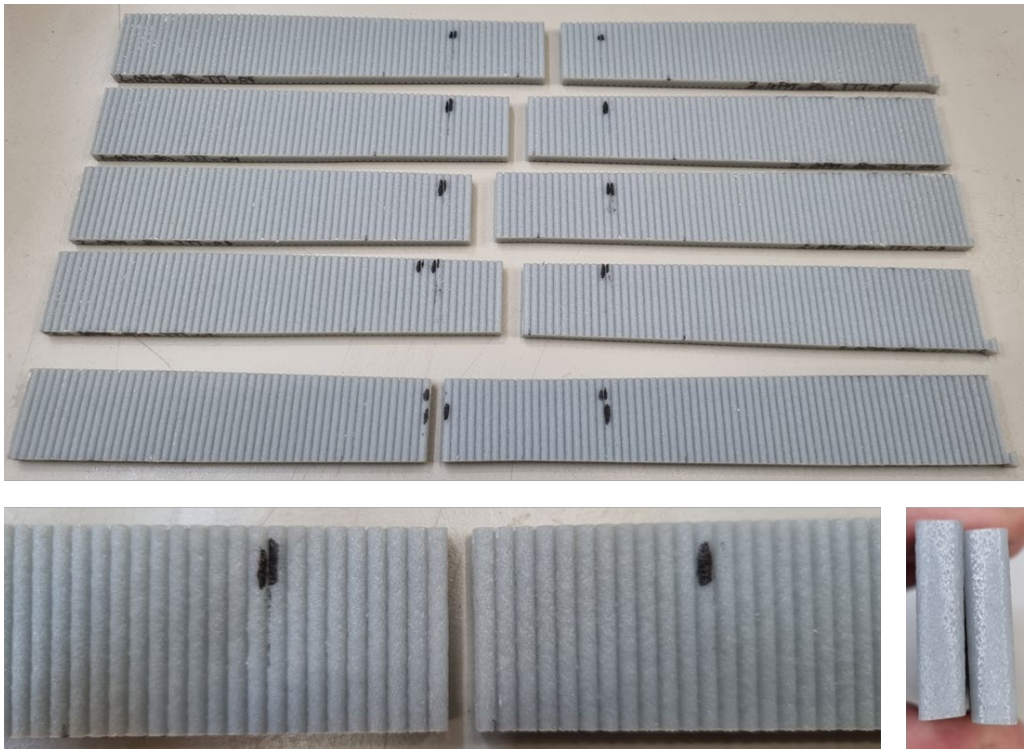

Figure 7-15 Failure mechanisms of the transverse tensile test coupon in the second stage of coupon testing

7.2.2.2 Comparison with first stage of coupon testing

Like the results of the longitudinal tensile tests, the results of the transverse tensile tests are compared with the results from the first stage of coupon testing to check the validity. The averaged stress-displacement curves of the two test series are shown in Figure 7-16. Regarding the ultimate strength, the specimens from the second stage reached a similar stress at failure as the specimens from the first stage of coupon testing. However, the stiffness of the coupons from the second stage is lower than the stiffness of the coupons from the first stage since the average stress-displacement curve is less steep. This difference could be caused by several factors: moisture content of the material, ambient temperature during printing, quality of the material compounds, or printing quality in general. Therefore, the stiffness obtained from the first stage of coupon testing could be an overestimation. Because the second stage showed that for the same tests executed with in principle the same material the stiffness could be lower, this lower stiffness should be considered as the tensile modulus in transverse direction for the PETG + 45 vol.% GF with a layer time of 80 s.

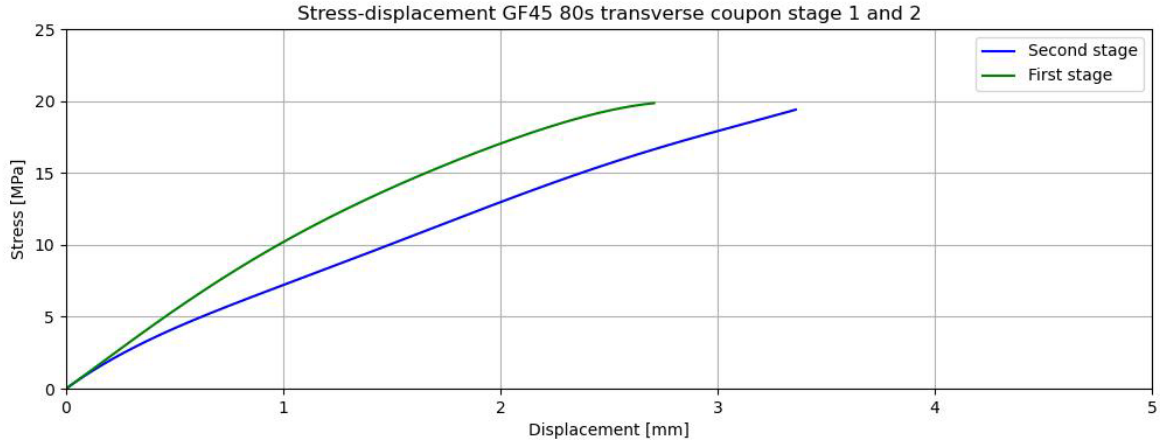

Figure 7-16 Averaged stress-strain diagram of the tensile behaviour in transverse direction from the first and second stage of coupon testing

7.2.3 Compression longitudinal

The compression tests in longitudinal directions resulted in a stress-strain diagram shown in Figure 7-17. The cross sectional area in the middle of the coupon is used to convert the force, measured by the machine. The strain is calculated by dividing the displacement, measured by the machine, by the distance between the end tabs for the clamping. The curves show quite similar behaviour. The curve of coupon CTL_04 had a discontinuity due measurement error of the machine. But this did not influence the test procedure and still a valuable result was obtained.

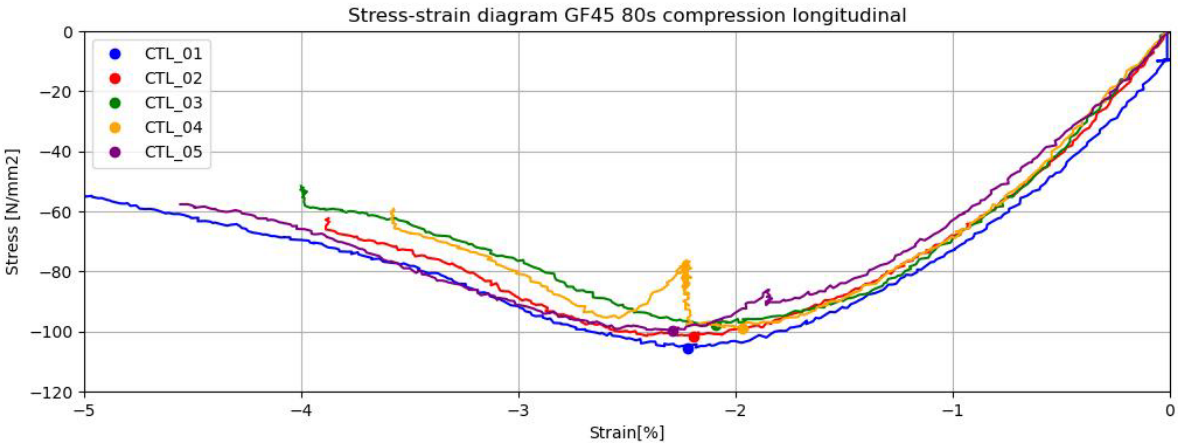

Figure 7-17 Stress-strain diagram of the results obtained from the compression tests in longitudinal direction

From the test results, the following values for the tensile mechanical properties in longitudinal direction were derived:

- $\sigma_{1,cm}$ = -100.7 ± 3.1 MPa
- $\varepsilon_{1,c}$ = -2.15 ± 0.13 %
- $E_{1,c}$ = 8,014 ± 613 N/mm^2
- $\sigma_{1,t}$ = -93.5 MPa

The stiffness is obtained from the stress-strain curves following the method from NEN-EN ISO 14126. The chord slope of the stress-strain curve in the interval between 0.05% and 0.25% strain is the tensile modulus. However, the displacement measured during these tests lead to an overestimation of the strain in the material. Due to the buckling shape that occurred during the test, the specimen has a lateral displacement. This means that the longitudinal displacement will be higher while there is no extra elongation of the material in the direction of the applied load. The calculated stiffness proves that the strain values are too large. The elastic modulus should be similar for both compression and tension and the elastic modulus from the compression tests is lower than the elastic modulus from the tensile tests.

Following the calculations from Annex D of NEN-EN 1990, the characteristic principal compression strength is determined. Although a buckling shape occurred, the established compressive strength will be close to the actual strength for these longitudinal tested coupons. Forming a buckling mode, the specimens failed at first in the compression zones. When the test was stopped, the moment at which the force already decreased significantly due to compression failure, no cracks were occurred yet in the tensile zones. See Figure 7-18 for the failure mechanism.

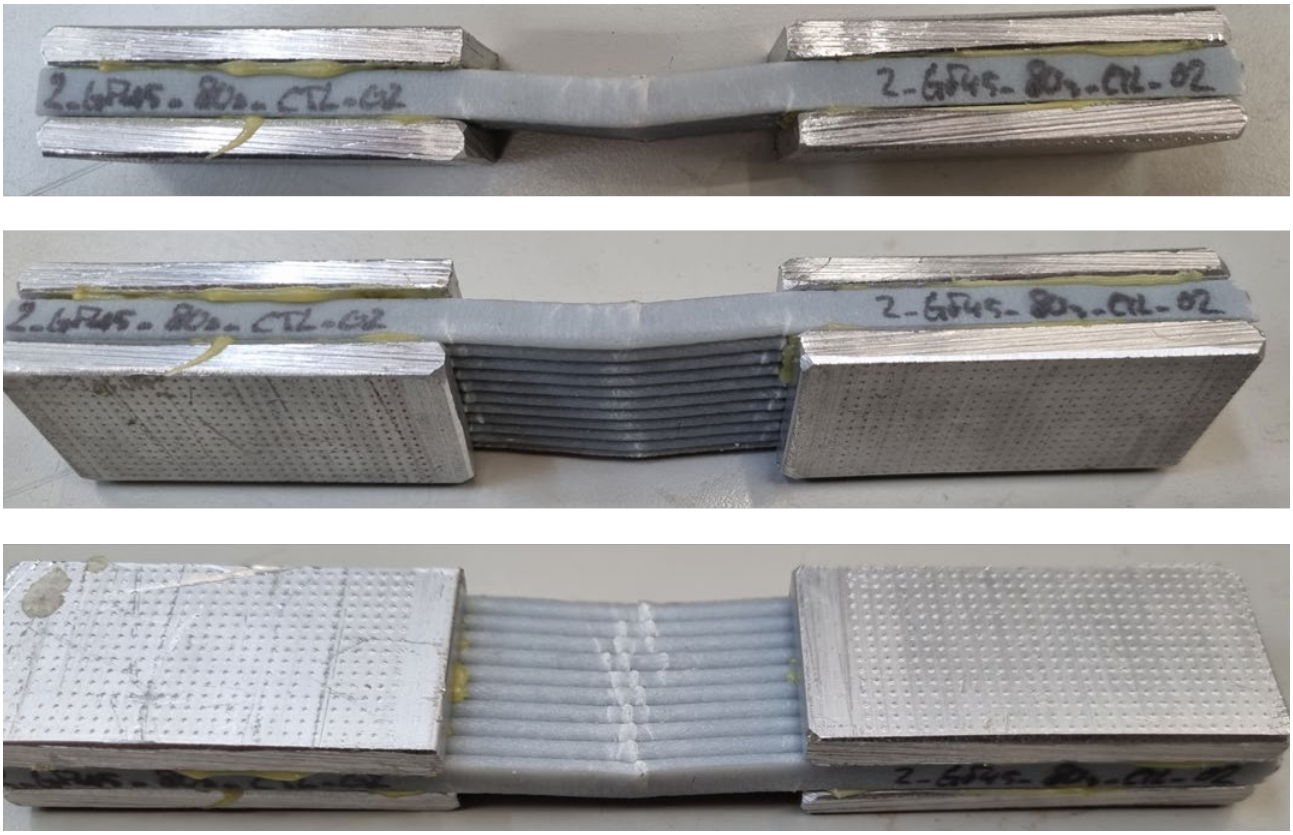

Figure 7-18 Failure mechanisms of the longitudinal compression test coupon in the second stage of coupon testing

7.2.4 Compression transverse

In Figure 7-19, the results from the compression tests in transverse direction are shown as stress-strain graphs. The cross sectional area in the middle of the coupon is used to convert the force measured by the machine. The strain is calculated by dividing the displacement, measured by the machine, by the distance between the end tabs for the clamping. The curves show quite similar behaviour, especially until the point of the maximum compressive stress is reached.

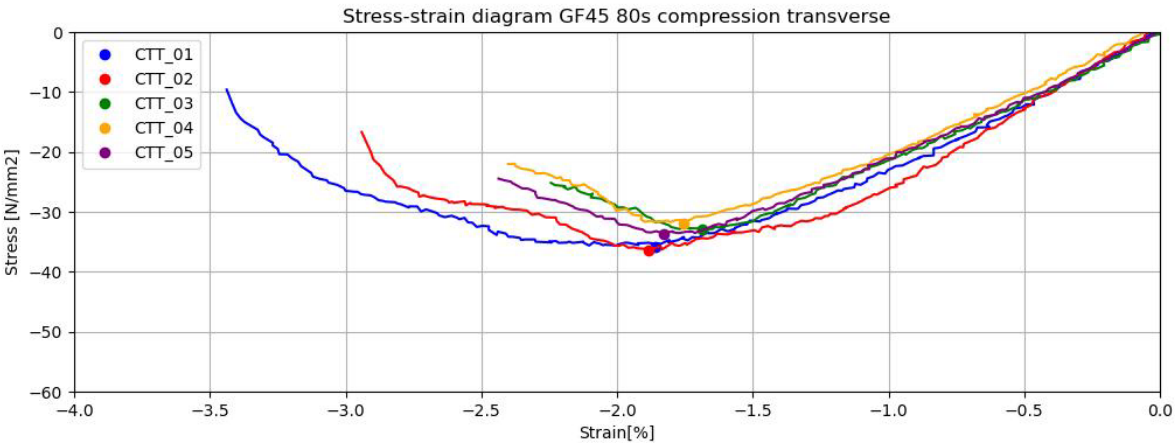

Figure 7-19 Stress-strain diagram of the results obtained from the compression tests in transverse direction

From the test results, the following values for the tensile mechanical properties in longitudinal direction were derived:

- $\sigma_{2,cm}$ = -34.1 ± 1.9 MPa
- $\varepsilon_{2,c}$ = -1.80 ± 0.08 %
- $E_{2,c}$ = 2,385 ± 55 N/mm^2
- $\sigma_{2,ck}$ = -29.8 MPa

Like the results from the compression tests in longitudinal direction, the strain values obtained from the tests are an overestimation, due to the buckling shape. This causes a lateral displacement which leads to more longitudinal displacement, while not all this measured displacement is equivalent to strains in the material in the direction of the applied load. This is also proved by the established value for the compressive elastic modulus. This value is lower than the tensile elastic modulus, while this should be similar. The stiffness is obtained from the stress-strain curves following the method from NEN-EN ISO 14126. The chord slope of the stress-strain curve in the interval between 0.05% and 0.25% strain is the tensile modulus.

Instead of the longitudinal compression tests, the maximum stress obtained from the transverse compression tests is an underestimation of the actual compressive strength. Also, with the transverse compression tests a buckling shape occurred for all the specimens. However, cracks developed in the tensile zone before compressive failure could occur. This failure mechanism is shown in Figure 7-20. Although the maximum stress observed is not the actual compressive strength in transverse direction, a characteristic value is determined based on the maximum stress from these tests. This is done according to the calculations from Annex D of NEN-EN 1990.

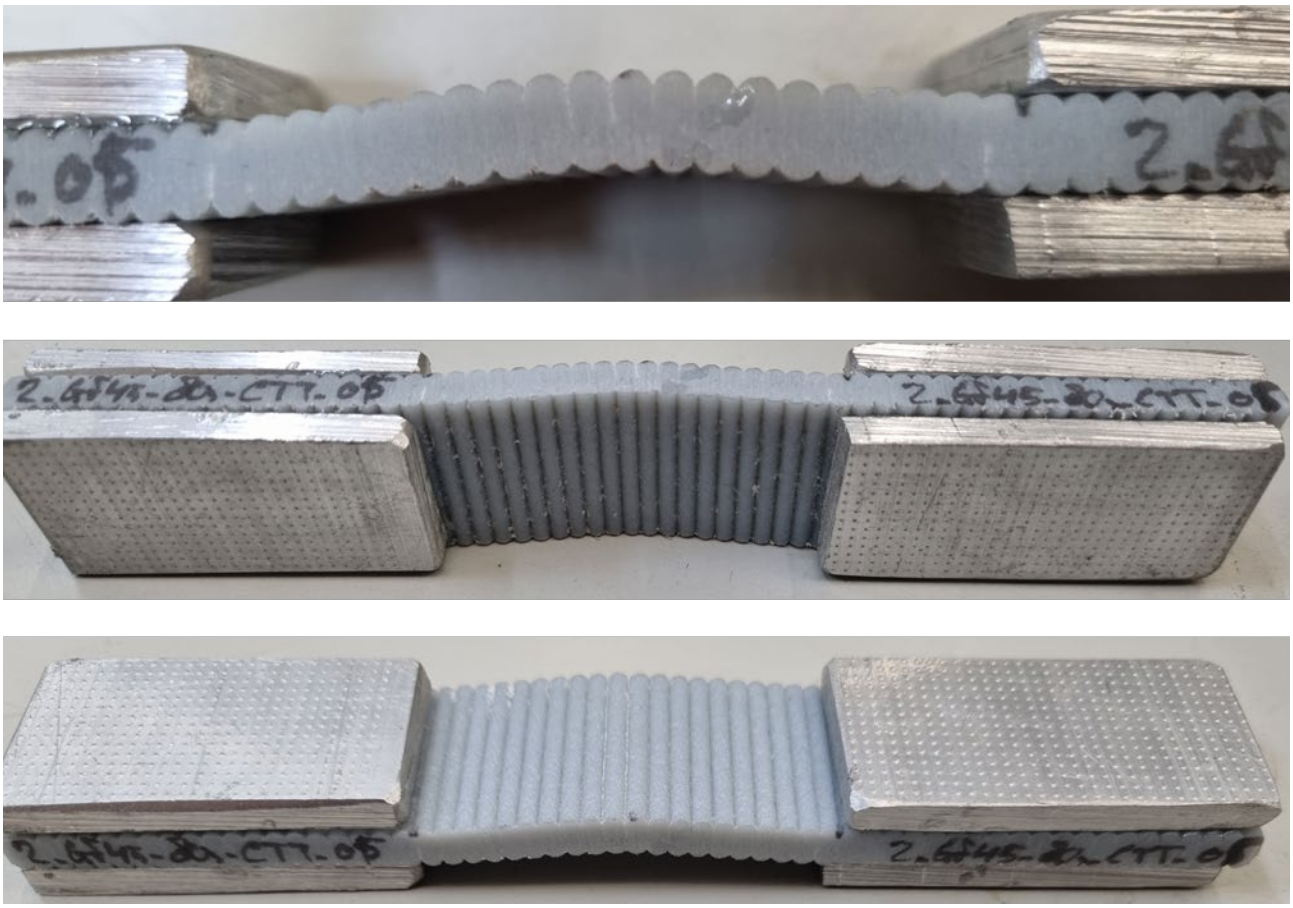

Figure 7-20 Failure mechanisms of the transverse compression test coupon in the second stage of coupon testing

7.2.5 Interbead shear (IBSS)

The IBSS tests resulted to the stress-strain curves presented in Figure 7-21. Due to the precuts, shear stress occurred in the part between the precuts, when the coupon was pulled. Because the precuts were dimensioned such that they had an overlap transversely, the tensile stress in the coupon had to be transferred via shear between the print layers. The length of the overlap between the precuts parallel to the print direction, and thus parallel to the applied force, multiplied with the thickness is the area of the failure surface considered to convert the applied force into a shear stress. The strain was measured by an extensometer. This strain was measured over the length of the overlap plus a slight part before and after the critical area between the precuts, since the extensometer measures over a length larger than the overlap length of the critical area. Two additional coupons were tested because specimens IBSS_01 (blue in Figure 7-21) and IBSS_05 (purple in Figure 7-21) showed slightly different behaviour.

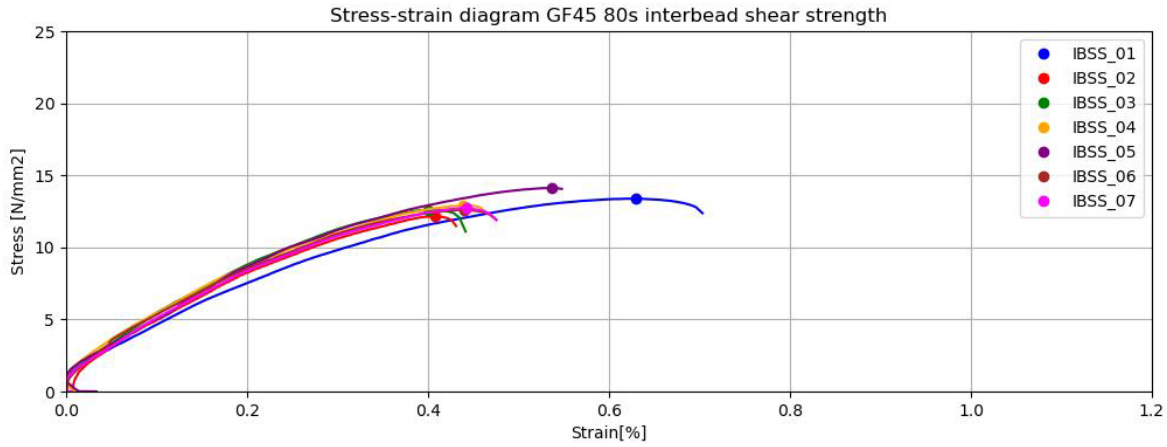

Figure 7-21 Stress-strain diagram of the results obtained from the IBSS tests

From the test results, the following values for the shear mechanical properties between the print layers were derived:

- $\tau_{21,m}$ = 12.9 ± 0.6 MPa
- γ_{21} = 0.47 ± 0.08 %
- G_{21} = 3,200 ± 173 N/mm^2
- $\tau_{21,k}$ = 11.6 MPa

To establish the shear stiffness, the same principal as with the tensile and compression tests is applied, since this test set-up was not based on a standard but derived from references and trials. So, the shear stiffness is established based on the chord slope between the points at γ = 0.05% and γ = 0.25%. Following the calculations from Annex D of NEN-EN 1990, the characteristic shear strength between the beads is determined.

As described before, the critical area is the part loaded in shear between the precuts. For all the tested coupons, the failure occurred indeed at this surface between two print layers at the overlap between the precuts. This failure mode is shown in Figure 7-22.

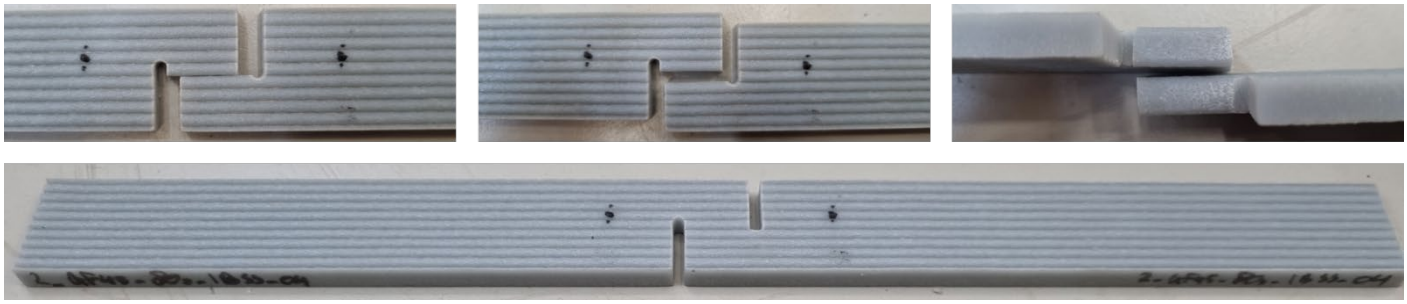

Figure 7-22 Failure mechanisms of the IBSS test coupon in the second stage of coupon testing

7.2.6 Summary

Overview of the results of coupon test series 4 is provided Table 7-2. The average stress-strain graphs of the tensile and compressive behaviour in both longitudinal and transverse direction are plotted in Figure 7-23.

Table 7-2 Summary of the results of the second stage of coupon testing: mechanical properties obtained from tensile (longitudinal and transverse), interbead shear, and compression (longitudinal and transverse) of test series 4

	Stress at failure [MPa]	**Strain at failure [%]**	**Stiffness [N/mm^2]**	**Char. Strength [MPa]**
Tensile long.	$\sigma_{1,tm}$ = 103.3 ± 4.6	$\varepsilon_{1,t}$ = 0.98	$E_{1,t}$ = 21,430	$\sigma_{1,tk}$ = 93.8
Tensile tran.	$\sigma_{2,tm}$ = 18.6 ± 0.8	$\varepsilon_{2,t}$ = 0.37	$E_{2,t}$ = 5,650	$\sigma_{2,tk}$ = 16.8
Compression long.	$\sigma_{1,cm}$ = 100.7 ± 3.1	$\varepsilon_{1,c}$ = 2.15	$E_{1,c}$ = 8,010	$\sigma_{1,ck}$ = 93.5
Compression tran.	$\sigma_{2,cm}$ = 34.1 ± 1.9	$\varepsilon_{2,c}$ = 1.80	$E_{2,c}$ = 2,380	$\sigma_{2,ck}$ = 29.8
IBSS	$\tau_{21,m}$ = 12.9 ± 0.6	γ_{21} = 0.47	G_{21} = 3,200	$\tau_{21,k}$ = 11.6

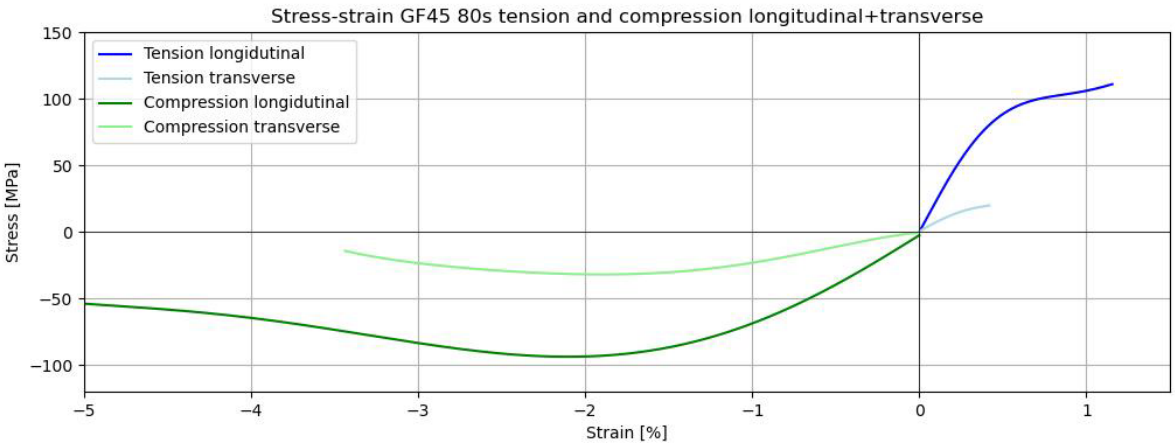

Figure 7-23 Stress-strain diagram of the averaged results from the tensile and compression tests in both longitudinal and transverse direction

7.2.7 Estimation of other properties

To perform an FEA for the design of the bridge deck element, some more mechanical properties are needed to be known. As the measurements during the tensile tests were done with an extensometer only in the principal direction of testing, the Poisson's ratios could not be established by the test results. The in-plane shear behaviour is not determined by coupon testing because there was no suitable test set-up available. Therefore, the values of these properties are estimated based on the properties of the Covestro material from the previous study and by using formulas from classical linear elastic theory to calculate with value that are established by the tests. The following values are set for the several required parameters for the design of the bridge deck component:

- **Poisson's ratio ν_{12}** = 0.38; This is the Poisson's ratio from the Covestro study.
- **Poisson's ratio ν_{23}** = 0.135; This is the Poisson's ratio from the Covestro study.
- **In-plane shear strength τ_{12}** = 11.6 MPa; The IBSS is also assumed for the in-plane shear strength. This may be a bit conservative. But the IBSS is already doubled compared to the previous Covestro material, so it will be suitable to apply for the design of the bridge deck element.
- **In-plane shear stiffness G_{12}** = 7,004 MPa; This is the shear stiffness ratio from the Covestro study. This will be a suitable estimation, since the other linear-elastic properties (E_1, E_1, G_{21}) are quite comparable with the values of the Covestro material.

Part III:
Bridge Deck Element

8

Design Variants and Analysis

Having the material properties determined, the design for the bridge deck design can be developed. Different variants will be design according to a certain design concept. These variants will be evaluated against criteria related to the printability and criteria related to the structural performance.

8.1 Design concept

The thickness of the top plate was one of the critical factors in the preliminary design. The top plate was predominantly single layered, which made that the top plate did not suffice in the transverse direction. Only at some small parts, the top plate was single layered due to the print path of the infill. At the positions of the 'flanges' of the stiffeners, the top plate was double layered because the layer of the top plate itself and the print layer of the infill come together. When this overlapping part will be extended, a double layered segment could be created. This extension of the 'flanges' of the infill part could be realized by printing the stiffeners in backward direction. The stiffeners will be printed from the top/bottom to the previously printed flange at the opposite top/bottom and then continue parallel to the top/bottom segment. When this flange is complete, the next stiffeners will go back to the previous top/bottom part to go back to the starting point of this triangle. In this way, a truss-like shape is created. The principle of this concept is sketched in Figure 8-1.

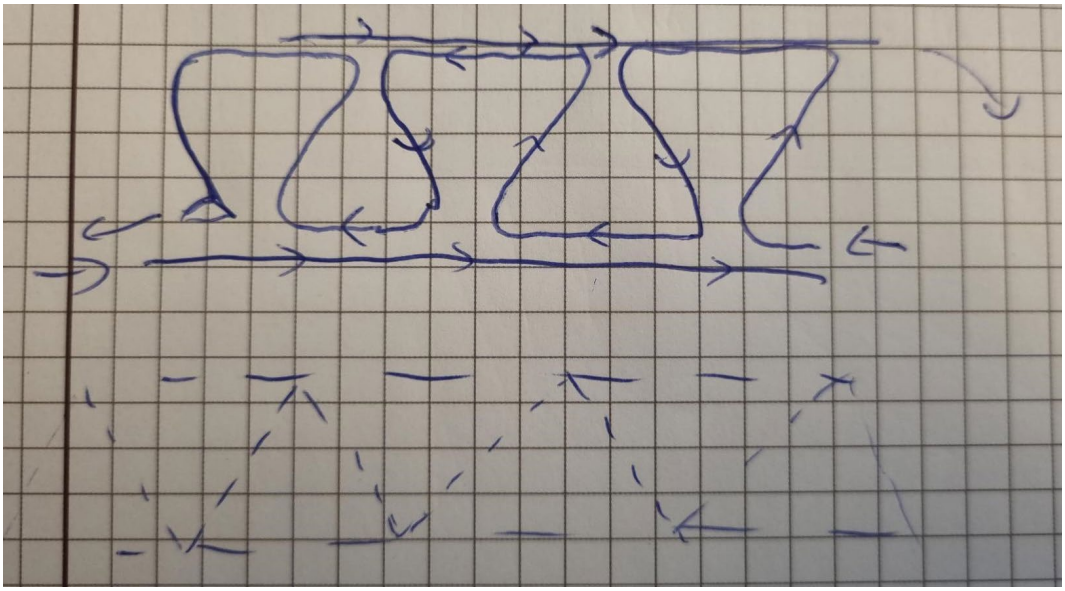

Figure 8-1 Idea of printing in the stiffeners of the infill in backwards direction to create a double layered top and bottom

8.2 Component variants

Based on the design concept, three distinctive design variants for the component were made. These variants are elaborated in Sections 8.2.1 - 8.2.3.

8.2.1 Variant 1: Most extensive infill

The print path of the first variant is drawn in Figure 8-2. The outer part including the top plate will be printed at first, then the infill is printed, and at last the arch is printed to close the element. In this way, the printer goes forth, back and forth, meaning that the end of the print path is not at the same point as where the print path starts. Because the element is symmetric, it is possible to print the next layer the other way around. This leads to asymmetric printing. It could be an option to print in this manner, but the disadvantage is that the layer time is varying over the print path. This means that the bonding strength is not the same at every point in the cross section. The bonding will be the weakest closest to the start/end points of the print path because the layer time is doubled at those points.

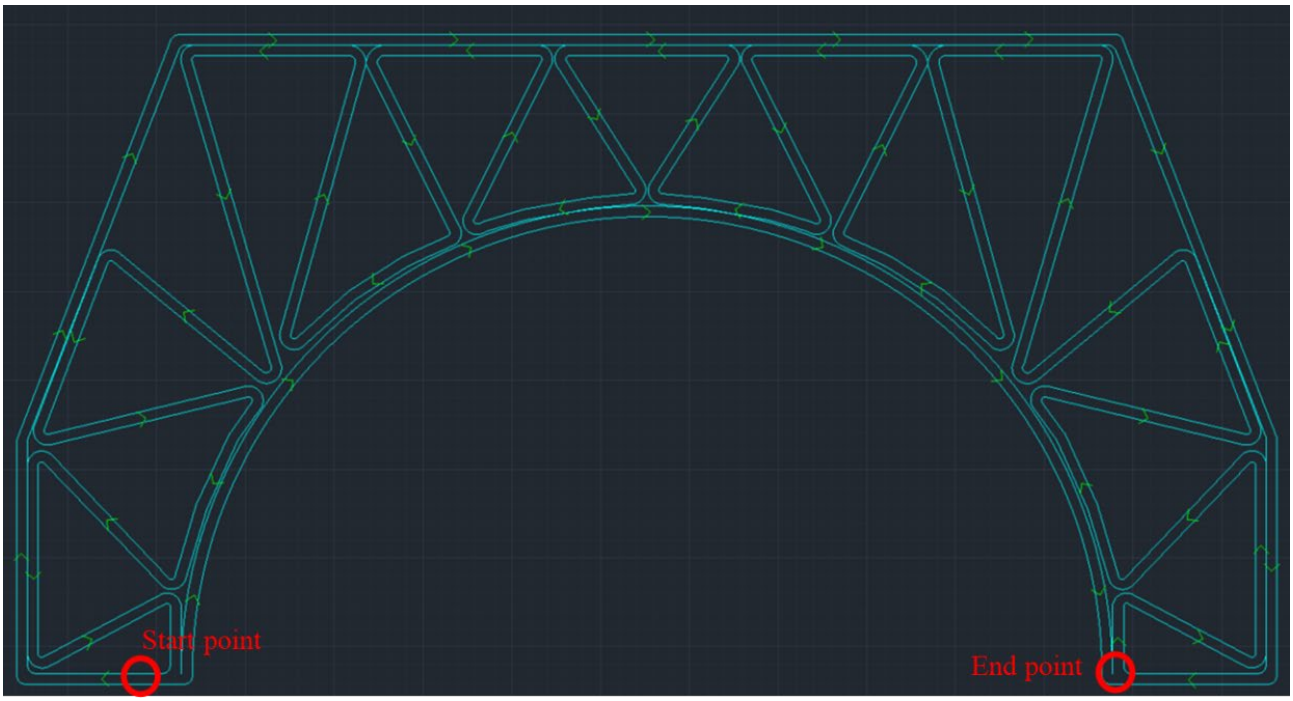

Figure 8-2 Print path of variant 1 with different start and end points leading to asymmetric printing

Another factor that influences the layer time is the length of the print path. The print path length of Variant 1 is 6.2 metres. The fact that this is an asymmetric print pattern, makes that there is no need to go back to the original starting point. This saves extra length of the print path. Moreover, because a way back to the original starting points is not necessary, an extra sharp corner is prevented. So, there is just one 180° corner in the print path of Variant 1. However, due to the relatively extensive infill, the length of the print path is increasing. The infill is designed in such a way that almost all the parts of the outer part and the inner arch are double layered except the upper half of the inclined side plates. The dimensions of this variant are sketched in Figure 8-3. In this sketch, the centre line of the print path is shown.

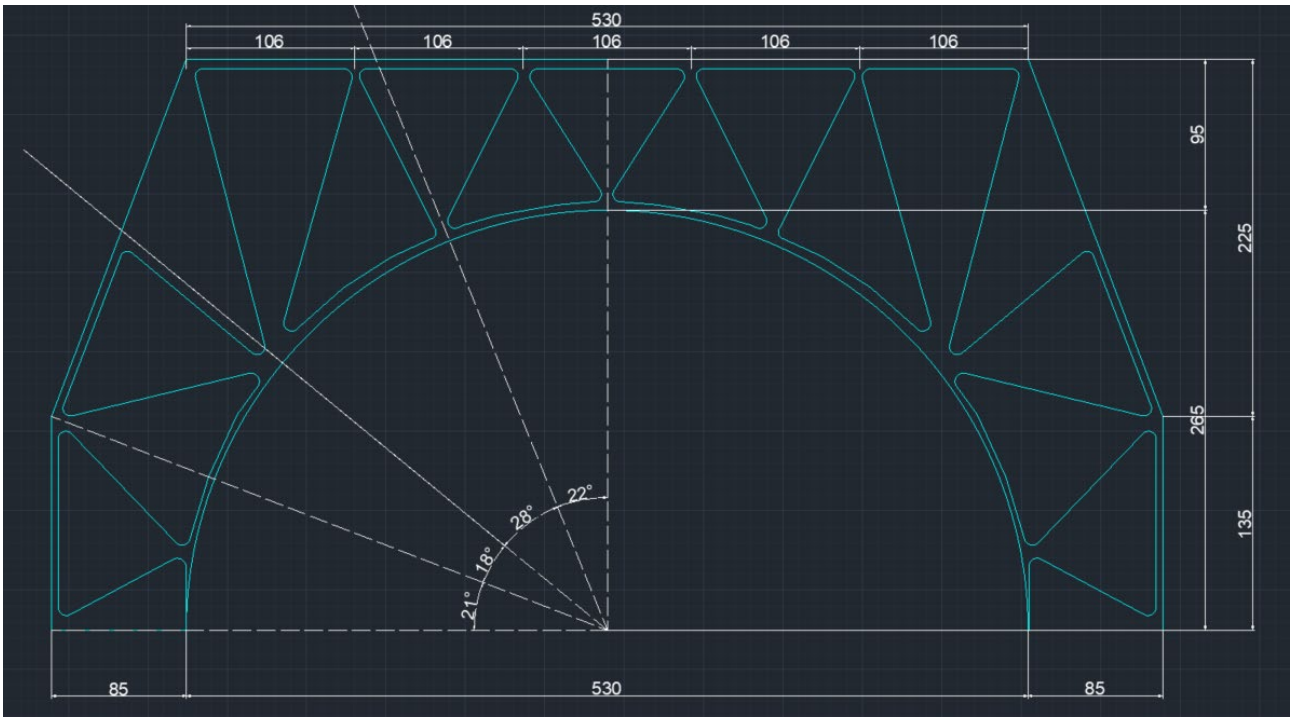

Figure 8-3 Dimensions of variant 1 of the arch component. The centre lines are drawn, so the dimensions are the centre-to-centre distances

8.2.2 Variant 2: Shorter infill with extra layer on top

To get a symmetric print pattern, the end point of the print path should be at the same location as the starting point. To go back to the original starting point, the print path can go either via the outer part via the top or via the inner arch. In the Variant 2, the way back is along the outside via the top plate. This does increase the length of the print path. Therefore, the infill is shortened, compared to the first variant. In Figure 8-4, the print path of the second variant is shown. The print path has a total length of 6.6 metres.

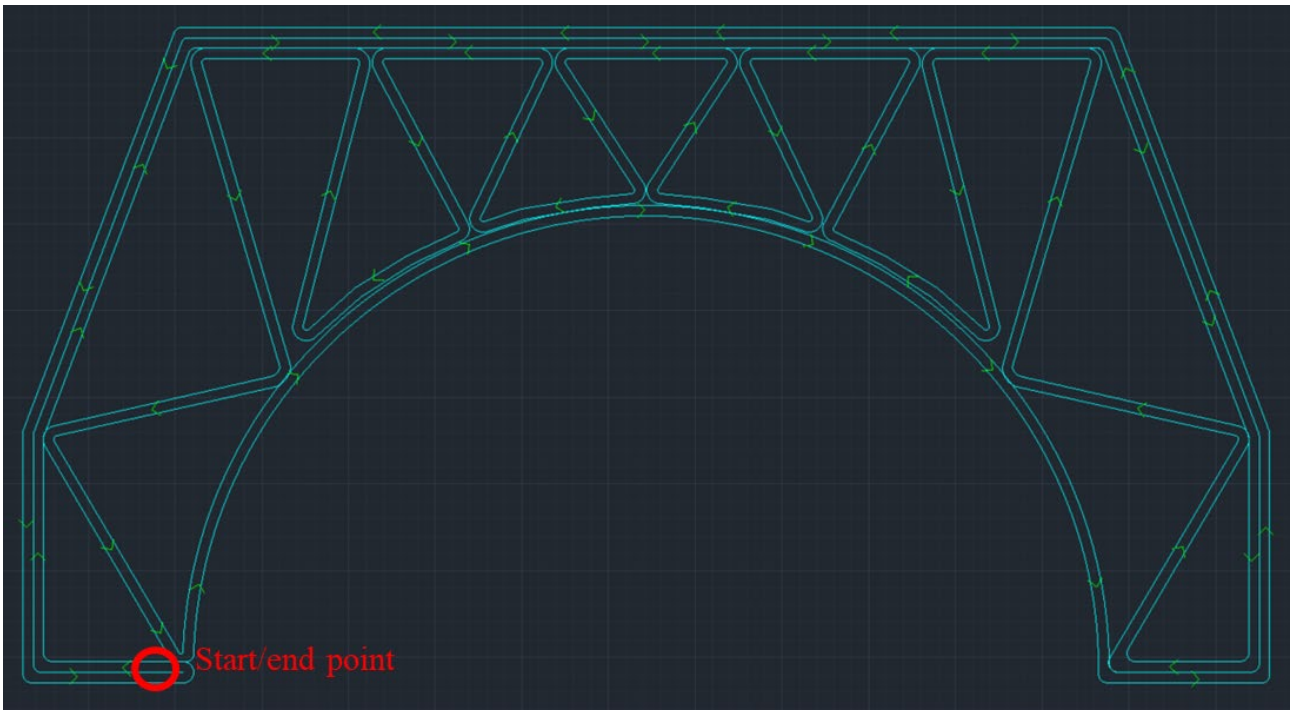

Figure 8-4 Print path of variant 2 with the same start and end points leading to a symmetric print pattern

The downside of the way back via the top plate and the simpler infill is that the bottom part of the arch single layered. Moreover, due to the transition point from double to single layered arch, local eccentricities are

introduced which causes additional local stresses due to bending. On the other hand, with a print path containing a way back via the top, the number of 180° turns is kept limited to one. The dimensions of this variant are given in Figure 8-5.

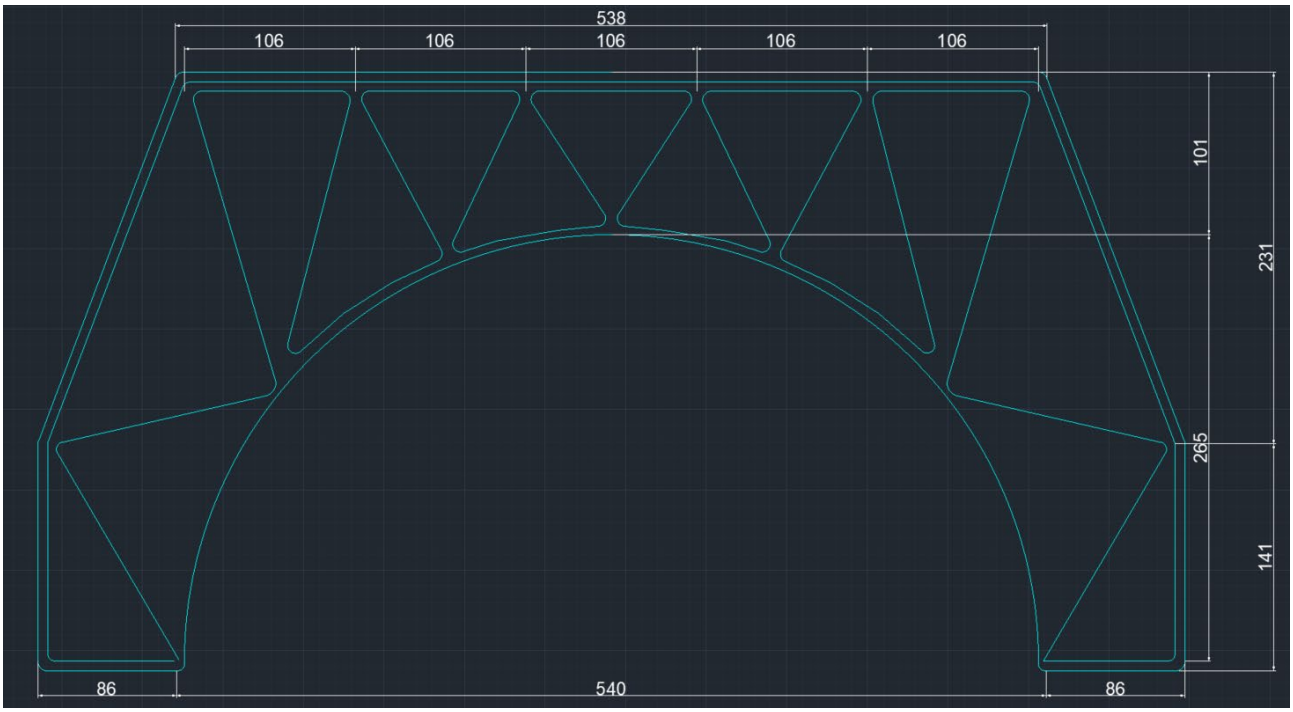

Figure 8-5 Dimensions of variant 2 of the arch component. The centre lines are drawn, so the dimensions are the centre-to-centre distances of the print layers

8.2.3 Variant 3: Medium infill and extra arch layer

Instead of a way back along the top plate at the outside, it is also possible to go back via the arch. This is implemented in the print path of Variant 3, see Figure 8-6. In this way, it is ensured that the print path will have the same start and end point, so a symmetric printing pattern is possible. The total length of the print path is 6.1 metres. A disadvantage of the way back via the inner arch is that there will be two sharp 180°. However, when the total length of the print path is still sufficient below the limit, this will not be an issue.

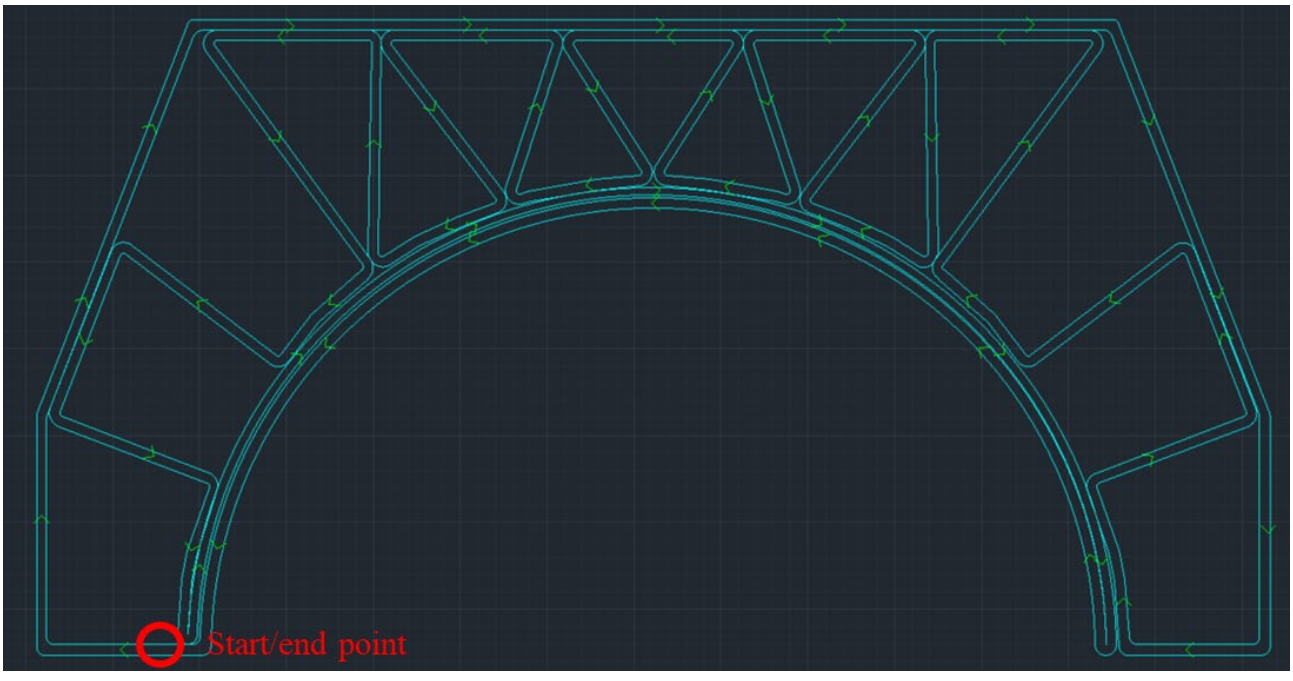

Figure 8-6 Print path of variant 3 with the same start and end points leading to a symmetric print pattern

The way back along the inner arch is a shorter way than the way back along the top plate. Therefore, the infill could be a bit longer than the infill of Variant 2. So, the infill of the third variant has the medium length of the infill of all the three variants. The infill is designed in such a way that there will be a Vierendeel pattern. This Vierendeel pattern causes changes in total thickness of the inner arch at the bottom, which is not desirable because of local additional bending stresses. These eccentricities are also introduced in the sides of this variant. Due to the Vierendeel pattern, there are two transitions between single and double layered parts. Also, the top part of the inclined side plate and the straight side plate are single layered, which could be fragile considering local buckling. In Figure 8-7, the dimensions of Variant 3 are given.

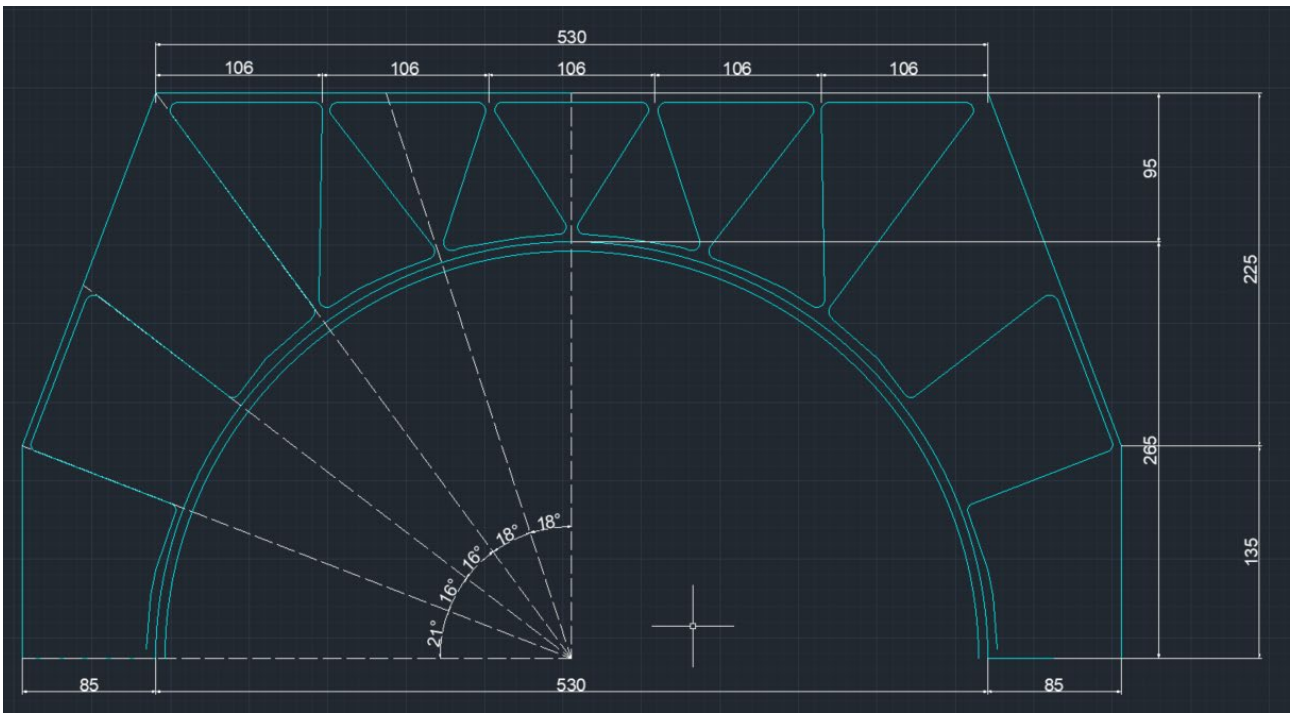

Figure 8-7 Dimensions of variant 3 of the arch component. The centre lines are drawn, so the dimensions are the centre-to-centre distances of the print layers

8.3 Design criteria

The design variants will be compared to each other according to certain design criteria. These criteria can be split into criteria related to the feasibility of printing and into criteria related to the structural performance.

8.3.1 Printing feasibility

The printability of the design variants will be examined on different criteria. These criteria focus on how ideal the design of the variant is for printing and what could be bottlenecks or challenges for a neat print. The following criteria will be considered:

- **Length of the print path**: Due to a maximum layer time and maximum print speed, the length of the print path is limited. So, the length of the print path of the variants should not exceed the maximum print path length. From the first stage of coupon testing was derived that the maximum layer time is 80 seconds. The maximum print speed prescribed by the printer is 10 kg/h. Considering bead dimensions 6 mm width and 2.5 mm thickness, the maximum print path length is 9.2 metres, given a density of 1.61E-6 kg/mm^3 from the material supplier. Moreover, the shorter the length, the more beneficial it could be in case some flexibility in deceleration for sharp corners of the printer is needed.
- **Sharp corners (180° turns)**: It could be that is necessary that a print path contains one or more sharp corners. Especially a 180° turn will lead to additional layer time. To ensure the quality of the extruded material in that sharp corner, the printer must decelerate. Otherwise, heat accumulation or a lack of material could occur. This will influence the quality and/or the adhesion of the extruded material negatively. However, the sharp corners could be tolerated in case the total layer time will still be below the maximum.

- **Same or different start/end point**: Considering a continuous print path, it is common to have the end point of the print path at the same location as the start point. This will be the stacking point of the print. Applying this principle of printing, staking of the layers will be the same for each layer, which leads to symmetric printing. However, in case the layout of the print path is symmetric, it is possible to have a separate start and end point. When the print path of one layer is completed, the next layer can be printed with the same print path but the other way around. This results in printing with asymmetric stacking. The downside of asymmetric printing is that the layer time is varying over the print path. Meaning that the bond strength between the beads is not the same at every point. Particularly the parts of the print path close to the start/end points will be affected negatively because the layer time at those points will be doubled. Therefore, asymmetric printing is only possible if the length of the print path is smaller than the half of the maximum print path length.
- **Single layered parts**: Besides the structural point of view, single layered parts of print paths could also influence the printability. This is because it is a challenge to print single beads perfectly straight, due to the temperature differences during extrusion and the shrinkage that occurs. When double layered sections are printed, one layer could act as a kind of support to stabilize the other layer during extrusion. Besides double layering could improve the quality of the printed bead, it could also have a structural benefit when single layered parts are prevented because single layered part will be more prone to local buckling.
- **Local eccentricities**: Depending on the design of the print path, there could be transitions from single to double layers or double to triple layers for example. These transition points introduce local eccentricities because at those points, the neutral axis will shift with half the bead width. The (outer) layer goes part from the other layer(s) at those transition points. Due to the local eccentricity, caused by the shift in neutral axis, local bending will occur.

8.3.2 Structural performance

The last point of the printing feasibility criteria is also related to the structural performance. The variants will be examined based on the structural behaviour of the element. What are the governing stresses and where do they occur? What is the load factor for (local) stability? What will be the maximum deflection? Ultimate limit state (ULS) checks will be done whether the design suffices or not, based on the following governing stresses, where they occur, and the governing load factor regarding stability:

- $\sigma_{xx,mid}$ mid-plane stress in the principal direction of printing
- $\sigma_{xx,top/bot}$ top or bottom stress in the principal direction of printing
- $\sigma_{yy,t,mid}$ tensile mid-plane stress perpendicular to the print direction
- $\sigma_{yy,t,top/bot}$ tensile top or bottom stress perpendicular to the print direction
- $\sigma_{yy,c,mid}$ compressive mid-plane stress perpendicular to the print direction
- $\sigma_{yy,c,top/bot}$ compressive top or bottom stress perpendicular to the print direction
- $\sigma_{xy,\ mid}$ in-plane shear stress
- α_{crit} load factor for stability

Besides these ULS checks, also a serviceability limit state (SLS) check will be performed in terms of the deflection. The global vertical deflection (z-axis) should not extend the deflection limit.

8.4 Evaluation of the three variants

Each design variant will be evaluated according to the design criteria from the previous section. From this evaluation, the three variants can be compared with each other to pick the benefits of each. These benefits will form the basis for the final design.

8.4.1 Evaluation of the printability

The criteria of the feasibility of printing are listed in Section 8.3.1. The comparison of the three design variants based on these criteria is presented in Table 8-1.

Table 8-1 Comparison of the three design variants in terms of feasibility of printing

	V1: Most extensive infill	V2: Shorter infill with extra layer on top	V3: Medium infill and extra arch layer
Length print path (max. 9.2 m)	6.2 m (+)	6.6 m (+)	6.1 m (+)
Same start/end point	No (---)	Yes (++)	Yes (++)
Sharp corners (180° turns)	1 (++)	1 (++)	2 (+)
Single layered parts	Only upper half inclined outer part (++)	Lower part of arch (--)	Upper half inclined outer part and vertical bottom outer part (+)
Local eccentricities	In the middle of the inclined side plates (-)	At the intersection of the arch with the stiffeners coming from the inclined side plate (--)	Both two times at the side plates and two times in the arch (---)

The criteria “Print path length” and “Same start/end point” do have a relation to each other. When a print path has not the same start and end point, the layers will be printed with asymmetric stacking. When the length of the print path is below the half the of maximum length, this will not be an issue because then the doubled layer time is still below the maximum layer time. However, the lengths of the print paths of all three variants are longer than half of the maximum print path length (9.2 m / 2 = 4.6 m). Therefore, a design with asymmetric printing is not a suitable option. So, the print path of the final design should have the same start and end point.

The “Print path length” criterium has also a link with the “Sharp corners” criterium. Since the print path length is not close to the maximum for any of the variants, two 2 180° turns are still manageable. This will not be a limiting factor choosing one of the three variants.

The single layered parts are important for both printing feasibility and structural performance. Regarding the structural performance, single layered parts are more sensitive for buckling. In terms of printing, double layered parts are beneficial because one layer can act as a support for the attached printed layer. This makes the print neater and thus improves the print quality. So, the arch component will perform better when parts of the cross section that are likely to carry relatively higher forces will be at least double layered. This is the case for Variants 1 and 3.

Local eccentricities occur due to transitions from single to double layered, double to triple layered, or the other way around. For the printing feasibility this is not a big issue. But it as an important criterium to take into account for the design of the print path. Local eccentricities could be acceptable for parts not prone to carry the largest forces, but for critical parts, it is not desirable. Since Variants 2 and 3 contain local eccentricities and plenty of the stresses is distributed via the arch, Variant 1 has the most preferable print path, despite Variant 1 contains a single to double layer transition point at the middle of the inclined side plates.

8.4.2 Evaluation of the structural performance by FEA

The three variants will be evaluated by a finite element analysis (FEA). In this GSA model, the variants of the component are modelled with 2D shell elements having an element size of 20 millimetres. Different parts of the components are modelled with either single, double, or triple layered sections, as it is in the sketches of the print path of each variant. At transition points between single and double or double and triple layered parts eccentricities are taken into account. In the connections, the model is simplified. The connections are modelled as rigid joints in which the connected members are perfectly aligned with each other. However, the joints are connected by double layering, or the infill is printed attached to the top plate and arch for example.

In reality, the neutral axes of the members do not intersect centrally in the corners, the print path does affect the connection in the corners. Moreover, the variants are modelled with a thickness of 1, 2, or 3 times the bead width, while this is a multi-layered build-up instead of one member with a magnified thickness. In Figure 8-8, the GSA model of Variant 1 is shown as an example of how the design variants are modelled as described An overview of how each variant is modelled can be found in Appendix D.

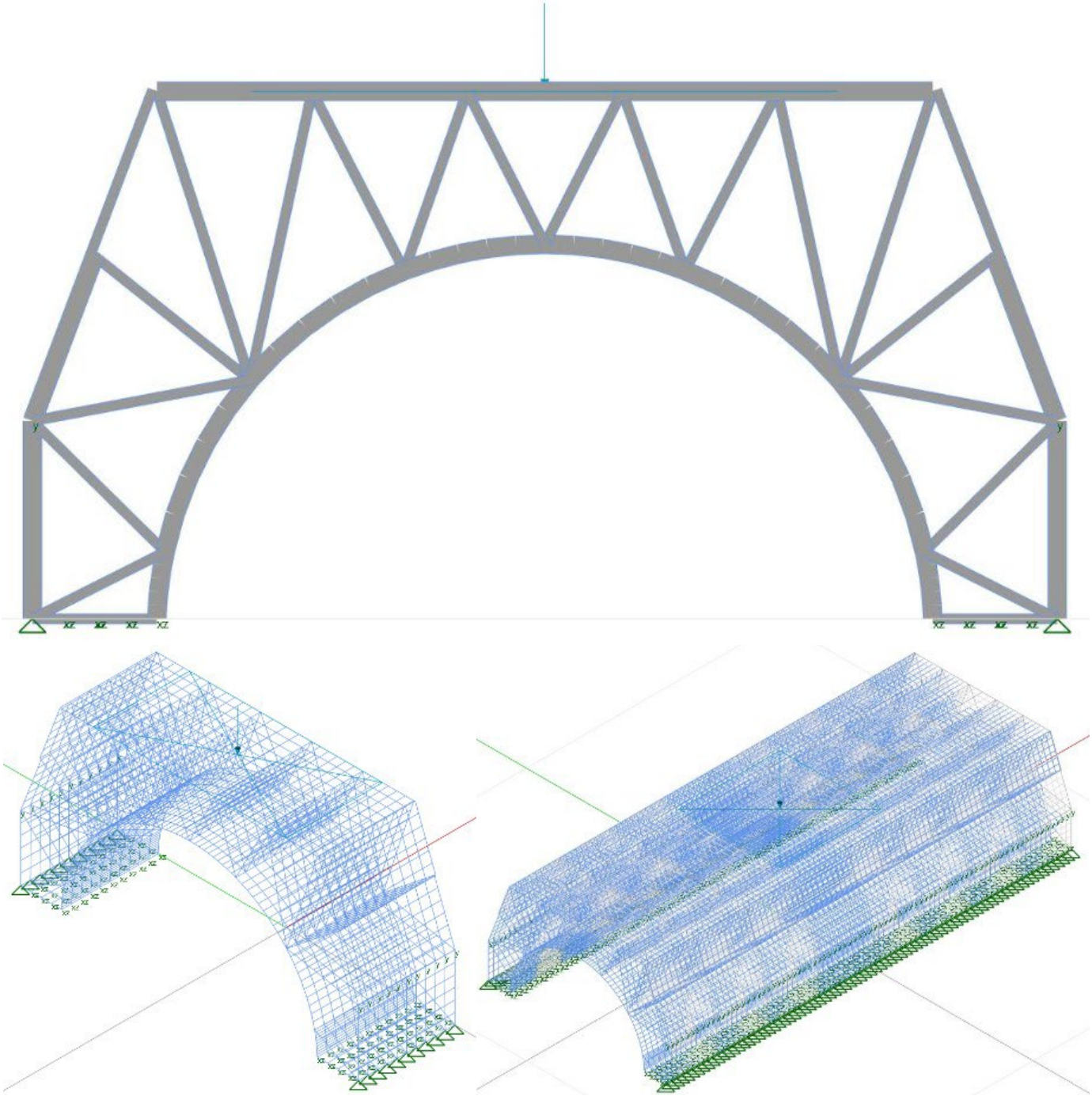

Figure 8-8 GSA model of Variant 1: the cross section with the corresponding section thicknesses (above), the model similar as the test set-up with the applied load and boundary conditions (lower left), and the elongated model with the load in the middle (lower right)

Each variant is analysed considering two models. In one model, the component has a depth of 200 millimetres. This corresponds with the set-up available to test the final design of the component. In this model, the component is loaded over the whole depth of the component to observe the in-plane behaviour of the cross section, which will also be the case during the test. This is done for the analysis of the normal stresses in principal direction, so in the direction of printing. The load is applied over a centred width of 400 mm,

corresponding to LM1, described in Section 5.3. The value of the load is scaled by the actual surface area of the load model and the surface area applied in the test and thus in the model. The load value corresponding to LM2 is applied to be on the conservative side. This scaled value is slightly higher than the load value corresponding to LM1, according to Equations (8-1) and (8-2). In the other model, the component is elongated to a depth of 1600 mm model for the analysis of the normal stresses in perpendicular to print direction and the shear stresses. In this model, the load is applied over a centred 400 mm by 400 mm area. The behaviour in transverse direction can be observed in this way.

The design load value considered in the FEA is an equivalent load value of a wheel load according to LM2 from NEN-EN 1991-2. That gives a slightly higher area load value compared to the wheel load according to LM 1, see Equations (8-1) and (8-2).

- LM1: $150\text{kN}/(400\text{mm} * 400\text{mm}) = 0.0009375\ \text{kN}/\text{mm}^2$ (8-1)
- LM2: $200\text{kN}/(600\text{mm} * 350\text{mm}) = 0.0009524\ \text{kN}/\text{mm}^2$ (8-2)

This is the characteristic value of the applied load. To convert this characteristic load value to the design value of the load, this value is multiplied by a partial safety factor of 1.5, according to NEN-EN 1990. This gives a design load value of 0.00143 kN/mm^2 for the ULS checks.

For the normal stresses in principal and transverse direction, the stress values at mid-plane of the cross section and at the outer fibre are observed. An overview of all the governing stresses of the three variants is presented in Table 8-2. First, the contour plots of the normal stress in both direction for the three variants are evaluated.

In Figure 8-9, the normal stresses at mid-plane of the three variants are shown. Variant 2 is the less efficient design, with relatively high tensile stress in the stiffener in the top corner and compression stress in the slightly horizontal stiffener from the kink in the side plate. Variants 1 and 3 have a better distribution of the forces since the maximum occurring compressive and tensile stresses are not as high as in Variant 2. The second stiffener at the top is the stiffener carrying the highest compressive stress.

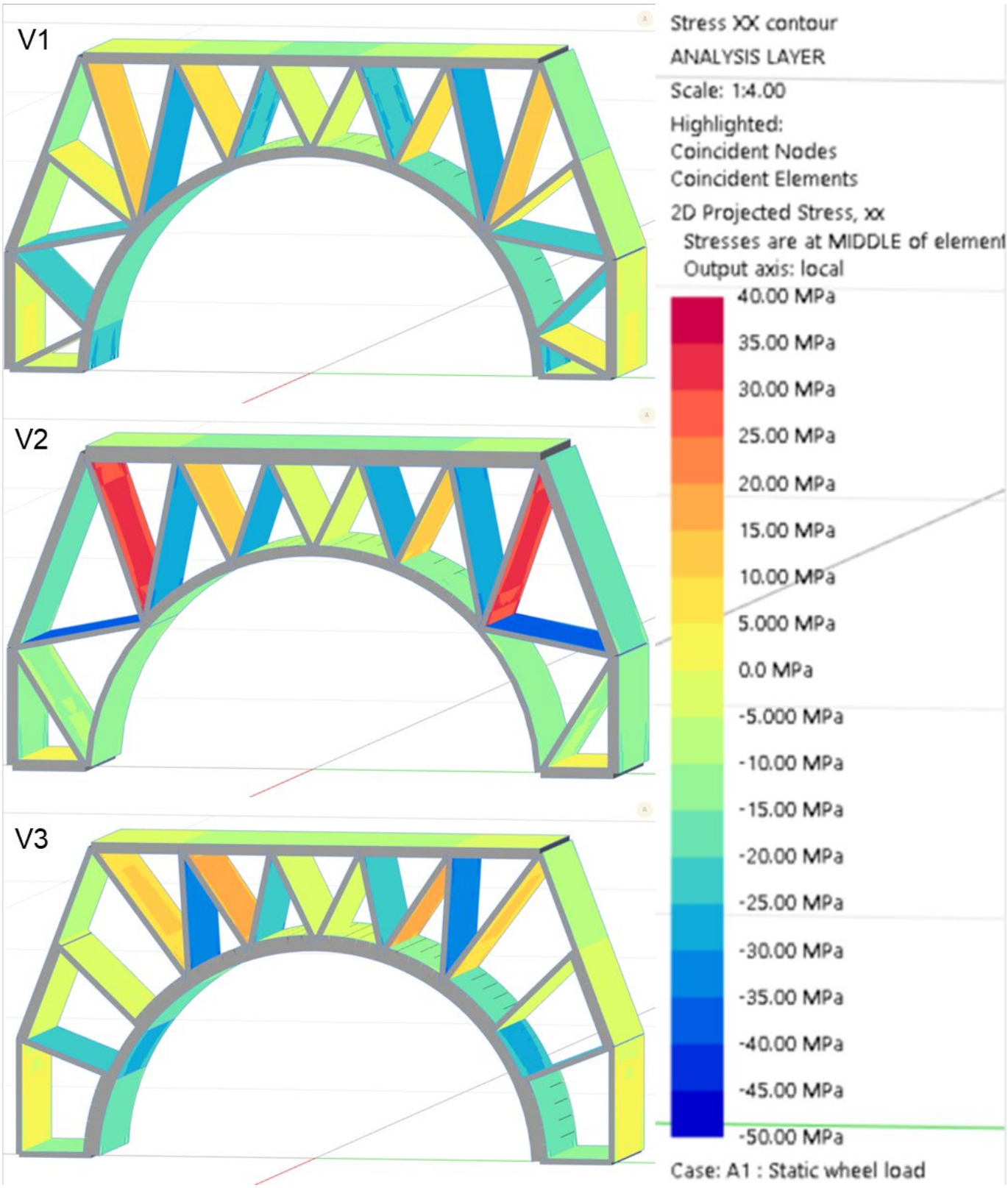

Figure 8-9 Normal stresses in the principal (print) direction at mid-plane from the FEA of the three variants

The values of the normal stresses in principal direction at mid-plane showed already a shift at the local eccentricity points, especially in Variant 3. The normal stresses at the outer fibre show clearly that the local eccentricities, introduced by the transition points, lead to unfavourable bending stresses, according to Figure 8-10. Extreme stress values occur in the arch part at the single/double or double/triple layer transition of Variants 2 and 3. Those values are exceeding the limit. The contour plot of Variant 1 does not contain such extreme stress values.

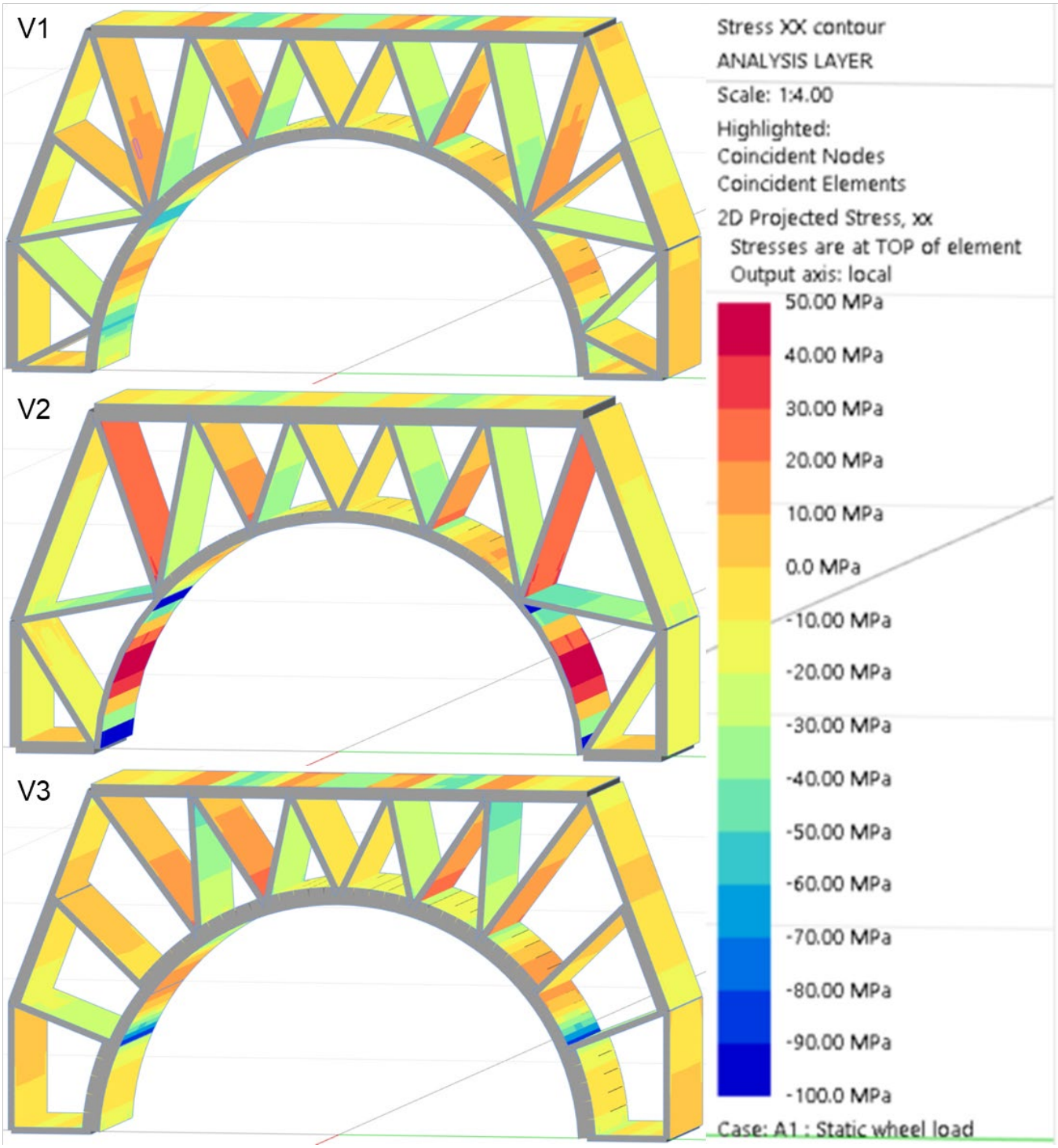

Figure 8-10 Normal stresses in the principal (print) direction at the outer fibre (top) from the FEA of the three variants

Figure 8-11 shows the normal stresses in transverse direction at mid-plane of the cross section. The cross section of the middle part of the elongated element at the middle of the load area is shown to have a clearer view on the contour plot of the stresses. The behaviour of Variants 1 and 3 is quite comparable. At the intersection between the arch and the stiffeners of Variant 2, some higher tensile stresses occur.

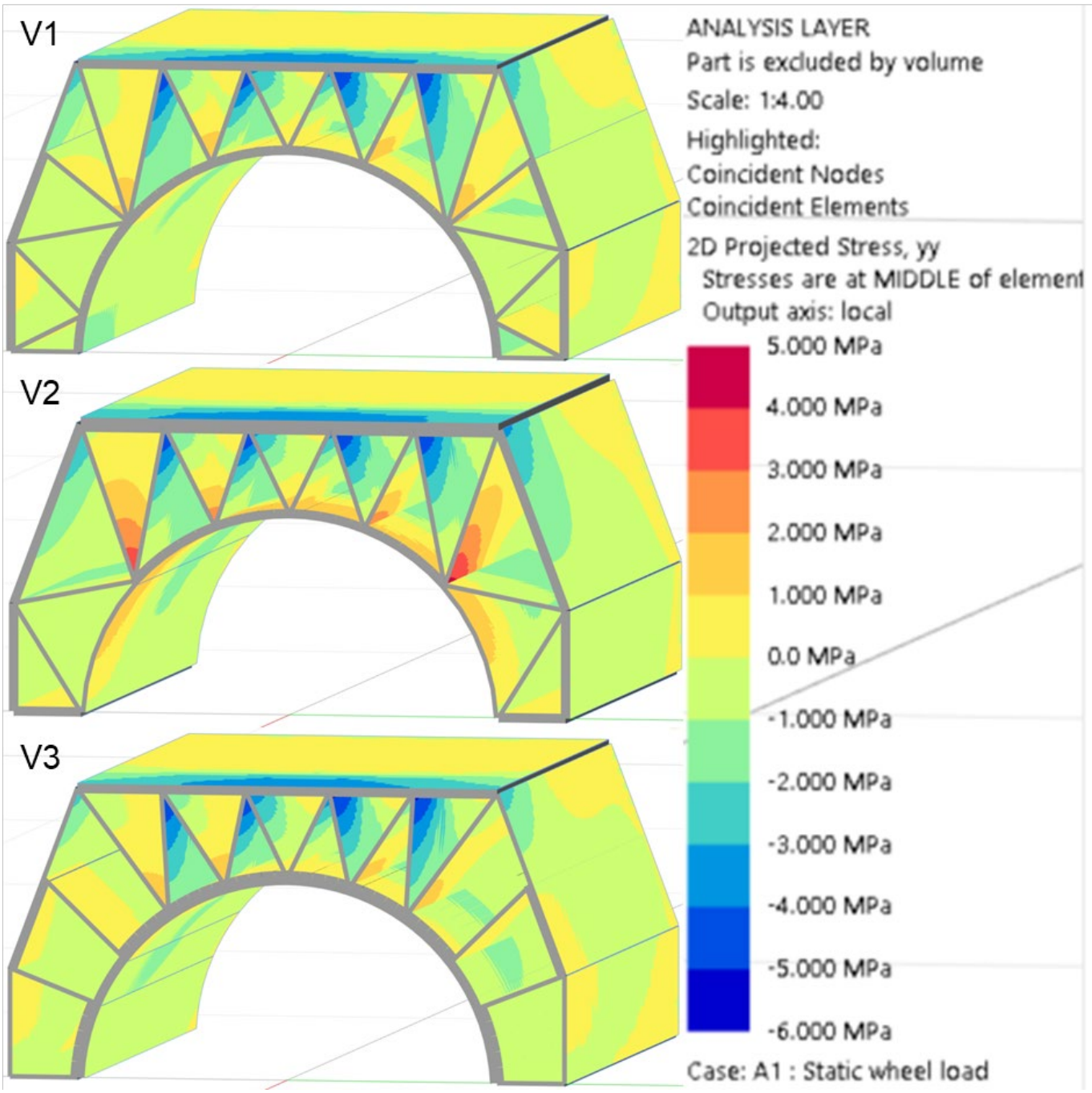

Figure 8-11 Normal stresses in the transverse (perpendicular to print) direction at mid-plane from the FEA of the three variants, the cross section at the middle of the load area at the middle of the elongated component is shown

For the normal stresses perpendicular to the print direction at the outer fibre of the cross section also, the stress distribution is comparable for Variants 1 and 3, see Figure 8-12. The tensile stresses in the arch are higher for Variant 2. Due to the triple layered top plate of Variant 2, the compressive stress is lower in that section compared to the other two. However, all these stress values are below the limit. This is a large benefit compared to the preliminary design of the previous study since the compressive stress in transverse direction in the top plate did exceed the limit.

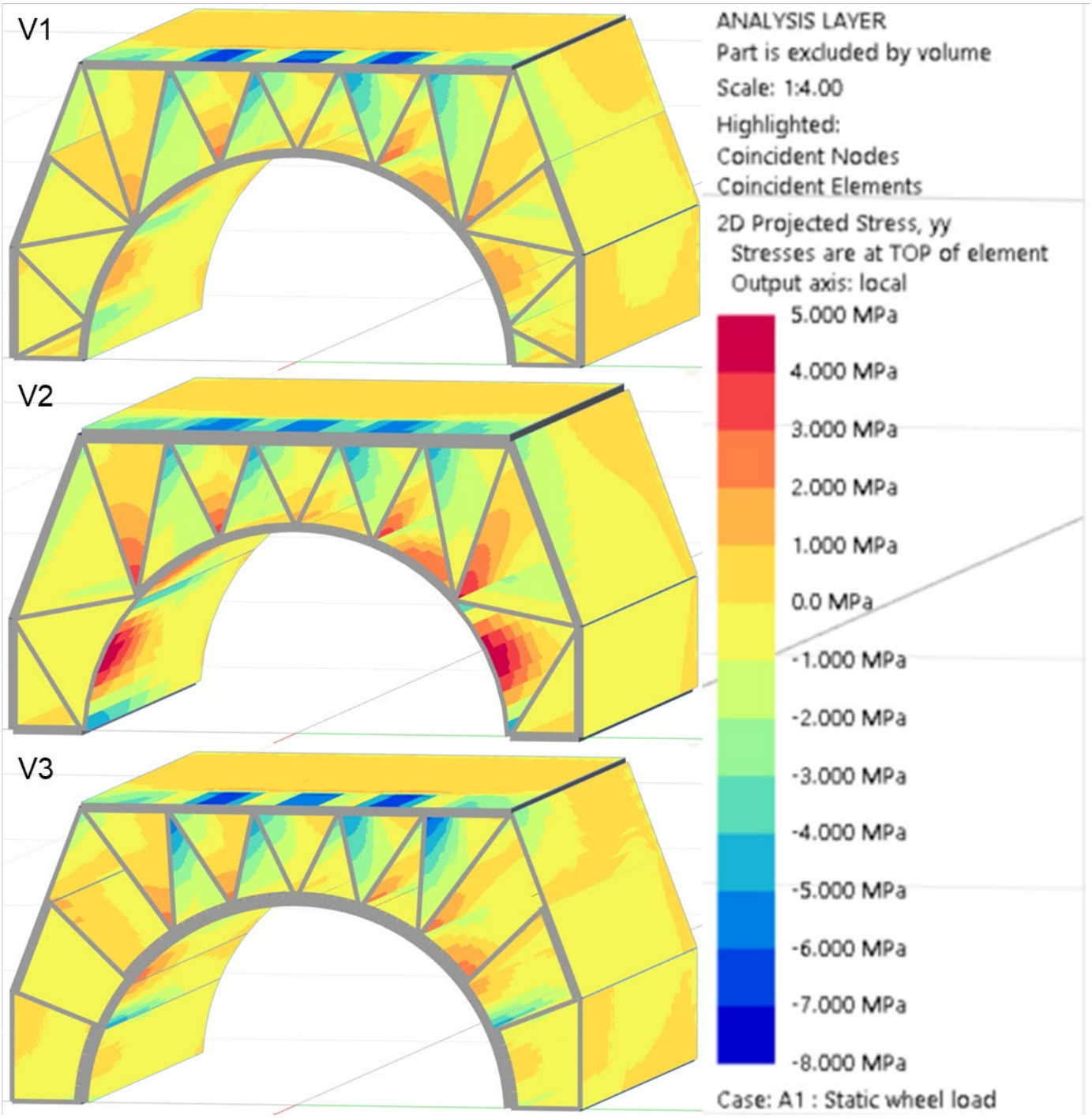

Figure 8-12 Normal stresses in the transverse (perpendicular to print) direction at outer fibre (top) from the FEA of the three variants, the cross section at the middle of the load area at the middle of the elongated component is shown

The shear stresses in the elongated model of the variants can be seen in Figure 8-13. Variant 2 suffers the largest shear stresses, compared to the other two. From a cross sectional point of view, these shear stresses mainly occur in the middle stiffeners and in the arch. When observing in the main direction of the element, the maximum shear stresses in the component are at the edge of the load area. This is logical since the load is introduced at that point, which results in a shift in the in-plane shear stress.

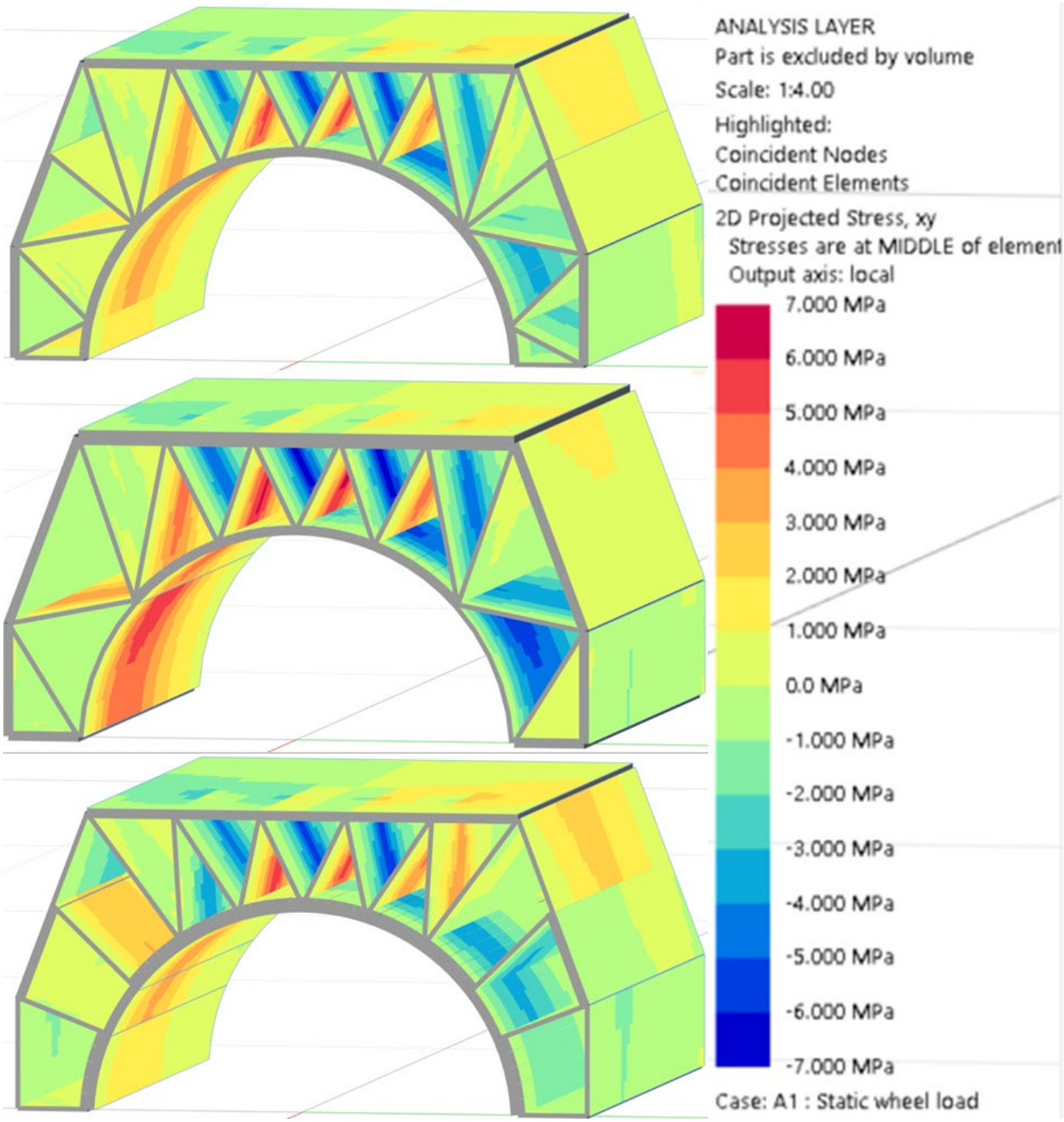

Figure 8-13 Shear stresses in at mid-plane from the FEA of the three variants, the cross section at the middle of the load area at the middle of the elongated component is shown

In Table 8-2, an overview of the checks for the governing stresses of each variant is presented. The design limit values are calculated with a conversion factor of 0.81 and a partial safety factor of 1.38. When the governing stress is below the limit, the cell is marked green and when the check does not suffice, the cell is marked red. As can be seen, the governing normal stress in principal direction at the outer fibre is exceeding the limit for each variant. The margin for Variant 1 is little, while the governing stress for Variants 2 and 3 are far too high. This can be explained by the local eccentricities due to the layer transition point, which introduce high local bending stresses. Therefore, such local eccentricities should be avoided in the final design. The load factor for the stability check is more than sufficient for each variant.

Table 8-2 Comparison of the three design variants in terms of structural performance based on the governing stresses from the test GSA models of each variant with uniform thicknesses (6mm/12mm/18mm) including local eccentricities

Aspect	**Limit value**		**V1: Most extensive infill**		**V2: Shorter infill with extra layer on top**		**V3: Medium infill and extra arch layer**	
	Char. value	**Design value**	**Value**	**Governing element**	**Value**	**Governing element**	**Value**	**Governing element**
$\sigma_{xx,mid}$	93.5 MPa	54.9 MPa	31.2 MPa	Compression in second top stiffener from the side	42.9 MPa	Compression in 'horizontal' stiffener from kink in side plate	36.4 MPa	Compression in stiffener corner triangle
$\sigma_{xx,top/bot}$	93.5 MPa	54.9 MPa	55.5 MPa	Compression at intersection arch with stiffeners	98.9 MPa	Compression at discontinuity ends single layered arch part	88.6 MPa	Compression (top) at discontinuity arch double layer
$\sigma_{yy,t,mid}$	16.8 MPa	9.9 MPa	2.3 MPa	Infill at intersection with arch	4.4 MPa	Top corner stiffener at intersection with arch	2.2 MPa	Stiffeners at intersection with arch
$\sigma_{yy,t,top/bot}$	16.8 MPa	9.9 MPa	3.7 MPa	Top plate in second and fourth span at edge load area	6.9 MPa	Transition point from double to single layer in the arch	3.7 MPa	Top plate in second and fourth span at edge load area
$\sigma_{yy,c,mid}$	29.5 MPa	17.5 MPa	5.3 MPa	Intersection infill with top plate	5.5 MPa	Stiffeners at intersection with top plate	5.4 MPa	Stiffeners at intersection with top plate
$\sigma_{yy,c,top/bot}$	29.5 MPa	17.5 MPa	7.4 MPa	Top plate in second and fourth span	5.9 MPa	Top plate in second and fourth span	7.4 MPa	Top plate in second and fourth span
$\sigma_{xy,mid}$	11.6 MPa	6.8 MPa	5.5 MPa	Edge load area intersection stiffeners	6.3 MPa	Middle stiffeners at edge load area	5.6 MPa	Edge load area intersection stiffeners
Stability factor α_{crit}	2.0	2.0	2.24	Second top stiffener from the side in compression	2.08	Top corner stiffener	3.35	Second top stiffener from the side in compression

Aspect	Limit value		V1: Most extensive infill		V2: Shorter infill with extra layer on top		V3: Medium infill and extra arch layer	
Global deflection u_z	1.8 mm	1.8 mm	0.71 mm		0.96 mm		0.75 mm	

The value for the global vertical deflection is given in Table 8-2. The check for the maximum deflection is not an ULS check but an SLS one. Meaning that the partial load factor is 1.0 instead of 1.5. The maximum deflection is determined by L/300, which results in (Equation (8-3)):

$$u_{max} = \frac{L}{300} = \frac{530}{300} = 1.77 \text{ mm} \tag{8-3}$$

Since the maximum global deflection for each variant is not exceeding this limit, it can be concluded that deflection is not a critical design criterium for the final design of the bridge deck element. The deformed shapes of the variants are shown in Figure 8-14.

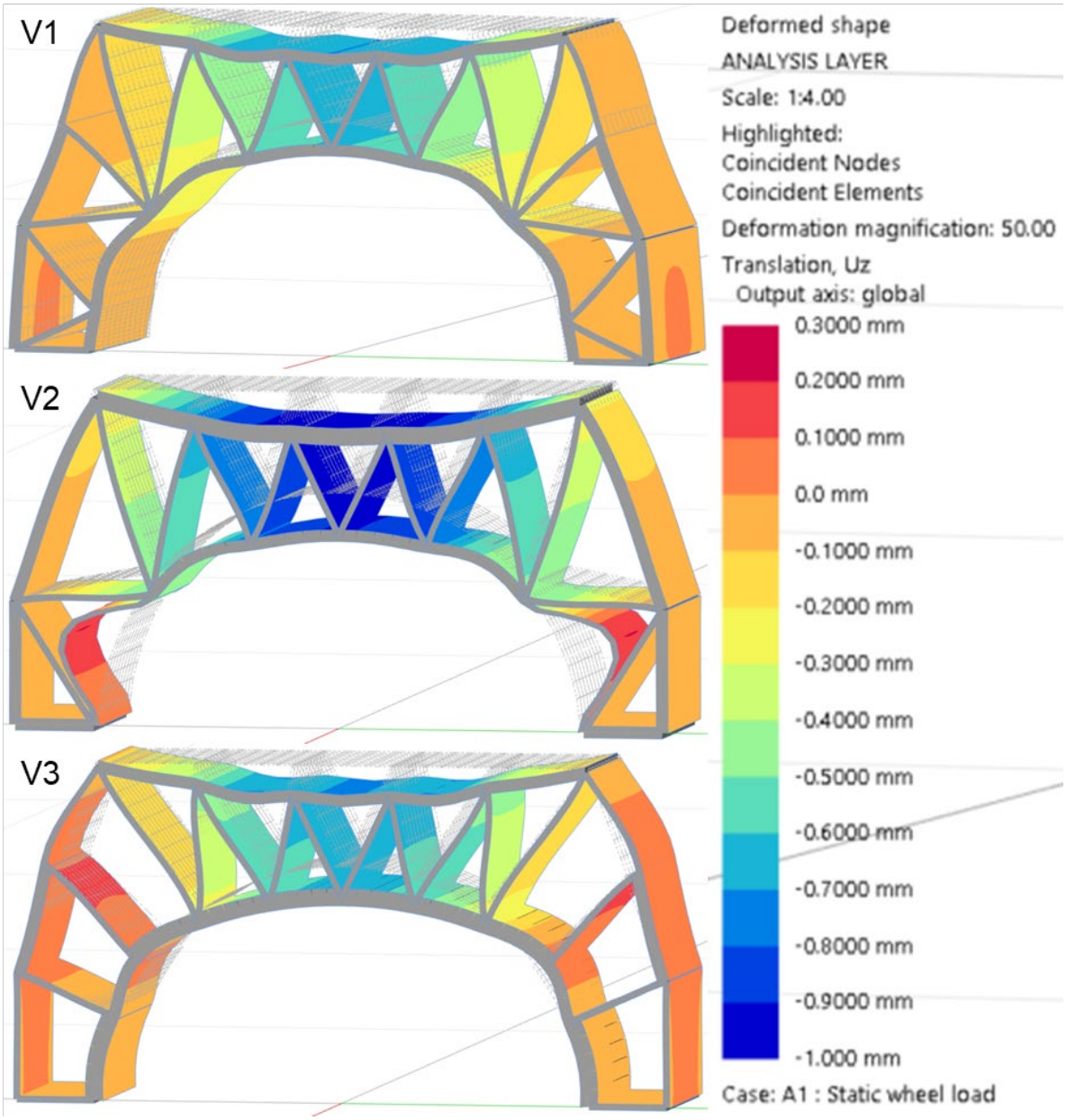

Figure 8-14 Deformed shapes of the three variants of with a magnification factor of 50 with a contour of the global vertical deflection

Considering the results from the printability comparison in Table 8-1 and the FEA comparison in Table 8-2, it can be said that a combination of Variants 1 and 3 could lead to the optimal design. The final design should not contain local eccentricities and that the print path should have the same start and end point. So, the infill of Variant 1 does not result in critical local eccentricities but a way back along the top plate or inner arch should be added. Therefore, an additional check in terms of thickness ratio's is performed. For the infill of each variant, the thicknesses of the arch, top plate, and side plates are adjusted, considering single/double/triple layered, and checked in terms of strength and stability. In this way, the minimal required thicknesses will come out. With these minimal required thicknesses, the thickness ratios of the different section can be determined. So, based on these thickness ratios, the print path could be designed taking into account how many layers which sections should contain. See Table 8-3 for the required thicknesses in terms of single/double/triple layered for the infill of each variant.

Table 8-3 Thickness ratios for the outer sections of the bridge deck element for the infill of each variant in terms of single/double/triple layered parts

Element section	**V1: Most extensive infill**		**V2: Shorter infill**		**V3: Medium infill**	
	Strength σ_{xx}	**Stability**	**Strength σ_{xx}**	**Stability**	**Strength σ_{xx}**	**Stability**
Arch	2	2	3	2	3	2
Top plate	2	2	2	2	2	2
Side plate (inclined)	1	1	1	2	1	1
Side plate (straight)	1	1	1	2	1	1

Variant 1 performs the best according to the thickness ratios. However, as concluded before, Variant 1 contains an asymmetric printing, which should be avoided. A way back to the original start point is required. This means that either via the arch or the side and top plates, an additional layer will be added. In this case, Variant 3 provides the solution by containing a way back via the arch. This makes that the arch will be triple layered, meaning that the required thickness ratios will be fulfilled.

9

Component Design and Test

From the analysis of the design variants in Chapter 8, the final design will be derived and constructed based on the benefits of Variants 1 and 3. This final design will be printed and tested to validate the model of the bridge deck element and to check the maximum applicable load with the corresponding failure mechanism.

9.1 Final design

Based on the comparison of the three design variants, the final design will be based on a combination of Variant 1 and 3. The infill will be comparable with Variant 1. The number of stiffeners from Variant 1 will be applied, but minor changes will be done. The transition point from single to double layer at the inclined side plate, causing a local eccentricity, will be avoided. Therefore, the intersection point of the stiffener with the inclined side plate will be moved to the upper corner. To prevent having two parallel stiffeners too close to each other, the intersection point of the two stiffeners more to the inside will be located as in Variant 3. By having the way back along the arch, the principle of the print path of Variant 3 is incorporated in the final design.

9.1.1 Final variant with two options for arch shape

With the print path, the infill, and the thicknesses of the outer parts (top plate, side plates, and arch) of the component chosen, the last design variant considered is the shape of the arch. The arch can have a circular shape, as in the previous three variants, or a parabolic shape. Both types of shapes are analysed with a Grasshopper model with 1D beam element. In this way, the optimal layout of the infill, so where should which stiffener be exactly placed, could be found. The output from this analysis is slightly adjusted to make some corners less sharp and to prevent stiffeners or intersection being too close to each other. The parameters optimized in this analysis are:

- Arch height factor: the height of the top of the arch (circular or parabolic).
- Arch knee height: the height of the kink in the side plate between the straight part and the inclined part.
- Angles between the vertical symmetry line in the middle of the element and the intersection point of each stiffener with the arch from the centre point at the bottom (intersection of the vertical symmetry line and the horizontal centre line at the bottom).

From this analysis, the two options for the final design are derived. In Figure 9-1, Variant 4a with the circular arch and Variant 4b with the parabolic arch are sketched with the dimensions related to the centre lines of the beads.

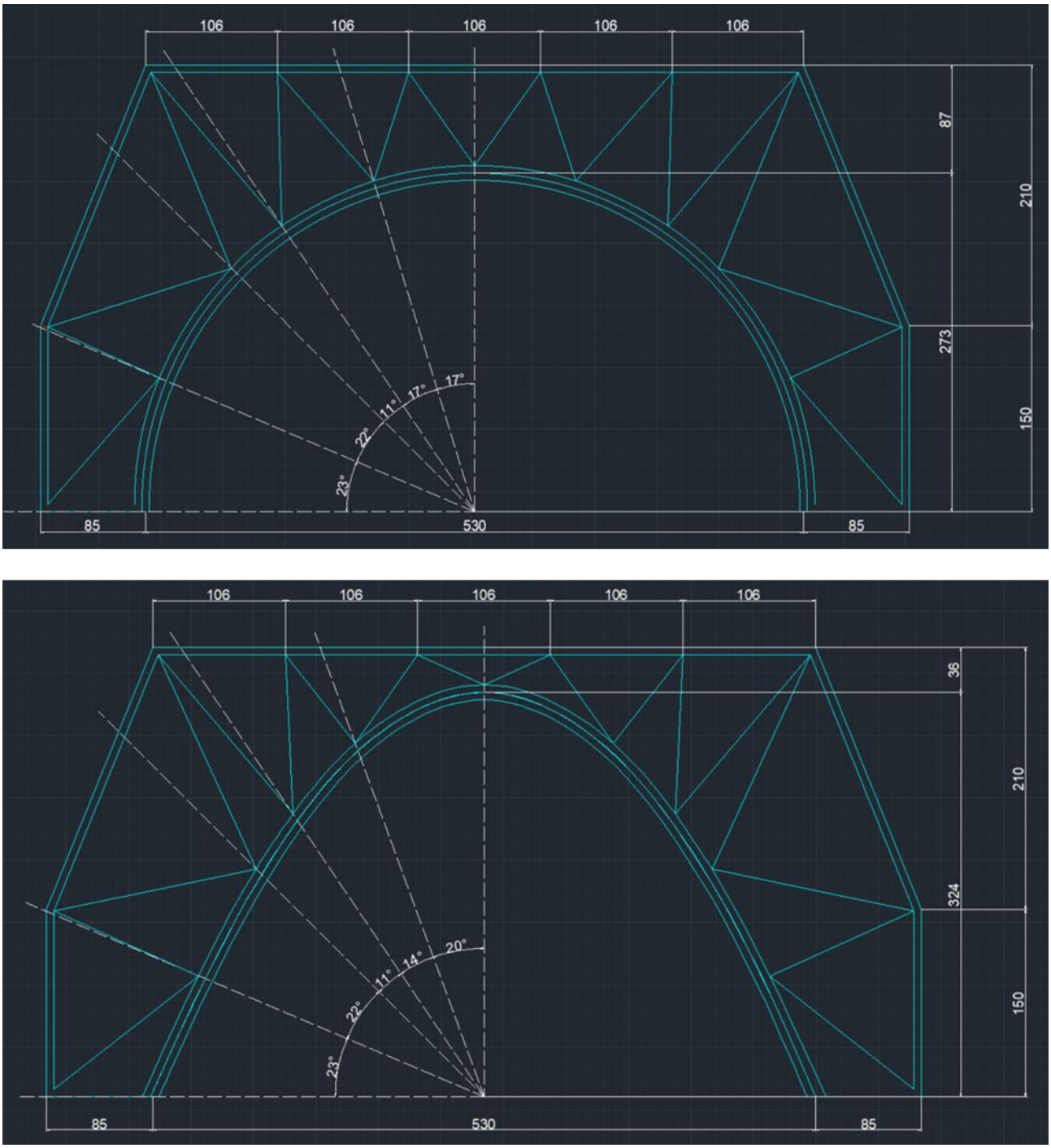

Figure 9-1 Variant 4a with the circular shaped arch (upper sketch) and Variant 4b with the parabolic shaped arch (lower sketch) presented with the centre lines of the bead with the corresponding dimensions

9.1.2 Comparison two options for arch shape

In the same way as the first three design variants, Variants 4a and 4b will be compared in terms of printability and structural performance. This is done to check that the final design satisfies all design criteria and to determine whether the circular or the parabolic shape should be applied for the arch.

Regarding the printability, the only relevant design criteria are the print path length and the sharp corners. Because the same principle for the print path yields for both options, they both have the same start and end point, they both do not contain transition points causing local eccentricities in a member, and only the infill and the bottom support plate is single layered for both variants. The print path length of the circular arch option is a bit short, with Variant 4a having a print path length of 7.3 metres and Variant 4b 7.5 metres. A disadvantage of the parabolic arch option is that the middle part at the top is very dense. A lot of beads are

coming together close to each other. The inner distance between the top plate and the intersection of the stiffeners with the arch is very small. Having the beads so close to each other will lead to heat accumulation. This heat accumulation in combination with the sharp and short corners at that part is not beneficial for printing. So, regarding printing feasibility, the circular arch option scores better due to not having the heat accumulation and sharp corner issue as the parabolic option and due to the print path length being slightly shorter.

Besides the printability, the options should be compared in terms of structural performance. The design checks of the governing stresses are presented in Table 9-1. Like the first three variants, the contour plots of the normal stresses in principal and transverse direction at mid-plane and at outer fibre, and of the shear stresses are given in Figure 9-2 – Figure 9-6. The deformed shape with the corresponding deflection values can be seen in Figure 9-7.

Table 9-1 Design checks of the governing stresses of Variants 4a and 4b in terms of structural performance based on the analysis of the FEM in GSA

Aspect	**Limit value**		**V4a: Circular arch**		**V4b: Parabolic arch**	
	Char. value	**Design value**	**Value**	**Governing element**	**Value**	**Governing element**
$\sigma_{xx,mid}$	93.5 MPa	54.9 MPa	27.5 MPa	Compression in the vertical stiffeners (second support) in the infill	24.4 MPa	Comp. in short stiffener of the infill next to middle
$\sigma_{xx,top/bot}$	93.5 MPa	54.9 MPa	42.6 MPa	Compression in the vertical stiffeners (second support) in the infill	35.7 MPa	Compression in top plate in second and fourth span
$\sigma_{yy,t,mid}$	16.8 MPa	9.9 MPa	2.1 MPa	Two intersections of the infill with arch next to middle stiffener below load	1.5 MPa	Stiffeners in the upper corners at intersection with arch below load
$\sigma_{yy,t,top/bot}$	16.8 MPa	9.9 MPa	3.8 MPa	Top plate in second and fourth span at edge load area	4.2 MPa	Top plate in second and fourth span at edge load area
$\sigma_{yy,c,mid}$	29.5 MPa	17.5 MPa	4.6 MPa	Four middle stiffeners at intersections with top plate below load	3.6 MPa	Two middle stiffeners at intersections with top plate below load
$\sigma_{yy,c,top/bot}$	29.5 MPa	17.5 MPa	6.7 MPa	Top plate in second and fourth span below load	6.1 MPa	Top plate in second and fourth span below load
$\sigma_{xy,mid}$	11.6 MPa	6.8 MPa	5.2 MPa	Four middle stiffeners of the infill below load	4.2 MPa	Four middle stiffeners of the infill below load
Stability factor α_{crit}	2.0	2.0	5.68	'Horizontal' stiffener from kink in side plate	7.90	Second support stiffener of the top plate (vertical stiffener)
Global deflection u_z	1.8 mm	1.8 mm	0.54 mm		0.39 mm	

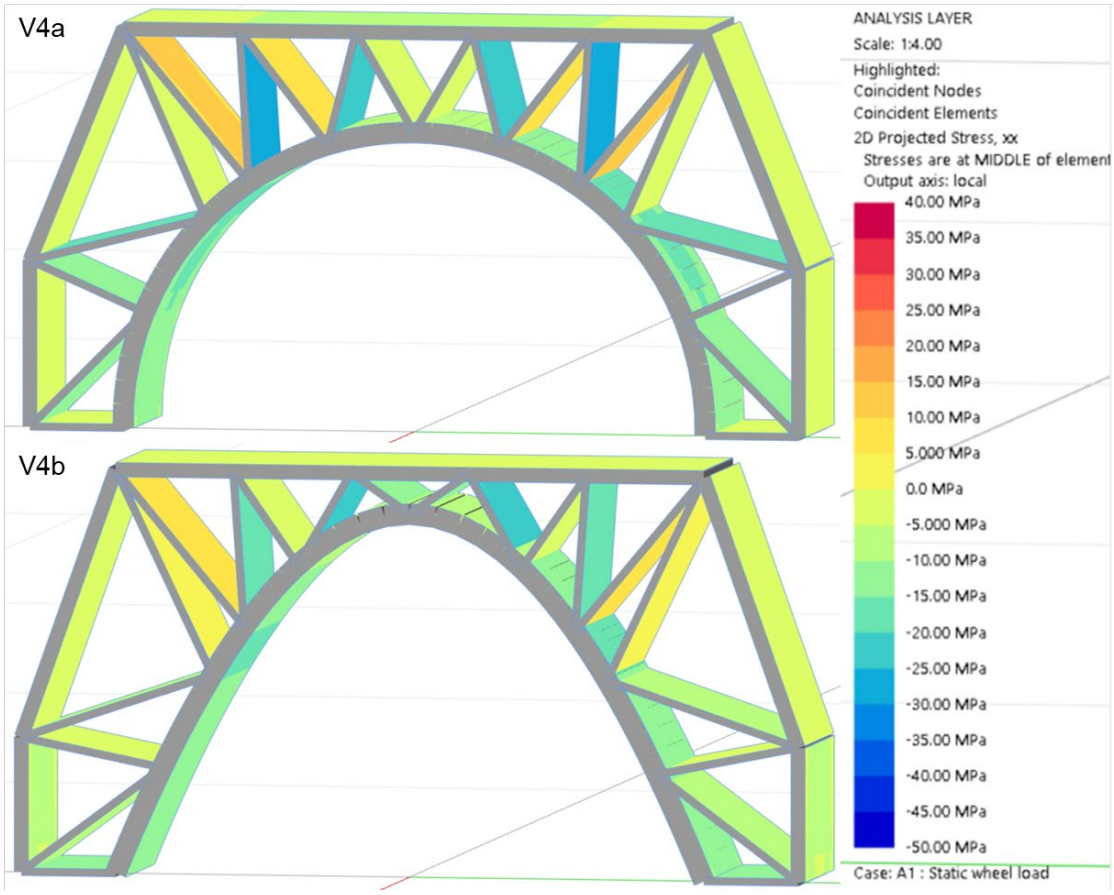

Figure 9-2 Normal stresses in the principal (print) direction at mid-plane from the FEA of Variants 4a and 4b

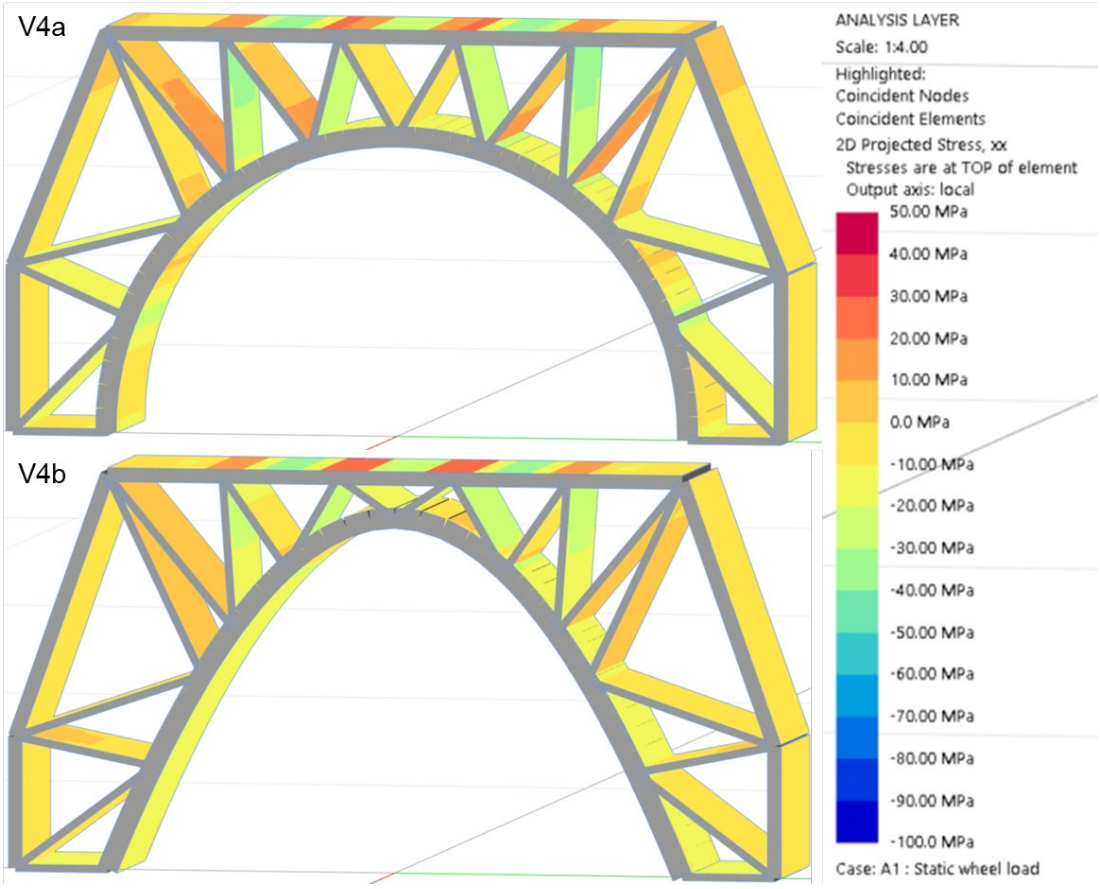

Figure 9-3 Normal stresses in the principal (print) direction at the outer fibre from the FEA of Variants 4a and 4b

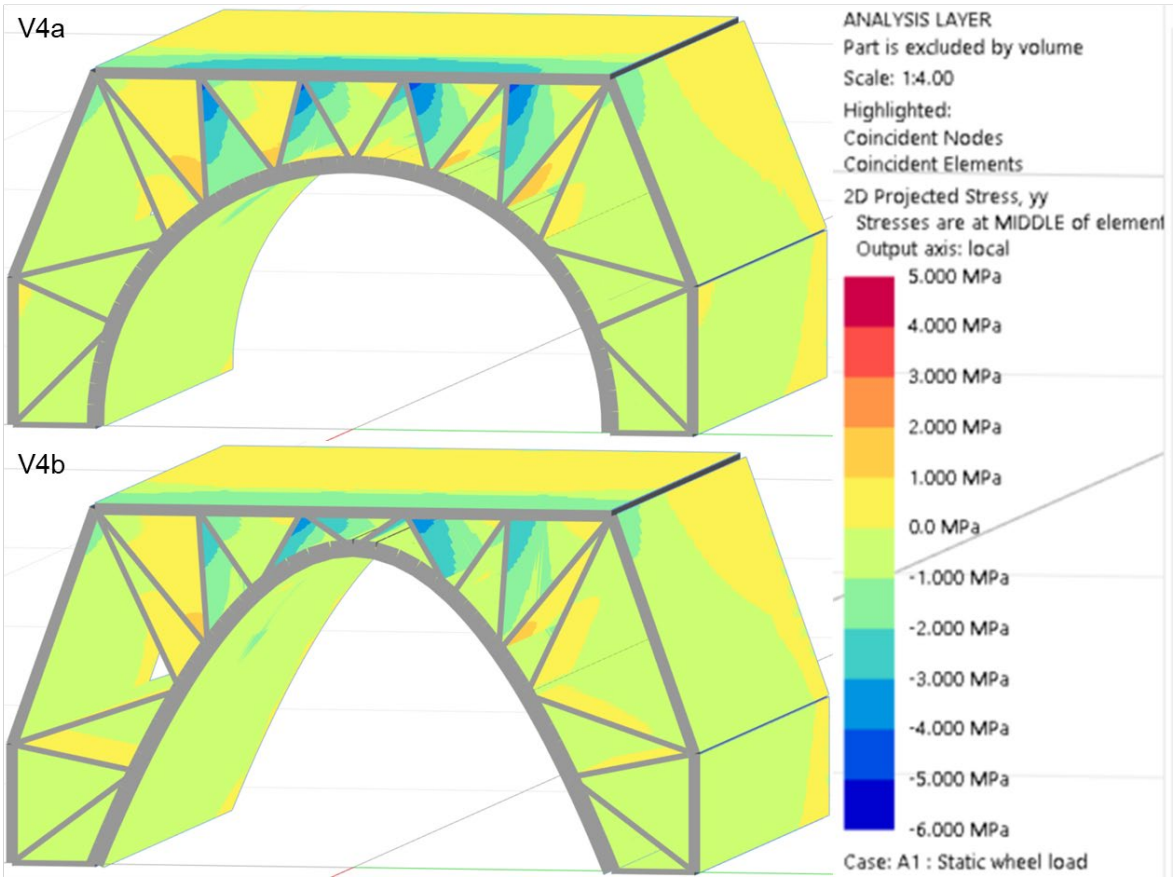

Figure 9-4 Normal stresses in the transverse (perpendicular to print) direction at mid-plane from the FEA of the Variants 4a and 4b, the cross section at the middle of the load area at the middle of the elongated component is shown

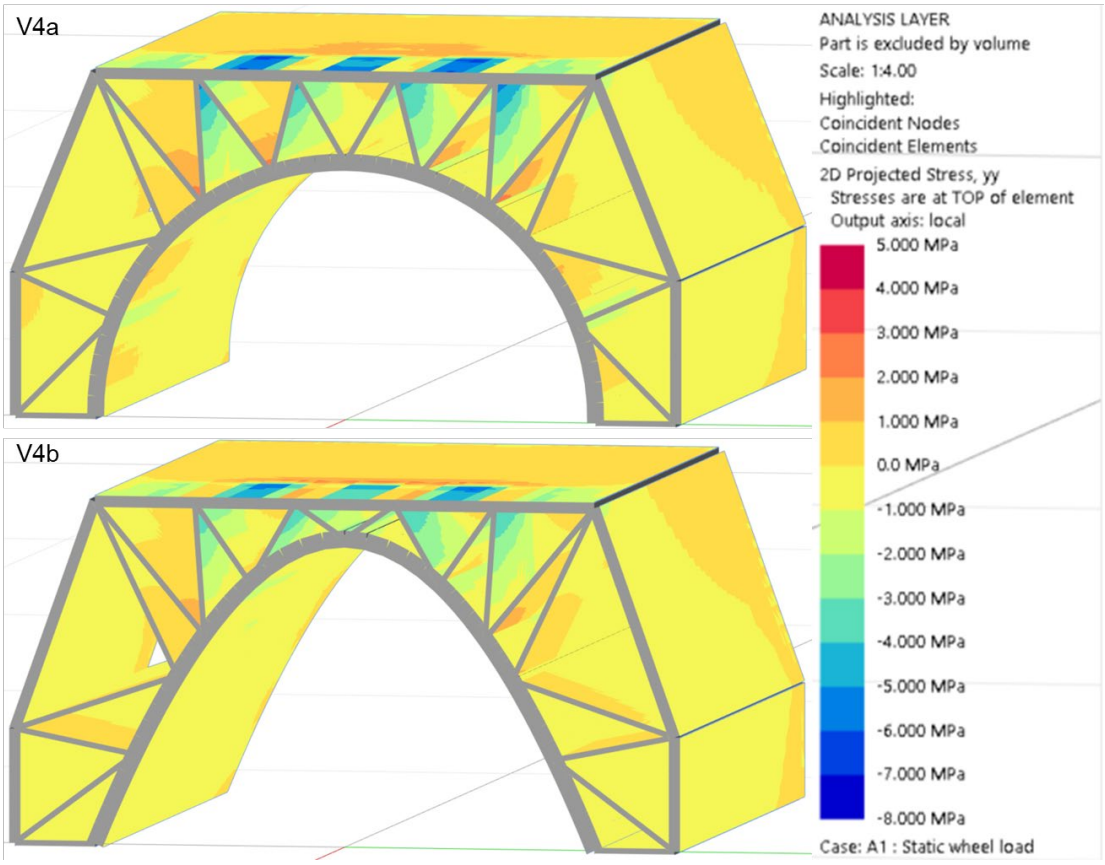

Figure 9-5 Normal stresses in the transverse (perpendicular to print) direction at outer fibre from the FEA of the Variants 4a and 4b, the cross section at the middle of the load area at the middle of the elongated component is shown

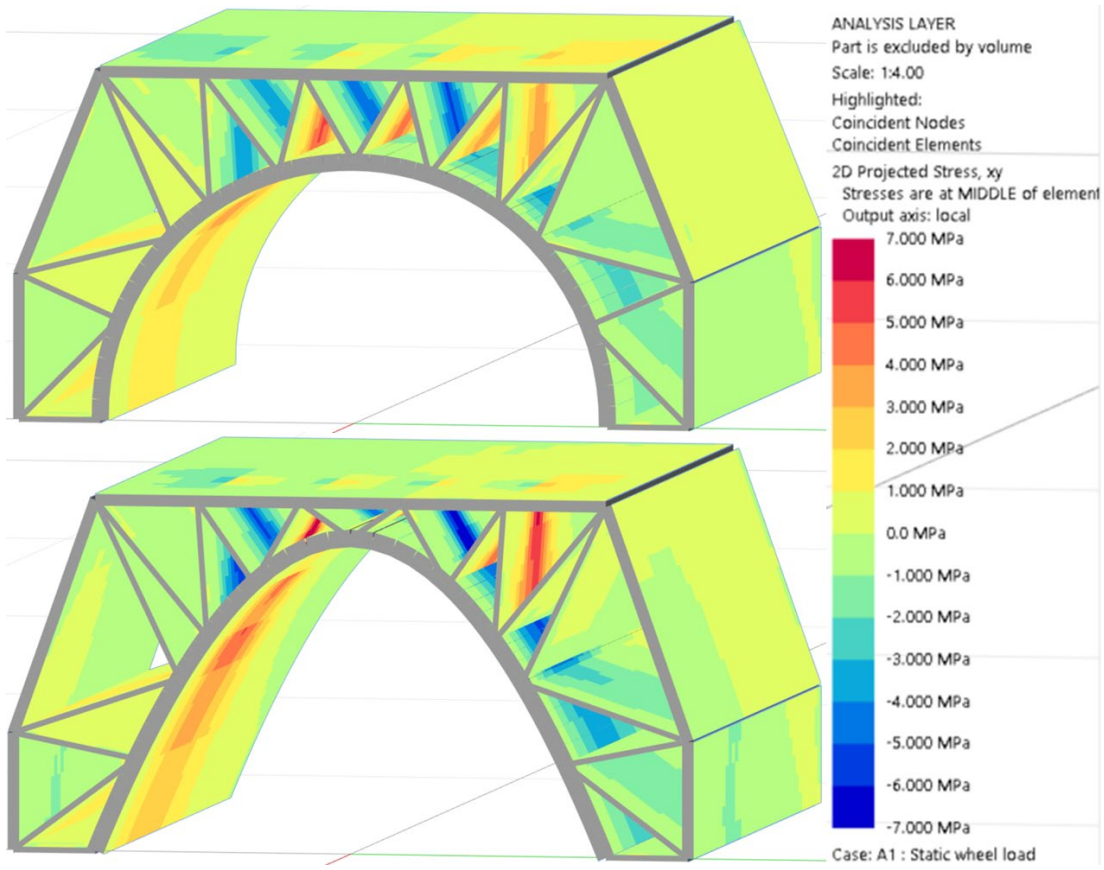

Figure 9-6 Shear stresses at mid-plane from the FEA of Variants 4a and 4b, the cross section at the middle of the load area at the middle of the elongated component is shown

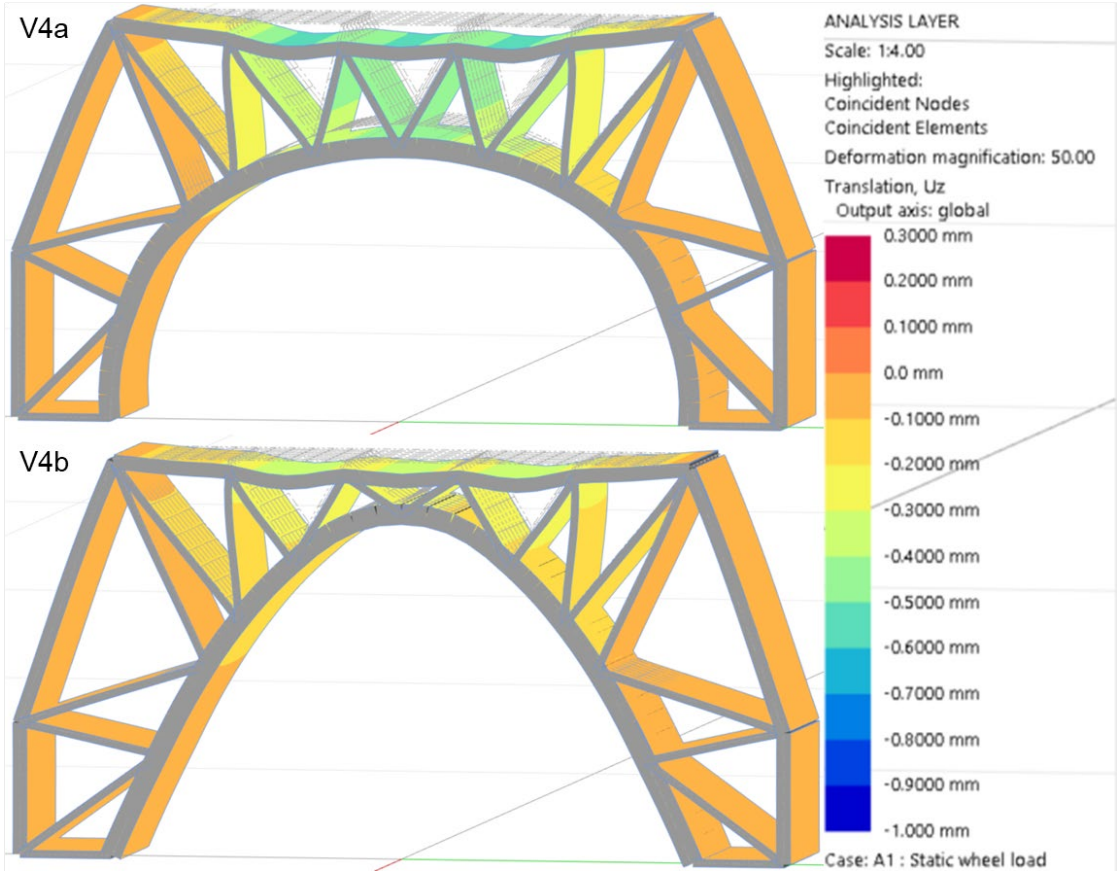

Figure 9-7 Deformed shapes of the Variants 4a and 4b of with a magnification factor of 50 with a contour of the global vertical deflection

9.1.3 Final design to be printed

One can say the option with the parabolic arch is performing slightly better from a structural point of view. However, both options suffice each design check very well. Moreover, this analysis is done with the load area located in the middle over a width of 400 mm. When the load will be placed more at the side, for example half of the top plate will be loaded from the side to the middle, the circular shaped arch option performs slightly better. So, both options for the arch will be a suitable final design from the structural point of view. From the printing feasibility point of view, Variant 4a is preferable. Therefore, Variant 4a will be the final design of the bridge deck component. This design will be printed and tested. The final design is shown in Figure 9-8 with the direction of the print drawn in the beads. How the design of the print path is delivered to the printer is shown in Figure 9-9.

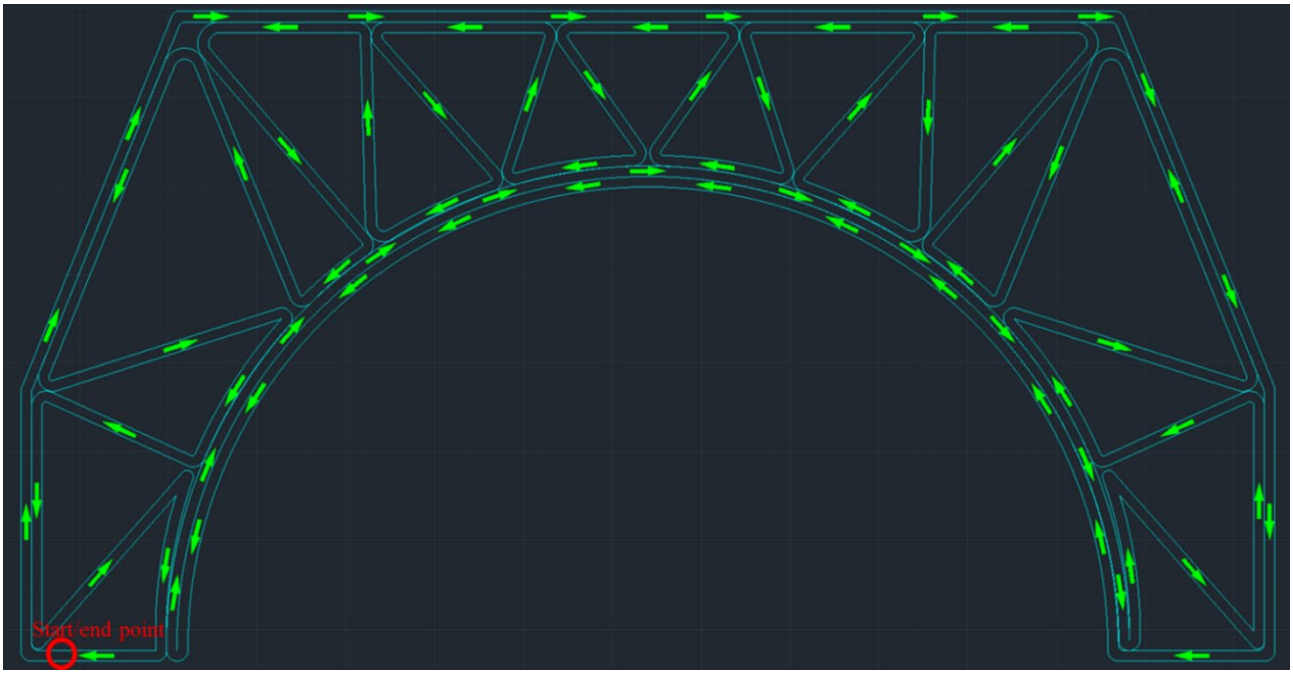

Figure 9-8 Print path of the final design of the bridge deck component

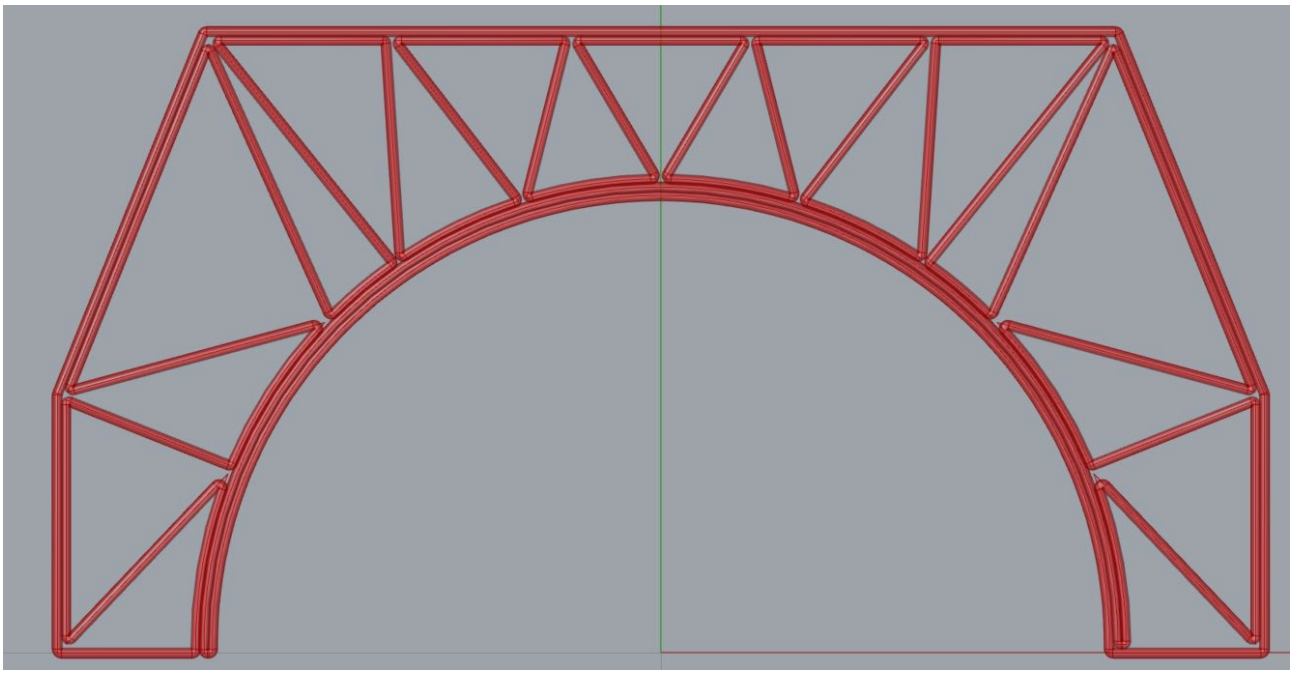

Figure 9-9 Final design of the print path in the model delivered to the printer

9.2 Printing of final design component

The final design is delivered to the 3D printing partner to print two components. In the model of the print path of the final design, an overlap of the beads should be taken into account. HB3D applies an overlap of 20% of the bead width as a rule of thumb. The bead dimensions are set the same as for the boxes, so a bead width of 6.0 mm and a bead thickness of 2.5 mm, see Figure 9-10. The reason for this overlap is to ensure that the beads will fuse well to have sufficient connectivity. This principle yields for both the parallel parts as the corners of the infill where the stiffeners come together. Due to the rounded shape of those corners, it is very likely that a small gap occurs in the print. This effect should be minimized.

Figure 9-10 Print settings of the bead dimensions (left), the ambient conditions during printing of the two bridge deck components (middle) and the temperatures in the extrusion arm of the printer (right)

Because the overlap is adjusted manually in the model, a trial print was made to check whether the fusion was sufficient. Based on this trial print, small adjustments were done to bring the corners of the infill a bit closer to each other. So, for the first printed element, the connectivity was already quite better. After the first one was finished, some small adjustments were made again to improve the fusion slightly more. These were small adjustments in terms of moving the intersection points of two stiffeners coming together at the arch 0.5 – 1.0 mm closer to each other. The final print of the first element is given in the upper picture in Figure 9-11, and the first printed layer of the second element in the lower picture. The difference is minor and due to cooling of the extruded material, the gap in the corners between the stiffeners does increase a small bit.

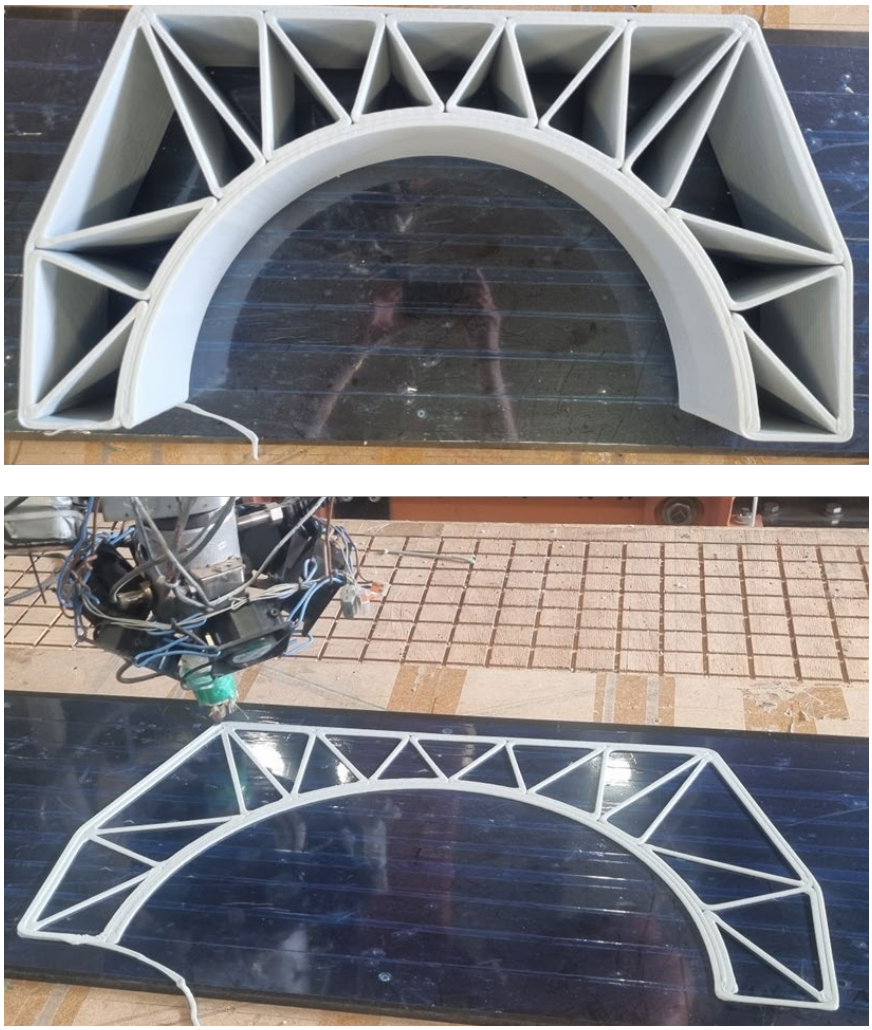

Figure 9-11 The final print of the first element with small openings at the corners between the stiffeners (upper picture) and the first layer of the second element with the gap slightly smaller

Except the print path, the printing process of the elements is comparable with the printing process of the boxes. The layers are extruded with a layer time of 80 seconds and stacked vertically. Some pictures of the printing process are shown in Figure 9-12.

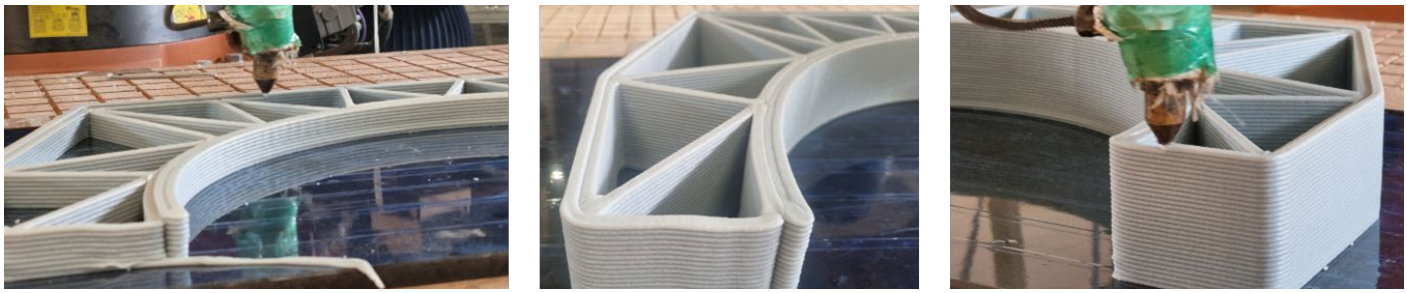

Figure 9-12 Printing process by extrusion layer by layer of the arch elements

The other difference, besides the print path layout, is the ambient temperature during printing of the arch elements and the boxes. In Figure 9-10, information of the temperatures during the printing process is also provided. The ambient temperature during printing of the boxes was around 15-16°C and during printing of the arch elements it ranges between 25°C and 28°C. However, in both circumstances, the differences between the ambient temperature and the temperature at which the material is extruded, is still comparable. The temperatures in the extrusion arm of the robot are in both cases similar. The extrusion temperature of the boxes was 237°C and of the arch elements 238°C. So, the impact of the different ambient temperatures is relatively small, since the difference in ambient and extrusion temperature is governing for the bonding of the layers and the difference in that temperature delta is small for printing of the boxes and arch elements.

Before the printed element was tested, a 3D scan of the components was made, see Figure 9-13. The white dots are stickers that are required for scanning so the camera can recognise the surface. Due to poor converting quality, the software was not able to convert the scan into the model perfectly. The purpose of this was to check the differences between the actual print and the model. These differences can be seen in Figure 9-14. The small gaps in the corners are not the same of the print path model and the actual print. The corners of the printed element are not as sharp as in the print path model. Also, the actual print differs from the model used for the FEA because of the simplifications in this analysis.

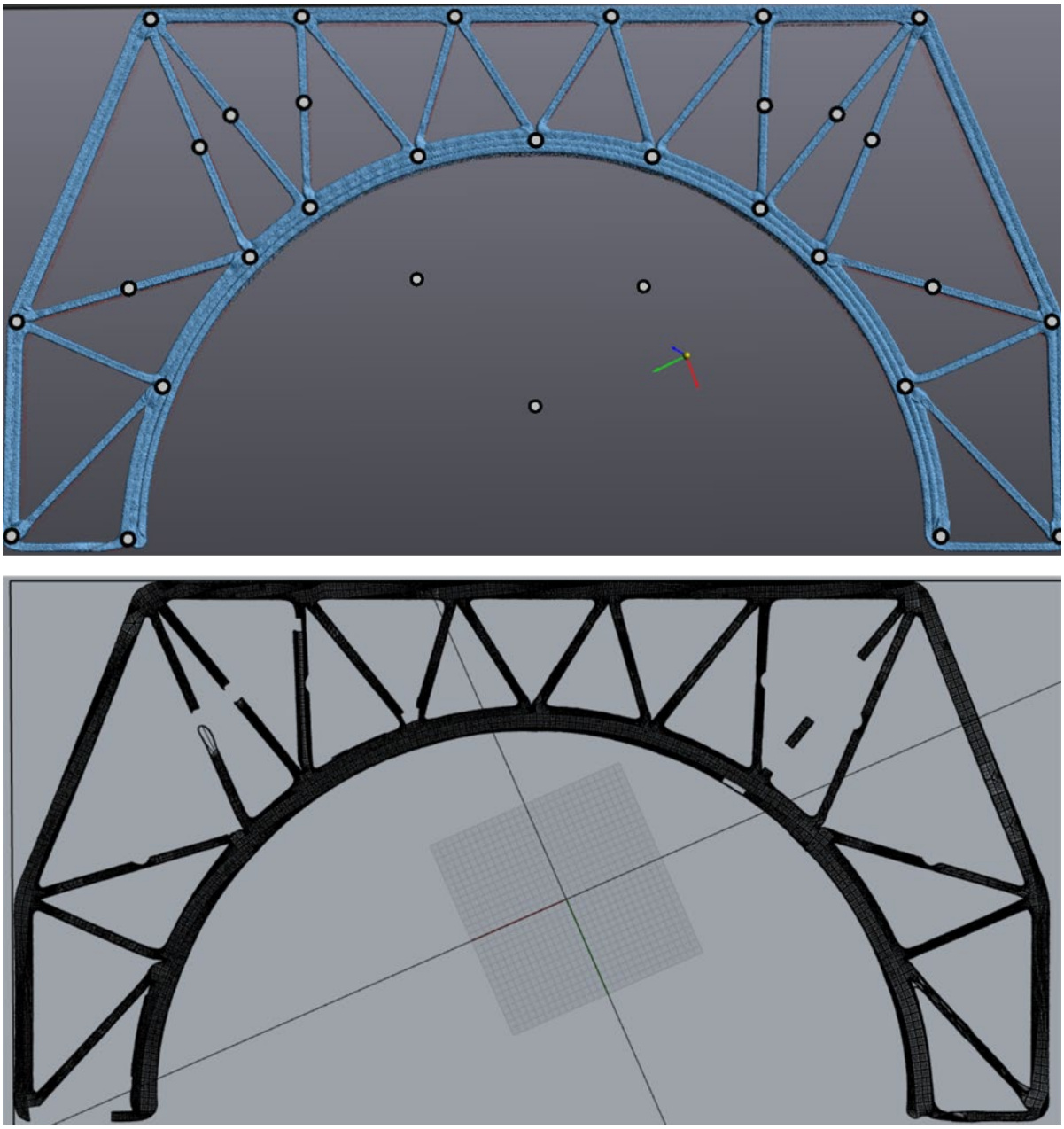

Figure 9-13 3D scan of the printed arch element (number 2) in the upper picture. The lower picture is the scan converted to model software

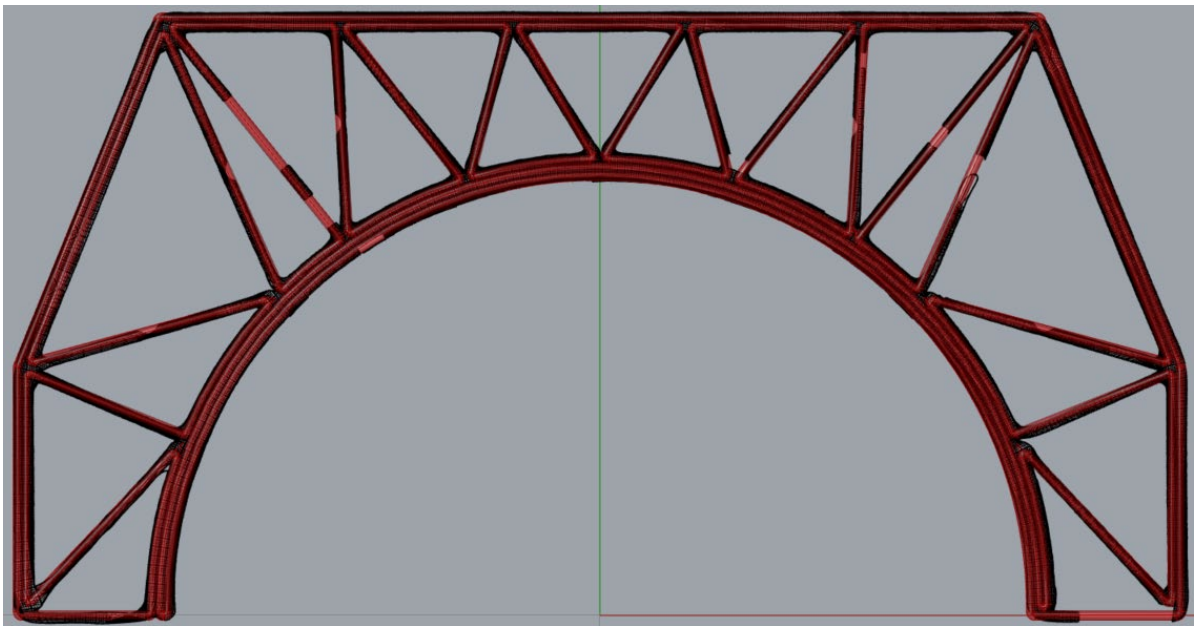

Figure 9-14 Overlay of the model of the print path (red) and the model of the scan of the printed element (black)

9.3 Component testing

The printed arch component will be tested. The goal of this test is to check whether the element withstands an (equivalent) wheel load, what the failure mechanism is, and how accurate the results from the FEA are. However, the expectation is that the FEA gives an overestimation since the model is a bit simplified without considering the eccentric connections and multi-layered buildup. Since the deflections in the FEM are quite small, the initial test speed will be set low. The test is displacement driven. During the test, the speed could be increased when the force increases too slow.

The component will be tested like the component is placed in between the stringers. At the bottom, the component will be supported with L-shaped supports. So, besides the vertical supports at the bottom plates of the component, the component will be supported horizontally over the height of the straight side part. There will be no lateral supports at the top. As with the models of the design variants, the load will be applied in the middle of the component over a width of 400 mm with the test.

In Figure 9-15, the arch component is put in the test set-up and the camera is installed for the DIC measurements. Digital Image Correlation (DIC) is used because it is not sure where failure will occur, so each point of the component can be observed. However, due to the test set-up, the straight side plates did not fit in the view of the camera. According to the FEA, it is not likely that failure will occur in this part, so it should not be an issue.

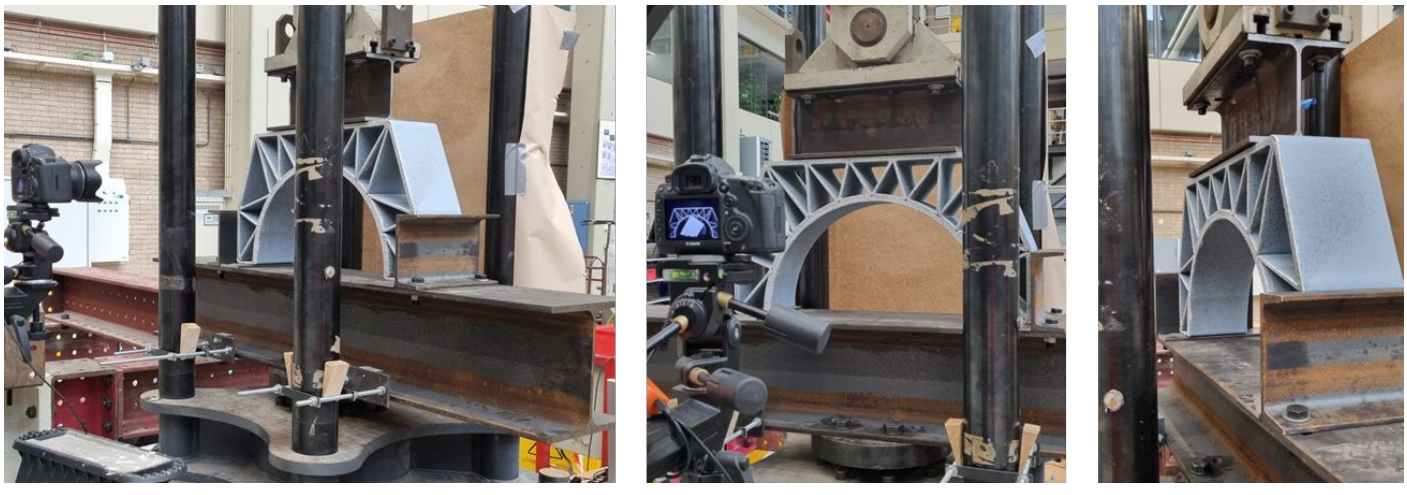

Figure 9-15 Arch component in the test set-up for the simulation of a wheel load with camera and the painted side for DIC measurements

In Section 8.4.2, the area load values of a wheel load from LM1 and LM2 were calculated. The area load from LM2 was higher, so LM2 is considered as the governing required load level for the tests. Since the element is not printed as long as a real component, the applied load will be an equivalent load. Dependent on the amount of material available, the depth of the element is set on 150 mm. Since the plate used to simulate the wheel load is 400 m wide and 160 mm depth, the load will be applied over a surface area of 400 × 150 mm^2, which lead to the following equivalent wheel load (Equation (9-1)):

$$\frac{200\ \text{kN}}{600 * 350\ \text{mm}^2} * (400 * 150\ \text{mm}^2) = 57.1\ \text{kN} \tag{9-1}$$

Besides the DIC measurements, the force and the displacement of the jack were measured by the machine. The results are plotted in a force-displacement diagram in Figure 9-16. As can be seen, both arch components showed similar behaviour. The first drop in force level, the force-displacement development, and the ultimate load level are comparable. Both components have drops in their load level and increase again afterwards. This indicates that cracks occurred and propagated during the tests and that the component finds an alternative way to distribute the forces. Therefore, the force could pick up again. At the first drop, the first crack initiated, and the load level was around 65.6 kN, which was already above the required load level of the equivalent wheel load. When the force increased further, a maximum load level was reached around 92.7 kN. This is about a factor 1.6 times the minimum required load level of the equivalent wheel load. After this maximum was reached, crack developed further. This resulted in a force-displacement behaviour with drops and increments. The first moment that the force become below the 57 kN limit was for Arch 2 when the displacement was 12.5 mm. For Arch 1, this was even at a displacement of 15.7 mm. In the end, the test was stopped. The force did not pick up again, failure was clearly observed, and the displacement was sufficiently large. So, the components did not have collapsing failure.

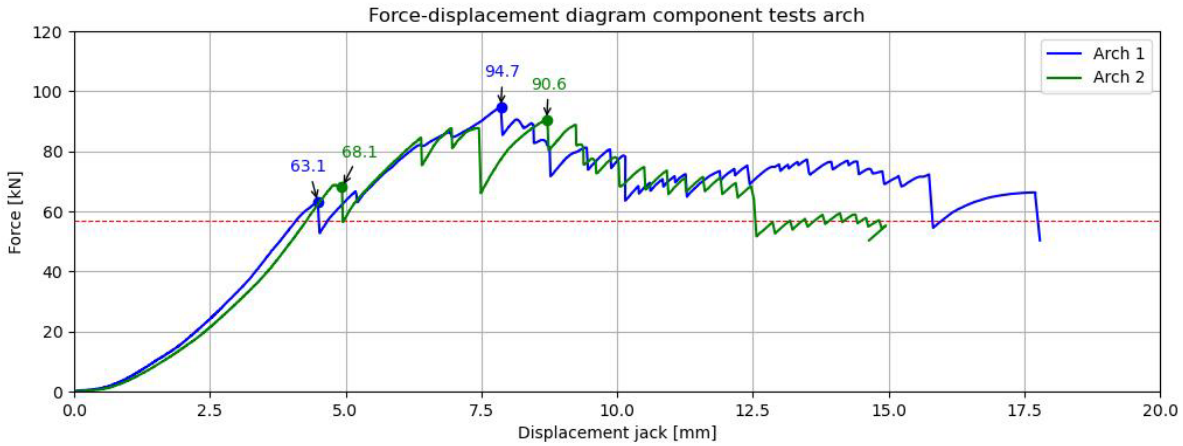

Figure 9-16 Force-displacement diagram of the arch component tests with the 57 kN limit indicated with the red line

From the DIC measurements, pictures are made of the side of component with the DIC paint on it. From this pattern, the software could translate this pattern from the pictures in a plane from which strains, displacements, and cracks could be derived. The translation from picture to surface component in the software is shown in Figure 9-17.

Figure 9-17 Picture from the DIC measurement converted to a surface component plane in the software

From the analysis of this surface component in the software, the point of the force drops, and the crack development could be indicated. For the component test of arch 1, the failure mechanism is elaborated in Figure 9-18. The first crack occurred at the intersection between the vertical stiffener in compression and the arch at the right. This crack developed and at the maximum load level, a similar crack is initiated on the same position on the left. From here, the force is decreasing, as another crack is initiated at the right half next to the first crack at the intersection between stiffener and arch to the right. The two cracks at the right propagated further in a way that the stiffeners and the arch do not interact anymore.

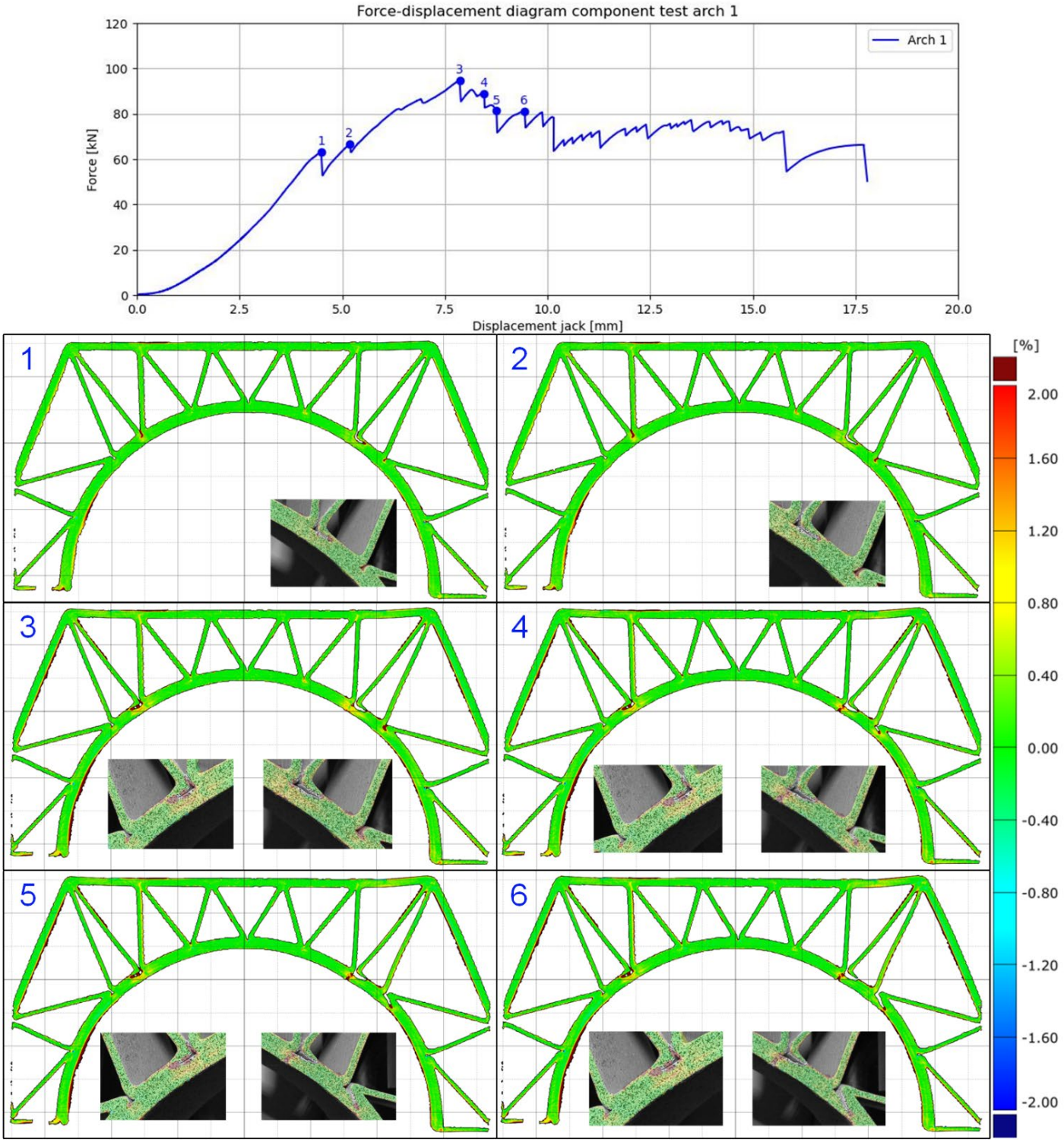

Figure 9-18 Failure mechanism of tested component arch 1 with the crack development over six different points along the force-displacement graph

The failure mechanism of the second arch component is similar as the first one, see Figure 9-19. The first crack initiated also at the intersection between the vertical compression stiffener and the arch at the right, corresponding to the first drop in force-displacement graph. As with the first component, a similar crack occurs at the left at the same position. At the largest force drop, at point 4, a similar crack is occurred at the left. When the maximum load level is reached, especially the crack at the left is propagated further, almost until the next intersection between arch and stiffener. On the right half, an extra crack is initiated in a similar way as for the first component.

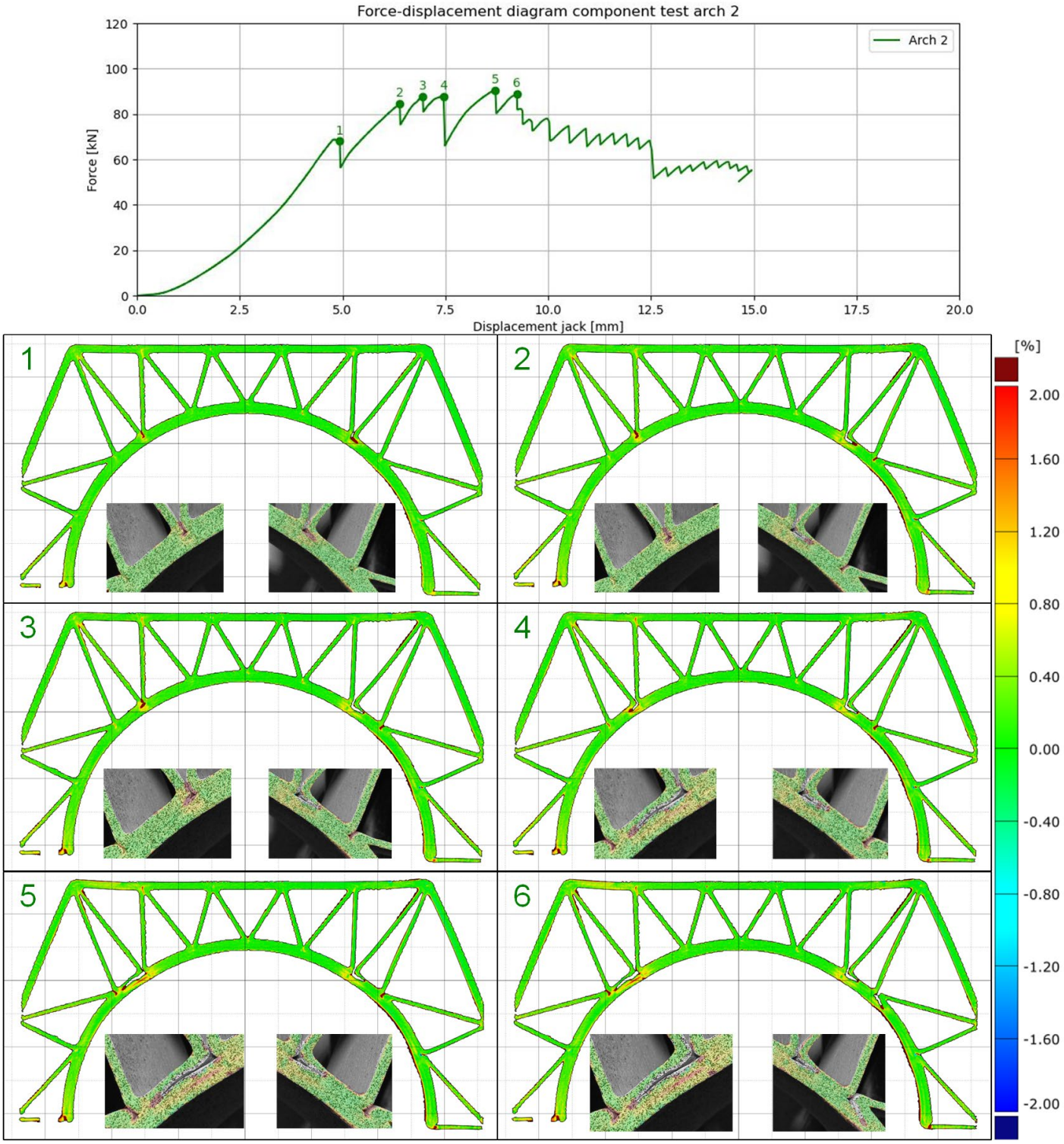

Figure 9-19 Failure mechanism of tested component arch 2 with the crack development over six different points along the force-displacement graph

As could be observed in the force-displacement diagram from the results of the component tests in Figure 9-16, the loss of resistance is limited. Cracks initiate and propagate, but still the force remains on a certain level. This is typical for fracture mechanics behaviour. In this case mode 1 behaviour since the cracks are opening and growing on the plane of tensile stress. This in combination with debonding of the print layers. The crack initiation and growth until the maximum load level are elaborated by the DIC analysis (Figure 9-18 and Figure 9-19). After the maximum load level was reached, the cracks did propagate further. There was no collapse of the element. They deflected further and at a certain point the test was stopped. The beginning and final state of the tests of the two elements are presented in Figure 9-20 and Figure 9-21, respectively.

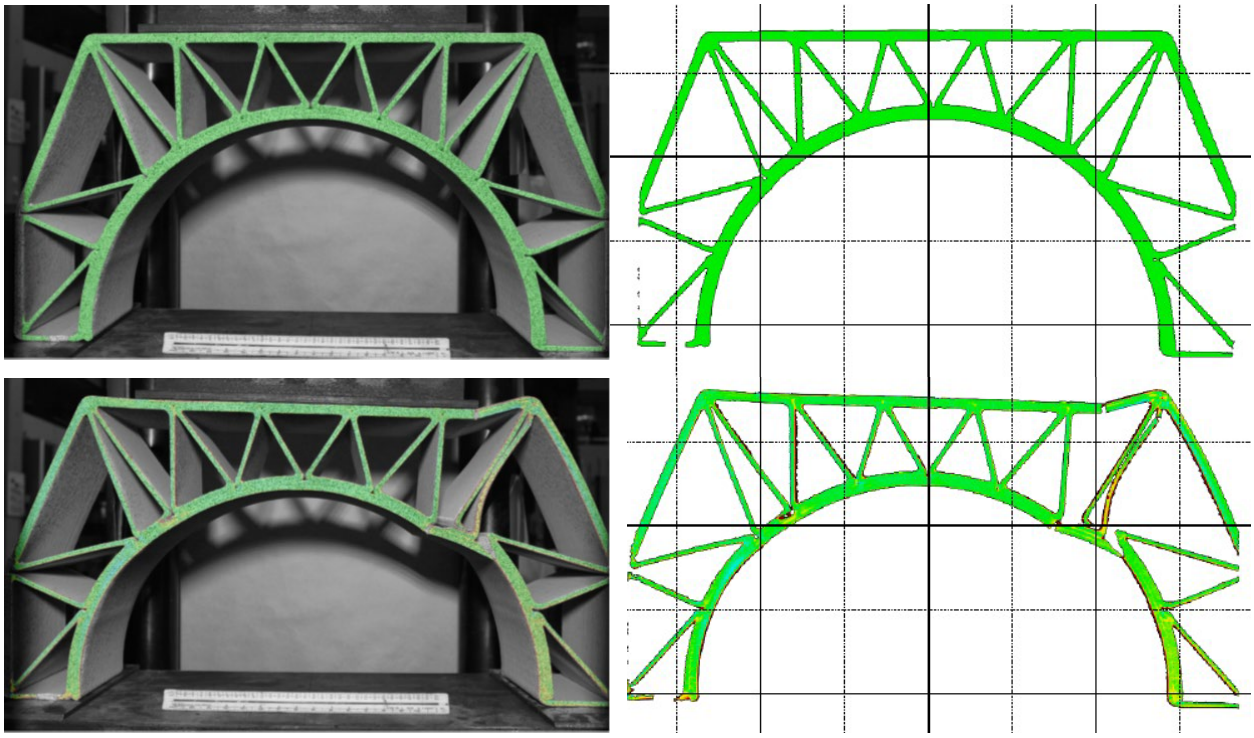

Figure 9-20 Beginning (above) and final (below) test state of arch component 1

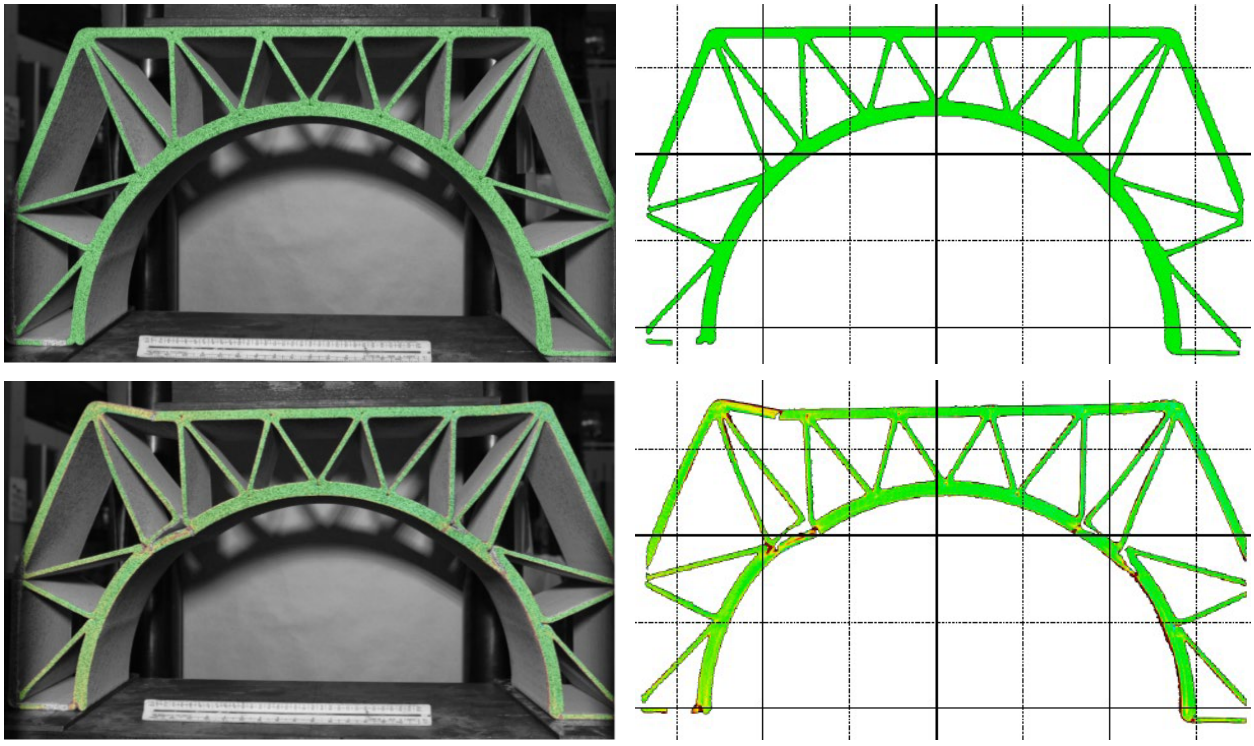

Figure 9-21 Beginning (above) and final (below) test stage of arch component 2

The tests showed that the designed bridge deck component can withstand a wheel load and that the two components have similar and consistent behaviour. Failure occurred in the connection between the stiffeners and the arch. When the first crack was initiated at this location, the load level was above the minimum required load level of the equivalent wheel load. To be more precise, this first crack occurred in the connection between the arch and the top corner stiffener in tension above the almost vertical compression stiffener. After this first crack initiation, cracks propagated, and the force increased further. So, there was an alternative way to distribute the forces. The stiffeners next to the stiffener that was losing connectivity with the arch due to crack development, is also in tension, according to the FEA. This could clarify the alternative force distribution. The maximum force reached was about a factor 1.6 higher compared to the minimum required equivalent wheel load. After the maximum force was reached, the load level stayed above the required minimum while the displacement still increased further. So, cracks were propagating but the force did not drop massively. After small drops, due to developed cracks, the force still picked up and no collapsing failure happened. The non-collapse failure in combination with the consistent behaviour and the ability to withstand a wheel load makes this design suitable for application in bridge decks.

When it will be applied in bridge decks, attention should be paid to the support conditions. In the test set-up, the component was supported both at the bottom and at the sides. These supports were perfectly attached to the component, so there were minimum openings and margins. Since the strain at failure is not that high for this material, opening margins for the supports should be avoided as much as possible. When there are some opening margins, the component will deform before it transfers the force when load is applied. As this deformation introduces additional strains and the strain at failure is relatively low, according to the results of the second stage of coupon testing, the resistance of the bridge deck element will be lower. When the girders, between which the element will be assembled, are too close to each other, the component will be compressed, and additional initial stresses are introduced. This will also decrease the capacity of the component because extra stresses besides the wheel load have to be carried. Therefore, the tolerances of the support conditions for assembly are limited.

Part IV:
Research Outcome

10

Discussion

During this research, there were some simplifications and assumptions. Some of them are already elaborated with the presentation of the results. In this Chapter, an overview of the points of attention is provided regarding the assumptions, simplifications, and limitations.

10.1 Printing

The 3D printing process consists of melting, extruding, and hardening of the material. This process is done layer by layer. Because the material cools down, after extrusion, the difference in temperature with the next layer printed on top increases when it takes longer before the next layer is extruded. This phenomenon is translated in the layer time. The longer it takes, the weaker the bonding between the layers will be, the lower the strength in transverse direction will be. To ensure a certain strength in transverse direction, the maximum layer time was tested and set on 80 seconds. This 80 s is the upper limit to ensure that the bonding between the beads is still sufficient.

Although the difference in temperature between the beads is governing for the bond strength, the limit is set in terms of time. However, besides the cooling rate of material, the design of the print path has an influence on the speed of cooling down, and thus the temperature difference between the beads. For the coupon test series, the material was printed in a box shape, which contained a large opening in the middle. Because of that, the material cooled down relatively quick because the material was surrounded by a lot of (cool) air. When the bridge deck elements were printed, the openings in the component are much smaller and the print path is designed denser so that the layers are closer to each other. Because the material is hot when extruded, the surrounding air will be warmer. The openings in the component are smaller, so there is more heat accumulation. Due to this, the ambient temperature is higher, so the material cools down slower. Therefore, the layer time could be longer in this case, without having a loss in bonding strength.

The longer the layer time can be the slower the printer can move. This improves the quality of the extrusion so the print will be neater. In a next phase, a heat camera could be used to investigate the temperatures and the cooling rates of the material. In this way, the most optimal combination of print speed, and adhesion between the layers could be achieved.

10.2 Testing

Regarding the tensile tests, in both directions, the strain at failure is low. Therefore, one can conclude that the material has a brittle failure mechanism. This could be unfavourable because the material does not show plastic deformation that much, that a ‘warning’ of the material could be observed. It is desirable to have in a structure that cracks or deformations could be observed before the material fails. However, during the component tests, cracks occurred without having collapse failure of the whole elements. The structure found an alternative way to distribute the forces. Due to this, the brittleness of the material could be less an issue.

During the first and the second stage of coupon testing, tensile test in transverse direction were performed. As discussed, there was a difference between the results from the transverse tensile tests in the first stage and second stage of coupon testing. This difference could be caused by several factors: moisture content of the material, ambient temperature during printing, quality of the material compounds, or printing quality in general. In addition to this, there could be another factor that may have an effect. The coupon of the second stage of coupon testing were cut by a water jetting machine that was less precise than the machine that cut the coupon for the first stage. Due to availability, the second stage coupon had to be cut on a larger and heavier machine. Because of this, the straight part in the middle of the tensile coupons was less precise. So, this part became pointier, as is followed the tapered shape. However, this was also the case for the longitudinal tensile coupons, and those did not seem to be affected by this less accurate shape. The results of the first and second stage of coupon testing were quite similar.

Another point to notice regarding the tensile tests in transverse direction is the possible maximum strength. In the second stage of coupon testing, a characteristic strength of 16.8 MPa is determined. However, the layer time set for this material is 80 seconds. If the layer time could be shorter, it could be that the bond strength, and thus the strength perpendicular to the print direction, increases. To check what could be the maximum capacity, one should investigate unreinforced PETG. However, because of the use of additives and glass fibres, the maximum strength of raw PETG will not be the maximum achievable transverse strength for this material. From discussions and evaluation with the material supplier and the print partner, it is likely that there is not much more capacity in the material. So, with a layer time of 80 seconds the material is already close to its maximum transverse strength. On the other hand, the layer time should not be minimized since there is also a minimum required layer time. The previously printed layer should be hardened enough before the next layer is printed on top. If it is not hardened enough, it could not support the next layer and the beads would sag.

The compression tests contained the risk that the coupon did not fail in compression, but that buckling was the governing failure mode. For the longitudinal compression tests, the coupon failed in compression, since the first cracks occurred in the compression zone. Unfortunately, the compression coupon in transverse direction had the buckling failure mode. Because of this, the measured maximum stress was not the actual capacity of the material in transverse compression. Due to the ribbed shape also, local stress concentrations could be introduced. This could make it more likely that cracks initiate in the tensile zones. Because cracks occurred in the tensile zones, imperfections were introduced, which lead to buckling of the coupon. Despite this behaviour, the stress at which the transverse compression coupon failed is still on sufficient level and much higher than the transverse tensile strength.

Lastly a note regarding the IBSS tests. The strains in the coupon are measured by an extensometer during the tests. However, these strains are measured over a longer distance than the overlap part of coupon. The overlap part, the part between the cuts, is deforming in shear and the part outside the cuts is deforming in tension. Because of this, the strain measured is partially tensile strain and partially shear strain. However, because the load level was still quite low, it is likely the contribution of shear strain is more than tensile strain. The longitudinal strain at the load level of failure of the IBSS coupon is low, according to the longitudinal tensile test results.

10.3 Design

The final design is made based on the FEAs of the three variants. The models of these variants were a bit simplified because the corners and intersections are better aligned, so less eccentrical, than the actual print path. In printed element, the centrelines of two stiffeners interacting with the top plate or the arch, intersect with the centreline of the inner bead of the top plate or arch, while in the model those stiffener centrelines intersect with the centrelines of the whole double layer of the top plate or triple layer of the arch. The corners are also not perfectly identical in the printed element, while this is the case in the model. Due to the print path, the connectivity in the corners is different. The corners cannot be as printed as sharp and straight as in the model because of extrusion of the material is not perfectly similar as the model. The print speed and heat accumulation at the corners make that the extruded bead tends to pull to the inside due to the fibres in the material. This effect causes small gaps in the corners at the intersections of the stiffeners with the top plate or arch, which are not present in the FEA model. The differences between the FEM, the print path model, 3D scan of the printed element, and model of the 3D scan are shown in Figure 10-1. The FEM and the 3D scan

of the printed element are laid on top of each other in Figure 10-2. It can be seen the model and the scan to not perfectly align with each other.

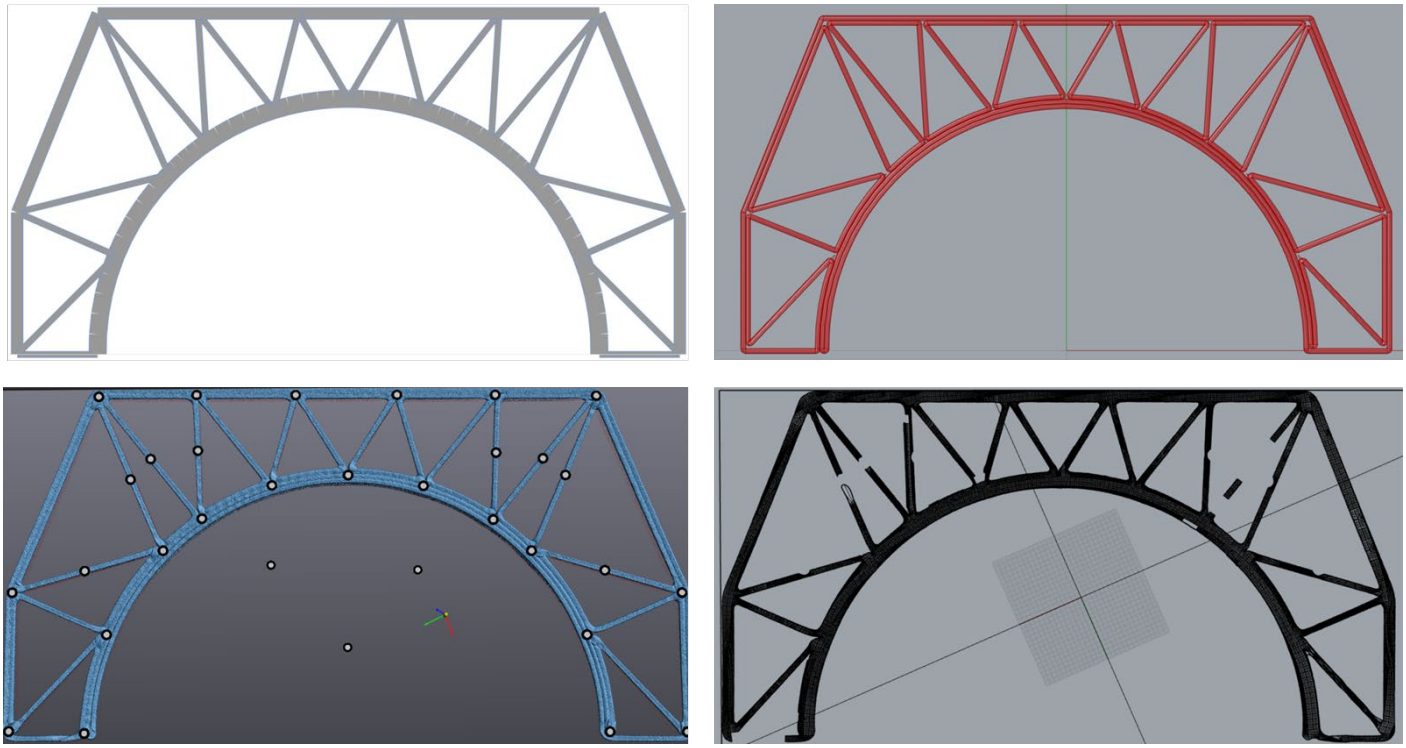

Figure 10-1 The simplified model for the FEA (upper left); the print path model as input for the printer (upper right); the 3D scan of the printed element (lower left); and the model converted from the scan in the same software as the print path model (lower right)

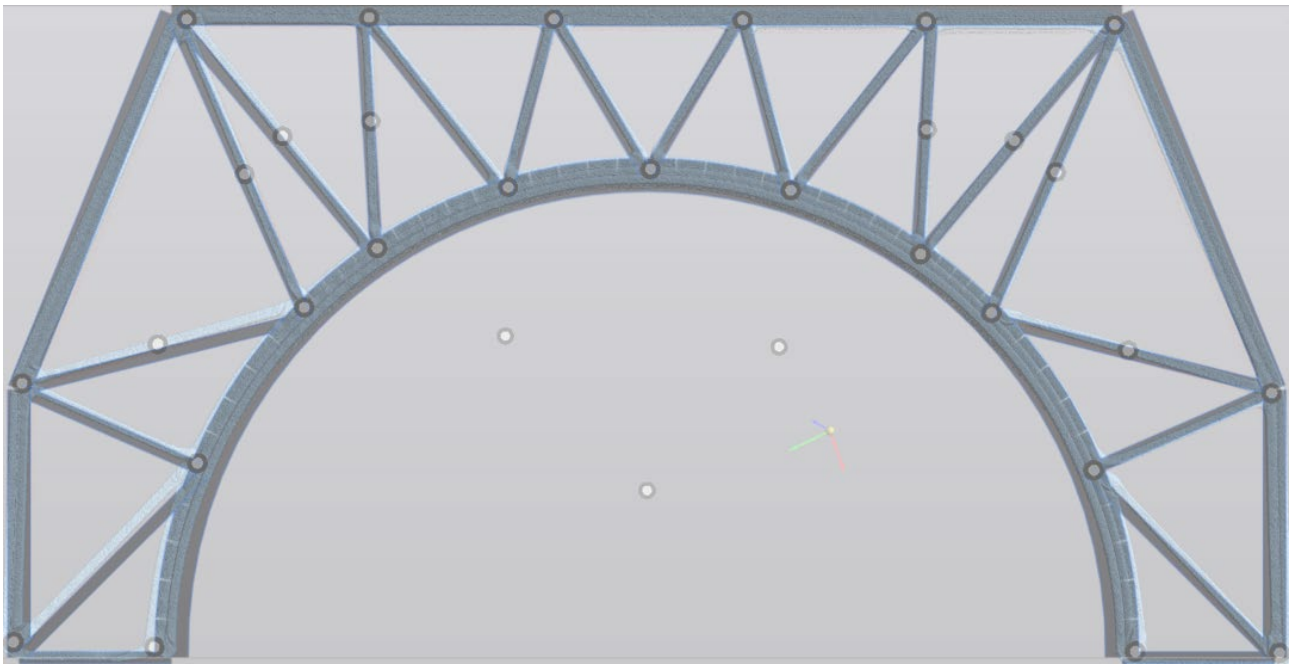

Figure 10-2 The FEM (grey) and the 3D scan (blue) laid on top of each other

11

Conclusions and Recommendations

Based on the results from the tests and the modelling, the research questions can be answered. These conclusions are drawn in this Chapter. These conclusions lead to recommendations on how to continue in this research field and what should be the next step in the development of the integration of 3D printed FRP in bridge engineering.

11.1 Answers to research questions

The first research question could be answered based on the results from the first stage of coupon testing. The optimal configuration in terms of fibre volume fraction (V_f) and layer time of printing had to be determined. Considering 30% and 45% for the V_f, and 80, 100, and 120 seconds for the maximum layer time, the following conclusion are derived from the test results:

- Continue with GF45%. Significantly more structural performance in the principal direction is obtained without being more brittle compared to GF30%. The GF45% material had an ultimate principal tensile strength of 102.1 MPa, while the ultimate principal tensile strength of the GF30% was 71.3 MPa, considering the original unpolished coupons. The stiffness in principal direction for GF45% is 22,040 N/mm^2 against 13,920 N/mm^2 for GF30%.
- When printed under normal conditions (room/industrial hall temperature), the maximum layer time should be 80 seconds. After 80 s, significant loss in structural performance of the bonding between the printed layers. This was shown by results from the tensile test in transverse direction. The ultimate tensile strength perpendicular to the print direction was with 80 s layer time 20.4 MPa and 19.7 MPa for GF30% and GF45% respectively. As expected, the difference in strength perpendicular to the print direction is minor for the two different V_f's, due to the orientation of the fibres in longitudinal direction. When the layer time was increased to 100s and 120s, the transverse tensile strength decreased significantly. The ultimate tensile strength for these layer times was 8.7 MPa and 7.7 MPa, respectively.

So, the research proceeded with the V_f = 45% and 80s layer time configuration.

Besides the V_f and the maximum layer time, the influence of the ribbed surface was investigated in the first stage of coupon testing. Due to the ribbed surface, local stress concentrations could occur which could cause earlier failure. As expected, stress at failure of the coupon in longitudinal direction is similar: 71.3 MPa for unpolished and 70.2 MPa for polished (both GF30%). The ribs are in the same direction as the direction of testing. Thus, the cross section is not changing of the length of the coupon in the direction of the applied load. However, this is the case for the coupons in transverse direction. The ultimate tensile strength of the polished coupon was slightly higher compared to the unpolished ones. For the GF30% the ultimate tensile strengths were 20.4 MPa for unpolished and 22.2 MPa for polished. The effect of the ribbed surface for the GF45% coupons was even bigger, concerning an ultimate tensile strength of 19.7 MPa for the unpolished coupons and 24.1 MPa for the polished coupons. However, when this material will be applied on a larger scale, it will not be feasible to polish all elements.

As concluded, the research continued with the GF45% material printed with a layer time of 80 seconds. To be able to make a design for a bridge deck element, the mechanical properties of the material are required to analyse the structural behaviour. During the second stage of coupon testing, several types of tests were performed to determine the strength and stiffness values of the tensile behaviour parallel and perpendicular to the direction of printing, the compressive behaviour parallel and perpendicular to the direction of printing, and the shear behaviour between the print layers (beads).The values of these properties established by testing, are presented in Table 11-1.

Table 11-1 Mechanical properties derived from the tensile tests in longitudinal and transverse direction, the compression tests in longitudinal and transverse direction, and the IBSS tests

Property	Characteristic strength value	Stiffness value
Tensile principal direction	$\sigma_{1,tk}$ = 93.8 MPa	$E_{1,t}$ = 21,430 N/mm^2
Tensile transverse direction	$\sigma_{2,tk}$ = 16.8 MPa	$E_{2,t}$ = 5,650 N/mm^2
Compression principal direction	$\sigma_{1,ck}$ = 93.5 MPa	$E_{1,c}$ = 8,010 N/mm^2
Compression transverse direction	$\sigma_{2,ck}$ = 29.8 MPa	$E_{2,c}$ = 2,380 N/mm^2
IBSS	$\tau_{21,k}$ = 11.6 MPa	G_{21} = 3,200 N/mm^2

With the mechanical properties of the material known, the focus was set on the design of bridge deck element. From a previous study, an arch shaped component to place in between the stringers in a bridge deck was already designed. Three design variants were made to optimize this preliminary design. Variations were made in the design of the infill, the way of printing with the same or a different start/end point, and additional layer(s) along the outside via the top plate or the inner arch. From an analysis of the three variants based on printing feasibility and structural performance (FEM), it turned out that a combination of variants 1 and 3 led to the final design. This design flow is visualized in Figure 11-1. For the final design, also a parabolic shape for the arch was considered. However, the circular shape was preferable from a printability point of view. From a structural point of view, the differences in behaviour were minor.

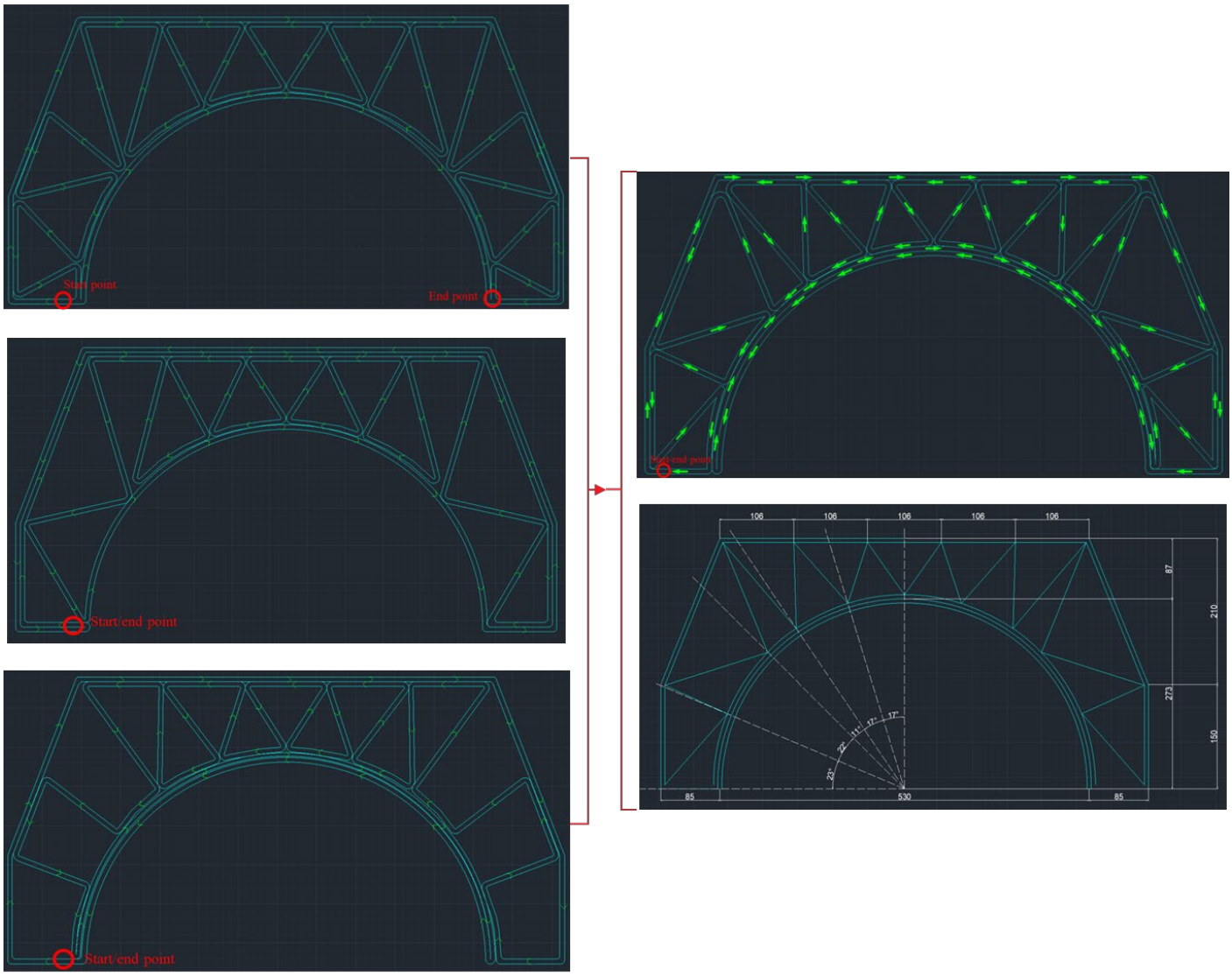

Figure 11-1 Design flow of the bridge deck element. The final design is based on a combination of variants 1 and 3

The shape of the component for the strengthening application is derived from the final design. This is converted to a print path design. Following this print path, the final design is printed according to the configuration determined before. The printed element of the design is presented in Figure 11-2. Two components of the design are printed and tested. From the tests can be concluded that the two components have similar behaviour and are able to carry a wheel load. The first cracks occur at a load level higher than the minimum required load level. After this initiation, cracks propagated but the force increased even further to a maximum of 1.6 times the equivalent wheel load. The force-displacement diagram showed some drops in the load level due to the crack development, but the force increased again. So, the component kept its load resistance by distributing the forces in an alternative way. The crack initiation and propagation by maintaining a sufficient and approximately constant load level is beneficial because there is no collapsing failure.

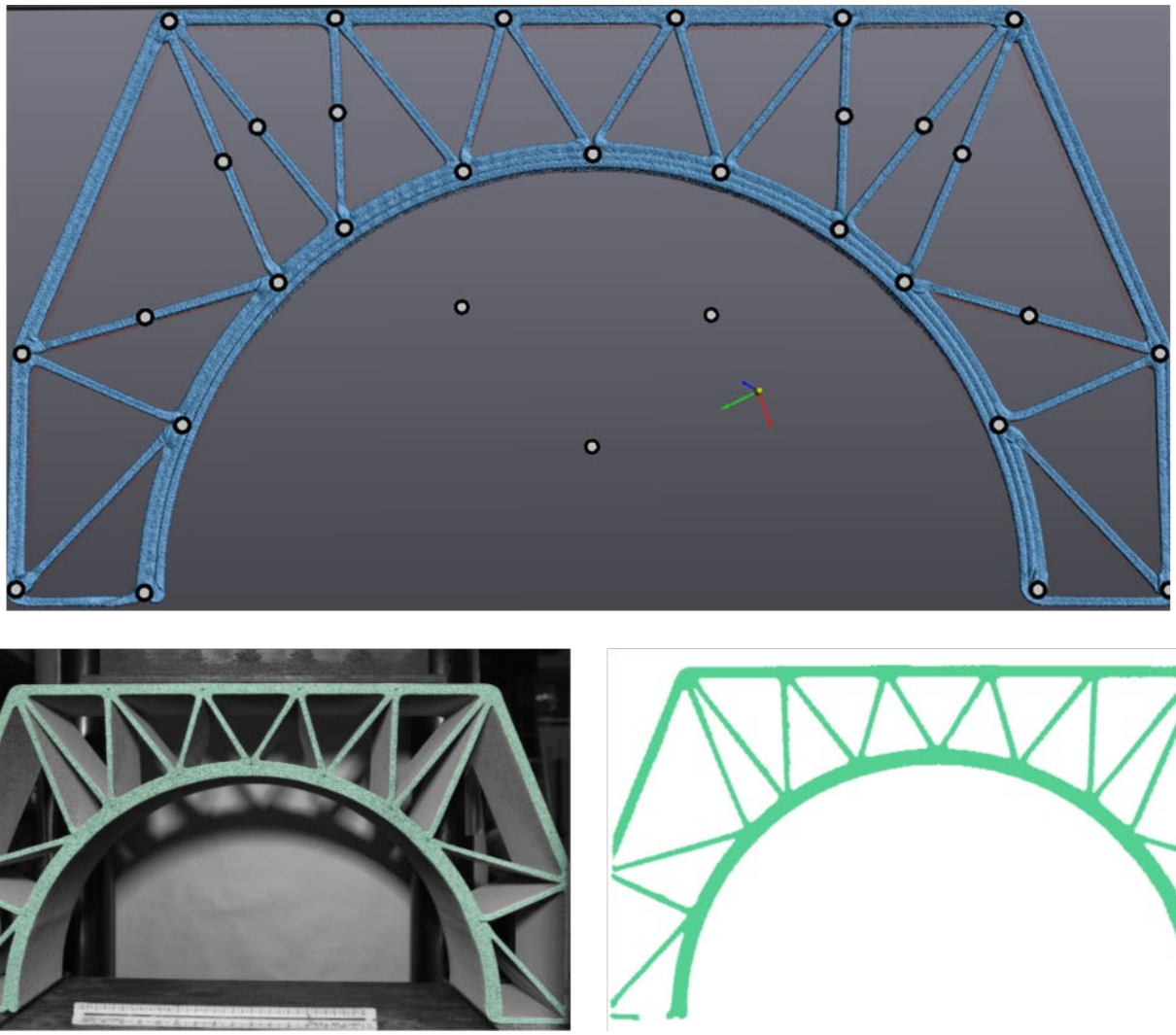

Figure 11-2 Model and shape of the printed final design with the 3D scan of the printed element above and the DIC picture with its corresponding surface component below

To answer the main research question, the answer consists of both the material and print configuration and the design of the shape of the bridge deck element. Considering the material studied in this project, a composite of recycled PETG with chopped glass fibres, one should apply a fibre volume fraction of 45%. During the 3D printing production process, the layer time should be no longer than 80 seconds. The combination of V_f = 45% and 80 s layer time leads to the best structural performance in the principal direction and perpendicular to the direction of printing.

Regarding the design of the bridge deck element, the FEA and the component test proved that the designed shape of the component is suitable for strengthening application. The component can carry a wheel load and does not collapse but warns by the crack initiation and propagation failure mode before the resistance significantly decreases. Moreover, the material is consistent, so its behaviour and performance can be accurately predicted.

This in combination with its free formability, high strength to weight ratio, modularity, and recyclability makes that 3D printed FRP is a lucrative solution for bridge decks that required strengthening. With the GF45% and 80 s layer time configuration and the shape according to the final design (Figure 11-1 and Figure 11-2), decks of movable bridge can be built or strengthened by implementation of 3D printed fibre-reinforced composite material containing a recyclable thermoplastic polymer like rPETG.

11.2 Recommendations for further research

After this research, there are still several aspects of the application of 3D printed FRP in bridge deck strengthening to be investigated. The points which should be research as follow-up of this project are listed below:

- This research is based on static analyses of the material. All coupon tests were static tests, and the component test was a static one. However, since the goal is to strengthen bridge decks with this application, the fatigue behaviour should be known. Because of the cyclic loading on a bridge, it is important that the fatigue performance of the material applied in the bridge deck structure is sufficient. According to the failure mode of the component, crack initiation and propagation following fracture mechanics mode 1, the double cantilever beam tests could be applied for the fatigue characterization.
- In addition to the fatigue behaviour, the long-term behaviour in terms of creep and shrinkage should be investigated. This will provide insight into how the material will behave after several years. From this, a prediction of the lifespan can be made. When it reaches its end of life, the material can be recycled again. However, the quality of the material after recycling for a following use stage is still unknown.
- The performed component test is a test to investigate the in-plane behaviour of the element. From the tests is concluded that the cross section of this design of the bridge deck element suffices. However, the behaviour in transverse direction should also be considered. According to the FEA, the bond strength between the layers should be sufficient to carry the wheel load in the transverse direction. Still, it will be valuable to check this by testing. In a similar way as the component tests in this research project, an elongated element could be tested to observe the behaviour in the other direction. The dimensions from the model are suitable for the test setup. So, one can have a 1.6-metres long element and a centrally applied wheel load over an area of 400 × 400 mm^2, for example.
- Although the load level at which the first crack occurred and the ultimate load level are sufficient above the required load level of the wheel load, one could investigate the possibility to improve to performance of the connection. Analysing the failure mechanism, it seemed like the stiffeners that intersect in the connection are not cooperating, since the stiffeners in the top corner was ‘pushed away’ be the stiffener next to it at the intersection at the arch. This connectivity, and thus the interaction, of the stiffeners in the corners could be improved by increasing the overlap in length direction of the beads (see Figure 11-3). Because of this adjustment, the stiffener will be less straight due to additional kinks are introduced. This will lead to an increase of local bending, which may be a challenge.

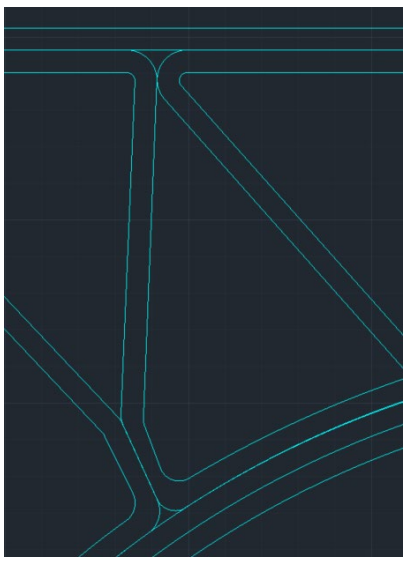

Figure 11-3 Increased overlap of the stiffeners at intersection with the arch

An alternative solution could be to combine the circular and parabolic arch shape to get an in-between design. In this way, the vertical compression stiffener will be more aligned with the arch. The force will be transferred more directly to the arch and the adjacent stiffeners has to take less force, which could make the connection less critical.

- Because this research project is purposed for strengthening of bridge decks, the practical point of view of this application should also be considered. How can this element be assembled in a suitable way? In the previous study, the arch component is placed in between the stringers of the bridge deck. However, they can only be assembled from the side. And how can they be connected to the stringers? A solution could be to apply inverted T-girders for the stringers, to be able to place the elements from the top and have the space to apply adhesive connections between the stringers and the 3D printed FRP component. To cover the openings between the arch components, a plate could be placed on top. A sketch of this idea is showed in Figure 11-4. Besides the assembly, the connections between the FRP element and the stringers should be designed. Adhesively bonded connections could be a suitable option for this.

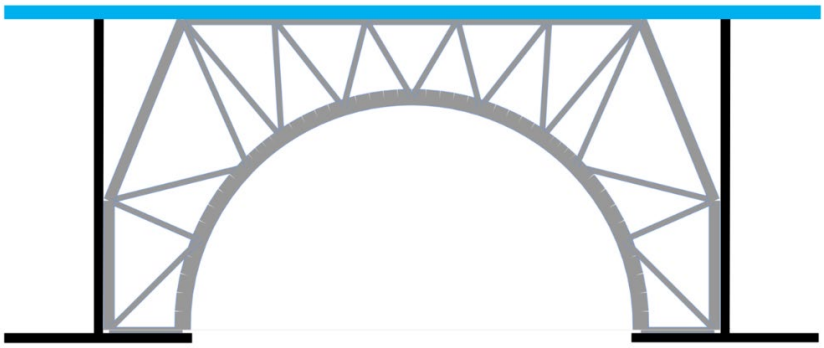

Figure 11-4 Idea to apply the arch component (grey) in between the inverted T-girders (black) with an additional plate on top (blue)

Bibliography

[1] Arup, ‘Rijkswaterstaat 3D geprint FRP brugdelen Start notitie’, Jul. 2021. [Online]. Available: www.arup.com

[2] Arup, ‘3D printed FRP bridge components Option Study and Preliminary Design Preliminary Design of application of 3D printed FRP on road bridges’, Feb. 2023.

[3] Sculpteo, ‘3D printing for construction and architecture projects: The Ultimate Guide 2022’, *3D Learning Hub 3D Printing Applications*, 2022, Accessed: Oct. 09, 2023. [Online]. Available: https://www.sculpteo.com/en/3d-learning-hub/applications-of-3d-printing/construction-and-architecture/

[4] P. G. Kossakowski and W. Wciślik, ‘Fiber-Reinforced Polymer Composites in the Construction of Bridges: Opportunities, Problems and Challenges’, *Fibers*, vol. 10, no. 4, Apr. 2022, doi: 10.3390/fib10040037.

[5] De Ingenieur, ‘Eerste brug van composiet uit de 3D-printer’, Sep. 2019, [Online]. Available: https://www.deingenieur.nl/artikel/eerste-brug-van-composiet-uit-de-3d-printer

[6] S. Goehrke, ‘Another world’s first 3D printed bridge’, *Design*, Sep. 2019, [Online]. Available: https://www.fabbaloo.com/2019/09/another-worlds-first-3d-printed-bridge

[7] De Ingenieur, ‘Europe’s biggest 3D printed unveiled’, Nov. 2018, Accessed: Nov. 16, 2023. [Online]. Available: https://www.deingenieur.nl/artikel/europe-s-biggest-3d-printer-unveiled

[8] A. Landman and 10-XL, ‘Primeur voor gemeente Alphen aan den Rijn. Eerste 3D geprinte circulaire brug’, *Kunststofafval*, Mar. 2021, [Online]. Available: https://www.recyclepro.nl/artikel/primeur-voor-gemeente-alphen-aan-den-rijn-eerste-3d-geprinte-circulaire-brug/

[9] B. Van Zonneveld, ‘Eerste 3D-geprinte composietbrug’, Feb. 2021, Accessed: Oct. 06, 2023. [Online]. Available: https://tw.nl/eerste-3d-geprinte-composietbrug/

[10] C. Ad Tissink, ‘In Alphen ligt niet zomaar een parkbruggetje, maar een Europese 3D-printprimeur’, *Cobouw*, Dec. 2020, Accessed: Dec. 01, 2023. [Online]. Available: https://www.cobouw.nl/291082/het-is-van-kunststof-komt-uit-de-printer-en-ligt-in-alphen-aan-den-rijn-rara

[11] P. Alexandrea, ‘China creates their first 3D printed bridges’, *3D printing news*, Jul. 2017, [Online]. Available: https://www.3dnatives.com/en/china-3d-printed-bridge310720174/#!

[12] C. Edo Beerda, ‘Treinstel en molenwieken verwerkt in 3D geprinte fietsbrug’, *Cobouw*, Nov. 2021, Accessed: Dec. 01, 2023. [Online]. Available: https://www.cobouw.nl/300047/treinstel-en-molenwieken-verwerkt-in-3d-geprinte-fietsbrug

[13] G. Nehls, ‘Dutch partnership constructs 3D printed composite pedestrian bridges’, *CompositesWorld*, May 2024, Accessed: Jun. 03, 2024. [Online]. Available: https://www.compositesworld.com/news/dutch-partnership-constructs-3d-printed-composite-pedestrian-bridges

[14] Nedcam, ‘Nedcam Circular 3D printed bridge’, Apr. 2024, Accessed: Jun. 03, 2024. [Online]. Available: https://nedcam.com/project/circular-3d-printed-bridge/?lang=en

[15] ‘SPARC Bridge’. Accessed: Oct. 11, 2023. [Online]. Available: https://www.sparcbridge.com/

[16] C. Pascual-González, M. Iragi, A. Fernández, J. P. Fernández-Blázquez, L. Aretxabaleta, and C. S. Lopes, ‘An approach to analyse the factors behind the micromechanical response of 3D-printed composites’, *Compos B Eng*, vol. 186, Apr. 2020, doi: 10.1016/j.compositesb.2020.107820.

[17] H. Al Abadi, H. T. Thai, V. Paton-Cole, and V. I. Patel, ‘Elastic properties of 3D printed fibre-reinforced structures’, *Compos Struct*, vol. 193, pp. 8–18, Jun. 2018, doi: 10.1016/j.compstruct.2018.03.051.

[18] M. Araya-Calvo *et al.*, ‘Evaluation of compressive and flexural properties of continuous fiber fabrication additive manufacturing technology’, *Addit Manuf*, vol. 22, pp. 157–164, Aug. 2018, doi: 10.1016/j.addma.2018.05.007.

[19] T. Fisher, J. H. S. Almeida, B. G. Falzon, and Z. Kazancı, ‘Tension and Compression Properties of 3D-Printed Composites: Print Orientation and Strain Rate Effects’, *Polymers (Basel)*, vol. 15, no. 7, Apr. 2023, doi: 10.3390/polym15071708.

[20] Y. Mao, C. Shao, P. Shang, Q. Li, X. He, and C. Wu, ‘Preparation of high strength PET/PE composites reinforced with continued long glass fibers’, *Mater Res Express*, vol. 6, no. 4, 2019, doi: 10.1088/2053-1591/aace48.

[21] V. V. Dubrovsky, V. A. Shapovalov, V. N. Aderikha, and S. S. Pesetskii, ‘Effect of hybrid filling with short glass fibers and expanded graphite on structure, rheological and mechanical properties of poly(ethylene terephthalate)’, *Mater Today Commun*, vol. 17, pp. 15–23, Dec. 2018, doi: 10.1016/j.mtcomm.2018.08.002.

[22] A. M. Alqaflah, M. L. Alotaibi, J. N. Aldossery, M. S. Alghamdi, and F. D. Alsewailem, ‘Preparation and characterization of glass fiber–reinforced polyethylene terephthalate/linear low density polyethylene (GF-PET/LLDPE) composites’, *Polym Adv Technol*, vol. 29, no. 1, pp. 52–60, Jan. 2018, doi: 10.1002/pat.4088.

[23] G. J. P. Bex, B. L. J. Ingenhut, T. ten Cate, M. Sezen, and G. Ozkoc, ‘Sustainable approach to produce 3D-printed continuous carbon fiber composites: “A comparison of virgin and recycled PETG”’, *Polym Compos*, vol. 42, no. 9, pp. 4253–4264, Sep. 2021, doi: 10.1002/pc.26143.

[24] H. R. Vanaei, A. El Magri, M. A. Rastak, S. Vanaei, S. Vaudreuil, and A. Tcharkhtchi, ‘Numerical–Experimental Analysis toward the Strain Rate Sensitivity of 3D-Printed Nylon Reinforced by Short Carbon Fiber’, *Materials*, vol. 15, no. 24, Dec. 2022, doi: 10.3390/ma15248722.

[25] M. Pavlovic and F. Csillag, ‘Reading 1.1 - Fibres, resins and cores’, *CIE5128 - FRP Structures*. 2022.

[26] S. Vemuganti, E. Soliman, and M. R. Taha, ‘3D-printed pseudo ductile fiber-reinforced polymer (FRP) composite using discrete fiber orientations’, *Fibers*, vol. 8, no. 9, Sep. 2020, doi: 10.3390/FIB8090053.

[27] M. Ichakpa *et al.*, ‘Investigation on Mechanical and Thermal Properties of 3D-Printed Polyamide 6, Graphene Oxide and Glass-Fibre-Reinforced Composites under Dry, Wet and High Temperature Conditions’, *Journal of Composites Science*, vol. 7, no. 6, Jun. 2023, doi: 10.3390/jcs7060227.

[28] L. Li, W. Liu, and L. Sun, ‘Mechanical characterization of 3D printed continuous carbon fiber reinforced thermoplastic composites’, *Compos Sci Technol*, vol. 227, Aug. 2022, doi: 10.1016/j.compscitech.2022.109618.

[29] X. Liu, A. Saigal, and M. Zimmerman, ‘Performance Study of 3D Printed Continuous Fiber Reinforced Composites’, in *Minerals, Metals and Materials Series*, Springer Science and Business Media Deutschland GmbH, 2023, pp. 89–105. doi: 10.1007/978-3-031-22576-5_9.

[30] Y. K. Yadav, G. Dixit, and S. Dixit, ‘Natural fiber reinforced rPET/polyester composites: a review on development, mechanical performance, and sustainable management’, *Polymer-Plastics Technology and Materials*, vol. 62, no. 14. Taylor and Francis Ltd., pp. 1823–1843, 2023. doi: 10.1080/25740881.2023.2237100.

[31] Mr. P. S. Ramalingam, Dr. K. Mayandi, Dr. N. Rajini, Prof. N. Ayirilimis, and Dr. S. Rajesh, ‘Effect of 3d Print Layer Orientation on Tensile Properties of Poly (Lactic Acid) Polymer’, *Int J Eng Adv Technol*, vol. 9, no. 1s4, pp. 926–929, Dec. 2019, doi: 10.35940/ijeat.A1071.1291S419.

[32] D. Pezer, F. Vukas, and M. Butir, ‘Experimental Study of Tensile Strength for 3D Printed Specimens of HI-PLA Polymer Material on In-house Tensile Test Machine’. [Online]. Available: www.techniumscience.com

[33] ASTM International, *ASTM B831 Standard Test Method for Shear Testing of Thin Aluminum Alloy Products 1*. 2019. doi: 10.1520/B0831-1.

[34] T. Van Kempen, P. Leen, W. Zoetelief, and L. Douven, ‘Data for Arup’, 2021.

[35] GOM, ‘Digital Image Correlation and Strain Computation Basics’, Jan. 2018.

[36] F. P. Van der Meer, ‘Lecture 10.1 - Failure Analysis’, *CIE5128 - FRP Structures*. Sep. 2018.

[37] D. H. Malschaert, ‘Fracture mechanics - theoretical background’, 2022.

[38] L. Gaget, ‘3D printing for construction: What is Contour Crafting?’, *Sculpteo*, Jun. 2018, Accessed: Jun. 07, 2024. [Online]. Available: https://www.sculpteo.com/blog/2018/06/27/3d-printing-for-construction-what-is-contour-crafting/

[39] D. Kazmer, ‘Three-Dimensional Printing of Plastics’, in *Applied Plastics Engineering Handbook: Processing, Materials, and Applications: Second Edition*, Elsevier Inc., 2017, pp. 617–634. doi: 10.1016/B978-0-323-39040-8.00029-8.

[40] Arup, ‘Rijkswaterstaat 3D geprinte FRP-brugdelen Exploration of FE modelling techniques’, Dec. 2021. [Online]. Available: www.arup.com

[41] W. M. Sebastian, M. Ralph, M. Poulton, and J. Goacher, ‘Lab and field studies into effectiveness of flat steel plate – rubber pad systems as tyre substitutes for local loading of cellular GFRP bridge decking’, *Compos B Eng*, vol. 125, pp. 100–122, Sep. 2017, doi: 10.1016/j.compositesb.2017.05.044.

[42] NEN, ‘NEN-EN 1991-2+C1 Eurocode 1: Actions on structures-Part 2: Traffic loads on bridges’, Oct. 2015.

[43] *NEN-EN-ISO 527-4*. 2019.

[44] ‘Designation: D4255/D4255M − 20´120´1 Standard Test Method for In-Plane Shear Properties of Polymer Matrix Composite Materials by the Rail Shear Method 1’, doi: 10.1520/D4255_D4255M-20E01.

[45] E. Polatidis, J. Čapek, and M. V. Upadhyay, ‘Validating texture and lattice strain evolution models via in-situ neutron diffraction and shear tests’, *Materialia (Oxf)*, vol. 28, May 2023, doi: 10.1016/j.mtla.2023.101752.

[46] Q. Yin *et al.*, ‘An experimental and numerical investigation of different shear test configurations for sheet metal characterization’, *Int J Solids Struct*, vol. 51, no. 5, pp. 1066–1074, Mar. 2014, doi: 10.1016/j.ijsolstr.2013.12.006.

[47] S. L. Lv, Z. Li, and X. S. Gao, ‘Damage in an aluminum alloy induced by the combined action of shear stress and environmental exposure’, *AIP Adv*, vol. 11, no. 2, Feb. 2021, doi: 10.1063/5.0035781.

[48] Y. Zhang, Y. Liu, and F. Yang, ‘Ductile fracture modelling of steel plates under tensile and shear dominated states’, *J Constr Steel Res*, vol. 197, Oct. 2022, doi: 10.1016/j.jcsr.2022.107469.

[49] X. W. Zhang, J. F. Wen, X. C. Zhang, X. G. Wang, and S. T. Tu, ‘Effects of the stress state on plastic deformation and ductile failure: Experiment and numerical simulation using a newly designed tension-shear specimen’, *Fatigue Fract Eng Mater Struct*, vol. 42, no. 9, pp. 2079–2092, 2019, doi: 10.1111/ffe.13084.

[50] J. Peirs, P. Verleysen, and J. Degrieck, ‘Novel Technique for Static and Dynamic Shear Testing of Ti6Al4V Sheet’, *Exp Mech*, vol. 52, no. 7, pp. 729–741, Sep. 2012, doi: 10.1007/s11340-011-9541-9.

[51] H. N. Han, C. G. Lee, C. S. Oh, T. H. Lee, and S. J. Kim, ‘A model for deformation behavior and mechanically induced martensitic transformation of metastable austenitic steel’, *Acta Mater*, vol. 52, no. 17, pp. 5203–5214, Oct. 2004, doi: 10.1016/j.actamat.2004.07.031.

[52] *NEN-EN-ISO 14126*. 1999.

Part V: Appendices

A

Collection of Data from Literature

From the literature review, data regarding properties of several types of 3D printed composites and FRP with a similar material configuration is collected. Especially relevant data was from the pre-study were the properties of Arnite from Covestro. The mechanical properties were already provided in Section 2.2.1 and in this Appendix some additional properties are given. In Section 3.3, a summary of properties obtained from references was given. This summary is based on the individual collected data given in this Appendix.

A.1 Data from Covestro

The mechanical properties of the Arnite material were relevant for this research and already presented in the report. Covestro provided some additional properties which are given in Table A-1.

Table A-1 Thermal properties of Arnite material from Covestro [1]

Property	Symbol	Value	Test method
Thermal expansion coefficient in print direction between 20 – 80°C	$\alpha_{LT,1}$	$13.6*10^{-6}$ 1/K	
Thermal expansion coefficient in print direction between 100 – 200°C	$\alpha_{LT,1}$	$9.9*10^{-6}$ 1/K	
Thermal expansion coefficient in build direction between 20 – 80°C	$\alpha_{LT,2}$	$62.8*10^{-6}$ 1/K	
Thermal expansion coefficient in build direction between 100 – 200°C	$\alpha_{LT,2}$	$154.1*10^{-6}$ 1/K	
Melting temperature (10°C/min)	T_{melt}	255°C	ISO 11357-1/-3
Glass transition temperature (10°C/min)	T_g	75°C	ISO 11357-1/-2

A.2 Basic mechanical properties of other FRP composites

In literature, a lot of tests are carried out on different configurations of composite fibre-reinforced polymer materials. Since this research focuses on 3D printed FRP with PET as the thermoplastic polymer, results of tests regarding an aspect of this type of material are useful to analyse. To have an insight into the basic

mechanical properties of 3D printed FRP and/or FRP composites consisting of PET, an overview of some data is given in Table A-2.

Table A-2 Overview of basic mechanical properties from literature [1,16,17,19-24,26-30]

Matrix	**Fibres**	**V_f [%]**	**Fibre length**	**Production technique**	**$\sigma_{1,t}$ [MPa]**	**$\sigma_{2,t}$ [MPa]**	**E_1 [MPa]**	**E_2 [MPa]**	**T_g [°C]**
Thermoplastic polymer	Carbon	33.9 - 36.4	Continuous	3D printing (FFF)					122
Thermoplastic polymer	Standard glass	31.5 - 38	Continuous	3D printing (FFF)					47
Thermoplastic polymer	HS-/HT-glass	27.3 - 31	Continuous	3D printing (FFF)					50
Thermoplastic polymer	Aramid (Kevlar)	38 - 40.4	Continuous	3D printing (FFF)					50
Nylon	Carbon	9.6 - 11	Short	3D printing (FFF)					27
Nylon	-	-	-	3D printing (FFF)					22
Nylon	Carbon	40	Continuous	3D printing (FDM)	~310		37,000		
Nylon	Glass	40	Continuous	3D printing (FDM)	~160		6,400		
Nylon	Kevlar	40	Continuous	3D printing (FDM)	~150		8,700		
Nylon White	-	-	-	3D printing (FFF)	35.65 - 51.95		1,230 - 1,810		
Nylon	Carbon	12	130 µm (short)	3D printing (FFF)	28.75 - 46.26		700 - 1,730		
Thermoplastic nylon-based	Glass	?	Continuous		623	18	16,500	1,900	
PA6	-	-	-	3D printing (FDM)	51		1,400		62
PA6	Glass	30%wt		3D printing (FDM)	82		2,700		70
PA6	Graphene oxide (nanofiller)	?		3D printing (FDM)	72		1,400		65

Matrix	Fibres	V_f [%]	Fibre length	Production technique	$\sigma_{1,t}$ [MPa]	$\sigma_{2,t}$ [MPa]	E_1 [MPa]	E_2 [MPa]	T_g [°C]
PA (Nylon)	Carbon	21 - 24	Continuous	3D printing (FDM)	374 - 551		13,180 - 45,790		
Nylon	Carbon	?	Short	3D printing (FFF)	70.7 - 89.3		1,500 - 1,900		
Nylon	-	-	-	3D printing (CFF)	18.77		529		
Nylon	Carbon	21	Continuous	3D printing (CFF)	228.02		10,111		
Nylon	Carbon	42.3	Continuous	3D printing (CFF)	427		19,111		
Nylon	Carbon	63.6	Continuous	3D printing (CFF)	634.52		52,001		
Nylon	Carbon	68.7	Continuous	3D printing (CFF)	691.97		24,989		
PETG	-	-	-	3D printing (FFF)	52.2	23.1	2,010	1,870	75
PETG	Carbon	25wt%	Continuous	3D printing (FFF)	696.6		39,700		75
rPETG	-	-	-	3D printing (FFF)	45	20	1915	1625	75
rPETG	Carbon	25wt%	Continuous	3D printing (FFF)	604.5		34,200		75
rPET	Flax	20	?	VARTM	188.6 - 230.7		15,300 - 20,300		
rPET	Hemp/wool	?	?	Pultrusion	122.12		16,840		
rPET	Sisal/jute/glass	?	?	Hand lay-up	111.2 - 232.1				
LPET	Glass	?	Long/continuous	?	298				83.1
HPET	Glass	?	Long/continuous	?	291				83.1
PET	-	-	-	?	~50		~2,000		
PET	Glass	15	0.1 - 0.3 mm (short)	?	~100		~4000		

Matrix	Fibres	V_f [%]	Fibre length	Production technique	$\sigma_{1,t}$ [MPa]	$\sigma_{2,t}$ [MPa]	E_1 [MPa]	E_2 [MPa]	T_g [°C]
PET	Glass	30	0.1 - 0.3 mm (short)	?	~120		~8000		
PET	Glass	45	0.1 - 0.3 mm (short)	?	110 - 130		10,000 - 12,000		
PET	Glass	60	0.1 - 0.3 mm (short)	?	120 - 140		~16,000		
PET	Glass	5 wt%	?	?	~28				81
PET	Glass	15 wt%	?	?	28 - 35				78
PET	Glass	30 wt%	?	?	30 - 44				78
PET (Arnite)	Glass	?	Short	3D printing	197	16.4	20,000	7,100	75

B

Nesting Coupon Cutting

In this Appendix, the nesting drawings of how the coupons for the tests are cut from the sides of the boxes. These nesting drawings are sketches of the sides of the box with the layout of how the coupons are cut from the boxes for test series 1, 2, 3, and 4. For some test series, the dimensions of the box are the same. The type and number of coupons can also be the same for different test series. For all the boxes, a margin should be taken into account at the edges of the sides. The corners of this square are rounded due to the printing process. With printed material, sharp corners are not desirable because local imperfections can occur due to heat accumulation and a rounded corner can be printed neater. Therefore, the corners of boxes are rounded. The radius of the corners is the margin at the edges which is not usable for coupons. There is also a margin taken into account for cutting of each single coupon. The water jetting company (247watersnijden) prescribed a margin of 10 mm at the sides of the box or plate and 5 mm in between the coupons. To be safe and to create the layout a bit more easily, a margin of 10 mm around each coupon is considered. In the sketches, the solid lines represent the actual dimensions of the coupon. The dotted lines around the coupon are the dimension including the cutting margin.

B.1 Coupon test series 1 and 2

For test series 1 and 2, the dimensions of the box are L × b × h = 370 × 370 × 320 mm. The same type and number of coupons are needed for both test series. Therefore, the layout of nesting of the coupons can be the same. For these test series, tensile coupon in longitudinal and transverse direction and (former) IBSS coupons are needed. Six specimens of each type of coupon were needed. Initially, there was the assumption that the two opposite sides of the box should have the same but mirrored nesting layout. Later, this was not necessary because the boxes were cut in single plates. However, the design for these test series, and for test series 3, was made symmetrical. The nesting drawings are shown in Figure B-1 and Figure B-2. Not all the material from the box is used for the coupons. This is due to the dimensions of the box which were required for the dimensions of the coupons. Because of the costs and the print quality, there are not separate boxes printed for the longitudinal and transverse coupons.

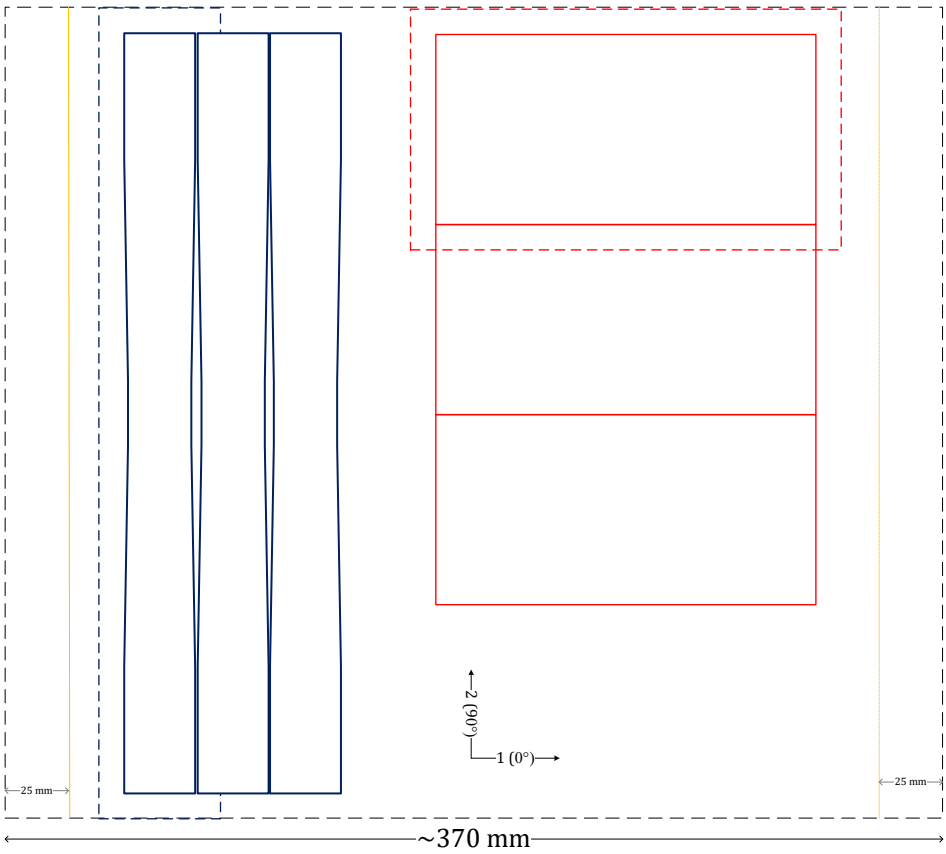

Figure B-1 Three transverse tensile coupons (dark blue) and three former IBSS (red) coupons to be cut from a side from a box

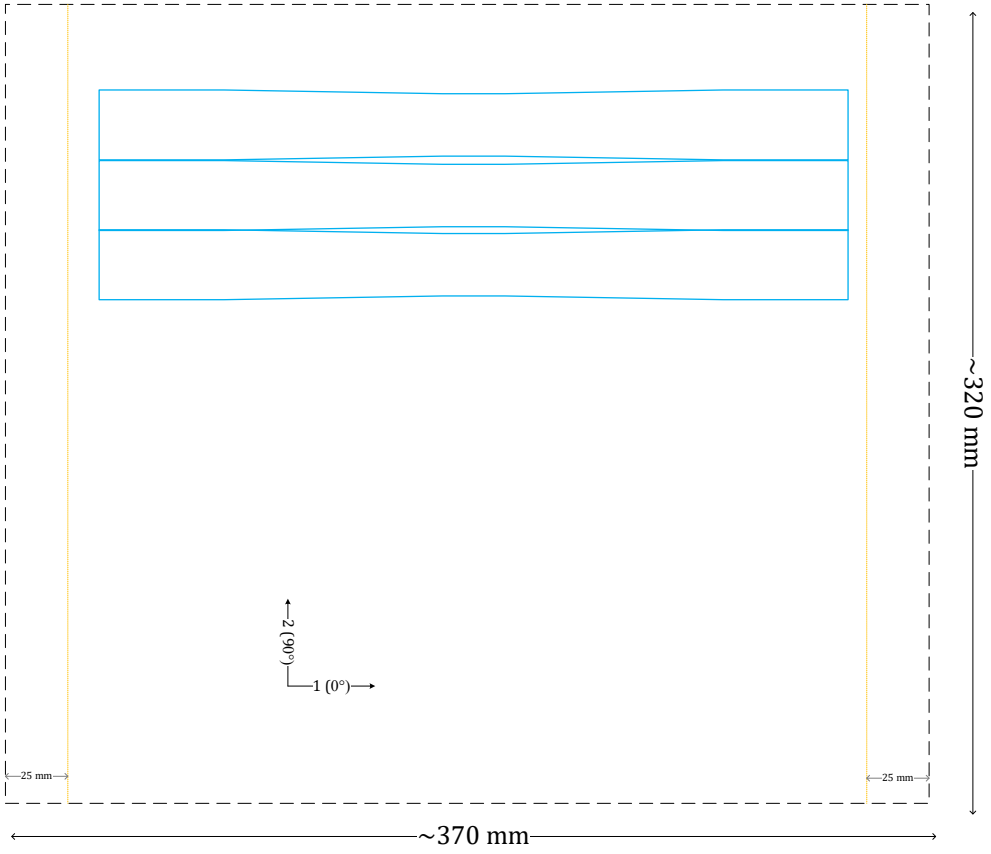

Figure B-2 Three longitudinal tensile coupons (light blue) to be cut from a side of a box

B.2 Coupon test series 3.1 and 3.2

The difference of the boxes of test series 3 compared to test series 1 and 2 is that there are no longitudinal coupons to be cut. Therefore, the width of the box could be a bit smaller, namely 270 mm instead of 370 mm. Initially, the plan was to obtain more coupon from this box. Moreover, the width of the box cannot be too small with the longer layer times, otherwise the printing speed will get too low, which will lead to poor material. So, there is some space left which will not be used for a coupon. This makes the nesting less critical because there is more freedom. How the coupons are roughly cut from the box sides is sketched in Figure B-3 and Figure B-4.

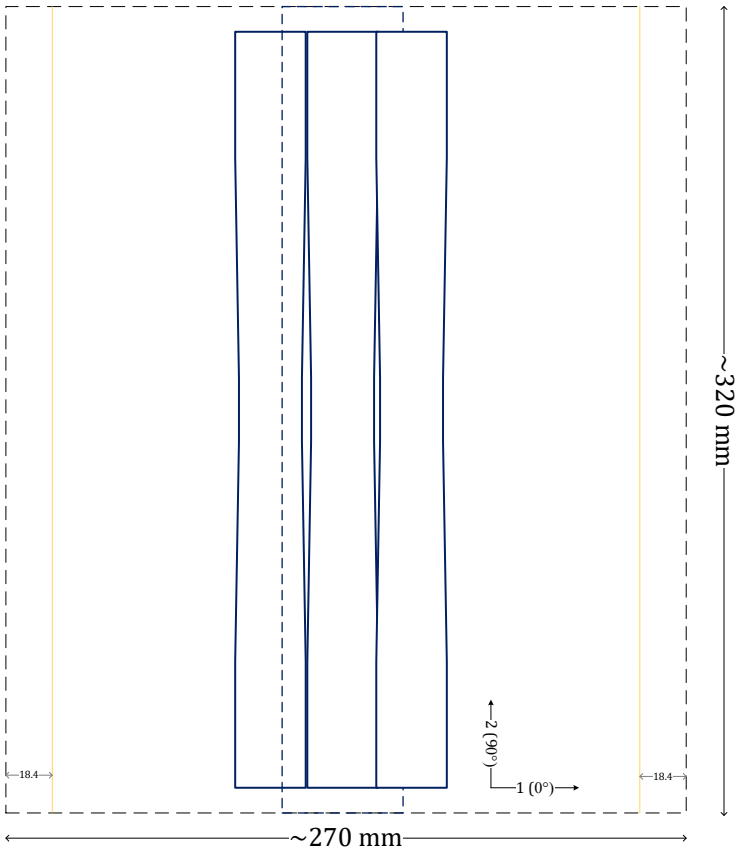

Figure B-3 Three transverse tensile coupons (dark blue) to be cut from a side of a box

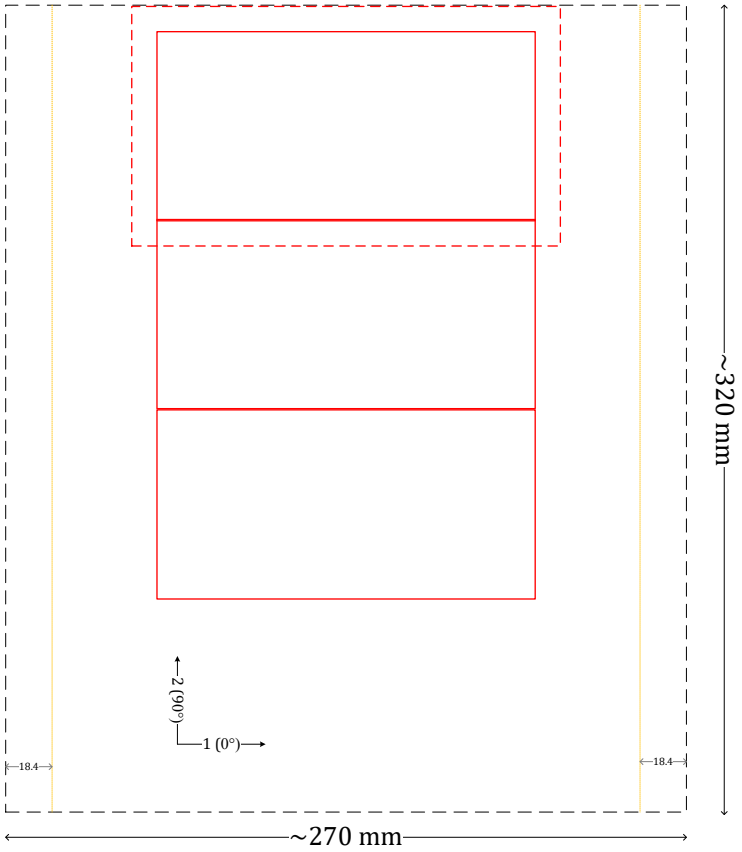

Figure B-4 Three former IBSS coupons (red) to be cut from a side of a box

B.3 Coupon test series 4

The coupons needed for test series 4, the characterization of the mechanical properties, two boxes are printed with the same dimension as from test series 1 and 2, namely L × b × h = 370 × 370 × 320 mm. These dimensions are minimum needed to make the one coupon fit in the side of the box. With the number of coupons required to be cut, six sides of the boxes were needed, so two were used as reserve. To have a valuable determination of mechanical property value, at least 5 specimens should be tested successfully. To have some margin in case anything will go wrong during a test, three additional coupons of each are cut. This makes a total of eight coupons for each type of coupon to be cut. How all these coupons are nest over the sides of the boxes for waterjet cutting is shown in Figure B-5 – Figure B-10.

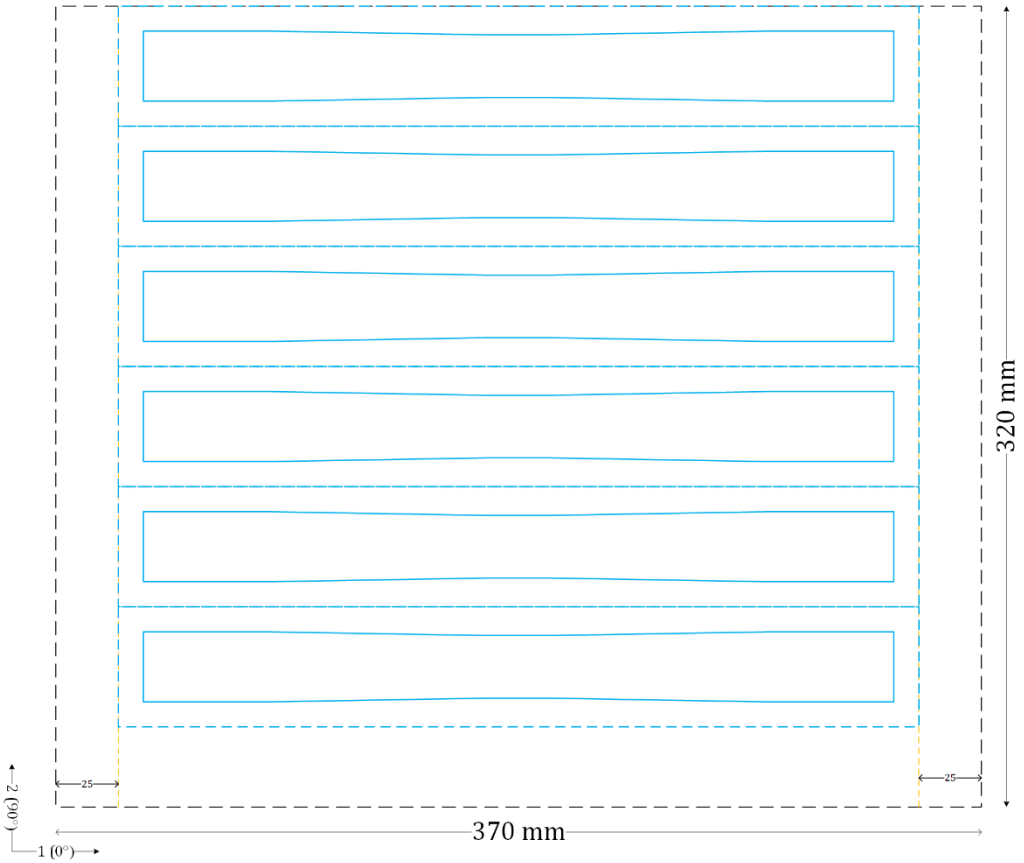

Figure B-5 Six longitudinal tensile coupons (light blue) to be cut from a side of a box

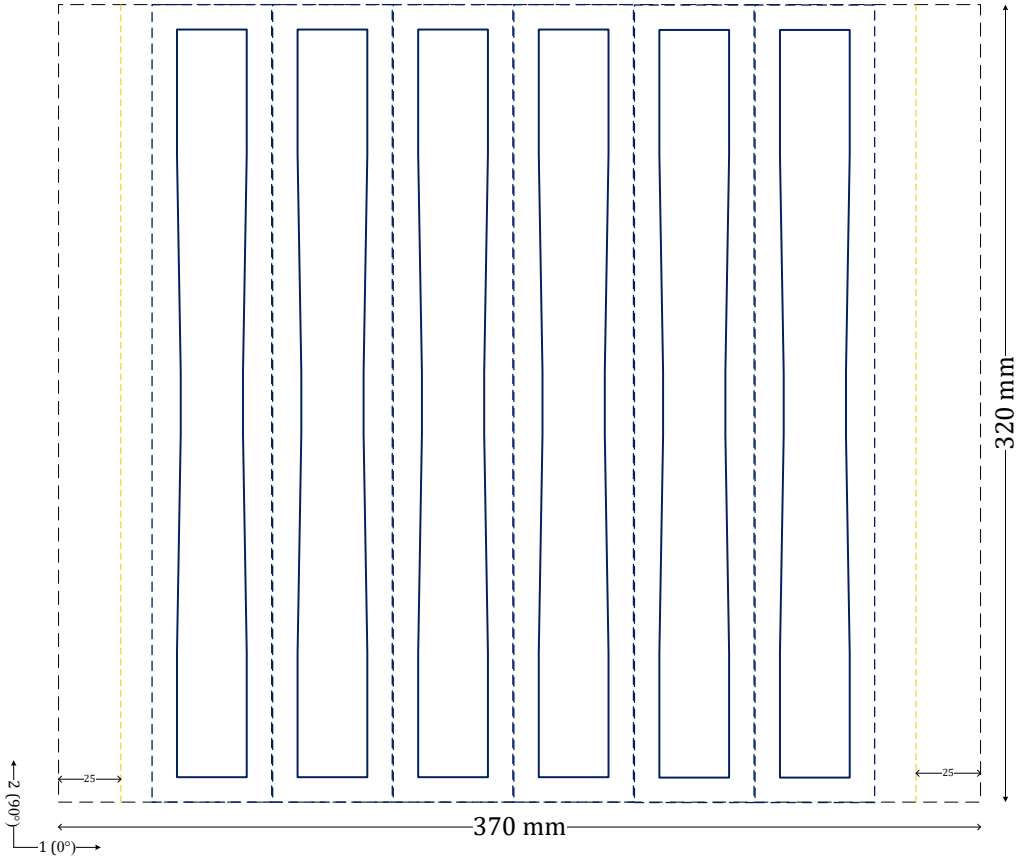

Figure B-6 Six transverse tensile coupons (dark blue) to be cut from a side of a box

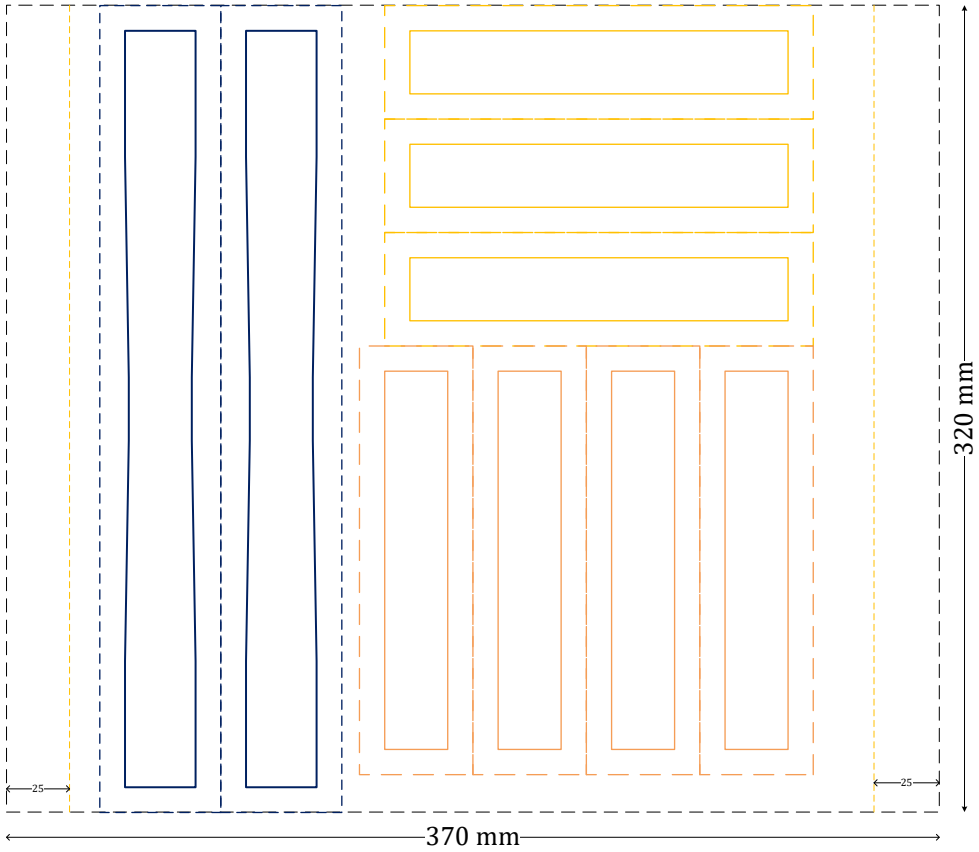

Figure B-7 Two transverse tensile coupons (dark blue), three longitudinal compression coupons (yellow) and four transverse compression coupons (orange) to be cut from a side from a box

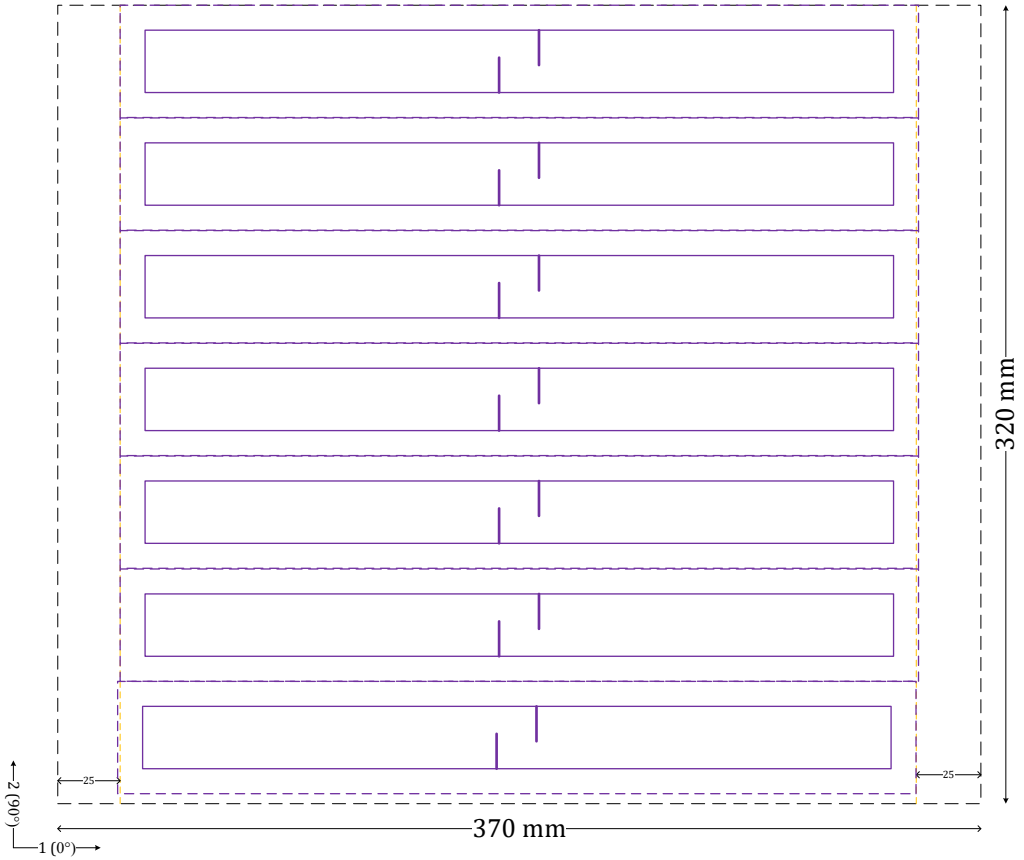

Figure B-8 Seven IBSS coupons (purple) to be cut from a side of a box

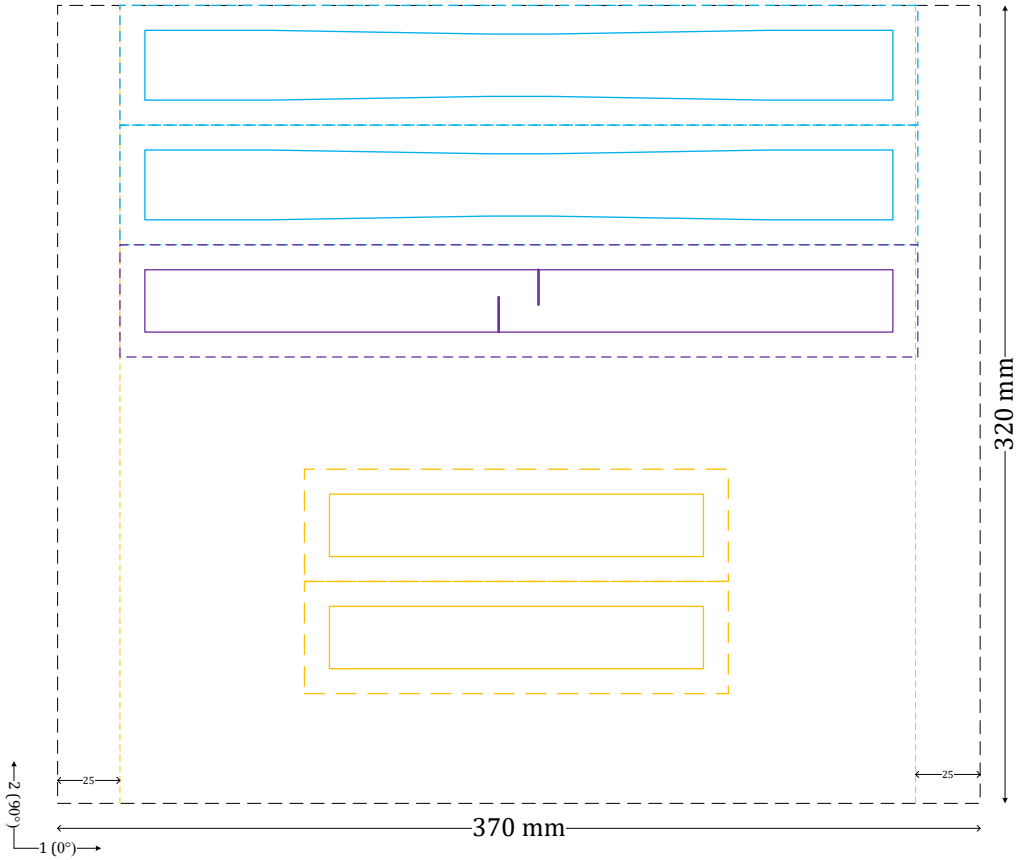

Figure B-9 Two longitudinal tensile coupons (light blue), one IBSS coupon (purple), and two longitudinal compression coupons (yellow) to be cut from a side from a box

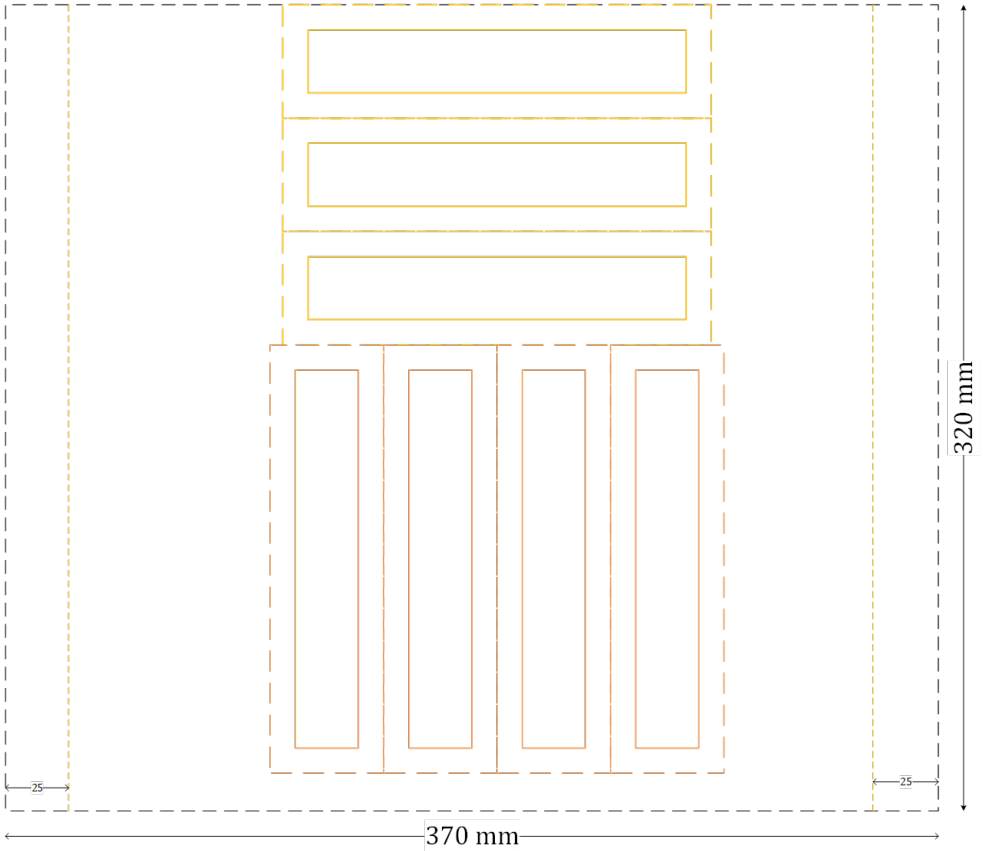

Figure B-10 Three longitudinal compression coupons (yellow) and four transverse compression coupons (orange) to be cut from a side from a box

C

Individual Test Results

From all the individual coupon tests performed, the results are given in this Appendix.

C.1 First stage of coupon testing

In the first stage of coupon testing, test series 1, 2, 3.1, and 3.2 were executed. For each different material configuration (GF30_80s; GF45_80s; GF30_100s; GF30_120s), the results are presented in Sections C.1.1, C.1.2, C.1.3, and C.1.4 respectively.

C.1.1 GF30 80s

The results of the GF30_80s coupons tested in longitudinal tension are presented in the stress-strain diagram in Figure C-1. The results of the GF30 80s coupons tested in transverse tension are presented in the stress-strain diagram in Figure C-2.

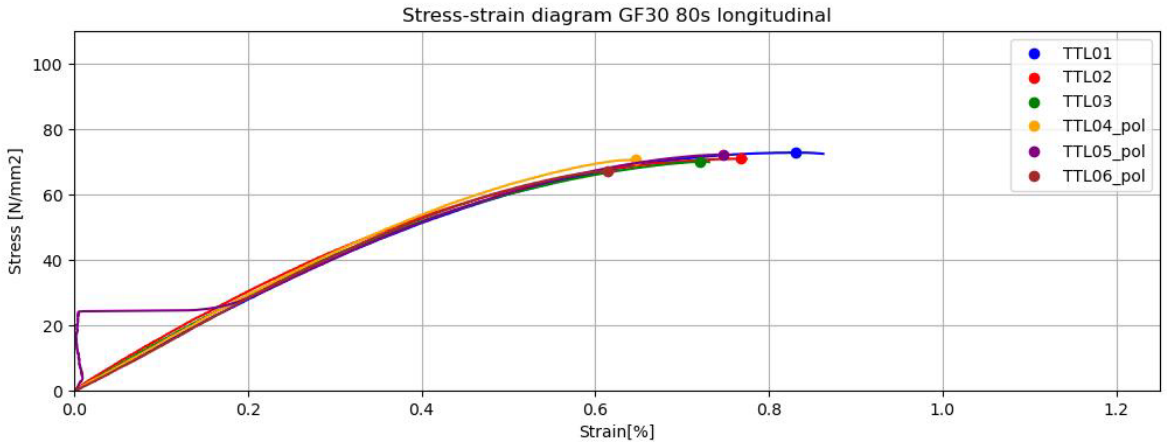

Figure C-1 Stress-strain curves of the GF30 80s coupons from the longitudinal tensile tests

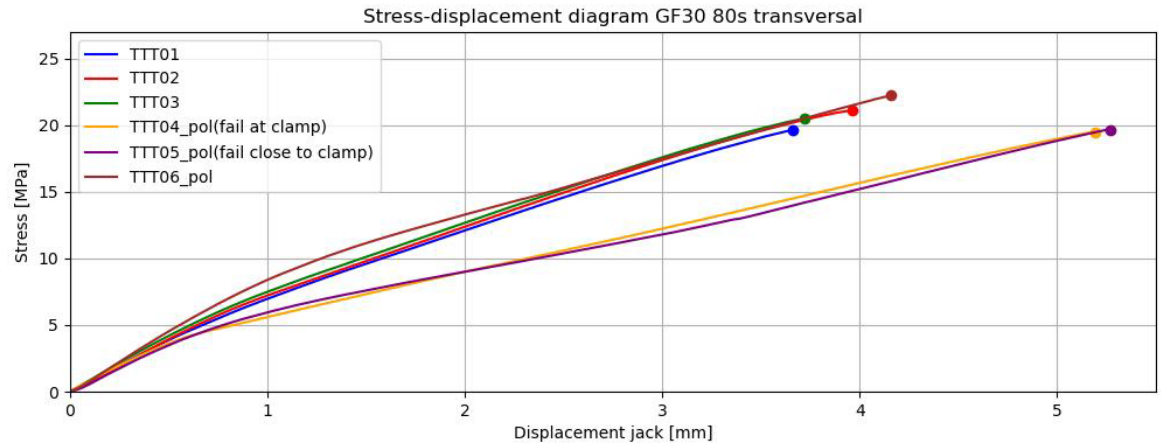

Figure C-2 Stress-strain curves of the GF30 80s coupons from the transverse tensile tests

C.1.2 GF45 30s

The results of the GF45_80s coupons tested in longitudinal tension are presented in the stress-strain diagram in Figure C-3. The results of the GF45 80s coupons tested in transverse tension are presented in the stress-strain diagram in Figure C-4.

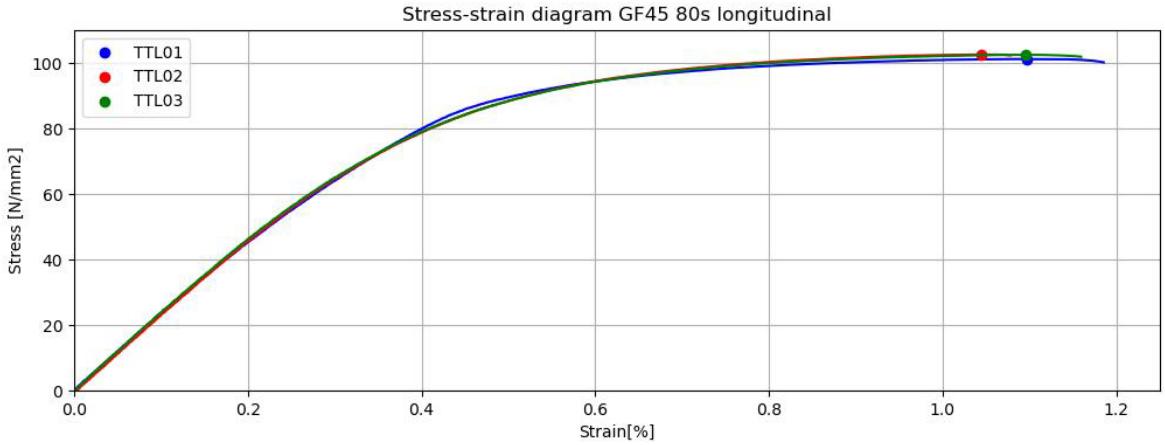

Figure C-3 Stress-strain curves of the GF45 80s coupons from the longitudinal tensile tests

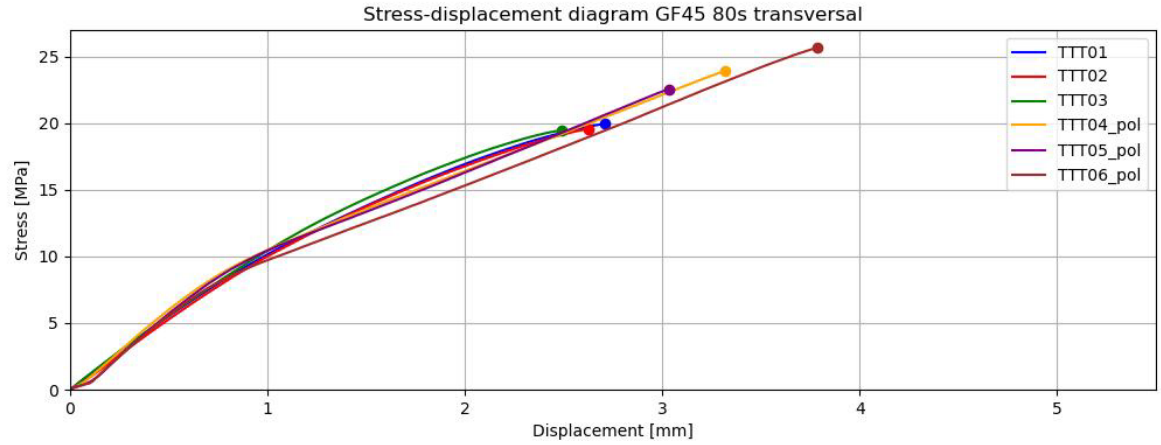

Figure C-4 Stress-strain curves of the GF45 80s coupons from the transverse tensile tests

C.1.3 GF30 100s

The results of the GF30_100s coupons tested in transverse tension are presented in the stress-strain diagram in Figure C-5.

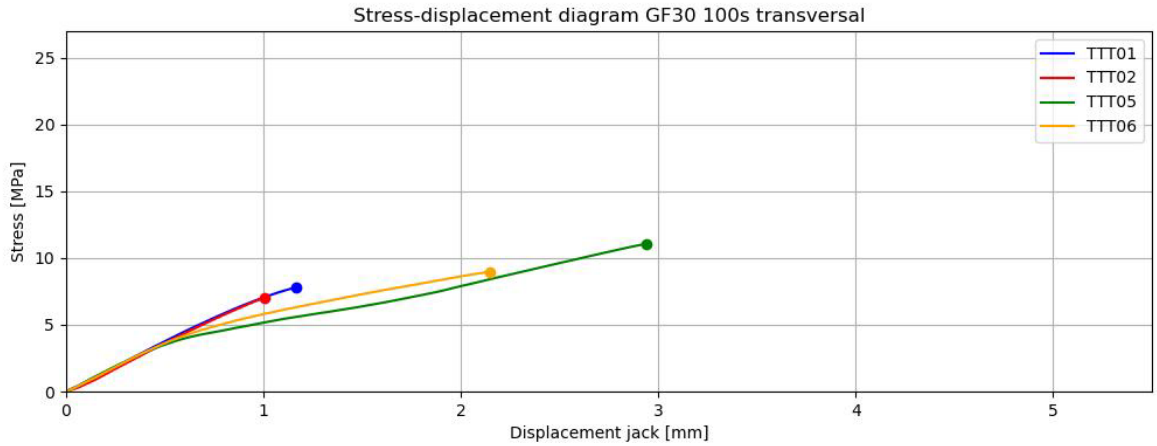

Figure C-5 Stress-strain curves of the GF30 100s coupons from the transverse tensile tests

C.1.4 GF30 120s

The results of the GF30_120s coupons tested in transverse tension are presented in the stress-strain diagram in Figure C-6.

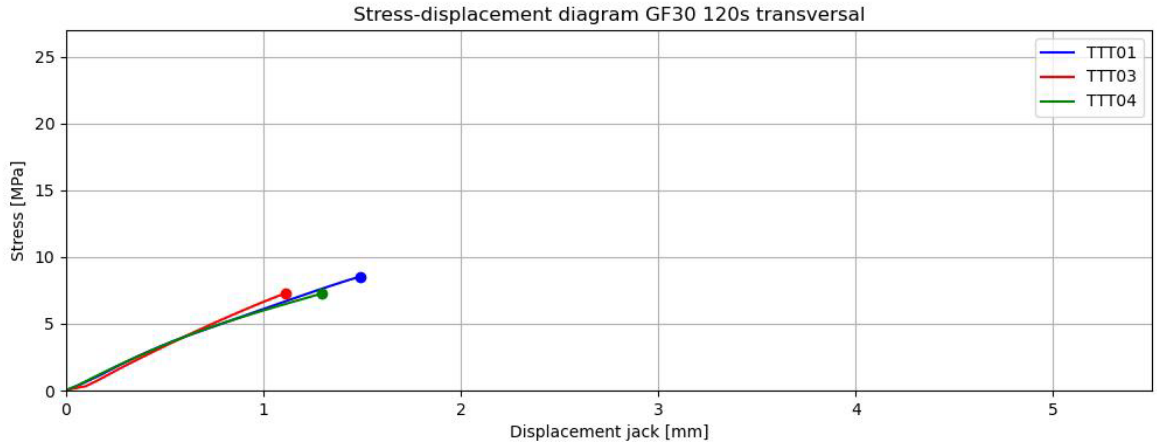

Figure C-6 Stress-strain curves of the GF30 120s coupons from the transverse tensile tests

C.2 Second stage of coupon testing

Coupon test series 4 was executed in the second stage of coupon testing. The tests in this stage were performed to establish the mechanical properties of the material with the configuration that turned out the be the most suitable from the first stage of coupon testing. This was the composite material GF45 80s. In Sections C.2.1, C.2.2, C.2.3, C.2.4, and C.2.5, the results from the longitudinal tensile tests, transverse tensile tests, longitudinal compression tests, transverse tensile tests, and IBSS tests are presented respectively.

C.2.1 Tensile longitudinal

The force-displacement curves of the tensile tests in longitudinal direction are plotted in Figure C-7. These are measured directly from the test machine. The stress-strain diagrams with the chord slope between the points corresponding to ε = 0.05% to ε = 0.25% for the determination of the elastic modulus of each individual test are given in Figure C-8. In Table C-1, the values of the mechanical properties obtained from the longitudinal tensile tests are listed.

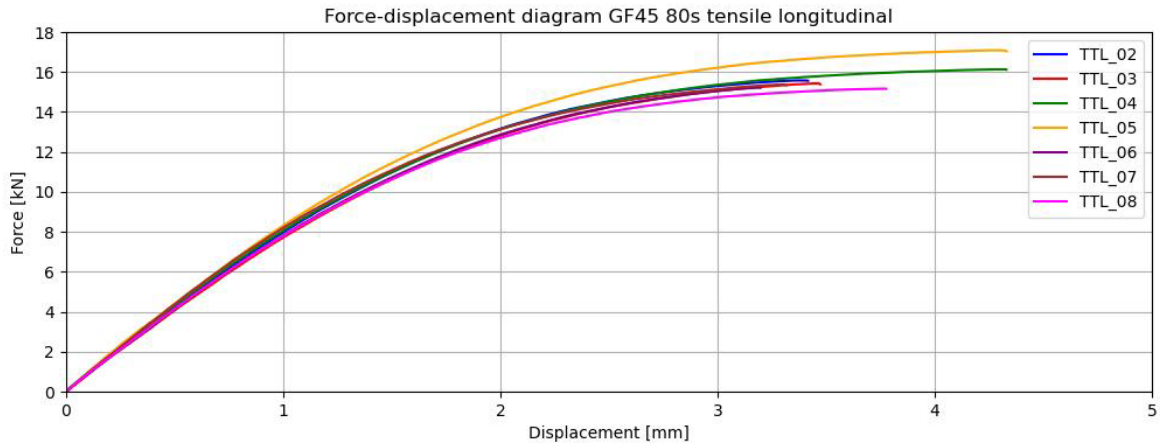

Figure C-7 Force-displacement diagram of the results obtained from the tensile tests in longitudinal direction

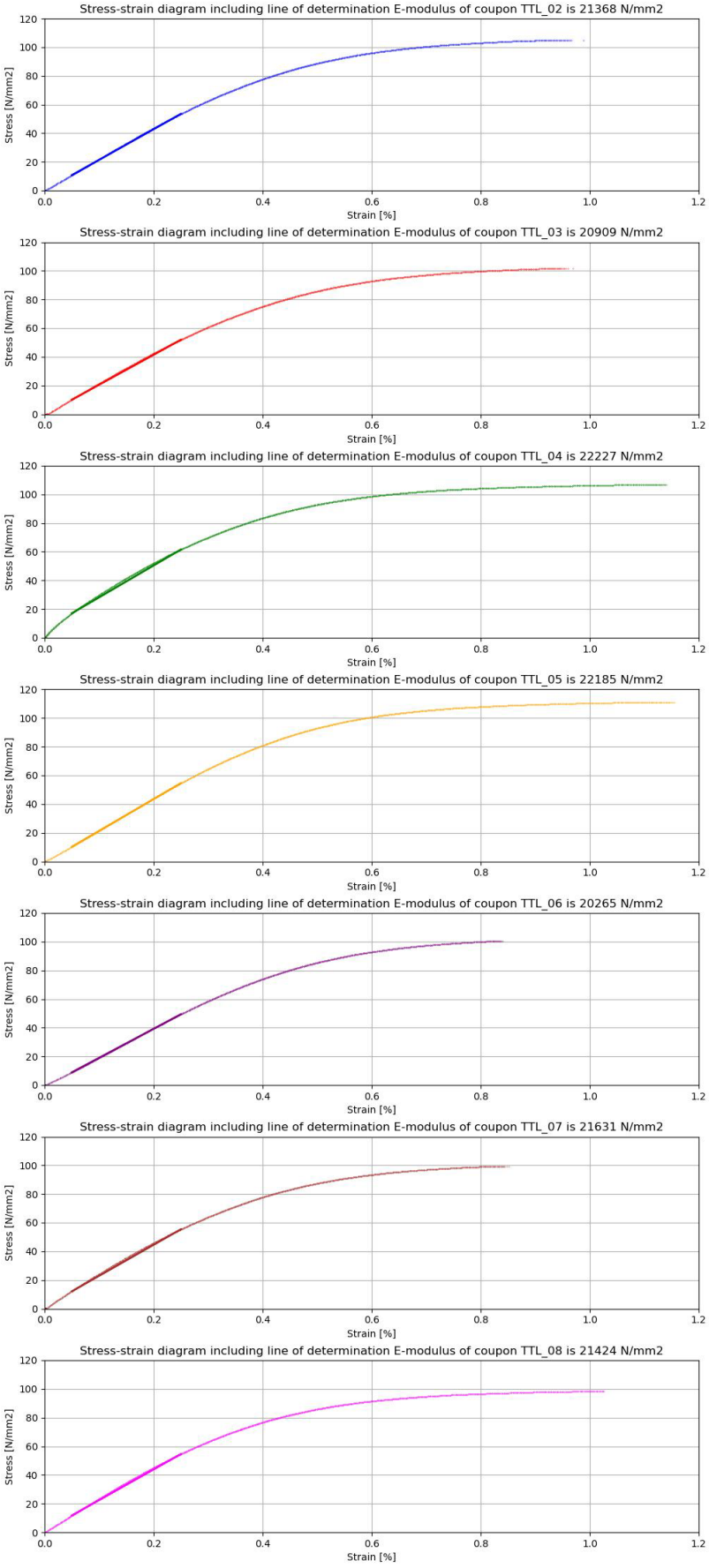

Figure C-8 Stress-strain curve of each individual longitudinal tensile test with the chord slope from ε=0.05% to ε=0.25% to determine the elastic modulus

Table C-1 Values of the mechanical properties derived from the longitudinal tensile tests

Test coupon	$\sigma_{1,t}$ [MPa}	$E_{1,t}$ [N/mm^2]	$\varepsilon_{1,t}$ [%]
TTL_02	104.92	21,367.6	0.952
TTL_03	101.75	20,909.4	0.952
TTL_04	106.85	22,227.4	1.125
TTL_05	111.12	22,185.3	1.128
TTL_06	100.46	20,265.5	0.835
TTL_07	99.38	21,630.6	0.839
TTL_08	98.43	21,423.6	1.019
Mean	103.27	21,429.9	0.979
Standard deviation	4.58	692.5	0.120
Characteristic value	93.83		

Equations (C-1) – (C-4) calculate the characteristic value of the tensile strength in longitudinal direction, $\sigma_{1,tk}$, according to Section D.7.2 from NEN-EN 1990:

$$s_X^2 = \frac{1}{n-1} * \Sigma(x_i - m_X)^2 = 4.58 \quad \text{(C-1)}$$

$$k_n = 2.06 \text{ for } n = 7 \quad \text{(C-2)}$$

$$V_X = s_X / m_X = 0.0444 \quad \text{(C-3)}$$

$$X_k = m_X * (1 - k_n * V_X) = 93.83 = \sigma_{1,tk} \quad \text{(C-4)}$$

C.2.2 Tensile transverse

The force-displacement curves of the tensile tests in transverse direction are plotted in Figure C-9. These are measured directly from the test machine. The stress-strain diagrams with the chord slope between the points corresponding to ε = 0.05% to ε = 0.25% for the determination of the elastic modulus of each individual test are given in Figure C-10. In Table C-2, the values of the mechanical properties obtained from the transverse tensile tests are listed.

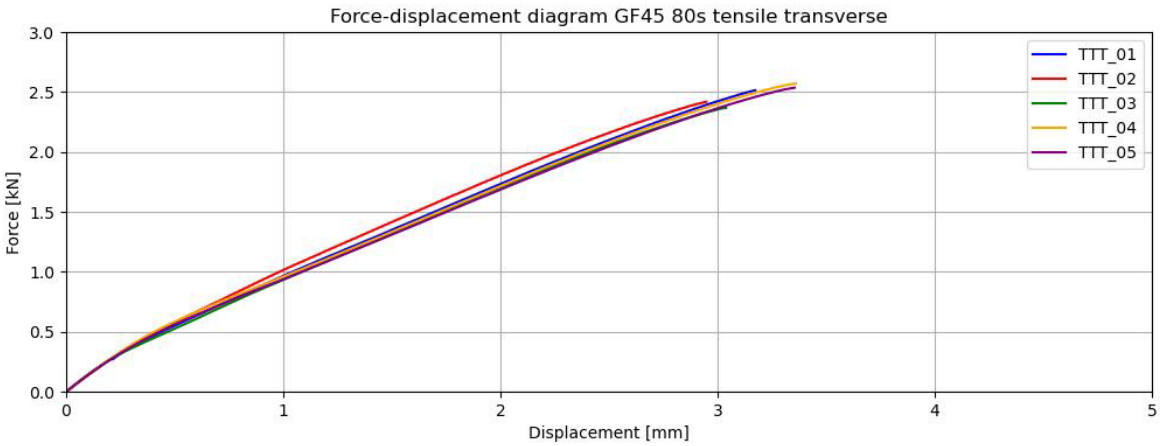

Figure C-9 Force-displacement diagram of the results obtained from the tensile tests in transverse direction

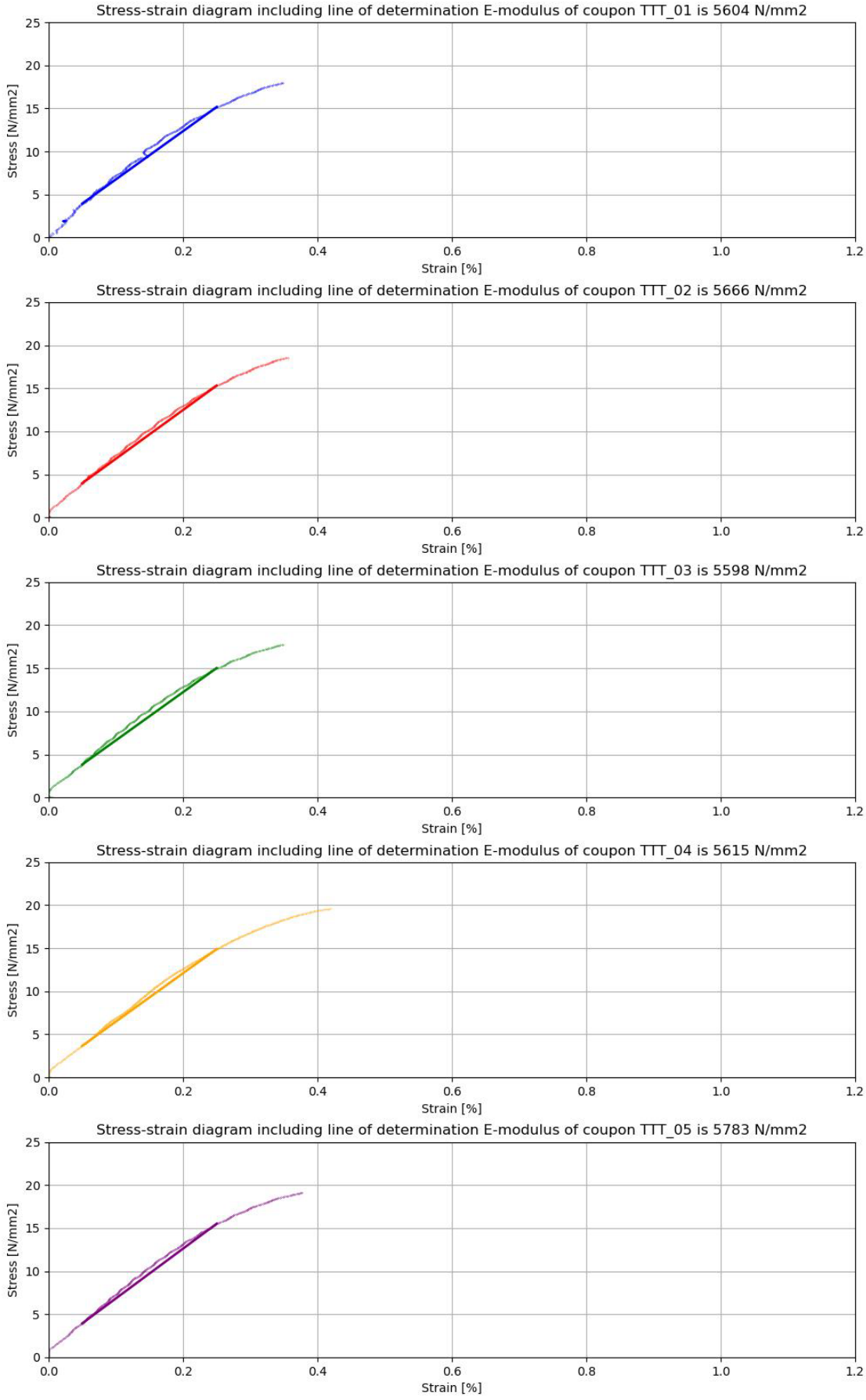

Figure C-10 Stress-strain curve of each individual transverse tensile test with the chord slope from ε=0.05% to ε=0.25% to determine the elastic modulus

Table C-2 Values of the mechanical properties derived from the transverse tensile tests

Test coupon	$\sigma_{2,t}$ [MPa}	$E_{2,t}$ [N/mm^2]	$\varepsilon_{2,t}$ [%]
TTT_01	17.97	5,604.2	0.349
TTT_02	18.55	5,666.0	0.356
TTT_03	17.73	5,598.4	0.348
TTT_04	19.59	5,615.5	0.419
TTT_05	19.11	5,783.1	0.377
Mean	18.59	5,653.4	0.370
Standard deviation	0.77	77.3	0.030
Characteristic value	16.79		

Equations (C-5) – (C-8) calculate the characteristic value of the tensile strength in transverse direction, $\sigma_{2,tk}$, according to Section D.7.2 from NEN-EN 1990:

$$s_X^2 = \frac{1}{n-1} * \Sigma(x_i - m_X)^2 = 0.77 \quad \text{(C-5)}$$

$$k_n = 2.33 \text{ for } n = 5 \quad \text{(C-6)}$$

$$V_X = s_X / m_X = 0.0416 \quad \text{(C-7)}$$

$$X_k = m_X * (1 - k_n * V_X) = 16.79 = \sigma_{2,tk} \quad \text{(C-8)}$$

C.2.3 Compression longitudinal

The force-displacement curves of the compression tests in longitudinal direction are plotted in Figure C-11. These are measured directly from the test machine. The stress-strain diagrams with the chord slope between the points corresponding to ε = 0.05% to ε = 0.25% for the determination of the elastic modulus of each individual test are given in Figure C-12. In Table C-3, the values of the mechanical properties obtained from the longitudinal compression tests are listed.

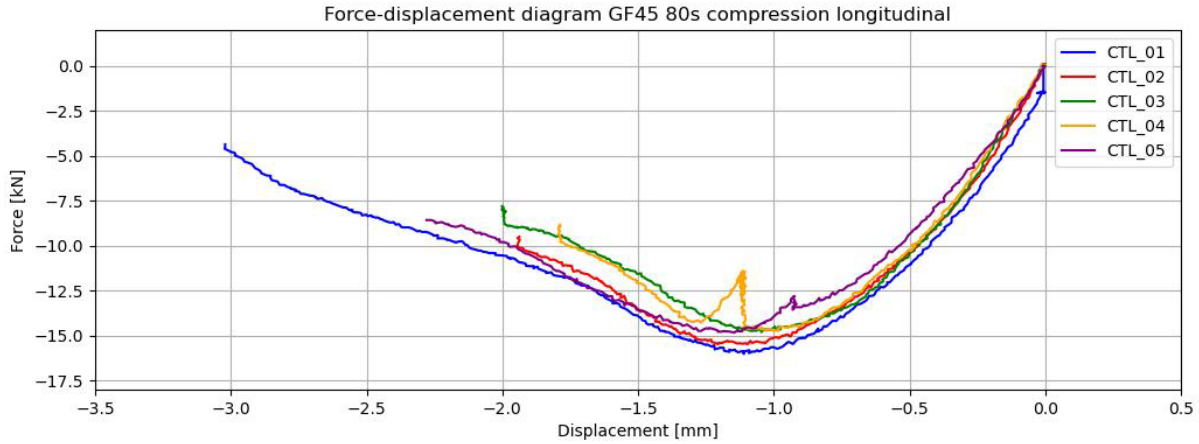

Figure C-11 Force-displacement diagram of the results obtained from the compression tests in longitudinal direction

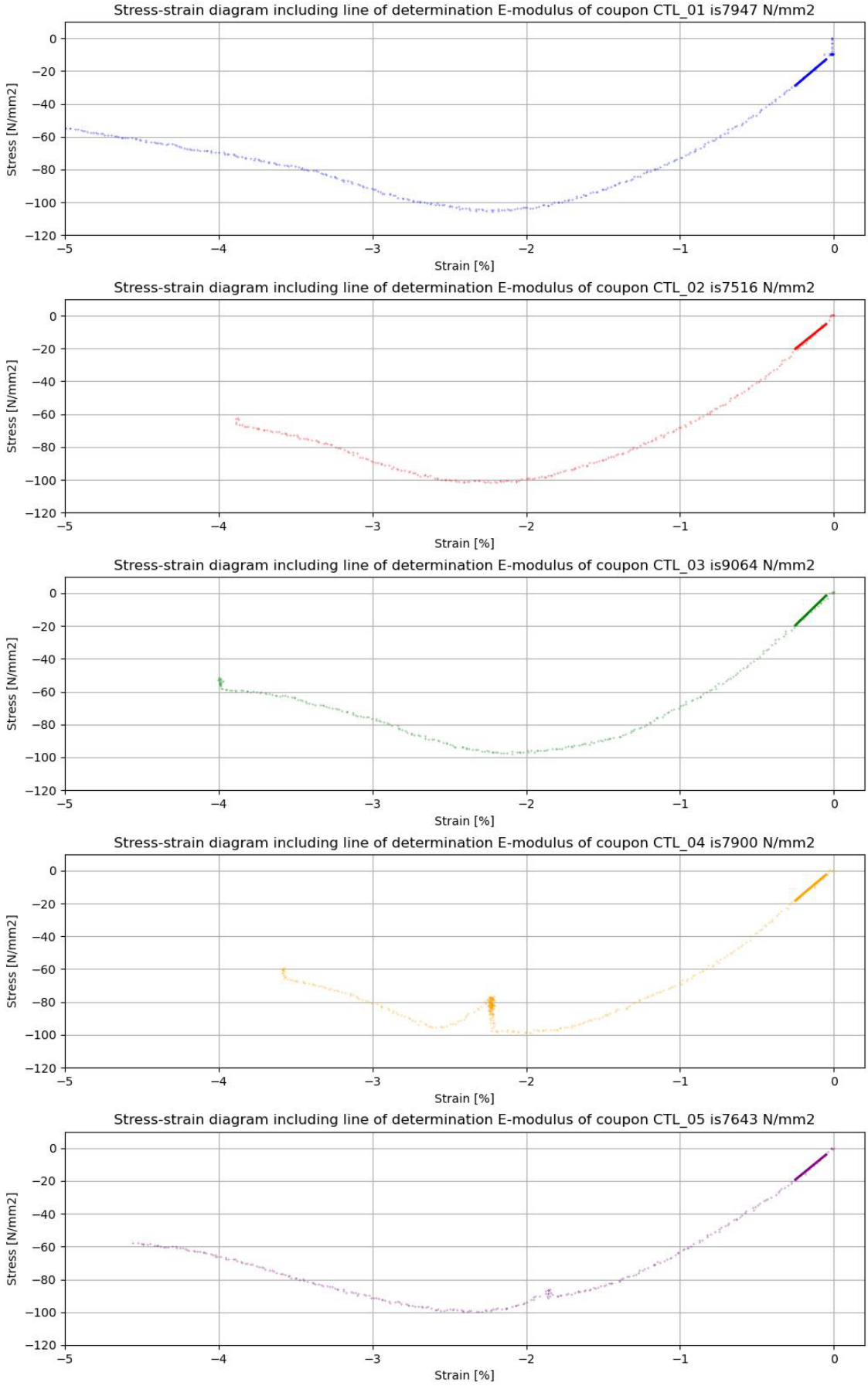

Figure C-12 Stress-strain curve of each individual longitudinal compression test with the chord slope from ε=0.05% to ε=0.25% to determine the elastic modulus

Table C-3 Values of the mechanical properties derived from the longitudinal compression tests

Test coupon	$\sigma_{1,c}$ [MPa}	$E_{1,c}$ [N/mm^2]	$\varepsilon_{1,c}$ [%]
CTL_01	-105.67	7947.0	-2.220
CTL_02	-101.56	7516.3	-2.194
CTL_03	-97.81	9063.5	-2.092
CTL_04	-98.78	7900.4	-1.970
CTL_05	-99.76	7643.0	-2.290
Mean	-100.72	8014.0	-2.153
Standard deviation	3.09	613.2	0.125
Characteristic value	-93.51		

Equations (C-9) – (C-12) calculate the characteristic value of the compression strength in longitudinal direction, $\sigma_{1,ck}$, according to Section D.7.2 from NEN-EN 1990:

$$s_X^2 = \frac{1}{n-1} * \Sigma(x_i - m_X)^2 = 3.09 \quad \text{(C-9)}$$

$$k_n = 2.33 \text{ for } n = 5 \quad \text{(C-10)}$$

$$V_X = s_X / m_X = 0.0307 \quad \text{(C-11)}$$

$$X_k = m_X * (1 - k_n * V_X) = 93.51 = \sigma_{1,ck} \quad \text{(C-12)}$$

C.2.4 Compression transverse

The force-displacement curves of the compression tests in transverse direction are plotted in Figure C-13. These are measured directly from the test machine. The stress-strain diagrams with the chord slope between the points corresponding to ε = 0.05% to ε = 0.25% for the determination of the elastic modulus of each individual test are given in Figure C-14. In Table C-4, the values of the mechanical properties obtained from the transverse compression tests are listed.

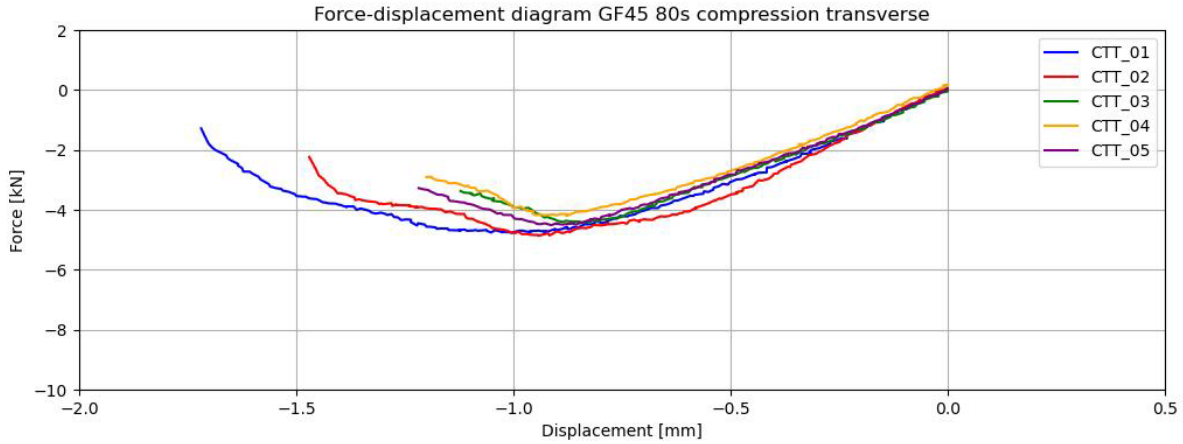

Figure C-13 Force-displacement diagram of the results obtained from the compression tests in transverse direction

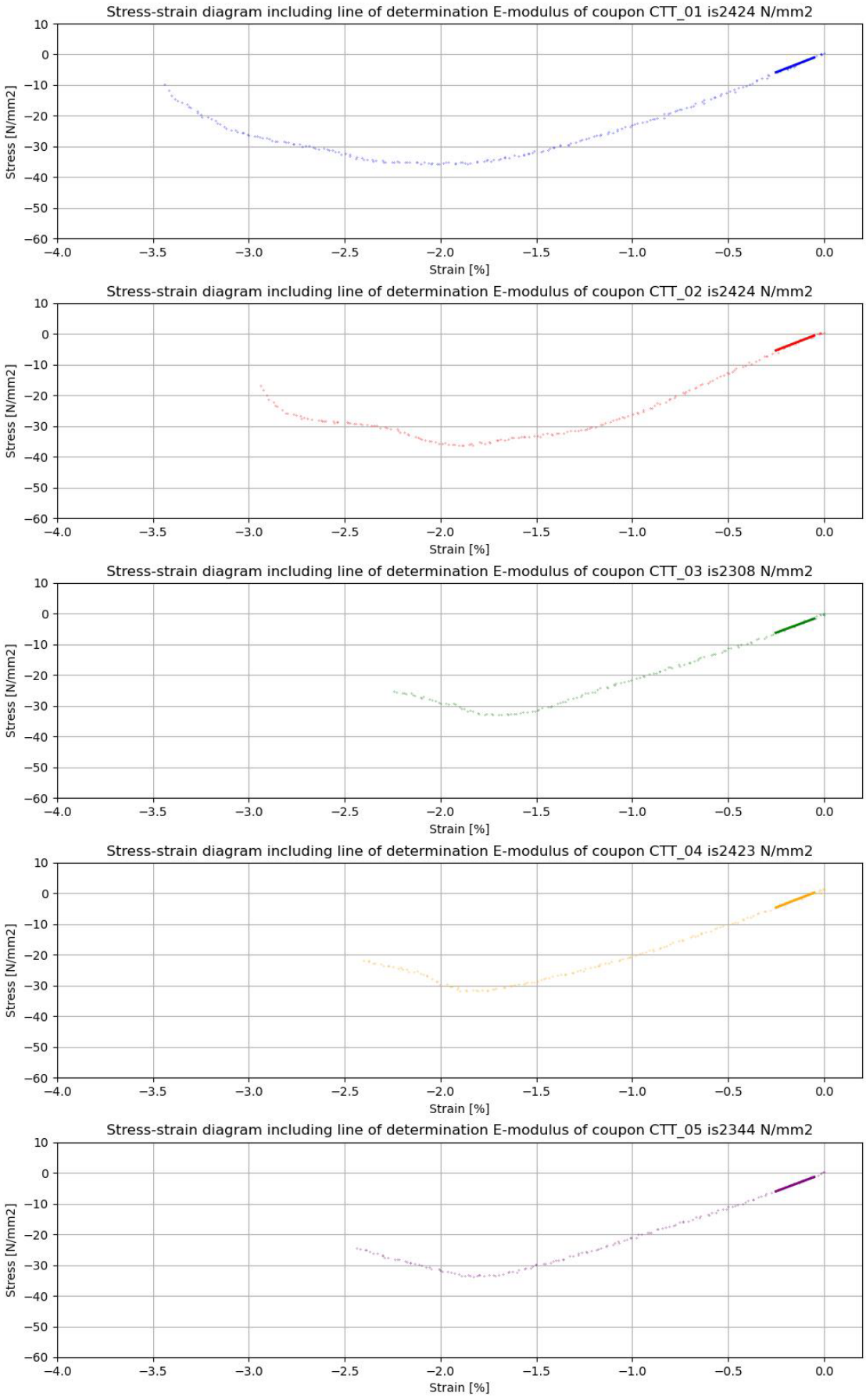

Figure C-14 Stress-strain curve of each individual transverse compression test with the chord slope from ε=0.05% to ε=0.25% to determine the elastic modulus

Table C-4 Values of the mechanical properties derived from the transverse compression tests

Test coupon	$\sigma_{2,c}$ [MPa}	$E_{2,c}$ [N/mm^2]	$\varepsilon_{2,c}$ [%]
CTT_01	-35.75	2,424.2	-1.859
CTT_02	-36.35	2,423.9	-1.884
CTT_03	-33.01	2,307.6	-1.684
CTT_04	-31.86	2,422.6	-1.757
CTT_05	-33.70	2,344.2	-1.826
Mean	-34.13	2,384.5	-1.802
Standard deviation	1.88	55.0	0.081
Characteristic value	-29.75		

Equations (C-13) – (C-16) calculate the characteristic value of the compression strength in transverse direction, $\sigma_{2,ck}$, according to Section D.7.2 from NEN-EN 1990:

$$s_X^2 = \frac{1}{n-1} * \Sigma(x_i - m_X)^2 = 1.88 \quad \text{(C-13)}$$

$$k_n = 2.33 \text{ for } n = 5 \quad \text{(C-14)}$$

$$V_X = s_X / m_X = 0.0551 \quad \text{(C-15)}$$

$$X_k = m_X * (1 - k_n * V_X) = 29.75 = \sigma_{2,ck} \quad \text{(C-16)}$$

C.2.5 IBSS

The force-displacement curves of the IBSS tests are plotted in Figure C-15. These are measured directly from the test machine. The stress-strain diagrams with the chord slope between the points corresponding to ε = 0.05% to ε = 0.25% for the determination of the elastic modulus of each individual test are given in Figure C-16. In Table C-5, the values of the mechanical properties obtained from the IBSS tests are listed.

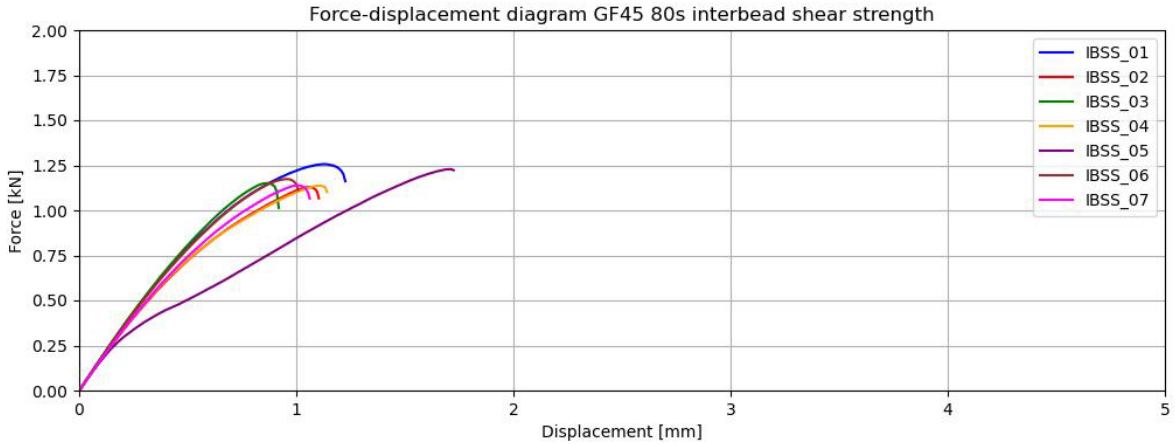

Figure C-15 Force-displacement diagram of the results obtained from the IBSS tests

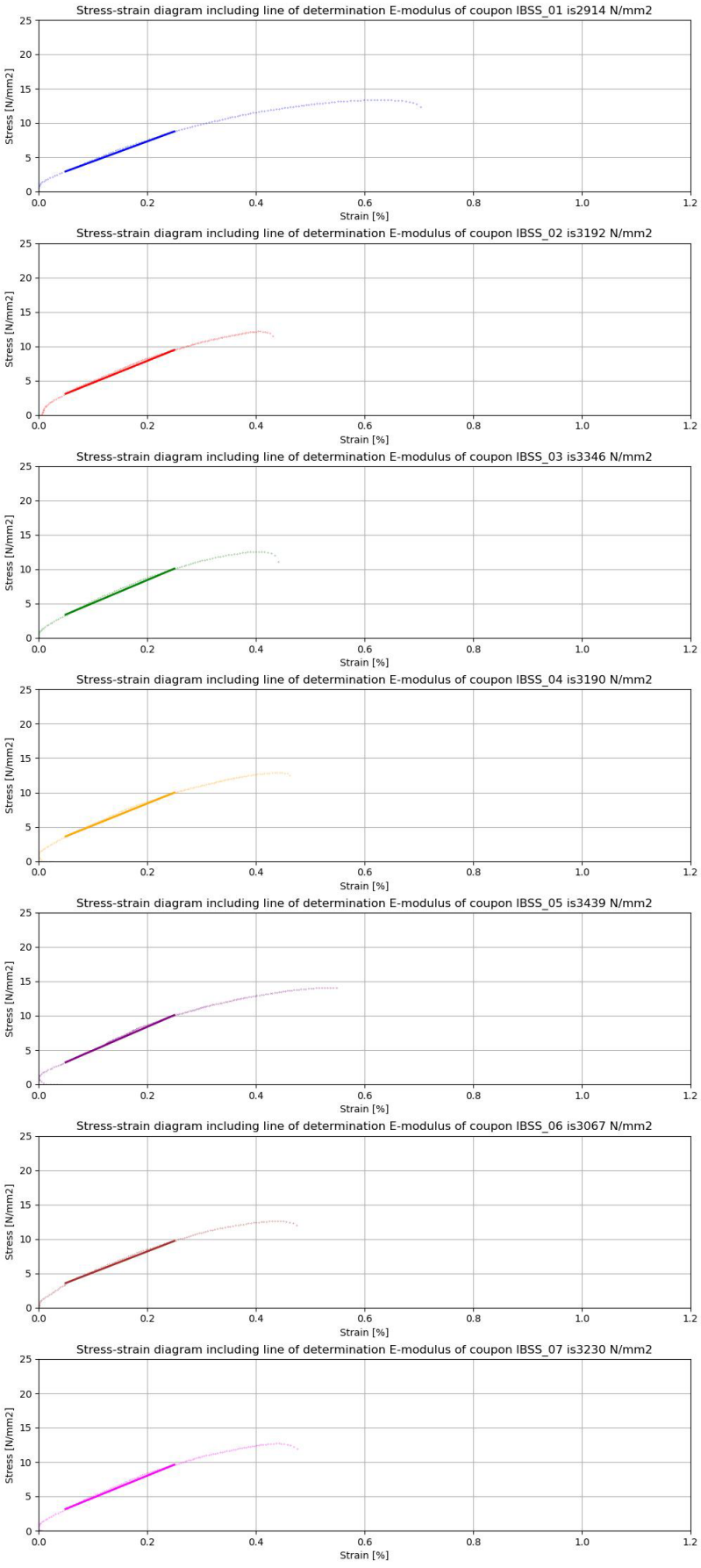

Figure C-16 Stress-strain curve of each individual IBSS test with the chord slope from ε=0.05% to ε=0.25% to determine the elastic modulus

Table C-5 Values of the mechanical properties derived from the IBSS tests

Test coupon	τ_{21} [MPa	G_{21} [N/mm^2]	γ_{21} [%]
IBSS_01	13.38	2,914.3	0.630
IBSS_02	12.16	3,192.1	0.408
IBSS_03	12.59	3,345.9	0.400
IBSS_04	12.91	3,190.4	0.439
IBSS_05	14.12	3,438.6	0.537
IBSS_06	12.59	3,067.3	0.440
IBSS_07	12.71	3,230.3	0.442
Mean	12.92	3,197.0	0.471
Standard deviation	0.64	172.5	0.083
Characteristic value	11.60		

Equations (C-17) – (C-20) calculate the characteristic value of the interbead shear strength, τ_{21}, according to Section D.7.2 from NEN-EN 1990:

$$s_X^2 = \frac{1}{n-1} * \Sigma(x_i - m_X)^2 = 0.64 \quad \text{(C-17)}$$

$$k_n = 2.06 \text{ for } n = 7 \quad \text{(C-18)}$$

$$V_X = s_X / m_X = 0.0498 \quad \text{(C-19)}$$

$$X_k = m_X * (1 - k_n * V_X) = 11.60 = \tau_{21,k} \quad \text{(C-20)}$$

D

Finite Element Analysis Component

In Chapters 8 and 9, design variants and the final variant are analysed based on FEM. For each variant, the model and the design checks are given in this Appendix.

D.1 Modelling of the component

The FEM of each variant is presented with three types of pictures: the cross section of bridge deck element modelled with the corresponding section thicknesses; the model similar to the test set-up to analyse the in-plane behaviour; and the elongated model to analyse the behaviour in the transverse direction. The loading area and the boundary conditions are shown in each figure of the models.

D.1.1 Variant 1

The FEM of Variant 1 is presented by Figure D-1 with the cross section of the bridge deck element, Figure D-2 with the model similar to the test set-up, and Figure D-3 with the elongated model.

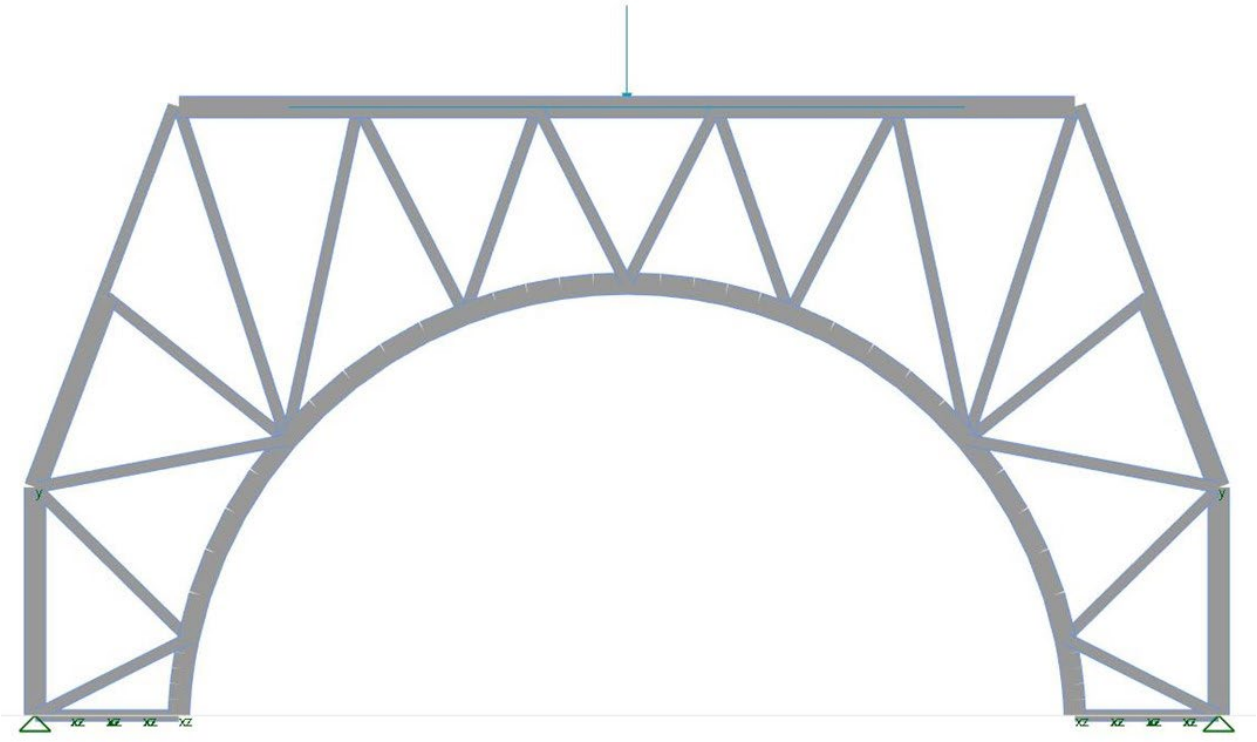

Figure D-1 Cross section of the model of component design Variant 1 in GSA with the corresponding section thicknesses

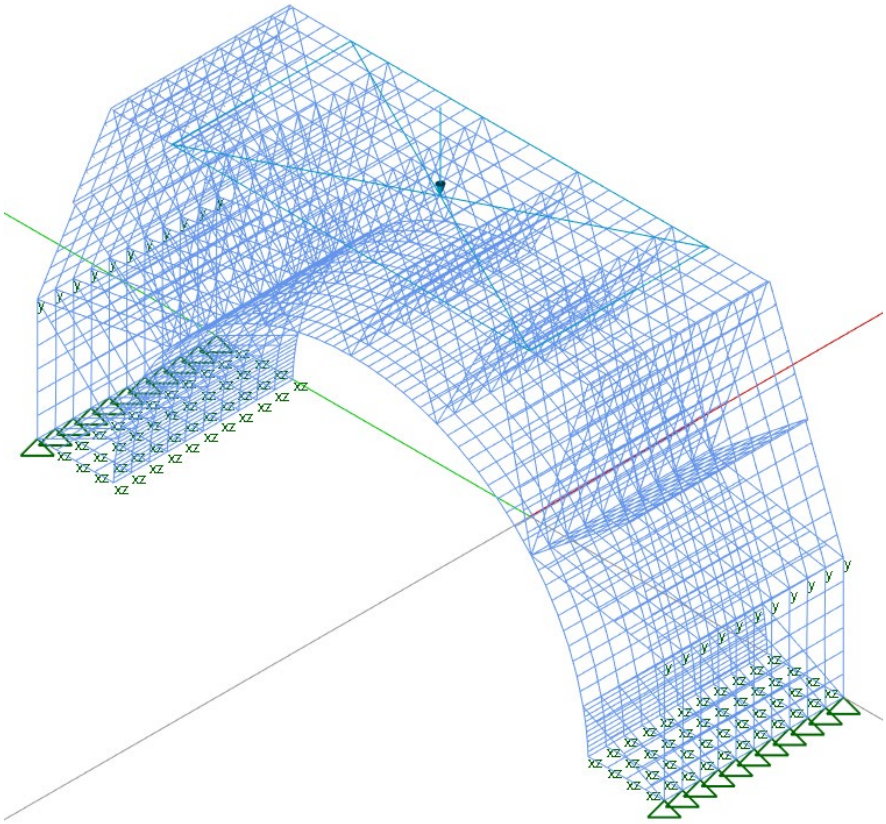

Figure D-2 GSA model similar as test set-up of Variant 1 with the applied load and the boundary conditions

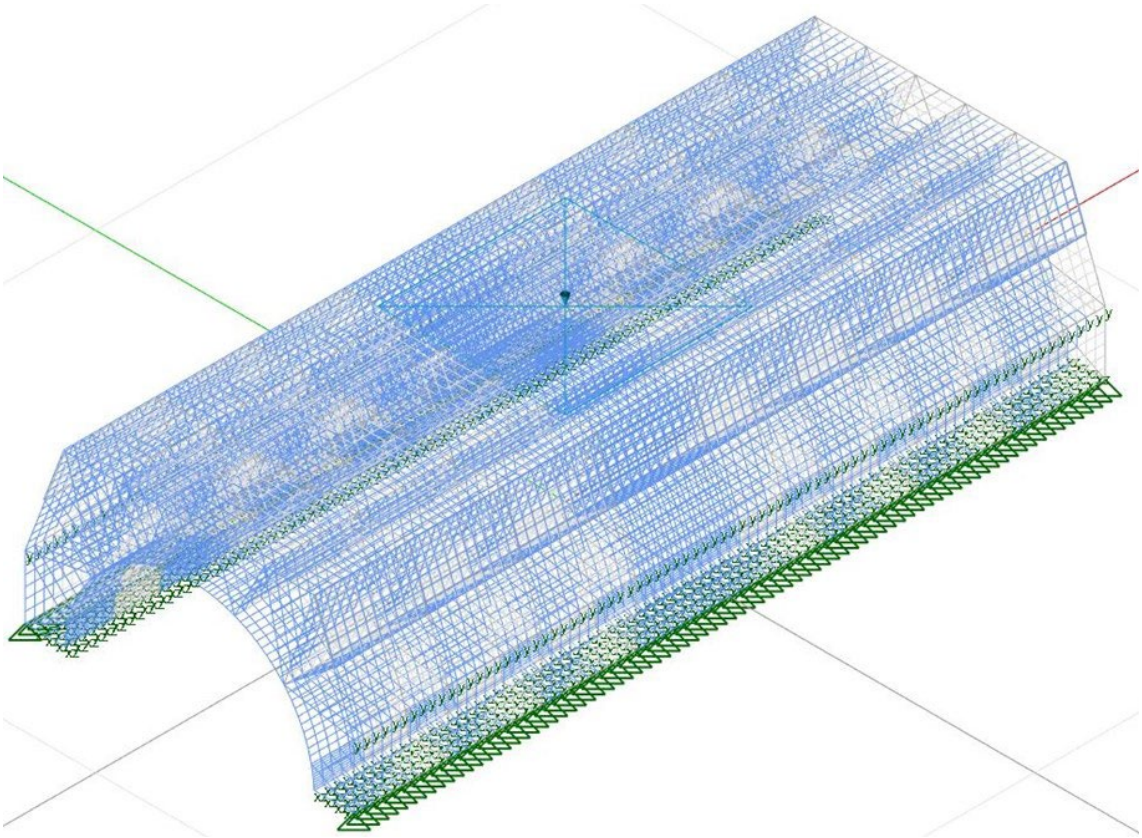

Figure D-3 Elongated GSA model of component design Variant 1 with the surface wheel load applied in the middle

D.1.2 Variant 2

The FEM of Variant 2 is presented by Figure D-4 with the cross section of the bridge deck element, Figure D-5 with the model similar to the test set-up, and Figure D-6 with the elongated model.

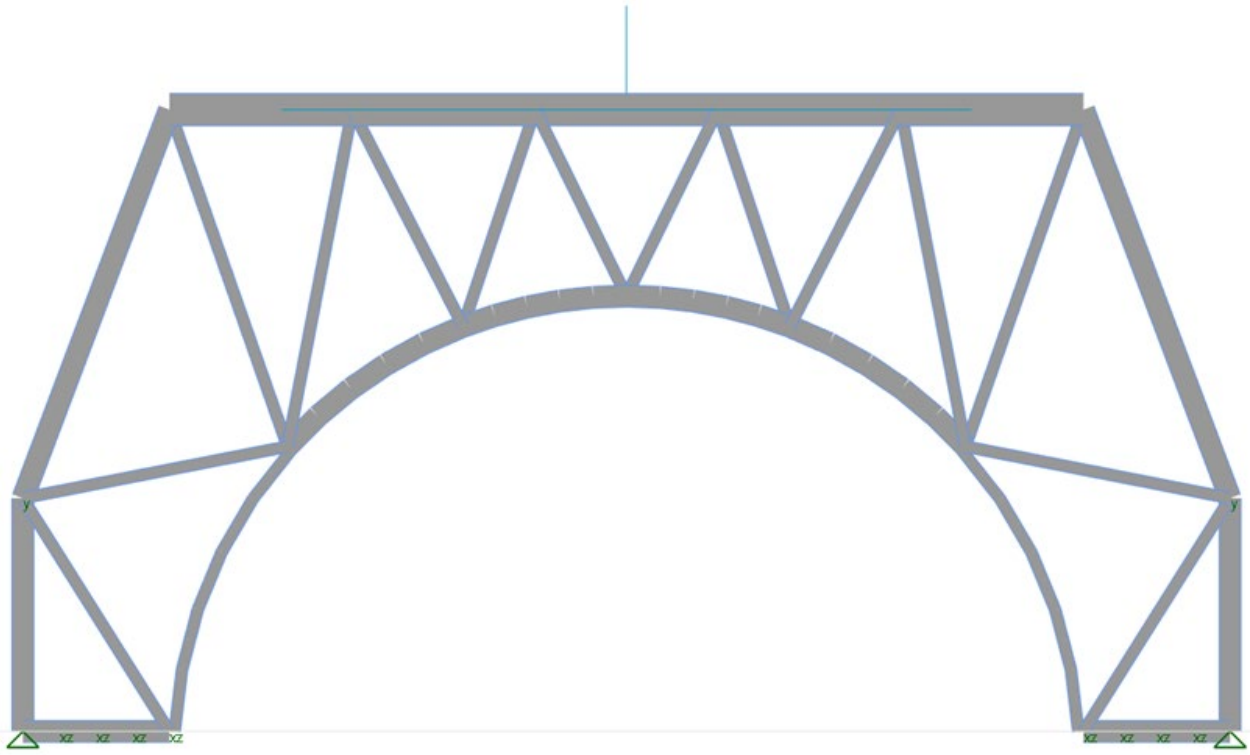

Figure D-4 Cross section of the model of component design Variant 2 in GSA with the corresponding section thicknesses

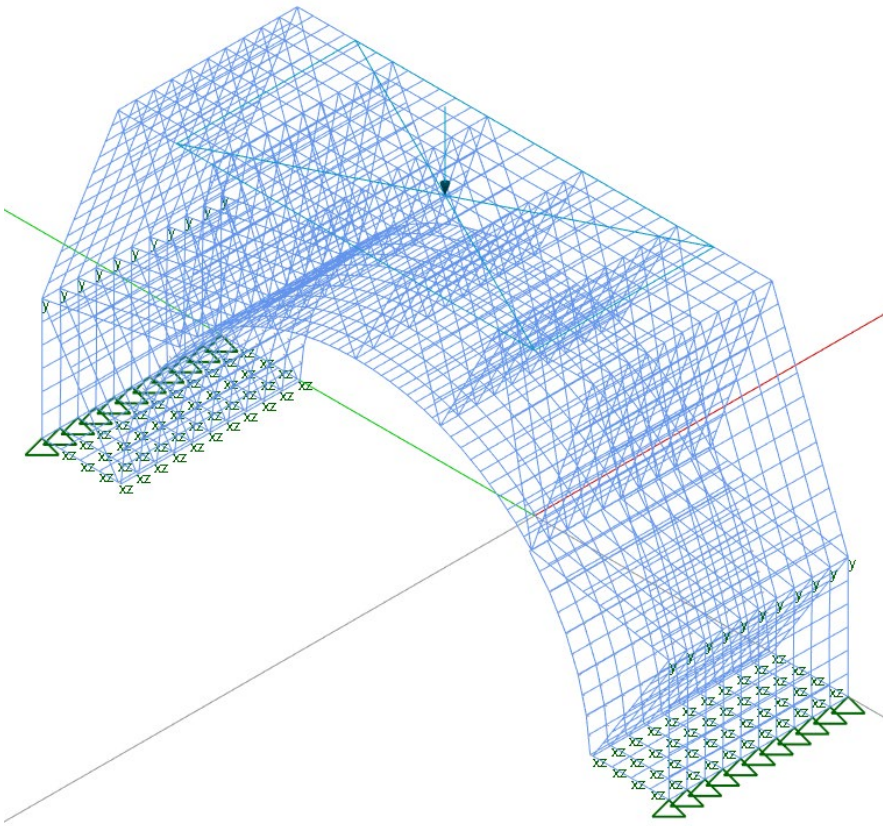

Figure D-5 GSA model similar as test set-up of Variant 2 with the applied load and the boundary conditions

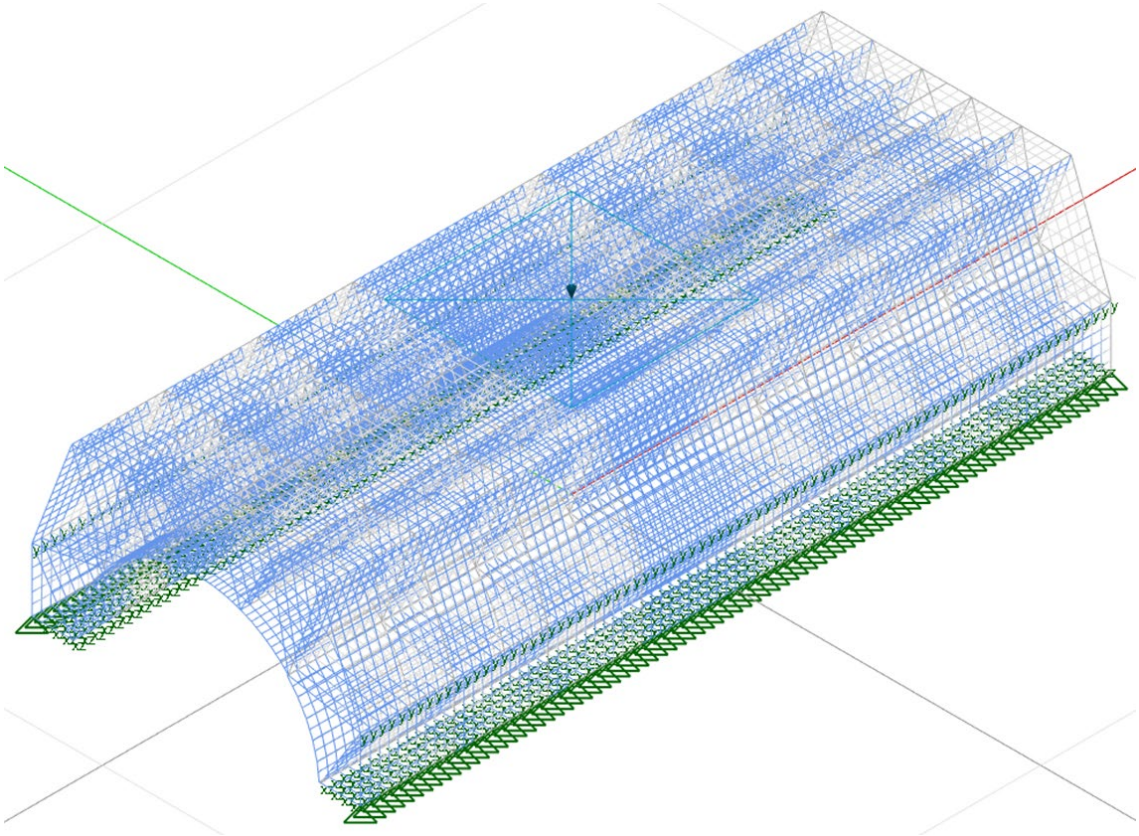

Figure D-6 Elongated GSA model of component design Variant 2 with the surface wheel load applied in the middle

D.1.3 Variant 3

The FEM of Variant 3 is presented by Figure D-7 with the cross section of the bridge deck element, Figure D-8 with the model similar to the test set-up, and Figure D-9 with the elongated model.

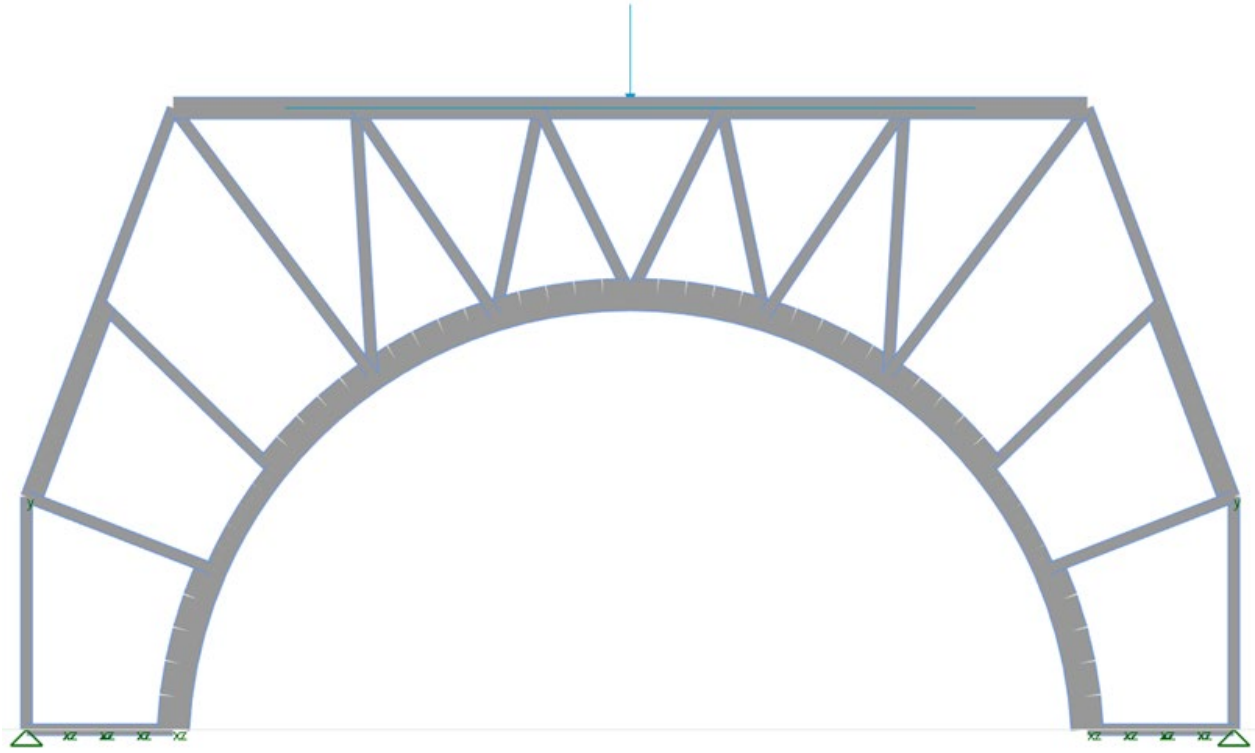

Figure D-7 Cross section of the model of component design Variant 3 in GSA with the corresponding section thicknesses

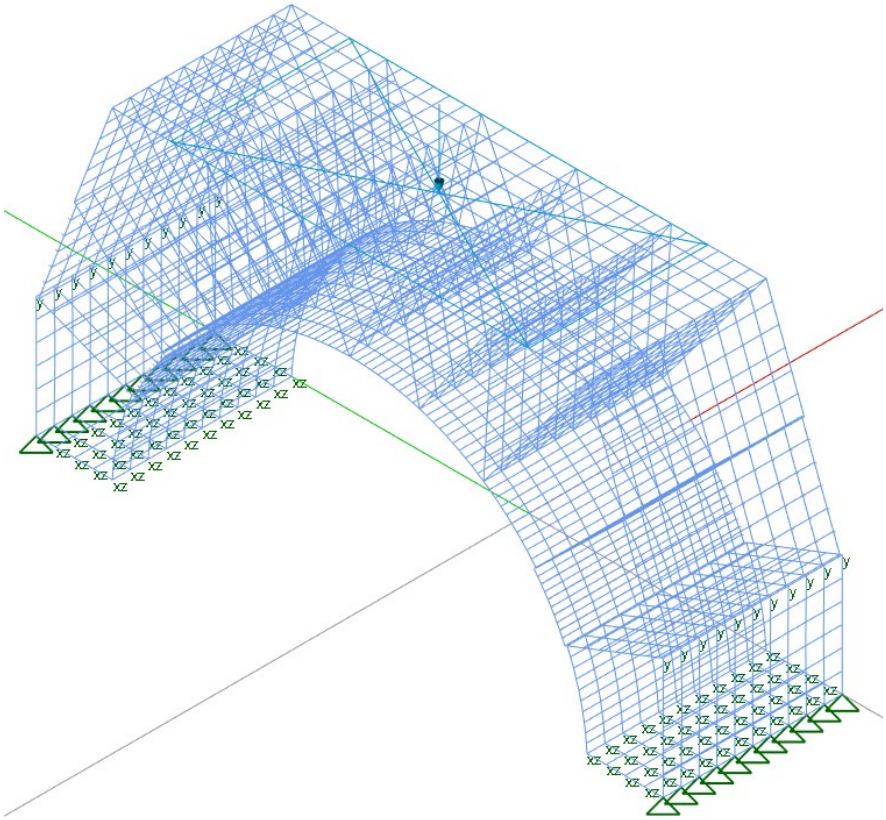

Figure D-8 GSA model similar as test set-up of Variant 3 with the applied load and the boundary conditions

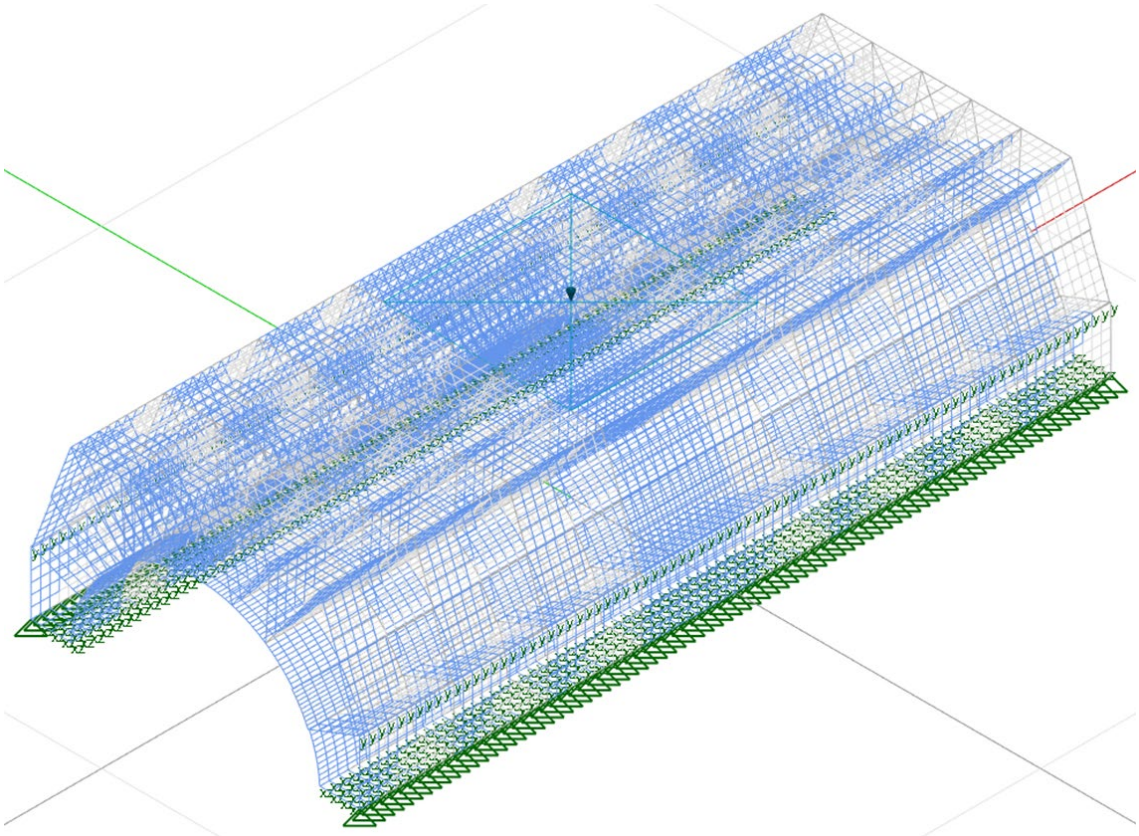

Figure D-9 Elongated GSA model of component design Variant 3 with the surface wheel load applied in the middle

D.1.4 Variant 4a

The FEM of Variant 4a is presented by Figure D-10 with the cross section of the bridge deck element, Figure D-11 with the model similar to the test set-up, and Figure D-12 with the elongated model.

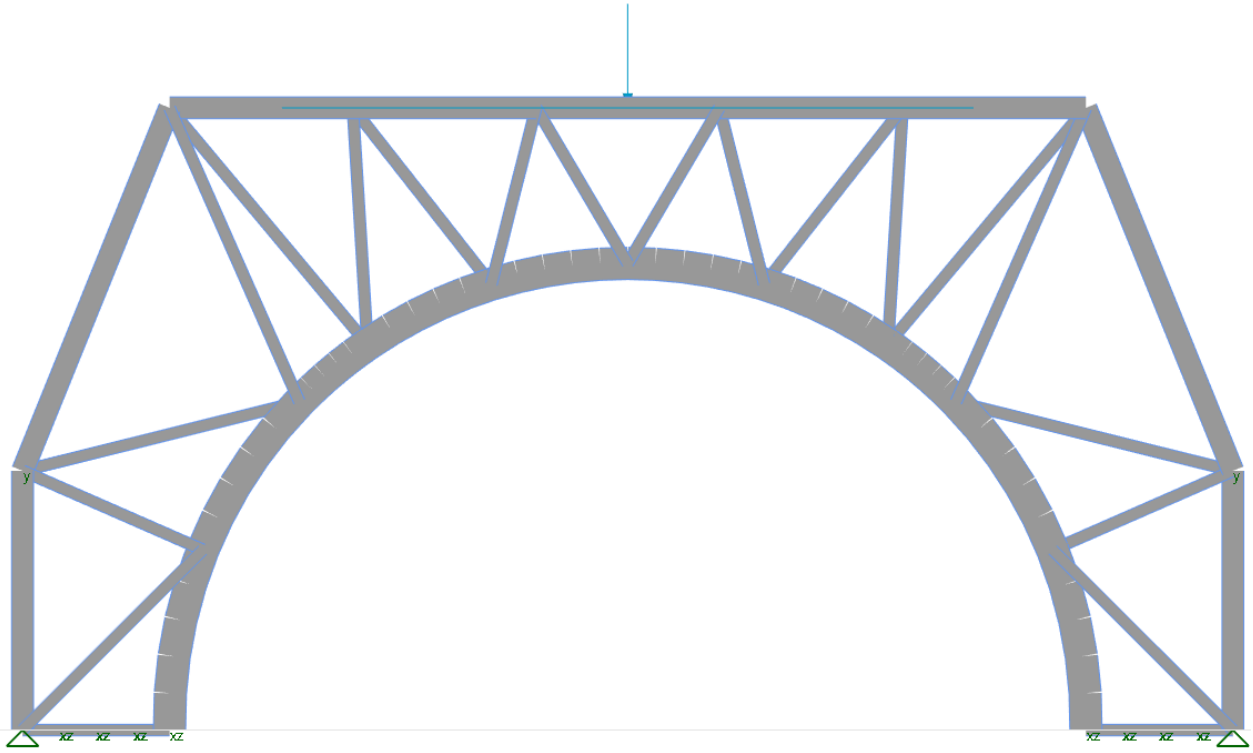

Figure D-10 Cross section of the model of component design Variant 4a in GSA with the corresponding section thicknesses

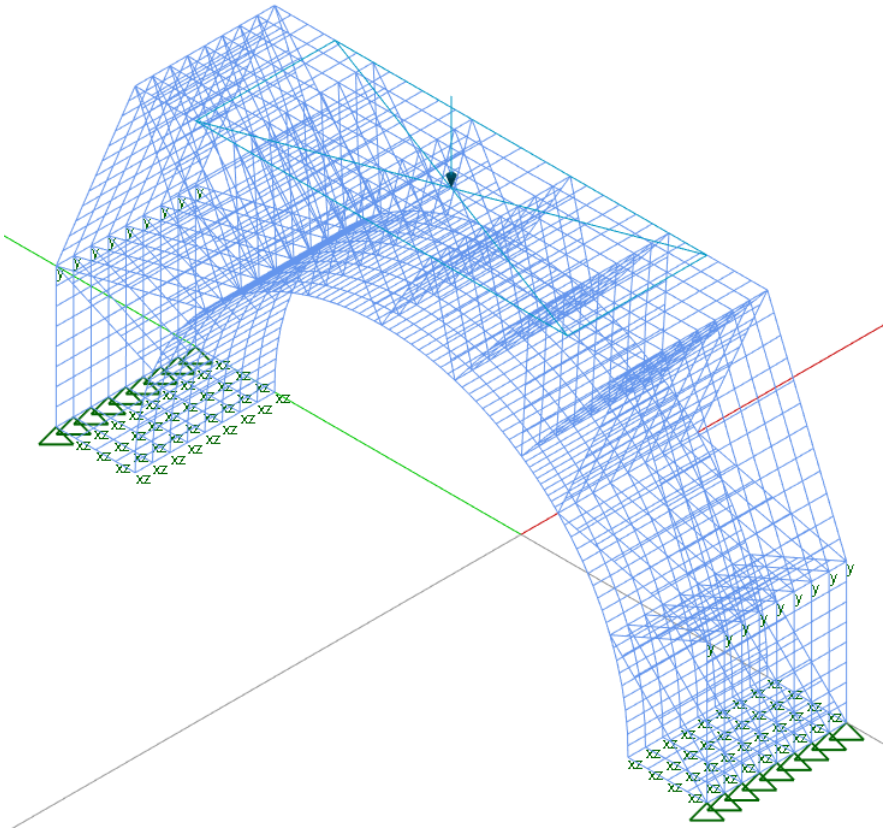

Figure D-11 GSA model similar as test set-up of Variant 4a with the applied load and the boundary conditions

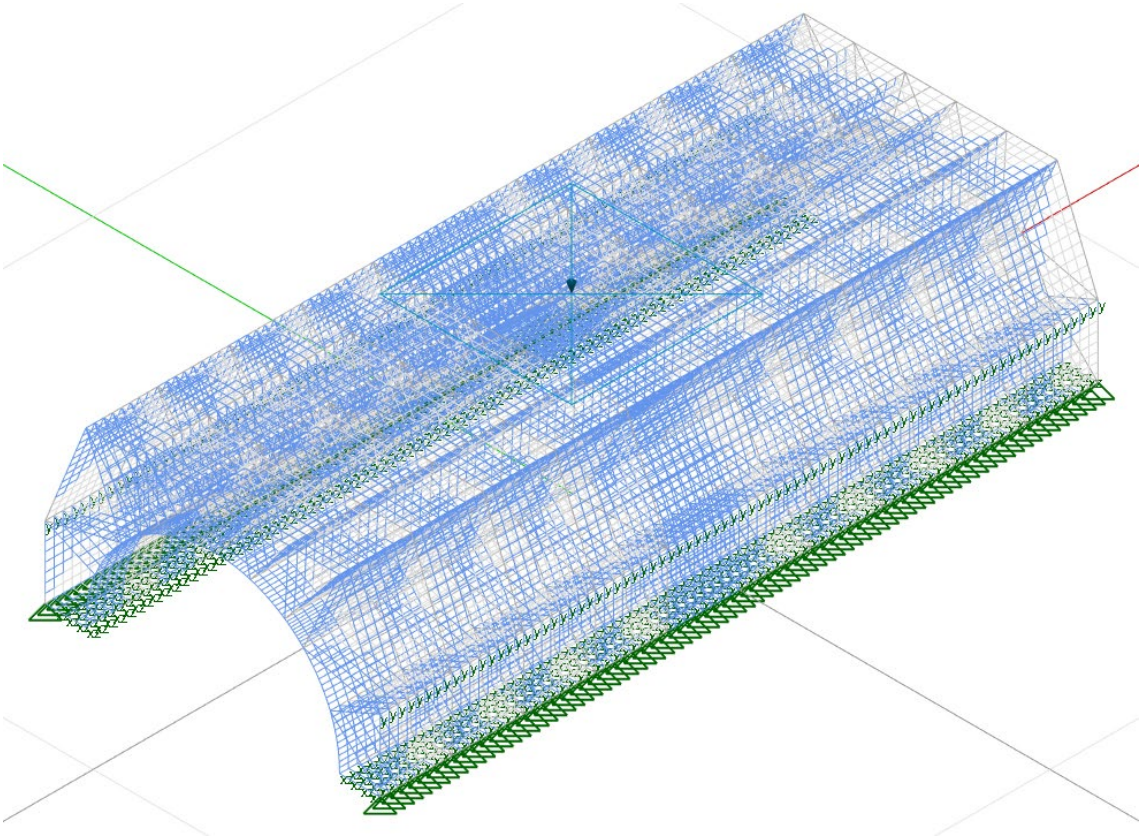

Figure D-12 Elongated GSA model of component design Variant 4a with the surface wheel load applied in the middle

D.1.5 Variant 4b

The FEM of Variant 4b is presented by Figure D-13 with the cross section of the bridge deck element, Figure D-14 with the model similar to the test set-up, and Figure D-15 with the elongated model.

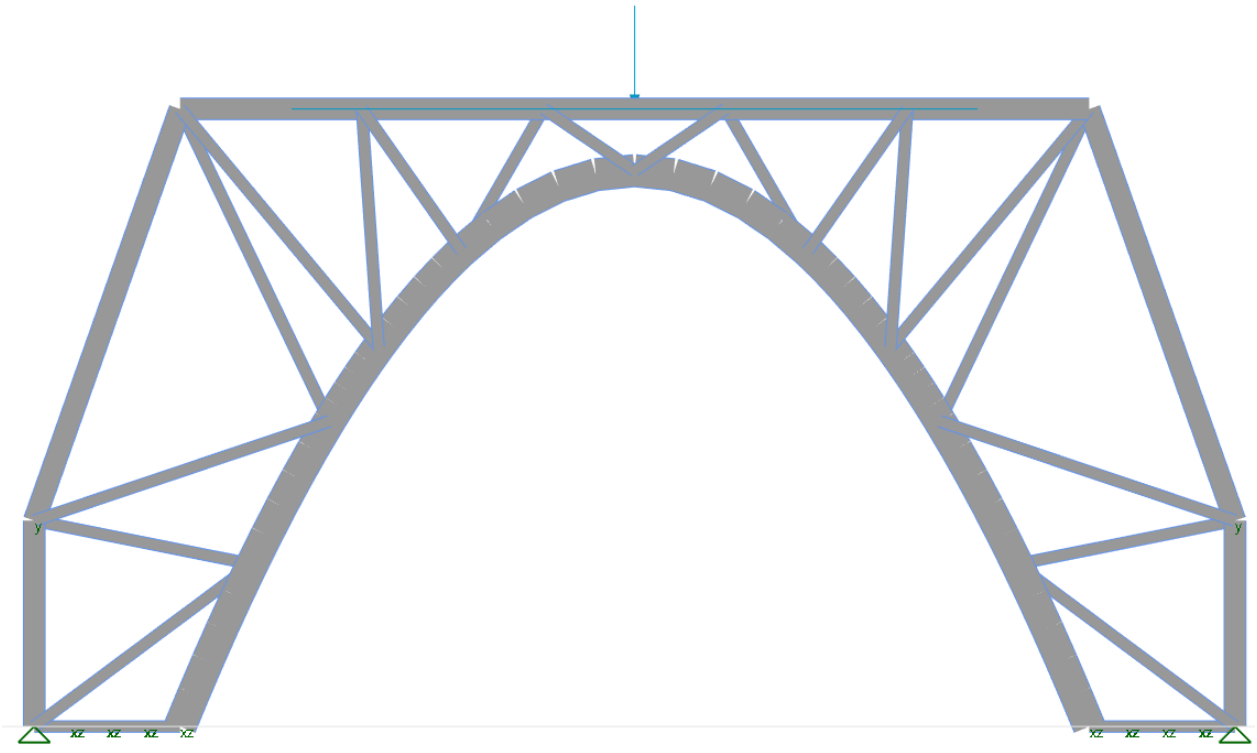

Figure D-13 Cross section of the model of component design Variant 4b in GSA with the corresponding section thicknesses

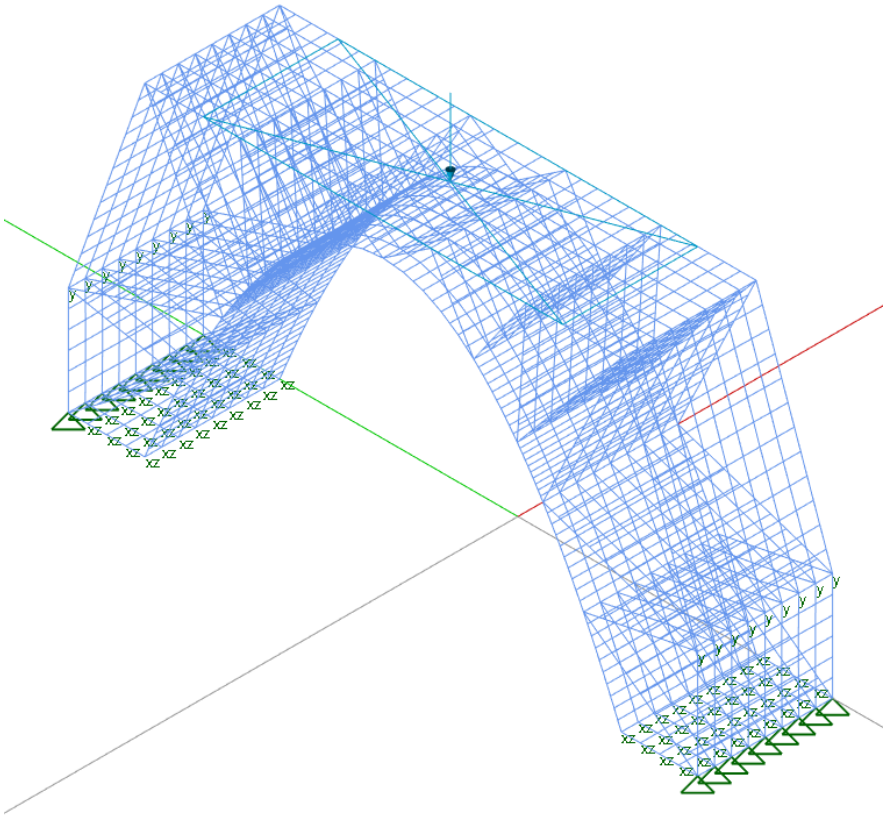

Figure D-14 GSA model similar as test set-up of Variant 4b with the applied load and the boundary conditions

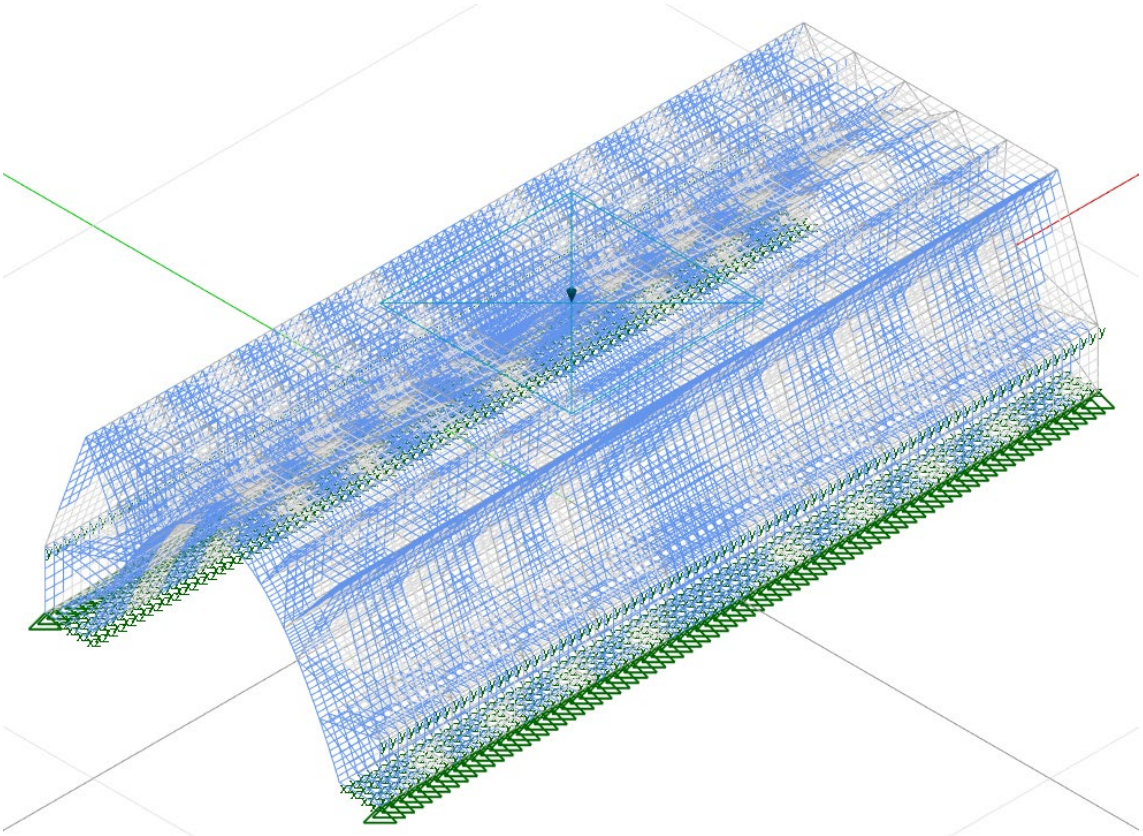

Figure D-15 Elongated GSA model of component design Variant 4b with the surface wheel load applied in the middle

D.2 Design checks

The analysis of the structural performance with the governing stresses for the design variants in Section 8.4.2 (V1, V2, V3) and Section 9.1.2 (V4a, V4b) is derived from the checks of the stresses in the different parts of the component. The considered stresses with the design limit values are listed below and the design checks in terms of the maximum stress in each part of the component are provided in Table D-1 for Variants 1, 2, and 3 and in Table D-2 for Variants 4a and 4b.

- Mid-plane stress in the principal direction of printing $\sigma_{xx,mid}$ 54.9 MPa
- Top or bottom stress in the principal direction of printing $\sigma_{xx,top/bot}$ 54.9 MPa
- Tensile mid-plane stress perpendicular to the print direction $\sigma_{yy,t,mid}$ 9.9 MPa
- Tensile top or bottom stress perpendicular to the print direction $\sigma_{yy,t,top/bot}$ 9.9 MPa
- Compression mid-plane stress perpendicular to the print direction $\sigma_{yy,c,mid}$ 17.5 MPa
- Compression top or bottom stress perpendicular to the print direction $\sigma_{yy,c,top/bot}$ 17.5 MPa
- In-plane shear stress $\sigma_{xy,mid}$ 6.8 MPa

Table D-1 Design checks of the maximum stresses in each part of the component for Variants 1, 2, and 3

Part	Aspect	V1: Most extensive infill		V2: Shorter infill with extra layer on top		V3: Medium infill and extra arch layer	
		Stress value [MPa]	Governing element	Stress value [MPa]	Governing element	Stress value [MPa]	Governing element
Arch	$\sigma_{xx,mid}$	25.80	Compression bottom part arch	15.50	Compression in outer double layer	26.30	Compression in double layered part
	$\sigma_{xx,top/bot}$	55.50	Compression intersection four stiffeners	98.90	Compression discontinuity ends single layered arch part	88.60	Compression at discontinuity arch double layer
	$\sigma_{yy,t,mid}$	1.00	Top part arch at intersection stiffeners	1.70	Top part arch at intersection stiffeners and at transition double to single layer	0.60	Top part arch at intersection stiffeners
	$\sigma_{yy,t,top/bot}$	3.00	Intersection four stiffeners	6.90	Transition from double to single layer	2.60	Lower discontinuity eccentric double layer
	$\sigma_{yy,c,mid}$	1.60	Top of arch next to the load and in bottom part arch beneath the load	1.60	Outer double layered part next to load area	1.30	Eccentric double layer next to load area

Part	Aspect	V1: Most extensive infill		V2: Shorter infill with extra layer on top		V3: Medium infill and extra arch layer	
	$\sigma_{yy,c,top/bot}$	3.00	Side part arch intersection with stiffeners	4.60	Ends single layered part	4.40	Lower discontinuity eccentric double layer
	$\sigma_{xy,mid}$	4.70	Side of the arch and at the edge of loading area	6.00	Single layered part next to load area	4.10	Eccentric double layer next to load area
Top plate	$\sigma_{xx,mid}$	12.60	Compression at middle part	13.40	Compression at middle part	9.96	Compression at middle part
	$\sigma_{xx,top/bot}$	42.30	Compression in second and fourth span	32.60	Compression in second and fourth span	41.80	Compression in second and fourth span
	$\sigma_{yy,t,mid}$	0.90	Middle part top plate next to load area	0.60	Middle part top plate next to load area	0.90	Middle part top plate next to load area
	$\sigma_{yy,t,top/bot}$	3.70	Second and fourth span edge load area	1.30	Second and fourth span edge load area	3.70	Second and fourth span edge load area
	$\sigma_{yy,c,mid}$	3.80	Middle part top plate beneath load	3.90	Middle part top plate below load area	3.70	Middle part top plate below load area
	$\sigma_{yy,c,top/bot}$	7.40	Second and fourth span	5.90	Second and fourth span	7.40	Second and fourth span
	$\sigma_{xy,mid}$	2.50	Edge load area intersection stiffeners	2.20	Edge load area intersection stiffeners	2.40	Edge load area intersection stiffeners
Side + bottom plates	$\sigma_{xx,mid}$	13.10	Compression at inclined side plate	18.40	Compression at inclined side plate	11.40	Compression at bottom support
	$\sigma_{xx,top/bot}$	23.90	Compression top part inclined side	31.40	Compression top part inclined side	26.40	Compression at bottom support
	$\sigma_{yy,t,mid}$	0.40	Next to load area and below load at top straight side plate	0.30	Next to load area and below load at top straight side plate	0.50	Next to load area and below load at top straight side plate
	$\sigma_{yy,t,top/bot}$	0.50	Next to load area at top	0.50	Next to load area at top inclined side plate	0.80	Next to load area at top

Part	Aspect	V1: Most extensive infill		V2: Shorter infill with extra layer on top		V3: Medium infill and extra arch layer	
			inclined side plate				inclined side plate
	$\sigma_{yy,c,mid}$	2.70	Top part inclined side plate	3.20	Top part inclined side plate	2.50	Top part inclined side plate
	$\sigma_{yy,c,top/bot}$	3.60	Top part inclined side plate	4.00	Top part inclined side plate	2.60	Top part inclined side plate
	$\sigma_{xy,mid}$	1.90	Top part inclined side plate next to load area	1.30	Top part inclined side plate next to load area	2.70	Top part inclined side plate next to load area
Infill	$\sigma_{xx,mid}$	31.20	Compression in stiffener top corner triangle	42.90	Compression in 'horizontal' stiffener from kink in side plate	36.40	Compression in stiffener top corner triangle
	$\sigma_{xx,top/bot}$	36.70	Compression in top stiffener corner triangle	52.00	Compression in 'horizontal' stiffener from kink in side plate at arch intersection	54.10	Compression in stiffener top corner triangle
	$\sigma_{yy,t,mid}$	2.30	Intersection with arch	4.40	Corner stiffener at intersection with arch	2.20	Intersection with arch
	$\sigma_{yy,t,top/bot}$	3.20	Intersection with arch	4.50	Corner stiffener at intersection with arch	2.80	Intersection with arch
	$\sigma_{yy,c,mid}$	5.30	Intersection with top plate	5.50	Intersection with top plate	5.40	Intersection with top plate
	$\sigma_{yy,c,top/bot}$	5.70	Intersection with top plate	5.70	Intersection with top plate	6.40	Intersection with top plate
	$\sigma_{xy,mid}$	5.50	Middle stiffeners edge load area	6.30	Middle stiffeners edge load area	5.60	Middle stiffeners edge load area

Table D-2 Design checks of the maximum stresses in each part of the component for Variants 4a and 4b

Part	Aspect	V4a: Circular arch		V4b: Parabolic arch	
		Stress value [MPa]	Governing element	Stress value [MPa]	Governing element
Arch	$\sigma_{xx,mid}$	19.90	Compression part between top corner stiffeners	17.10	Compression part between top corner stiffeners
	$\sigma_{xx,top/bot}$	30.70	Compression between 'horizontal' stiffeners	23.00	Compression at intersection with stiffener next to middle one
	$\sigma_{yy,t,mid}$	0.30	Intersection with stiffeners next to middle below load	0.20	Intersection with stiffeners next to middle below load and in middle part next to load
	$\sigma_{yy,t,top/bot}$	1.60	Intersection middle three stiffeners below load	1.20	Intersection with stiffeners next to middle below load
	$\sigma_{yy,c,mid}$	1.30	Intersection with middle five stiffeners next to load	1.20	Part between corner stiffeners next to load
	$\sigma_{yy,c,top/bot}$	1.60	Intersection with stiffeners next to middle below load	2.30	Middle part below load
	$\sigma_{xy,mid}$	3.40	Between top corner triangle stiffeners next to load	3.10	Part between corner stiffeners next to load
Top plate	$\sigma_{xx,mid}$	7.80	Compression middle span	4.30	Compression side spans
	$\sigma_{xx,top/bot}$	39.90	Compression in second and fourth span	35.70	Compression in second and fourth span
	$\sigma_{yy,t,mid}$	1.00	Middle three spans next to load	0.70	Middle three spans next to load
	$\sigma_{yy,t,top/bot}$	3.80	Second and fourth span at edge of load	4.20	Second and fourth span at edge of load
	$\sigma_{yy,c,mid}$	2.90	Middle part below load	1.60	Whole width
	$\sigma_{yy,c,top/bot}$	6.70	Second and fourth span below load	6.10	Second and fourth span below load
	$\sigma_{xy,mid}$	2.20	Edge load area intersection stiffeners	1.30	Edge load area intersection stiffeners

Part	Aspect	V4a: Circular arch		V4b: Parabolic arch	
Side + bottom plates	$\sigma_{xx,mid}$	4.90	Compression bottom support plate / inclined part	14.60	Compression bottom support plate / inclined part
	$\sigma_{xx,top/bot}$	12.90	Compression support plate in top inclined side plate	16.50	Compression inner edge bottom support plate
	$\sigma_{yy,t,mid}$	0.44	Next to load area at top inclined part	0.34	Next to load area at top inclined part
	$\sigma_{yy,t,top/bot}$	0.50	Next to load area at top inclined part	0.36	Next to load area at top inclined part
	$\sigma_{yy,c,mid}$	1.60	Top inclined part below load	1.40	Top inclined part below load
	$\sigma_{yy,c,top/bot}$	2.00	Top inclined part below load	1.80	Top inclined part below load
	$\sigma_{xy,mid}$	0.80	Top inclined part and top straight part next to load	0.70	Straight parts edge load
Infill	$\sigma_{xx,mid}$	27.50	Compression in vertical stiffener	24.40	Compression in short stiffener next to middle
	$\sigma_{xx,top/bot}$	42.60	Compression in vertical stiffener	25.50	Compression in middle four stiffeners
	$\sigma_{yy,t,mid}$	2.10	Two intersections with arch next to middle stiffener below load	1.50	Corner stiffeners intersection with arch below load
	$\sigma_{yy,t,top/bot}$	2.40	Two intersections with arch next to middle stiffener below load	1.70	Corner stiffeners intersection with arch below load
	$\sigma_{yy,c,mid}$	4.60	Four middle intersections with top plate below load	3.60	Two middle intersections with top plate below load
	$\sigma_{yy,c,top/bot}$	5.50	Second and fifth intersection with top plate below load	3.90	Two middle intersections with top plate below load
	$\sigma_{xy,mid}$	5.20	Four middle stiffeners below load	4.20	Four middle stiffeners below load